Aus dem Institut für Pharmakologie
der Medizinischen Fakultät Charité – Universitätsmedizin Berlin

DISSERTATION

Proteomanalytik und bildgebende Diagnostik am Maus-Modellsystem

zur Erlangung des akademischen Grades
Doctor rerum medicinalium (Dr. rer. medic.)

vorgelegt der Medizinischen Fakultät
Charité – Universitätsmedizin Berlin

von

Boris Alexander Neumann

aus Berlin

Datum der Promotion: 30.11.2023

Inhaltsverzeichnis

Abstract

In der vorliegenden Arbeit wurden mittels Proteomanalyse geschlechtsspezifische Abundanzunterschiede für eine Reihe von Proteinen im murinen Myokardium identifiziert, darunter auch solche die sich als potentielle Biomarker für kardiovaskuläre Erkrankungen eignen. In einer zweiten Studie wurde an einem Maus-Modellsystem für Frontotemporale Demenz mittels Fraktionierung und Charakterisierung der isolierten Protein-Spezies gezeigt, dass sich pathologische Tau-Proteinspezies in den Synapsen akkumulieren. Diese nicht-phosphorylierten und oligomerisierten Proteinspezies könnten in direktem Zusammenhang mit kognitiven Einschränkungen der Tiere stehen. In den drei Veröffentlichungen zum Bioimaging wurde ein Standardisierungsverfahren für die bildgebende LA-ICP-Massenspektrometrie entwickelt. Durch das neuartige Verfahren, bei dem ein Standard durch Tintenstrahldruck homogen und reproduzierbar auf FFPE-Gewebeproben aufgebracht wird, konnte das Problem der instrumentellen Drift von LA-ICP-Messgeräten ausgeglichen werden. Dies erlaubte die eindeutige Zuordnung kleinster Abundanzunterschiede für Biomarker in einem Mausmodell für Morbus Parkinson.

In this thesis proteome analysis was utilized to identify proteins in murine myocardium that are regulated by gonadal hormones. Some of these could potentially act as biomarkers for cardiovascular diseases. In a second study protein fractionation and characterization was performed for a murine model of frontotemporal dementia. Analysis of the isolated protein-species revealed that pathologic tau-protein species are accumulated within the synapse. These non-phosphorylated and oligomeric protein species could have a direct impact on cognitive impairment of the animals. Within the three papers on bioimaging a standardization technique for LA-ICP mass spectrometry was developed. The novel approach is using ink-jet printing to apply a standard homogenously and reproducible onto the surface of FFPE-sample slides. The new method allows to compensate instrumental drifts and therefore to discriminate minimal variations of biomarker abundances within a murine model for parkinson's disease.

1 Einführung

Im Gegensatz zur Genomik mit ihrem Fokus auf das starre Genom eines Individuums, bezieht sich die Proteomik [1], [2] auf die Gesamtheit aller Proteine in einen Zell- oder Gewebetyp oder Organismus zu einem möglichst definiertem Zeitpunkt oder Zustand. Während das Genom eines Individuums als festgelegt betrachtet werden kann, zeigt sich das Proteom als sehr dynamisch, im Hinblick auf äußere oder innere Faktoren. Seine Veränderlichkeit prädestiniert das Proteom für die medizinische Forschung als Untersuchungsgegenstand für die Wirkung von Arzneistoffen und die Identifikation von Biomarkern für bestimmte Krankheitszustände. Anders als in klassischen biochemischen Untersuchungsmethoden, z.B. der Analyse eines bestimmten Proteins, kann die Analyse des Proteoms weitgehend hypothesefrei erfolgen, was die Aufklärung unbekannter Wirkmechanismen und Regulationen vereinfacht. In Proteomen biologischer Flüssigkeiten, bei denen die Proteinmasse aus nur wenigen Proteinen besteht (z.B. 98% verteilt auf nur 20 Proteine in Serum) [3], stoßen auch moderne Techniken auf Grenzen [4]–[6], gleiches gilt für hochkomplexe Proteome (z.B. Hirnproteome). Proteomanalytische Verfahren bestehen deshalb meist aus kombinierten Techniken wie 1D-/2D-Gelelektrophorese mit Massenspektrometrie (MS) [7] oder Flüssigkeitschromatographie mit MS [8], bei Serum auch in mehrstufigen Verfahren zur Vor-Abreicherung hochabundanter Proteine [9].

Die Methoden der Proteomanalytik haben sich in den letzten Jahrzehnten aufgrund von Fortschritten in der Massenspektrometrie, der Fraktionierungstechnik und Bioinformatik stark erweitert. So können differentiell abundante Proteine im Proteom nicht nur identifiziert sondern auch charakterisiert werden, zum Beispiel im Hinblick auf post-translationale Modifikationen (PTM) und *Splice*-Isoformen. In diesem Zusammenhang spricht man von Proteoformen [10] oder Proteinspezies [11], [12]. Schätzungen zufolge, werden aus den 20.000 genetisch kodierten Proteinen Millionen verschiedene Proteinspezies gebildet, mit unterschiedlichen Funktionen[13], [14].

Die Identifikation und Aufklärung im Hinblick auf Splice-Isoformen oder PTMs von charakteristischen Proteinspezies, die einem Zustand zugeordnet werden können, ermöglicht deren Nutzung als Biomarker für die Diagnostik [15], [5]. Ein klassisches Beispiel für einen Biomarker ist die humane Erb-b2 *receptor tyrosine kinase 2*, oder auch Her2/neu. Her2/neu ist in bestimmten Mammakarzinomen stark überexprimiert

und kann zur Klassifikation in der Histologie über immunhistochemische Methoden genutzt werden, darüber hinaus kann Her2/neu in Brust- und anderen Tumoren als sogenanntes *Target* von pharmazeutischen monoklonalen Antikörpern adressiert werden [16]. In der Histologie können Biomarker über immunhistochemische Methoden (IHC) angefärbt und lichtmikroskopisch untersucht werden. Hierbei werden meist einzelne Biomarker auf Gewebeschnitten angefärbt, die semi-quantitative Auswertung erfolgt subjektiv durch Pathologen, teilweise unter Zuhilfenahme von Bildanalysesoftware [17]. Durch Fortschritte im Bereich der ICP-MS-Element-Massenspektrometrie und deren Kopplung an Laser-Ablationssysteme (LA) können Biomarker in Gewebeschnitten auch massenspektrometrisch nachgewiesen werden. Die Vorteile des sogenannten Bioimagings per LA-ICP-MS als bildgebendes Verfahren [18] sind, der hohe dynamische Bereich [19] heutiger ICP-MS Instrumente und die Möglichkeit mehrere Biomarker parallel im Multiplex-Verfahren zu detektieren. Methodisch ist die Probenvorbereitung hierfür an etablierte IHC-Protokolle angelehnt, mit dem Unterschied, dass die eingesetzten spezifischen Antikörper als *Tag* ein Heteroatom tragen. Als Heteroatome für die indirekte Detektion eines Biomarkers über einen konjugierten ge*tagg*ten-Antikörper kommen häufig Lanthanide und andere Metalle zum Einsatz, da sie natürlicherweise nicht in Geweben vorkommen und in stabilen Komplexen an Antikörper gebunden werden können [20]–[22]. Nachteile beim Bioimaging über LA-ICP-MS sind die lange Ablationszeit und die damit einhergehende instrumentelle Drift des Messaufbaus [23] bei kaum geeigneten Standardisierungs- oder Normalisierungstechniken [24]. In der vorliegenden Arbeit wurden durch den Einsatz proteomanalytischer Techniken potentielle Biomarker identifiziert, in einer zweiten Studie Biomarker fraktioniert und charakterisiert. Als bildgebendes Verfahren wurde in weiteren Studien ein Bioimaging-Ansatz entwickelt. Die inhärenten Nachteile der LA-ICP-MS konnten durch die Entwicklung eines geeigneten Standardisierungs- und Normalisierungsverfahrens minimiert werden. Durch diese neuartige Standardisierung wurde eine konstante Bildqualität und Reproduzierbarkeit über lange Messzeiten hinweg ermöglicht.

2 Material und Methodik

Alle Tierversuche erfolgten in Übereinstimmung mit genehmigten Tierversuchsanträgen (G 0050/07) oder gemäß der EU Richtlinie 2010/63/EU und nach Genehmigung durch das LAGESO (A0213/13).

In den fünf eingereichten Publikationen wurde eine Vielzahl von Methoden eingesetzt. Diese erstrecken sich über proteom- und proteinanalytische Verfahren, massenspektrometrische Proteinidentifikation und –charakterisierung, Histologie, molekularbiologische Verfahren bis zu Element-massenspektrometrischen Techniken zum Nachweis von Heteroatomen in biologischen Proben.

Alle eingesetzten Methoden sind in den beigefügten Publikationen oder deren *Electronic Supplementary Material* (ESI) detailliert beschrieben.

3 Ergebnisse

3.1 Studie 1: Sex differences in murine myocardium are not exclusively regulated by gonadal hormones

In dieser Studie [25] wurden geschlechtsspezifische Unterschiede im kardialen Proteinmuster von intakten und kastrierten Mäusen untersucht. Als Analysenmethoden kamen dabei hochauflösende 2D-Gelelektrophorese, Massenspektrometrie (MS) zur Proteinidentifikation und –charakterisierung, molekularbiologische Techniken sowie Immunoblotting (1- und 2-dimensional) zum Einsatz. Um Entwicklungsunterschiede durch die Gonadektomie auszuschließen, erfolgte diese bei den Tieren erst im Alter von drei Monaten.

Komparative 2D-Gelanalysen ergaben mehr als 100 differentiell regulierte Proteine bzw. Proteinspezies zwischen den Tiergruppen der Studie. Von diesen konnten 90 per MS identifiziert werden. Die meisten geschlechtsspezifischen Unterschiede konnten per Netzwerkanalyse dem Metabolimus des Myokardiums zugeordnet werden. Bei zwei Drittel der regulierten Proteinspezies beschrieben die Abundanzen in den 2D-Gelen für die Gruppen 1 Monat intakt, 6 Monate intakt und 6 Monate kastriert eine charakteristische V-Form, sie stiegen oder fielen in Abhängigkeit zur sexuellen Reifung

der Tiere (1 Monat vs. 6 Monate intakt). Nach der Gonadektomie (mit 3 Monaten) stiegen bzw. fielen die Abundanzen der 6 Monate alten, kastrierten Tiere auf das Niveau der juvenilen Tiere. Diese Beobachtung legte nahe, dass diese Spezies direkt über Geschlechtshormone reguliert werden. Ein Drittel der festgestellten Unterschiede entfiel auf Proteinspezies, die in weiblichen und männlichen Tieren annähernd gleich abundant waren, teilweise aber nach Kastration, unabhängig vom Geschlecht, verstärkt auftraten. Für letzteres Drittel kann deshalb angenommen werden, dass sie entweder unabhängig von den Geschlechtshormonen exprimiert werden oder, wie für den Fall der höheren Expression nach der Gonadektomie, Geschlechtshormone in intakten Tieren herabregulierend auf deren Expression wirken. Einige Schlüsselregulatoren der per Netzwerkanalyse identifizierten Stoffwechselwege wurden per Quantitativer Real-Time PCR (Q-RT-PCR) untersucht, diese zeigten aber keine geschlechterspezifischen Unterschiede. Die Identitäten von mehrfach auf den 2D-Gelen aufgefundenen Proteinen konnten mittels 2D-Immunoblotting bestätigt werden.

3.2 Studie 2: Differential compartmental processing and phosphorylation of pathogenic human tau and native mouse tau in the Line 66 model of frontotemporal dementia

Tauopathien sind neurodegenerative Erkrankungen, bei denen eine Akkumulation des Tau-Proteins in Nervenzellen des Gehirns beobachtet wird. Beispiele hierfür sind die Frontotemporale Demenz (FTD) und Morbus Alzheimer (AD). Beide Krankheitsbilder sind mit dem Verlust motorischer und kognitiver Fähigkeiten durch den Untergang von Synapsen verbunden, dem auch durch Umlagerung oder Fehllokation bestimmter Tau-Proteinspezies Vorschub geleistet wird. Die Studie [26] beschäftigt sich mit der Verteilung von unterschiedlichen Tau-Proteinspezies in den Zellen eines transgenen Mausmodells für erbliche Formen der FTD (Stamm L66). L66-Mäuse überexprimieren mutiertes humanes Tau-Protein, was zu dessen Aggregation in den Nervenzellen des Gehirns der Tiere führt. Derartige Tiere weisen sensomotorische Probleme und eine Störung des motorischen Lernens auf [26].

In histologischen IHC-Experimenten unter Nutzung einer Reihe von Anti-Tau Antikörpern gegen unterschiedlichste bekannte Formen des Tau-Proteins konnte

festgestellt werden, dass sich die nicht-phosphorylierten Formen des humanen Tau-Proteins in den Synapsen anreichern, während phosphoryliertes Tau-Protein in den Axonen und Zellkörpern akkumuliert wird. Zur Aufklärung der von einer Anreicherung des human Tau-Proteins betroffenen Zellkompartimente wurde eine Trennung dieser mittels verschiedener Zentrifugations- und Ultrazentrifugationsschritte durchgeführt. Die erhaltenen subzellulären Fraktionen bzw. Pellets wurden durch Immunoblotting auf das Vorhandensein von Tau und die beiden Marker Synapsin und PSD95 untersucht, letztere dienten der Kategorisierung der Fraktionen als „synaptosomal“. Der anti-Tau Antikörper reagierte sowohl gegen humanes Tau als auch gegen endogenes der Maus, ein leichter Größenunterschied ermöglichte die Unterscheidung im 1D-Immunoblot. So zeigte sich, dass das humane Tau hauptsächlich als unlöslicher Bestandteil in den cytosolischen und synaptosomalen Fraktionen vorkam, während das endogene Tau-Protein dort nur in geringen Mengen vorzufinden war (~20%). Das in den Pellets der Cytosol-Fraktionen vorliegende Tau konnte durch Zugabe von 7 M Harnstoff oder Triton X-100 nicht in Lösung gebracht werden, was dafür spricht, dass es in Form größerer Aggregate in den Pellets vorlag. Das synaptische Tau hingegen war teilweise durch Zugabe von Triton X-100 zu lösen, ein Hinweis auf kleinere Aggregate. Im Rahmen der massenspektrometrischen Charakterisierung in Bezug auf PTMs konnte bestätigt werden, dass es sich bei dem unlöslichen, synaptosomalen humanen Tau um nicht-phosphorylierte Formen handelt. Phosphorylierte Tau-peptide wurden hauptsächlich in den Überständen der mehrstufigen Fraktionierung gefunden, in Pellets nur selten. [26]

3.3 Studie 3: Development of a calibration and standardization procedure for LA-ICP-MS using a conventional ink-jet printer for quantification of proteins in electro- and Western-blot assays

Die Veröffentlichung [27] hat die Entwicklung eines Kalibrier- und Standardisierungverfahrens für die *Laser Ablation Inductively Coupled Plasma-Mass-Spectrometry* (LA-ICP-MS) im Einsatz für Proteinnachweis und -quantifizierung auf Blotmembranen zum Thema. Es wurde evaluiert inwieweit das Auftragen solcher Standards über einen handelsüblichen Tintenstrahldrucker (*Ink-Jet*) erfolgen kann.

Grundlegende Versuche mit der entwickelten Tintenformulierung zeigten, dass die Aufbringung des Standards per *Ink-Jet* auf Nitrocellulosemembranen homogen und reproduzierbar erfolgte. So konnte für definierte Flächen nach Verflüssigung von bedruckten Membranabschnitten der Gehalt an dem per Tintenstrahldruck aufgebrachten Metall Indium per *liquid* ICP-MS mit einer relativen Standardabweichung (*RSD*) von 5% bestimmt werden. Wurden die Membranen nicht verflüssigt, sondern direkt per Laser abgetragen und vermessen, so ergaben sich RSD-Werte von 2%.

Als Probenmatrix für die Versuche mit Proteinen dienten zwei Arten von Gemischen. Erstens solche, bei denen die Einzelproteine vorab chemisch mit unterschiedlichen Lanthanidmetallen markiert (*lanthanide-tag*) wurden und zweitens unmodifizierte Proteine.

Für beide Arten von Proteingemischen erfolgte einleitend eine Trennung mittels *SDS-PAGE* mit nachfolgender Übertragung der Proteine auf Nitrozellulosemembranen per Elektroblotting. Die Membranen mit metallmarkierten Proteinen konnten nach Aufdrucken der hierfür entwickelten Tintenformulierungen per LA-ICP-MS im „direkten Nachweis“ vermessen werden. Die unmodifizierten Proteine wurden nach Konjugation ihrer jeweiligen lanthanidmarkierten Antikörper indirekt nachgewiesen, auch hier dienten aufgebrachte Tinten als interner Standard oder Quantifizierungsstandard.

Für die Standardisierung ergab sich so eine homogene, reproduzierbare Verteilung des Indium-Standards auch auf Membranflächen, die elektrogeblottete Proteine, nachträglich konjugierte Antikörper und somit Lanthanidmetalle enthielten. Darauf aufbauend konnte gezeigt werden, dass eine derartige Standardisierung/Normalisierung Drift-Effekte innerhalb der mehrstündigen Messung am Laser-Ablations-System erfolgreich kompensieren kann. So wurden die Relativen Standardabweichungen (RSD) von Messungen, die sich über Stunden erstreckten, von durchschnittlich 10% auf 1% verbessert.

Zur Quantifizierung einzelner Proteine wurde eine zweite Tintenformulierung gewählt. Diese enthielt die Lanthanide, welche auch zur Markierung der Modellproteine verwendet wurden. Um eine Quantifizierung der Modellproteine mit einen bekannten Markierungsgrad an Lanthanidatomen zu ermöglichen, wurde mittels *Ink-Jet* eine Konzentrationsreihe der Lanthanid-Tinte in Form von Quadraten mit unterschiedlicher Druckdichte neben die Bereiche mit geblotteten Proteinen gedruckt, anschließend

wurden die Membranen vollflächig mit der indiumhaltigen Tinte als interner Standard überdruckt. In diesen Versuchen konnten RSD Werte von 1% ermittelt werden, bei berechneten Detektionslimits (LOD) von 4 fmol. [27]

Für ein Protein mit einem gebundenem Lanthanidatom (*-tag*) und einem Molekulargewicht von 50 kDa, entsprächen diese Werte einem absoluten Detektionslimit von 0,2 ng.

3.4 Studie 4: Internal standardization of LA-ICP-MS immuno imaging via printing of universal metal spiked inks onto tissue sections

Diese Studie beschäftigte sich mit der Weiterentwicklung der *Ink-Jet* basierten internen Standardisierung zur Anwendung auf Formalin-fixierte Paraffin-eingebettete (FFPE) Gewebeproben für bildgebende *LA-ICP-MS* [28]. Dieser Probentyp ist weit verbreitet bei Pathologen bzw. allgemein in der medizinischen Forschung. Als Modellsysteme für diese Arbeit dienten murine FFPE-Hirnschnitte und humane FFPE-Brustgewebeschnitte (Tumore vs. Kontrollen), die nach etablierter Antigenfreilegung immunhistochemisch mit metallge*tag*gten Antikörpern selektiv konjugiert und anschließend über einen sekundären Antikörper angefärbt wurden. Um die *Ink-Jet* Methode der internen Standardisierung für derartige Proben zu evaluieren, wurde sie der chemischen Jodierung der Gewebeschnitte gegenüber gestellt.

Für die Anwendung der Technik an Gewebeschnitten auf Glasobjektträgern wurde für letztere eine Haltevorrichtung für den eingesetzten Tintenstrahldrucker entwickelt und die Aufbringungsmethode der *Ink-Jet*-Tinte im Rahmen der Methodenentwicklung derart angepasst, dass Metallkomplexe für die Standardisierung auf die inhomogene Oberfläche der Antikörper-konjugierten Gewebeschnitte aufgetragen werden konnten.

Für das Maushirngewebe wurde ein (Lanthanid-)metallmarkierter Antikörper zur Detektion des *House-Keeping*-Proteins Glycerinaldehyd-3-phosphat-Dehydrogenase (GADPH) verwendet, für die beiden humanen Brustgewebetypen ein solcher gegen den Mammakarzinom-Biomarker erb-b2 receptor tyrosine kinase 2 (ERBB2 bzw. Her2/neu).

Nach Anfärbung mittels IHC-Protokoll wurden die Gewebeschnitte lichtmikroskopisch analysiert und anschließend chemisch jodiert, nachfolgend wurde der Standard (Indium) per *Ink-Jet* aufgetragen bevor die Schnitte per LA-ICP-MS ablatiert und

vermessen wurden (die Druckausgabe der Publikation [28] enthält als Abbildung 2 ein Schema dieses Ablaufs). Das *ICP-MS* Instrument zeichnete dabei die Signale für Jod, Indium und für die Metall-*tags* Erbium (indirekt für GADPH in Maushirnschnitten) bzw. Holmium (indirekt für Her2/neu in humanem Brustgewebe) auf.

Für Jod innerhalb des vollständig ablatierten Gewebeschnittes ergab sich nach Transformation, der als Linienscans aufgezeichneten ICP-MS-Daten in Abbilder, eine ungleichmäßige Verteilung. Das aufgedruckte Indium zeigte sich über weite Teile des Gewebes homogen verteilt. Die Abbilder für die Lanthanidmetallsignale (Holmium für Her2/neu-AK, Erbium für GADPH-AK) entsprachen für das Brustgewebe in Umrissen den lichtmikroskopischen Aufnahmen der IHC-Färbung, für die Verteilung von Erbium (GADPH-AK) in den untersuchten Maushirnschnitten ergab sich eine über die Messzeit stetig abfallende Signalhöhe.

Durch Normalisierung über das aufgedruckte Indium konnten für Her2/neu positive Bereiche der humanen Brustgewebetumorproben erhebliche Kontraststeigerungen erzielt werden, die auch Details in den Schnitten sichtbar machten. Diese entsprachen den lichtmikroskopischen IHC-Bildern. Im Gegensatz dazu konnte über eine Normalisierung durch das Jodsignal keine Steigerung des Kontrasts gewonnen werden. Das Signal-zu-Hintergrund-Verhältnis konnte über die Normierung mittels Indium gesteigert werden von 18 im Rohsignal auf 39. Die Normierung über das Jodsignal verschlechterte dieses Verhältnis auf 11.

Für das Maushirngewebe konnten durch Normalisierung über das Indiumsignal der augenscheinlich durch instrumentelle Drift verursachte Signalabfall über die Zeit ausgeglichen und eine zu erwartende gleichmäßige Verteilung des *House-Keeping*-Proteins GADPH festgestellt werden. [28]

3.5 Studie 5: Multiplex LA-ICP-MS bio-imaging of brain tissue of a parkinsonian mouse model stained with metal-coded affinity-tagged antibodies and coated with indium-spiked commercial inks as internal standards

Diese Veröffentlichung beschäftigte sich mit der Untersuchung von Maushirnschnitten in einem bildgebenden Multiplexverfahren[29]. Als Probenquelle dienten zwei Mausmodelle: ein Modell für Morbus Parkinson (Stamm L62) und ein Wildtypstamm (C57BL6/J) [29]. Konsekutive FFPE-Hirnschnitte aus zwanzig Tieren (10 pro Gruppe) wurden jeweils mit einem von sieben spezifischen, lanthanid-markierten Antikörpern nach IHC-Färbung lichtmikroskopisch untersucht und per LA-ICP-MS vermessen. Davon waren vier Antikörper gegen krankheitsassoziierte Proteine und drei gegen sogenannte *House-Keeping*-Proteine gerichtet. Die Ergebnisse dieser konventionellen Färbung wurden denen der LA-ICP-MS Methodik im Singleplex- oder im Multiplex-Verfahren gegenüber gestellt. Im Multiplex-Verfahren wurden die Gewebeschnitte mit allen sieben Antikörpern parallel inkubiert und anschließend per LA-ICP-MS detektiert. Um instrumentelle Drift-Effekte des LA-ICP-MS auszugleichen, wurden die Objektträger mit den Gewebeschnitten nach der Antikörper-Konjugation im *Ink-Jet*-Verfahren mit Indium beschichtet, nachdem sie mit einer Gelatineschicht überzogen wurden. Die Gelatinebeschichtung erwies sich für die Anhaftung der Tinte auf teilweise hydrophoben Gewebeteilen als vorteilhaft. Sie absorbierte die homogen aufgetragene *Ink-Jet*-Tinte durch schnelle Fixierung *in-situ*.

Im Rahmen der Studie wurde evaluiert, inwiefern sich *House-Keeping*-Proteine als interner Standard nutzen lassen, im Vergleich zu einer Normalisierung über die *Ink-Jet*-vermittelte Aufbringung eines Standards. Hier konnte gezeigt werden, dass einzelne *House-Keeping*-Proteine sich nicht als allgemeiner Standard für die krankheitsassoziierten Proteine eignen. So wiesen Glasflächen außerhalb der Gewebegrenzen hohe Signale auf oder relativ homogene Rohsignale wurden verzerrt zu punktuellen *Hotspots*. Für die Normalisierung über das per *Ink-Jet* aufgetragene Indium konnten derartige Effekte kaum beobachtet werden. [29]

4 Diskussion

4.1 Studie 1: Sex differences in murine myocardium are not exclusively regulated by gonadal hormones

Die Studie lieferte Einblicke in die Regulation von Stoffwechselproteinen im murinen Myokardium[25]. Unter den identifizierten, differentiell abundanten Proteinspezies stellten Stoffwechselproteine auch zahlenmäßig die größte Gruppe. Dabei konnten solche des Fettsäuremetabolismus und der Mitochondrialfunktion voneinander abgegrenzt werden. Drei regulierte Proteine des Fettsäuremetabolismus (ECHA, ECHB und THIM) wurden jeweils in mehreren Spots aus den Gelen identifiziert. Eine Validierung dieser Ergebnisse per 2D-Immunoblottingverfahren ergab zusammen 21 positive Spots für die drei Proteine. Der Umstand, dass Proteine in mehreren Proteinspezies an verschiedenen Positionen, also in prozessierter Form, mit anderen physikochemischen Eigenschaften, auf 2D-Gelen auftreten können, ist mehrfach beschrieben [30], [31] und stellt den Ausgangspunkt für das sogenannte „*Proteomics Quantification Dilemma*“ [32] dar. Manche der Proteinspezies der drei Stoffwechselproteine zeigen keine signifikanten Abundanzunterschiede, während für bestimmte Formen der Proteine starke Unterschiede, teilweise in gegenläufiger Tendenz zwischen den Formen, zu erkennen sind. Bei den nachgewiesenen Proteinspezies handelt es sich anscheinend um prozessierte Formen, die im Stoffwechsel eine spezialisierte Rolle spielen. Im Rahmen der Studie konnten einige PTMs bestimmten Proteinspezies zugeordnet werden, die auch in den Uniprot-Datenbankeinträgen zu den Proteinen aufgeführt sind. Eine genauere Charakterisierung dieser Einzelspezies könnte weitere Einblicke in die geschlechtsspezifische Regulation des Stoffwechsels des Myokardiums liefern, dessen Energiebedarf zu 90% aus dem Fettsäuremetabolismus gedeckt wird [33]. Die angewandte *Top-Down*-Analysestrategie mit initialer Proteintrennung per 2DGE, gefolgt von Massenspektrometrie für einzelne Proteinspots hat sich für das Auffinden unterschiedlich prozessierter Spezies bewährt, mit einer Hochdurchsatz-*Bottom-Up* Analysestrategie und modernsten MS-Geräten wäre es nicht möglich gewesen, derartige Details aufzudecken.

4.2 Studie 2: Differential compartmental processing and phosphorylation of pathogenic human tau and native mouse tau in the Line 66 model of frontotemporal dementia

Die Studie [26] stellt einen Ansatz vor, mit dem Tau-Proteinspecies in verschiedenen Zellkompartimenten des L66-Mausmodells für Frontotemporale Demenz (FTD) nachgewiesen und im Hinblick auf Aggregation und Phosphorylierung charakterisiert werden können. Es konnte gezeigt werden, dass sich überexprimiertes, mutiertes Tau-Protein atypisch auch in Synapsen akkumuliert, während endogenes Maus-Tau dort nicht nachzuweisen war. Die einzelnen Tau-Protein Fraktionen unterschieden sich teilweise auch in ihrem Phosphorylierungsgrad. Für die Entstehung von Morbus Alzheimer (AD) ist ein Einfluss von unterschiedlicher oder gesteigerter Phosphorylierung beschrieben [34], [35], wird aber noch diskutiert. Die Ergebnisse der Studie lassen für FTD ebenfalls einen Zusammenhang vermuten. Dass nicht-phosphoryliertes Tau-Protein zur Aggregation neigt [36], [37], ist für AD und FTD bekannt, die Ergebnisse dieser Studie bestätigen dies [38]. Ein Abgleich dieser Ergebnisse für ein FTD-Modell mit entsprechenden Mausmodellen für Morbus Alzheimer (AD), könnte Einblicke in die Entstehung verschiedener Konformationen des Tau-Protein liefern und eine Abgrenzung der beiden Tauopathien auf Proteinspeziesebene ermöglichen. Eine solche Abgrenzung könnte dabei helfen, therapeutische Targets oder Biomarker für beide Krankheiten oder gezielte Ansätze für eine Form der beiden Formen der Tauopathie zu finden.

4.3 Studie 3-5 (Bioimaging):

In den drei Bioimaging Studien wurde die Anwendung eines per *Ink-Jet*-Druck aufgebrachten Standards entwickelt und geprüft, beginnend mit Druckexperimenten an Nitrozellulosemembranen in der ersten Bioimaging-Studie [27], auf die im Elektroblot-Verfahren Lanthanid-markierte Proteine übertragen wurden. Derartige Membranen verhielten sich im Tintenstrahldrucker analog zu Papier, sie konnten mit hoher Detailtreue bedruckt werden. Die ermittelte Nachweisgrenze für elektrogeblottete Proteine (50 kDa) mit nur einem für die LA-ICP-MS-Detektion notwendigem Heteroatom lag mit 0,2 ng im Bereich sensitiver Silberfärbungsprotokolle

für SDS-PAGE Gele [39] und weit unterhalb von Färbetechniken für Blotmembranen [40].

In der zweiten Bioimaging-Studie [28] wurde das *Ink-Jet* Verfahren des Standardauftrags für IHC-gefärbte Gewebeschnitte auf Glasobjektträger angepasst und erweitert. Es zeigte sich, dass die Metallmarkierung der eingesetzten Antikörper für die IHC-Färbung keinen negativen Einfluss hatte. Im Gegensatz zu der als Vergleich durchgeführten Jodierung des Gewebeschnitts erwies sich der *Ink-Jet*-Standardauftrag als robuster und homogener. Dies kann mit dem Umstand erklärt werden, dass die Jodierung durch Überschichtung mit reaktiver Jodlösung stattfindet, bei der die relativ kleinen Jodmoleküle schnell in den Gewebeschnitt eindiffundieren können und auch in der Tiefe mit Proteinen reagieren. Der Proteingehalt eines Gewebeabschnitts und dessen individuelle Zusammensetzung auf Aminosäureebene haben ebenfalls einen Einfluss auf die spätere Jodkonzentration im jodierten Gewebe. Beim Auftrag per *Ink-Jet* hingegen wird der Standard parallel zur späteren Detektionsebene aufgebracht und trocknet schnell ab. Ein Eindringen in den Gewebeschnitt und die Diffusion im selbigen wird so minimiert.

Die dritte Studie [29] zum Imaging von Biomarkern wurde im Multiplexverfahren an Gewebeschnitten eines Morbus Parkinson Mausmodells durchgeführt. Die Ergebnisse der LA-ICP-MS Detektion deckten sich mit denen der konventionellen IHC-Färbung, so konnten für den L62 Stamm eine fortschreitende Gliose und eine Erniedrigung der Neuronen [41] festgestellt werden. Erwartungsgemäß zeigten beide Methoden eine Erhöhung des α-Synuclein-Gehalts in den Geweben der L62-Proben. Durch die Normalisierung der LA-ICP-MS Daten über das aufgedruckte Indium konnten die erzielten Ergebnisse in ihrer statistischen Signifikanz weiter gesteigert werden. Die normalisierten Werte erwiesen sich in der Signifikanz gegenüber manuell ausgezählten IHC-Ergebnissen als überlegen. So konnte für das Enzym Tyrosin-Hydroxylase (TH), ein aus der Charakterisierung der Mauslinie L62 bekannter Abundanzunterschied [42] mit statistischer Sicherheit nachgewiesen werden. Dank Letzterer und der erreichten hohen Reproduzierbarkeit würde sich das Verfahren für den Einsatz in der Diagnostik empfehlen. Dies gilt im Besonderen für sogenannte IHC-*Tissue Microarrays* (TMA) [43], bei denen auf kleiner Fläche eine Vielzahl von Biopsien untergebracht sind. TMA könnten im Multiplexverfahren mit mehreren Antikörpern für verschiedene Biomarker parallel inkubiert, mit Standard bedruckt und anschließend

per LA-ICP-MS vermessen werden. Während in der vorliegenden Studie mit sieben Elementen gearbeitet wurde[29], könnten in Multiplexmessungen zukünftig bis zu 40 Isotope zur Antikörper-vermittelten Detektion von Biomarkern eingesetzt werden [44]. Derartige Tinten könnten neben einem chemischen Element zur Normalisierung auch Isotope für die Quantifizierung über Isotopenverdünnungsanalyse (ID) beinhalten [45]–[47].

5 Literaturverzeichnis

[1] Williams, K. L. and Hochstrasser, D. F., “Introduction to the Proteome,” 1997, pp. 1–12.

[2] Blackstock, W. P. and Weir, M. P., “Proteomics: Quantitative and physical mapping of cellular proteins,” *Trends in Biotechnology*, vol. 17, no. 3. pp. 121–127, 1999.

[3] Righetti, P. G., “Proteome,” in *Brenner’s Encyclopedia of Genetics: Second Edition*, 2013, pp. 504–507.

[4] Nielsen, M. L., Savitski, M. M., and Zubarev, R. A., “Extent of modifications in human proteome samples and their effect on dynamic range of analysis in shotgun proteomics,” *Mol. Cell. Proteomics*, vol. 5, no. 12, pp. 2384–2391, 2006.

[5] Schiess, R., Wollscheid, B., and Aebersold, R., “Targeted proteomic strategy for clinical biomarker discovery,” *Molecular Oncology*, vol. 3, no. 1. pp. 33–44, 2009.

[6] McDonald, W. H. and Yates, J. R., “Shotgun proteomics and biomarker discovery,” *Dis. Markers*, vol. 18, no. 2, pp. 99–105, 2002.

[7] Jungblut, P. and Thiede, B., “Protein identification from 2-DE gels by MALDI mass spectrometry,” *Mass Spectrom. Rev.*, vol. 16, no. 3, pp. 145–162, 1997.

[8] Coorssen, J. R., “Proteomics,” in *Brenner’s Encyclopedia of Genetics: Second Edition*, 2013, pp. 508–510.

[9] Björhall, K., Miliotis, T., and Davidsson, P., “Comparison of different depletion strategies for improved resolution in proteomic analysis of human serum samples,” *Proteomics*, vol. 5, no. 1, pp. 307–317, 2005.

[10] Smith, L. M. and Kelleher, N. L., “Proteoform: A single term describing protein complexity,” *Nature Methods*, vol. 10, no. 3. pp. 186–187, 2013.

[11] Schlüter, H., Apweiler, R., Holzhütter, H. G., and Jungblut, P. R., “Finding one’s way in proteomics: A protein species nomenclature,” *Chem. Cent. J.*, vol. 3, no. 1, 2009.

[12] Jungblut, P. R., Holzhütter, H. G., Apweiler, R., and Schlüter, H., “The speciation of the proteome,” *Chemistry Central Journal*, vol. 2, no. 1. 2008.

[13] Aebersold, R., Agar, J. N., Amster, I. J., Baker, M. S., Bertozzi, C. R., Boja, E. S., Costello, C. E., Cravatt, B. F., Fenselau, C., Garcia, B. A., Ge, Y., Gunawardena, J., Hendrickson, R. C., Hergenrother, P. J., Huber, C. G., Ivanov, A. R., Jensen, O. N., Jewett, M. C., Kelleher, N. L., Kiessling, L. L., Krogan, N. J., Larsen, M. R., Loo, J. A., Ogorzalek Loo, R. R., Lundberg, E., Maccoss, M. J., Mallick, P., Mootha, V. K., Mrksich, M., Muir, T. W., Patrie, S. M., Pesavento, J. J., Pitteri, S. J., Rodriguez, H., Saghatelian, A., Sandoval, W., Schlüter, H., Sechi, S., Slavoff, S. A., Smith, L. M., Snyder, M. P., Thomas, P. M., Uhlén, M., Van Eyk, J. E., Vidal, M., Walt, D. R., White, F. M., Williams, E. R., Wohlschlager, T., Wysocki, V. H., Yates, N. A., Young, N. L., and Zhang, B., “How many human proteoforms are there?,” *Nature Chemical Biology*, vol.

14, no. 3. pp. 206–214, 2018.

[14] Sirover, M. A., “New insights into an old protein: The functional diversity of mammalian glyceraldehyde-3-phosphate dehydrogenase,” *Biochimica et Biophysica Acta - Protein Structure and Molecular Enzymology*, vol. 1432, no. 2. pp. 159–184, 1999.

[15] Rifai, N., Gillette, M. A., and Carr, S. A., “Protein biomarker discovery and validation: The long and uncertain path to clinical utility,” *Nature Biotechnology*, vol. 24, no. 8. pp. 971–983, 2006.

[16] Ross, J. S., Fletcher, J. A., Linette, G. P., Stec, J., Clark, E., Ayers, M., Symmans, W. F., Pusztai, L., and Bloom, K. J., “ The HER- 2/ neu Gene and Protein in Breast Cancer 2003: Biomarker and Target of Therapy ,” *Oncologist*, vol. 8, no. 4, pp. 307–325, 2003.

[17] Rizzardi, A. E., Johnson, A. T., Vogel, R. I., Pambuccian, S. E., Henriksen, J., Skubitz, A. P. N., Metzger, G. J., and Schmechel, S. C., “Quantitative comparison of immunohistochemical staining measured by digital image analysis versus pathologist visual scoring,” *Diagn. Pathol.*, vol. 7, no. 1, 2012.

[18] Seuma, J., Bunch, J., Cox, A., McLeod, C., Bell, J., and Murray, C., “Combination of immunohistochemistry and laser ablation ICP mass spectrometry for imaging of cancer biomarkers,” *Proteomics*, vol. 8, no. 18, pp. 3775–3784, Sep. 2008.

[19] Murphy, R. C. and Merrill, A. H., “Lipidomics and imaging mass spectrometry,” *Biochimica et Biophysica Acta - Molecular and Cell Biology of Lipids*, vol. 1811, no. 11. pp. 635–636, 2011.

[20] Ahrends, R., Pieper, S., Neumann, B., Scheler, C., and Linscheid, M. W., “Metal-coded affinity tag labeling: A demonstration of analytical robustness and suitability for biological applications,” *Anal. Chem.*, vol. 81, no. 6, pp. 2176–2184, 2009.

[21] Waentig, L., Jakubowski, N., Hardt, S., Scheler, C., Roos, P. H., and Linscheid, M. W., “Comparison of different chelates for lanthanide labeling of antibodies and application in a Western blot immunoassay combined with detection by laser ablation (LA-)ICP-MS,” *J. Anal. At. Spectrom.*, vol. 27, no. 8, p. 1311, Aug. 2012.

[22] Krause, M., Scheler, C., Bottger, U., Weisshoff, H., and Linscheid, M. W., “Method and reagent for specifically identifying and quantifying one or more proteins in a sample,” Jun. 2002, Accessed: Oct. 29, 2018. [Online]. Available: https://patents.google.com/patent/US20060246530A1/en.

[23] Konz, I., Fernández, B., Fernández, M. L., Pereiro, R., and Sanz-Medel, A., “Laser ablation ICP-MS for quantitative biomedical applications,” *Anal. Bioanal. Chem.*, vol. 403, no. 8, pp. 2113–2125, Jun. 2012.

[24] Hare, D., Austin, C., and Doble, P., “Quantification strategies for elemental imaging of biological samples using laser ablation-inductively coupled plasma-mass spectrometry,” *Analyst*, vol. 137, no. 7. pp. 1527–1537, 2012.

[25] Theuring, F., Neumann, B., Scheler, C., Jungblut, P. R., and Schwab, K., “Sex differences in murine myocardium are not exclusively regulated by gonadal

hormones," *J. Proteomics*, vol. 178, pp. 43–56, Apr. 2018.

[26] Lemke, N., Melis, V., Lauer, D., Magbagbeolu, M., Neumann, B., Harrington, C. R., Riedel, G., Wischik, C. M., Theuring, F., and Schwab, K., "Differential compartmental processing and phosphorylation of pathogenic human tau and native mouse tau in the line 66 model of frontotemporal dementia," *J. Biol. Chem.*, vol. 295, no. 52, pp. 18508–18523, Dec. 2020.

[27] Hoesl, S., Neumann, B., Techritz, S., Linscheid, M., Theuring, F., Scheler, C., Jakubowski, N., and Mueller, L., "Development of a calibration and standardization procedure for LA-ICP-MS using a conventional ink-jet printer for quantification of proteins in electro- and Western-blot assays," *J. Anal. At. Spectrom.*, vol. 29, no. 7, pp. 1282–1291, Jun. 2014.

[28] Hoesl, S., Neumann, B., Techritz, S., Sauter, G., Simon, R., Schlüter, H., W. Linscheid, M., Theuring, F., Jakubowski, N., and Mueller, L., "Internal standardization of LA-ICP-MS immuno imaging via printing of universal metal spiked inks onto tissue sections," *J. Anal. At. Spectrom.*, vol. 31, no. 3, pp. 801–808, 2016.

[29] Neumann, B., Hösl, S., Schwab, K., Theuring, F., and Jakubowski, N., "Multiplex LA-ICP-MS bio-imaging of brain tissue of a parkinsonian mouse model stained with metal-coded affinity-tagged antibodies and coated with indium-spiked commercial inks as internal standards," *J. Neurosci. Methods*, vol. 334, 2020.

[30] Scheler, C., Müller, E. C., Stahl, J., Müller-Werdan, U., Salnikow, J., and Jungblut, P., "Identification and characterization of heat shock protein 27 protein species in human myocardial two-dimensional electrophoresis patterns," *Electrophoresis*, vol. 18, no. 15, pp. 2823–2831, 1997.

[31] Jungblut, P. R., Thiede, B., and Schlüter, H., "Towards deciphering proteomes via the proteoform, protein speciation, moonlighting and protein code concepts," *Journal of Proteomics*, vol. 134. pp. 1–4, 2016.

[32] Jungblut, P. R., "The proteomics quantification dilemma," *Journal of Proteomics*, vol. 107. pp. 98–102, 2014.

[33] Kodde, I. F., van der Stok, J., Smolenski, R. T., and de Jong, J. W., "Metabolic and genetic regulation of cardiac energy substrate preference," *Comparative Biochemistry and Physiology - A Molecular and Integrative Physiology*, vol. 146, no. 1. pp. 26–39, 2007.

[34] Johnson, G. V. W. and Stoothoff, W. H., "Tau phosphorylation in neuronal cell function and dysfunction," *Journal of Cell Science*, vol. 117, no. 24. pp. 5721–5729, 2004.

[35] Billingsley, M. L. and Kincaid, R. L., "Regulated phosphorylation and dephosphorylation of tau protein: Effects on microtubule interaction, intracellular trafficking and neurodegeneration," *Biochemical Journal*, vol. 323, no. 3. pp. 577–591, 1997.

[36] Lai, R. Y. K., Harrington, C. R., and Wischik, C. M., "Absence of a role for phosphorylation in the tau pathology of Alzheimer's disease," *Biomolecules*, vol. 6, no. 2, 2016.

[37] Schneider, A., Biernat, J., Von Bergen, M., Mandelkow, E., and Mandelkow, E. M., “Phosphorylation that detaches tau protein from microtubules (Ser262, Ser214) also protects it against aggregation into Alzheimer paired helical filaments,” *Biochemistry*, vol. 38, no. 12, pp. 3549–3558, 1999.

[38] Melis, V., Zabke, C., Stamer, K., Magbagbeolu, M., Schwab, K., Marschall, P., Veh, R. W., Bachmann, S., Deiana, S., Moreau, P. H., Davidson, K., Harrington, K. A., Rickard, J. E., Horsley, D., Garman, R., Mazurkiewicz, M., Niewiadomska, G., Wischik, C. M., Harrington, C. R., Riedel, G., and Theuring, F., “Different pathways of molecular pathophysiology underlie cognitive and motor tauopathy phenotypes in transgenic models for Alzheimer’s disease and frontotemporal lobar degeneration,” *Cell. Mol. Life Sci.*, vol. 72, no. 11, pp. 2199–2222, 2015.

[39] Jin, L. T., Hwang, S. Y., Yoo, G. S., and Choi, J. K., “Sensitive silver staining of protein in sodium dodecyl sulfate-polyacrylamide gels using an azo dye, calconcarboxylic acid, as a silver-ion sensitizer,” *Electrophoresis*, vol. 25, no. 15, pp. 2494–2500, 2004.

[40] Goldman, A., Harper, S., and Speicher, D. W., “Detection of proteins on blot membranes,” *Curr. Protoc. Protein Sci.*, vol. 2016, pp. 10.8.1-10.8.11, 2016.

[41] Wan, O. W. and Chung, K. K. K., “The role of alpha-synuclein oligomerization and aggregation in cellular and animal models of Parkinson’s disease,” *PLoS One*, vol. 7, no. 6, 2012.

[42] Frahm, S., Melis, V., Horsley, D., Rickard, J. E., Riedel, G., Fadda, P., Scherma, M., Harrington, C. R., Wischik, C. M., Theuring, F., and Schwab, K., “Alpha-Synuclein transgenic mice, h-α-SynL62, display α-Syn aggregation and a dopaminergic phenotype reminiscent of Parkinson’s disease,” *Behav. Brain Res.*, vol. 339, pp. 153–168, Feb. 2018.

[43] Rimm, D. L., Camp, R. L., Charette, L. A., Costa, J., Olsen, D. A., and Reiss, M., “Tissue microarray: A new technology for amplification of tissue resources,” *Cancer Journal*, vol. 7, no. 1. pp. 24–31, 2001.

[44] Wang, H. A. O., Grolimund, D., Giesen, C., Borca, C. N., Shaw-Stewart, J. R. H., Bodenmiller, B., and Günther, D., “Fast Chemical Imaging at High Spatial Resolution by Laser Ablation Inductively Coupled Plasma Mass Spectrometry,” *Anal. Chem.*, vol. 85, no. 21, pp. 10107–10116, Nov. 2013.

[45] Haldimann, M., Baduraux, M., Eastgate, A., Froidevaux, P., O’Donovan, S., Von Gunten, D., and Zoller, O., “Determining picogram quantities of uranium in urine by isotope dilution inductively coupled plasma mass spectrometry. Comparison with α-spectrometry,” *J. Anal. At. Spectrom.*, vol. 16, no. 12, pp. 1364–1369, 2001.

[46] Keyes, W. R. and Turnlund, J. R., “Determination of molybdenum and enriched Mo stable isotope concentrations in human blood plasma by isotope dilution ICP-MS,” in *Journal of Analytical Atomic Spectrometry*, 2002, vol. 17, no. 9, pp. 1153–1156.

[47] Moraleja, I., Mena, M. L., Lázaro, A., Neumann, B., Tejedor, A., Jakubowski, N., Gómez-Gómez, M. M., and Esteban-Fernández, D., “An approach for quantification of platinum distribution in tissues by LA-ICP-MS imaging using

isotope dilution analysis,” *Talanta*, vol. 178, pp. 166–171, Feb. 2018.

6 Eidesstattliche Versicherung

Ich, Boris Alexander Neumann, versichere an Eides statt durch meine eigenhändige Unterschrift, dass ich die vorgelegte Dissertation mit dem Thema: Proteomanalytik und bildgebende Diagnostik am Maus-Modellsystem [Englisch: *Proteome Analysis and Bioimaging for Murine Models*] selbstständig und ohne nicht offengelegte Hilfe Dritter verfasst und keine anderen als die angegebenen Quellen und Hilfsmittel genutzt habe.

Alle Stellen, die wörtlich oder dem Sinne nach auf Publikationen oder Vorträgen anderer Autoren/innen beruhen, sind als solche in korrekter Zitierung kenntlich gemacht. Die Abschnitte zu Methodik (insbesondere praktische Arbeiten, Laborbestimmungen, statistische Aufarbeitung) und Resultaten (insbesondere Abbildungen, Graphiken und Tabellen) werden von mir verantwortet.

Ich versichere ferner, dass ich die in Zusammenarbeit mit anderen Personen generierten Daten, Datenauswertungen und Schlussfolgerungen korrekt gekennzeichnet und meinen eigenen Beitrag sowie die Beiträge anderer Personen korrekt kenntlich gemacht habe (siehe Anteilserklärung). Texte oder Textteile, die gemeinsam mit anderen erstellt oder verwendet wurden, habe ich korrekt kenntlich gemacht.

Meine Anteile an etwaigen Publikationen zu dieser Dissertation entsprechen denen, die in der untenstehenden gemeinsamen Erklärung mit dem Erstbetreuer, angegeben sind. Für sämtliche im Rahmen der Dissertation entstandenen Publikationen wurden die Richtlinien des ICMJE (International Committee of Medical Journal Editors; www.icmje.og) zur Autorenschaft eingehalten. Ich erkläre ferner, dass ich mich zur Einhaltung der Satzung der Charité – Universitätsmedizin Berlin zur Sicherung Guter Wissenschaftlicher Praxis verpflichte.

Weiterhin versichere ich, dass ich diese Dissertation weder in gleicher noch in ähnlicher Form bereits an einer anderen Fakultät eingereicht habe.

Die Bedeutung dieser eidesstattlichen Versicherung und die strafrechtlichen Folgen einer unwahren eidesstattlichen Versicherung (§§156, 161 des Strafgesetzbuches) sind mir bekannt und bewusst.

Berlin, den 30.8.21

Unterschrift

7 Anteilserklärung an den ausgewählten Publikationen

Publikation 1: Theuring F., Neumann B., Scheler C., Jungblut P.R., Schwab K. (2017) *Sex differences in murine myocardium are not exclusively regulated by gonadal hormones; Journal of Proteomics, Volume 178, 30 April 2018, Pages 43-56*

Beitrag im Einzelnen:

- Mitarbeit Probenahme aus Versuchstieren: Alle Herzproben wurden von mir, nach der Entnahme durch Frau Dr. Schwab, mittels Passage durch eisgekühlten Puffer gereinigt, von Blut und Anhaftungen befreit und anschließend schockgefrostet.
- Probenvorbereitung für MS-Analytik, Durchführung aller massenspektrometrischen Studienmessungen, Auswertung der MS-Daten, Interpretation der MS-Ergebnisse: Aus diesen Arbeiten sind die Tabellen 1 und 2 entstanden; alle 90 Proteinidentifikationen der Studie wurden vor mir durchgeführt, aus ihnen sind die Abbildungen 2 und 8 entstanden; die nähere Charakterisierung im Hinblick auf PTMs von ausgewählten 21 Proteinen durch weitere MS-Experimente wurden von mir durchgeführt. Die Ergebnisteile 3.6 und 3.7 basieren auf diesen Ergebnissen. Dem Diskussions- und Conclusionteil steuerte ich die MS-bezogenen Passagen zu.
- Überarbeiten der Publikationsschrift.

Publikation 2: Lemke N., Melis V., Lauer D., Magbagbeolu M., Neumann B., Harrington C., Riedel G., Wischik C., Theuring F., Schwab K. (2020). *Differential compartmental processing and phosphorylation of pathogenic human tau and native mouse tau in the Line 66 model of frontotemporal dementia. Journal of Biological Chemistry. 295(52):18508-18523.*

Beitrag im Einzelnen:

- Vorbereitung und Durchführung der Studienmessungen (MS), Auswertung der MS-Daten, Interpretation der Daten zu post-translationalen Modifikationen: Aus diesen Ergebnissen sind die Tabellen 2, S1, S2 entstanden und Teile von Tabelle 3. Die 18 Abbildungen S3ff stammen von mir. Der Ergebnisteil „Synaptic hTau in L66 is nonphosphorylated“ basiert auf meiner Interpretation der von mir durchgeführten MS Messungen.
- Überarbeiten der Publikationsschrift.

Publikation 3: Hoesl S., Neumann B., Techritz S., Linscheid M.W., Theuring F., Scheler C., Jakubowski N., Mueller L. (2014) *Development of a calibration and standardization procedure for LA-ICP-MS using a conventional ink-jet printer for quantification of proteins in electro- and Western-blot assays; Journal of Analytical Atomic Spectrometry 29(7):1282*

Beitrag im Einzelnen:

- Herstellung der Markierungsreagenzien: HPLC Aufreinigung der MeCAT-Reagenzien, Quantifizierung per liquid ICP-MS.
- Die Entwicklung und die Herstellung der lanthanid- und indiumhaltigen Tinten wurden von mir durchgeführt.
- Das Aufbringen der Standards per *Ink-Jet* erfolgte durch mich.

- Die Publikationsschrift wurde von Frau Dr. Hösl und mir zu gleichen Teilen angefertigt.

Publikation 4: Hoesl S., Neumann B., Techritz S., Sauter G., Simon R., Schlüter H., Linscheid M.W., Theuring F., Jakubowski N., Mueller L. (2015) *Internal standardization of LA-ICP-MS immuno imaging via printing of universal metal spiked inks onto tissue sections; Journal of Analytical Atomic Spectrometry 31(3)*

Beitrag im Einzelnen:

- Herstellung der Markierungsreagenzien: HPLC Aufreinigung der MeCAT-Reagenzien, Quantifizierung per liquid ICP-MS.
- Die Entwicklung und die Herstellung der indiumhaltigen Tinten wurden von mir durchgeführt.
- Die Halterung für das Bedrucken von Glasobjektträgern wurde von mir hergestellt, Umbauten am *Ink-Jet* Drucker wurden von mir durchgeführt.
- Das Aufbringen der Standards per *Ink-Jet* erfolgte durch mich.

- Die Ergebnis- und Conclusionteil der Publikationsschrift wurde von Frau Dr. Hösl und mir zu gleichen Teilen angefertigt.

Publikation 5: Neumann B., Hoesl S., Schwab K., Theuring F., Jakubowski N. (2020) *Multiplex LA-ICP-MS bio-imaging of brain tissue of a parkinsonian mouse model stained with metal-coded affinity-tagged antibodies and coated with indium-spiked commercial inks as internal standards; Journal of Neuroscience Methods Volume 334, 15 March 2020, 108591*

Beitrag im Einzelnen:

- Herstellung der Markierungsreagenzien: HPLC Aufreinigung der MeCAT-Reagenzien, Quantifizierung per liquid ICP-MS.
- Die Herstellung der indiumhaltigen Tinten wurde von mir durchgeführt.
- Das Protokoll zur Gelatinebeschichtung der FFPE-Gewebeschnitte wurde von mir für diese Studie entwickelt und eingesetzt.
- Das Aufbringen von Gelatine und der Standards (letztere per *Ink-Jet)* auf alle Gewebeschnitt erfolgte durch mich.

Die Ergebnisteil und Conclusionteil der Publikationsschrift wurde von mir verfasst, die Abbildungen 1, 3 und 4 von mir zusammengestellt.

_____

Unterschrift des Doktoranden

8 Druckexemplare der ausgewählten Publikationen

Publikation 1: Sex differences in murine myocardium are not exclusively regulated by gonadal hormones

Journal of Proteomics 178 (2018) 43–56

Contents lists available at ScienceDirect

Journal of Proteomics

journal homepage: www.elsevier.com/locate/jprot

Sex differences in murine myocardium are not exclusively regulated by gonadal hormones

Franz Theuring[a], Boris Neumann[a,b], Christian Scheler[b], Peter R. Jungblut[c], Karima Schwab[a,*]

[a] Charité – Universitätsmedizin Berlin, corporate member of Freie Universität Berlin, Humboldt-Universität zu Berlin, and Berlin Institute of Health, Center for Cardiovascular Research, Institute of Pharmacology, Berlin, Germany
[b] Proteome Factory AG, Berlin, Germany
[c] Max Planck Institute for Infection Biology, Core Facility Protein Analysis, Berlin, Germany

ARTICLE INFO

Keywords:
Cardiovascular disease
Sex differences
2-DE
Mass spectrometry
Post-translational modifications

ABSTRACT

We investigated sex differences in cardiac protein patterns of intact and castrated mice using proteomics and 1D and 2D immunoblotting. To exclude differences concerning developmental aspects gonadectomy was conducted in mature mice at the age of three months. The main sex-related regulation in the protein pattern of the myocardium occurred for proteins involved in metabolic processes whereas only few proteins involved in other pathways underwent a regulation. Many regulated proteins (2/3) displayed a characteristic V form, which means that these proteins are up- or down-regulated in sexually mature compared to young mice and are back-regulated after castration, emphasizing a direct regulation by gonadal hormones. Several other spots (1/3) showed the same male/female regulation or a drastic increase in male/female spot intensity ratio after castration, suggesting either a regulation independent of sex hormones or a removal of an inhibiting feedback mechanism by gonadectomy. Technically, we found that it cannot be expected that a single spot contains only one protein species and that one protein is present in only one spot. We thus propose for proteomic investigations to identify/quantify all spots of a 2-DE pattern to obtain information about protein speciation and its potential importance for function and pathology.

Biological significance: Sex related differences in cardiovascular disease, including risk factors, disease manifestation and outcomes, are far from being well understood, and improved biological understanding of these differences in the healthy myocardium is of great importance. We investigated sex related changes of myocardial protein pattern in intact and castrated mice at different ages and found metabolic proteins to be highly regulated, some of which independently from gonadal hormones.

1. Introduction

Cardiovascular disease (CVD) is a worldwide continuously growing health concern, accounting for more than 50% of global deaths [1]. Generally, there is a greater and earlier manifestation of CVD in men compared to premenopausal women [2] but the cardiovascular risk for women rises after menopause [3]. Conflicting findings from randomized hormone replacement trials led to a controversy over protective actions of estrogens [4] and improved biological understanding of sex-related differences is of great importance to ameliorate diagnosis and treatment of CVD in the future [1].

There is an increasing number of studies reporting sex differences in the cardiovasculature [5]. Several genetic and experimental rodent models have been used to anlayze these aspects, e.g. models of ischemic injury, pressure overload and atherosclerosis (for summary see [6]) and most sex-related cardiac proteomics studies conducted in rodents use those disease models [7–9]. Only a few proteomics reports analyze the healthy myocardium, for example by mapping the murine cardiac proteome [10–12] or by studying age-related aspects in the rodent heart [13,14]. Cases in which sex differences in the healthy heart have been studied are rare [15–18].

In our study, we characterized sex-related protein differences in the non-diseased myocardium of intact mice and under hormone deprivation and for some proteins we did so at the protein species level. In the last two decades, it has become clear that the view on proteins has to be extended to the protein species level [19–21]. After synthesis at the

Abbreviations: CVD, cardiovascular disease; FA, fatty acid; ECHA, trifunctional enzyme subunit alpha; ECHB, trifunctional enzyme subunit beta; THIM, 3-ketoacyl-CoA thiolase; ER, estrogen receptor; PPARA, peroxisome proliferator-activated receptor alpha; PRGC1, peroxisome proliferator-activated receptor gamma coactivator 1-alpha; PTM, post-translational modification; Q-RT-PCR, quantitative real time PCR; RF, regulation factor; 1D-IB, one dimensional immunoblotting; 2D-IB, two dimensional immunoblotting

* Corresponding author at: Hessische Strasse 3-4, D-10115 Berlin, Germany.
E-mail address: karima.schwab@charite.de (K. Schwab).

https://doi.org/10.1016/j.jprot.2017.12.005
Received 1 August 2017; Received in revised form 6 December 2017; Accepted 11 December 2017
Available online 19 December 2017

ribosome, the primary protein species is chemically modified by post-translational modifications including addition of residues such as phosphates, methyl or acetyl groups and many others, truncations or even protein splicing processes. This results for each protein in the production of a huge diversity of protein species, each with a different chemical composition and a potentially different biological function. After protein synthesis there is an additional regulation level, which is ignored by the conventional bottom-up LC-MS techniques. Many phosphorylated peptides may be accessed [22], but the measurement of phosphorylated peptides completely ignores the fact that the combination of different PTMs determines the function and the combination of PTMs, represented in each protein species, is already destroyed by tryptic digestion before the MS identification. 2-DE-MS is a powerful tool to recognize protein speciation [23,24] but complete primary structure elucidation was obtained only in rare cases [25]. However, this complete characterization is necessary to understand which protein species is responsible for a certain function of a protein.

In the current work, we observed protein speciation for some proteins. Though a complete primary structure characterization of single protein species was not reached, even by the use of Orbitrap MS technology, our findings show that protein species separation before MS should be aspired and high-resolution 2-DE is the key method to reach the protein species level. Our differential proteomics analysis revealed mainly metabolic proteins to undergo a regulation in a sex-dependent manner, and among them especially proteins involved in fatty acid (FA) metabolism and mitochondrial function. Differential cardiac energetic between male and female mice was seen regardless of gonadectomy and this might contribute, at least in part, to the cardioprotective effect of the female sex.

2. Materials and methods

2.1. Animals and diets

Male and female C57BL/6J mice were maintained on basic, phytoestrogen free chow (2014S Teklad, Harlan, Germany) and had free access to food and water. Six animal groups, each comprising 10 mice, were included in this study: i) intact male mice, aged 1 month, ii) intact female mice, aged 1 month, iii) intact male mice, aged 6 month, iv) intact female mice, aged 6 month, v) castrated male mice, aged 6 month and vi) castrated female mice, aged 6 month. Gonadectomy was conducted in mice, aged 3 months, following standard procedures [26,27]. The relatively late time point for gonadectomy was chosen to allow the investigation of cardiac function in mature mice, while avoiding any development-related aspects. Animals ($n = 10$ per group) were sacrificed by cervical dislocation, hearts excised, washed thoroughly and were either snap-frozen in liquid nitrogen or fixed in formalin for histological analysis. Animal's body and heart weights were recorded and were expressed as group mean with SEM (standard error of the mean). All animal experiments were performed in accordance with the German Guidelines for the care and use of laboratory animals.

2.2. Urea protein extraction

Briefly, crushed frozen tissue was incubated for 45 min in 6 volumes of extraction buffer (7 M urea, 2 M thiourea, 2% ampholyte 2–4, 70 mM DTT, 25 mM Tris/HCl, 50 mM KCl, 3 mM EDTA, 2.9 mM benzamidine and 2.1 μM leupeptin) and centrifuged for 45 min at 16,000 × *g* at RT. To avoid carbamylation, ultrapure urea (#161-0731 from Biorad, Germany) was used. The supernatant was transferred to new tubes and the protein concentration was determined with the Bradford Reagent (Carl Roth, Germany).

2.3. 2-DE and comparative image analysis

Large-scale 2-DE (23 cm × 30 cm × 0.75 mm) and image analyses were conducted as described before [28]. Seven mice per group were analysed by 2-DE. For analytical gels 100 μg protein extract was loaded at the anodic side of IEF gels, focused at 8500Vh in a gradient between pI 2 and 11 and further separated in 15% acrylamide gels in Tris-glycine buffer (25 mM Tris and 192 mM glycine). Gels were fixed in 50% ethanol 10% acetic acid overnight and silver-stained according to Heukeshoven and Dernick [29]. Image analysis was performed with the Proteomweaver software version 3.0.9.9 (Biorad, Germany) according to the manufacturer's instructions. Briefly, spots were detected, their intensities normalized to total intensity of all spots (on one gel) and matching was carried out first inside groups and then between groups. Spot were edited and matched manually to reduce inaccurate spot matching. They were considered to be regulated when the relative spot density was significantly different ($p < 0.05$) with a regulation factor (RF) following the minimal significant factor and the considered spot present in at least five out of the seven gels in each study group. No further cut-off was applied and all protein spots with the above-described behavior were subjected to MS analysis.

2.4. ESI-MS/MS for 2-DE spot identification

All spots with significant change in amount were excised from preparative gels (23 cm × 30 cm × 1.5 mm, stained according to Nebrich [30]), in-gel digested with 200 ng trypsin per spot and tryptic peptides were subjected to nanoLC-ESI-MS/MS. The 2-DE spot positions and their peak lists (mgf files) are accessible via https://transfer.mpiib-berlin.mpg.de/index.php/s/dVzcs3VU3Of8ZFm, using the password murine.mgf.

The MS system consisted of an Agilent 1100 nanoLC system (Agilent, Germany), PicoTip emitter (New Objective, USA) and an Esquire 3000 plus ion trap MS (Bruker, Germany). Peptide separation and MS criteria are described in details [28]. Peak lists were generated by DataAnalysis 3.2 (Bruker, Germany) with fragments qualified by amino acids, a minimal intensity of 25,000 and a maximum of 300 spectra.

Proteins were identified using MS/MS ion search of Mascot search engine Version No. 2.2 (www.matrixscience.com, Matrix Science, England) and the SwissProt data base (SwissProt 2010_07, Swiss Institute of Bioinformatics, Switzerland) with 16,299 sequences for *Mus musculus*. Parameters for data base searching were: *Mus musculus*, type of search (MS/MS Ion Search), enzyme (trypsin), variable modifications (oxidation M, propionamide C), mass values (monoisotopic), peptide mass tolerance (± 0.1%), fragment mass tolerance (± 0.5 Da) and maximal missed cleavages (1). Proteins with a significant score (significance threshold $p < 0.05$) and a minimum of 2 matched peptides have been considered to be properly identified. The pathway analysis tools Ingenuity Pathway Analysis (IPA, version 7.5, Ingenuity Systems, USA) was further used to identify prominent pathways altered due to conditions used in this study.

2.5. 1Dimensional immunoblotting (1D-IB)

20 μg urea protein extracts were separated in 10% acrylamide gels and transferred at low voltage overnight to a PVDF membrane in Towbin buffer, containing 25 mM Tris, 192 mM glycine and 20% (v/v) methanol [31], at 4 °C by semi-dry blotting following standard procedure [32]. The next day, membranes were blocked for 1 h in blocking solution (4% (w/v) BSA in TBS with 0.2% (v/v) Tween-20), incubated overnight at 4 °C in primary antibody (provider and dilutions, see below), diluted in blocking solution, washed 3 times in TBS-T and incubated for 1 h in secondary antibody (Dako, Denmark), diluted 1:5000 in blocking solution. After washing additional 3 times in TBS-T, membranes were overlaid with ECL solution (GE Healthcare, USA) and chemiluminescent signals were detected on hyper-films (GE Healthcare, USA). Antibodies against ER alpha (sc-544, diluted 1:500), ECHA (sc-292195, diluted 1:1000), ECHB (sc-55661, diluted 1:1000), THIM (sc-

100847, diluted 1:1000) and β-actin (sc-1615, diluted 1:5000) were used. All primary antibodies were purchased from Santa Cruz Biotechnology, USA. Densitometric quantification was performed based on seven biological and two technical replicates for each study group and antibody normalized to beta actin (Alpha Ease software, version 3.1.2, Alpha Innotech Corporation, USA). The data were expressed as group mean with SEM. Females were used as reference and their group mean value was set to 1. Seven mice were analysed per group and antibody.

2.6. Small-scale 2-dimensional immunoblotting (2D-IB) and MS by LTQ-FT-ICR and Q-Exactive

2D-IB was done in a qualitative manner, where one pooled sample per study group was analysed. 20 μg of protein were loaded on 10 cm × 1.5 mm IEF gels (pI 2–11), focused at 1800 Vh and further separated by 7 cm × 8 cm 10% acrylamide SDS-PAGE [33]. Small-scale blots were generated by blotting the proteins onto a PVDF membrane in Towbin buffer. The immunoreaction for ECHA, ECHB and THIM was conducted as described above and parallel membranes were gold stained (Colloidal gold staining kit, Proteome Factory, Germany) to facilitate finding the protein species corresponding to the immunoreactive spots. Based on the triangulation principle all immunoreactive spots (21 in total, see Fig. 8A–C) were taken in duplicates from large-scale preparative gels, digested with 200 ng trypsin per spot and each replicate was subjected to LTQ-FT-ICR or to Q-Exactive (Q-E) tandem MS. Settings for FT-analysis with CID fragmentation were described before [34]. The Q-E system consisted of an Agilent 1100 nanoLC system (Agilent, Germany), PicoTip emitter (New Objective, USA) and a Q-Exactive quadrupole-Orbitrap mass spectrometer (ThermoFisher, Germany). Separation was conducted using an acetonitrile, 0.1% formic acid gradient from 5% to 35% acetonitrile within 40 min. The mass spectrometer was operated in a data-dependent mode by subjecting the ten most abundant ions of each survey spectrum (nominal resolution 35.000) to HCD fragmentation (normalized collision energy at 30%, resolution 17.500). Identification of proteins was carried out with Mascot search engine (peptide mass tolerance of 10 ppm and MS/MS tolerance of 0.6 Da). All proteins within each hit list were considered and rank of proteins of interest (ECHA, ECHB and THIM) is given in Tables 1 and 2. Additionally, an error-tolerant search for the Orbitrap spectra was performed to identify PTMs.

2.7. Histology

Formalin-fixed and paraffin-embedded cardiac tissue was cut into 3 μm sections and hematoxylin/eosin staining was performed. Pictures were taken using a light microscope (Carl Zeiss, Germnay) and the cardiomyocyte diameter for each mouse was measured in 130 random cells by an investigator, blinded with respect to sex and age, using the Image J software (NIH Image, National Institutes of Health, USA). Three mice were analysed per group and the data expressed as group mean with SEM.

2.8. Quantitative Real time PCR (Q-RT-PCR)

Total RNA was extracted from frozen tissue with TRIzol Reagent (Invitrogen, USA) and concentration was measured with a nano drop 1000 spectrophotometer (ThermoFisher, USA). 5 mg of RNA were DNAse-treated (Applied Biosystems, USA), reverse-transcribed with the iScript cDNA synthesis Kit (Bio-Rad, Germany) and diluted to a final concentration of 2 ng/μL. Q-RT-PCR was carried out with SYBR Green (Maxima SYBR Green, Life Sciences, Canada), in animal cohorts of five mice each. Ppara and ppargc1a were quantified with the delta Ct method normalized to 18sRNA [28]. Seven mice were analysed per group and the data expressed as group mean with SEM.

Table 1
Identification of the 21 immunoreactive spots by LTQ-FT-ICR MS. IB001-IB010: Spots reactive with ECHA antibody, IB011-IB017: Spots reactive with ECHB antibody and IB018-IB021: Spots reactive with THIM antibody. Protein rank within the hit list, protein score and unique peptide matches (excluding multiple matches) are given.

Reactive with antibody against	Spot ID	Protein name	Ranking in hit list	Score	Unique peptide matches
ECHA	IB001	ECHA	1	1859	32
	IB002	DHB4	1	506	8
		ECHA	2	220	4
	IB003	ECHA	1	48	1
	IB004	No match for ECHA			
	IB005	TRY1	1	30	1
		ECHA	2	28	1
	IB006	No match for ECHA			
	IB007	No match for ECHA			
	IB008	ECHA	1	92	2
	IB009	PAIRB	1	450	10
		K22E	2–4, 8	44–95	1–2
		TRY1	5	65	1
		Q6IFT3	6	61	1
		TRY1	7	53	1
		ECHA	9	40	1
	IB010	No match for ECHA			
ECHB	IB011	ECHB	1	1463	24
	IB012	MDHC	1	151	2
		ECHB	2	102	1
	IB013	No match for ECHB			
	IB014	No match for ECHB			
	IB015	No significant hit			
	IB016	No match for ECHB			
	IB017	No significant hit			
THIM	IB018	No significant hit			
	IB019	No significant hit			
	IB020	No significant hit			
	IB021	No significant hit			

2.9. Data analysis

No further cut-off or post-analyses were applied to the data set obtained from the Proteomweaver, as the software tools automatically calculate average spot intensities, regulation factors and *p*-values. Data for immunoblotting, histology and Q-RT-PCR are expressed as group mean and SEM. Statistical analysis was conducted using either two-tailed *t*-test or multifactorial analysis of variance (ANOVA), followed by Bonferroni corrected t-test (GraphPad Prism software version 6.00; GraphPad Software Inc., USA). Differences were considered statistically significant at $p < 0.05$.

3. Results

To identify protein networks differing between the sexes during aging, as well as to determine the influence of deprivation of sexual hormones, the myocardium of young (1 month), adult (6 months) and castrated (6 months) male and female mice was subjected to histological, comparative 2-DE analyses and further to RNA analysis by RT-PCR and protein analysis by immunoblotting. Gonadectomy was conducted in 3 months old mice to ensure that the observed changes are related to cardiac function in mature mice and not to developmental aspects.

3.1. General parameters

All mice seemed in good health conditions during life span. As indicator for cardiac hypertrophy, we first measured the ratio between the heart weight and the body weight (HW/BW), as well as the cardiomyocyte diameter. As shown in Fig. 1A, no sex-related differences for the HW/BW ratio were observed, but a gonadectomy effect for male and female mice (see § in Fig. 1A). Male mice had higher body weights

Table 2
Identification of the 21 immunoreactive spots by Q-Exactive Orbitrap MS. IB001-IB010: Spots reactive with ECHA antibody, IB011-IB017: Spots reactive with ECHB antibody and IB018-IB021: Spots reactive with THIM antibody. An error-tolerant search was performed to identify posttranslational modifications. T: Threonine, S: Serine, Y: Tyrosine, D: Aspartic acid, E: Glutamic acid, s: sulfation, p: phosphorylation, a: acetylation, c: carboxylation.

Reactive with antibody against	Spot ID	Protein name	Ranking in hit list	Score	Unique peptide matches	PTM
ECHA	IB001	ECHA	1	1747	32	T30-s, T39-s, T270-s, T387-s, S474-p, T476-p, S477-p, T517-s, T521-s/p, T547-p, Y637-s, S668-s/p, S738-p, T742-p, T745-s/p
	IB002	Not applicable				
	IB003	ECHA	1	804	19	
	IB004	MCCA	1	1771	36	
		ACON	2	522	16	
		ECHA	3	496	15	
	IB005	ECHA	1	398	14	
	IB006	ATAD3	1	722	21	
		ECHA	2	393	12	
	IB007	NONO	1	756	19	
		PAIRB	2	396	13	
		ECHA	3	231	10	
	IB008	ECHA	1	312	11	
	IB009	PAIRB	1	731	24	
		ECHA	2	358	11	
	IB010	PURA1	1	1043	24	
		IDHC	2	540	16	
		ECHB	3	261	7	
		RCBT2	4	196	5	
		ALDOA	5	162	4	
		ECHA	6	153	4	
ECHB	IB011	ECHB	1	1321	24	S35-a/p, S68-p, D74-c, S86-p, S141-s/p, S142-s, S219-p, E241-c, T275-s, D340-p, D350-p, D395-p, S396-s, S426-s
	IB012	MDHM	1	1156	25	
		HNRPQ	2	670	16	
		G3PT	3 and 4	512–575	11–14	
		ECHB	5	465	13	
	IB013	MDHM	1	1190	24	
		K22E	2–8, 10–12, 14–16	123–378	5–10	
		G3PT	9	194	6	
		HNRPQ	13	147	5	
		ECHB	17	118	3	
	IB014	MDHM	1	868	15	
		FHL2	2	321	13	
		G3PT	3	234	6	
		ECHB	4	211	5	
	IB015	MDHM	1	690	12	
		SUCB1	2	687	16	
		K22E	3 and 4	151–171	3–4	
		ECHB	5	127	3	
	IB016	MDHM	1	698	15	
		SUCB1	2	290	7	
		RM03	3	238	10	
		K22E	4–14	50–177	2–5	
		ECHB	15	38	1	
	IB017	No match for ECHB				
THIM	IB018	No match for THIM				
	IB019	No match for THIM				
	IB020	CACP	1	1117	25	
		CMC2	2	731	18	
		ROA1	3	603	13	
		Unnamed protein	4–5	530–569	13–18	
		MDHM	6	465	10	
		CACP	7	386	8	
		PROD	8	338	12	
		CPT1A	9	300	9	
		DJC11	10	256	8	
		K22E	11	216	5	
		THIM	12	204	6	
	IB021	No match for THIM				

and heart weights compared to female mice (Fig. 1B and C, see asterisks) and this was true for intact mice only. Also, there was an overall significant effect of sex, age and interaction for body weights and heart weights (Fig. 1B and C p's < 0.0001), visible as increased body and heart weights for male and female mice during aging, but a steady state or even a decrease of these 2 parameters due to gonadectomy (see §, Fig. 1B and C). Furthermore, no sex- or gonadectomy-related differences were observed for the cardiomyocyte diameter (Fig. 1D). However, there was a significant age effect for this parameter, and 6 months old mice, of both sexes, showed an enlarged cardiomyocyte diameter when compared to 1 month old mice, at both time points and with and without gonadectomy (Fig. 1D, ANOVA age effect $p = 0.008$). Taken

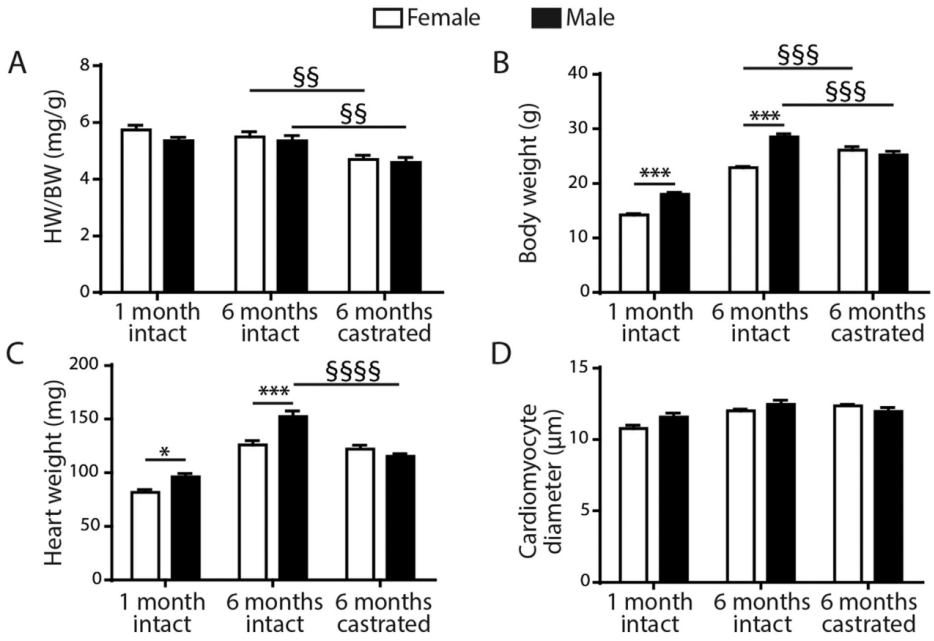

Fig. 1. Sex-related effects on general parameters. (A) The heart to body weight ratio, (B) the body weight, (C) the heart weight and (D) the cardiomyocyte diameter for female (white bars) and male (black bars) animals are shown. Mean values and SEM are plotted. Bonferroni post-test for males vs. females *: $p < 0.05$ and ***: $p < 0.001$. Bonferroni post-test for gonadectomy effects §§: $p < 0.01$, §§§: $p < 0.001$ and §§§§: $p < 0.0001$. $N = 10$ mice per group.

together, these first assessments emphasize normal cardiac function in mice, despite aging and/or gonadectomy.

3.2. Comparative 2-DE analysis

To unravel sexually dimorphic protein species, regulated due to aging and gonadectomy, we performed large-scale 2-DE. The generated large-scale 2-DE gels were highly reproducible, displaying around 1200 spots. Comparative 2-DE analyses revealed a total number of 107 spots significantly differing due to sex in the three age/hormonal deprivation groups tested. Of those 107 spots, 90 were identified by MS and are shown in Fig. 2, in which they are numbered and highlighted by arrows. The numbering of the regulated spots is the same as the protein ID's given in the Supplementary Table 1. All raw 2-DE data, including RF (RF, calculated as group mean value for males vs. group mean value for females, and females getting a reference value of 1) and the entire identification list of the protein species is documented in the Supplementary Table 1. In one-month-old mice, 8 protein spots were different, while in 6 months old mice 51 spots and in castrated mice 32 spots were regulated between male and female mice (Fig. 3). Note that for several proteins multiple single spots were differentially regulated and that for several highly abundant metabolic proteins only low-abundance spots were significantly changed, e.g. ATPB, ECHA and THIM. The most prominent differences between male and female mice in all three conditions were found for metabolic proteins and for proteins involved in energy generation (Fig. 3 and Supplementary Table 1). Out of the 90 spots showing a different male/female ratio 70 spots belonged to metabolic proteins (54 of different pathways and 16 proteins involved in electron transport), whereas only 20 spots had other functions e.g. morphogenesis, signal transduction or cell cycle.

To understand whether sex-related differences are preserved during aging and abolished by castration we further clustered the 90 spots according to male/female spot ratios of 1 month, 6 months/intact and 6 months/castrated and plotted them as shown in Fig. 4. Out of those 90 spots 58 showed a characteristic V-shaped curve (upright or upside down V), meaning an alteration induced by sexual maturity and a return to premature levels by castration, emphasizing them to be directly influenced by gonadal hormones (Fig. 4A). For the remaining 32 spots, the deprivation of gonadal hormones seemed rather to enhance differences between male/female mice, with several spots showing drastic increase in the male/female spot intensity ratio after castration (Fig. 4B, e.g. spots 90, 235 and 362). In total, we found that most protein changes induced by sexual hormones in adult mice were missing/absent after castration for a majority of the differentially abundant spots. Because only eight spots were regulated due to sex in one-month-old mice, this age group was omitted from following analyses.

3.3. Differential regulation of the FA pathway between male and female mice

Next, we performed pathway analyses to identify prominent pathways regulated between the sexes in intact and castrated adult mice and found the FA metabolism and mitochondrial dysfunction being the top two pathway matches between male and female mice. Three proteins, the insulin receptor (INSR), PPARA and PRGC1, were predicted with high probability as upstream regulators (Fig. 5A and 5B; $p \leq 1.2E-6$). For sex-related differences in intact mice the most significant changes were found in FA oxidation; all regulated proteins related to FA oxidation are displayed in the interconnecting network, with PPARA taking a central position within this network (Fig. 5A). For castrated male/female comparison, the most significant pathway was mitochondrial function (Fig. 5B). Noteworthy is that the protein RICTOR, which is part of the mammalian Target of Rapamycin Complex 2 (mTORC2, [35]), seems to take a central role as well and is present in both IPA

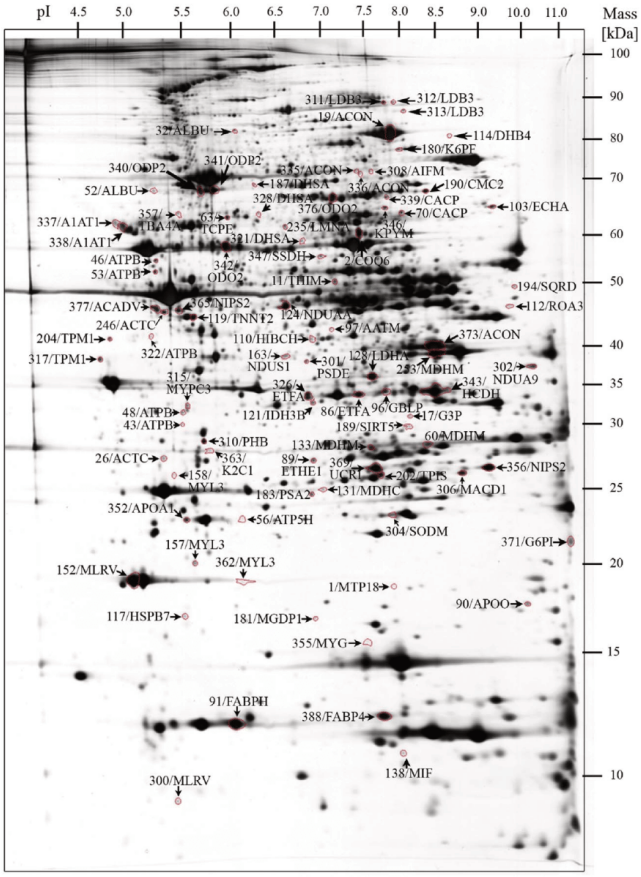

Fig. 2. Silver-stained large-scale 2-DE gel pattern of murine heart protein extract. 107 spots were differently regulated between the study groups and 90 were identified by ESI-MS/MS. These 90 spots are numbered and are highlighted by arrows (corresponding spot IDs and protein identification, see Supplementary Table 1). Seven mice per group were analysed by 2-DE.

analyses. The involvement of mTORC2 in regulating cardiac function via interaction with mitochondria is currently receiving much attention, but will not be in focus of this work.

As FA metabolism i) plays a crucial role in maintaining normal heart function and ii) is changing during heart disease, we focused in this work on certain aspects of species regulation of selected proteins, involved in the FA pathway. As key regulators of the FA metabolism in cardiac tissue [36,37], ER alpha, PPARA and their coactivator PGCA1 were quantified. ER alpha and PPARA have considerable signal cross-talk and regulate numerous genes involved in FA metabolism [37]. At the protein level, we found only sex-related changes for ER alpha (Fig. 6A, ANOVA sex effect $p < 0.0001$), and ER alpha was significantly decreased in male compared to female mice, irrespective of gonadectomy (Fig. 6A, see asterisks), while PPARA and PGCA1 m-RNA levels were not changing (6C and 6D, ANOVA: ns).

Furthermore, three enzymes important for FA-oxidation, namely ECHA, ECHB and THIM, were assessed at the protein level. Herein, we determined their total abundance by 1D-IB, as well as their speciation using 2D-IB. At the 1D total protein level, we found ECHA higher in females only, due to castration, but lower in males compared to females, irrespective of the hormonal status (Fig. 7A, ANOVA age effect $p = 0.022$ and sex effect $p < 0.0001$, also see asterisks for post-ANOVA comparison). For ECHB, 2 bands were visible by 1D-IB. For the 50 kDa band, no sex-related effects were seen but age and interaction effects. This means that the abundance of this species was increased in females but not different in males due to castration, and that sex-related differences were only present between castrated male and female animals (Fig. 7B, ANOVA age effect $p = 0.0002$ and interaction effect $p < 0.0001$, also see asterisks for post-ANOVA comparison). The 40 kDa band was very faint and was not changing with respect to either of the parameters (Fig. 7C). For THIM the interaction of the parameters proved to be highly significant (Fig. 7D, ANOVA interaction effect $p < 0.001$): THIM abundance was increased in females only due to castration, and increased in intact male compared to intact female mice, while no sex-related differences were observed in castrated mice (Fig. 7D, ANOVA interaction effect $p < 0.001$).

3.4. Speciation of ECHA, ECHB and THIM

1D-immunoblotting is the most used method to assess protein abundance. As stated earlier, we found during 2-DE analysis many proteins being present in multiple single spots. This phenomenon is called protein speciation [15] and has been addressed in this work for the three selected proteins ECHA, ECHB and THIM. Consequently, to identify the protein species of ECHA, ECHB and THIM responsible for the regulation, as found during 1D-IB examinations, we subjected these

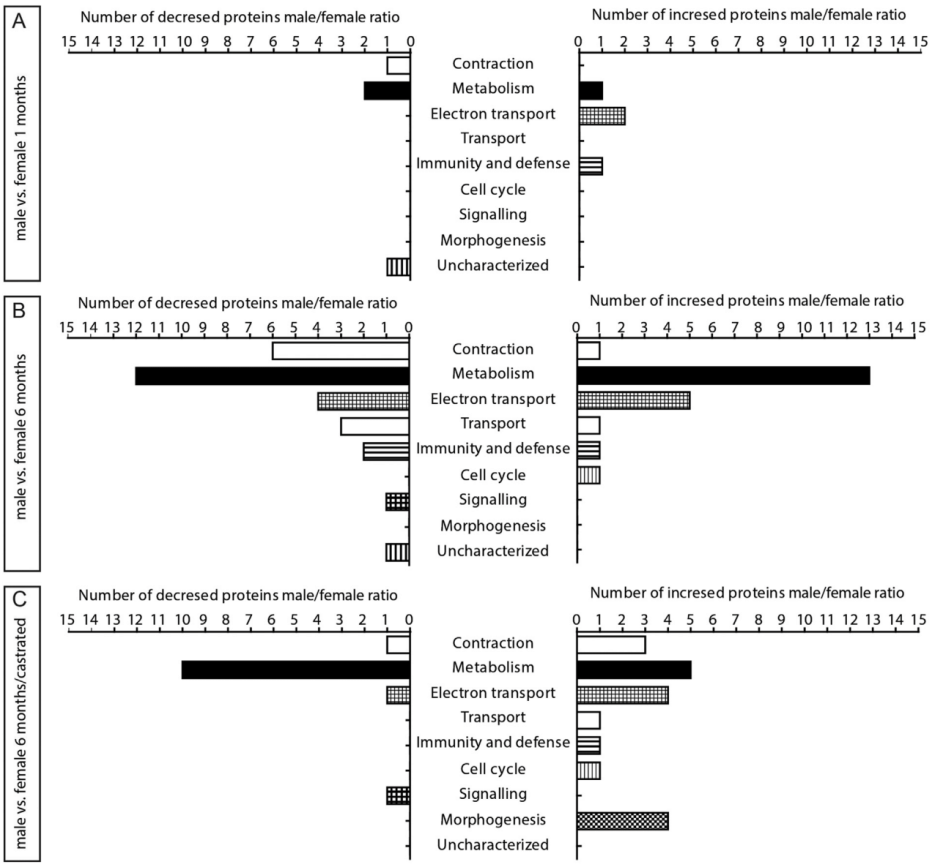

Fig. 3. Number of decreased and increased proteins in male compared to female mice in young (A, 8 protein species), 6 months old (B, 51 protein species) and castrated (C, 32 protein species) mice. The differentially regulated proteins are clustered according to their biological processes.

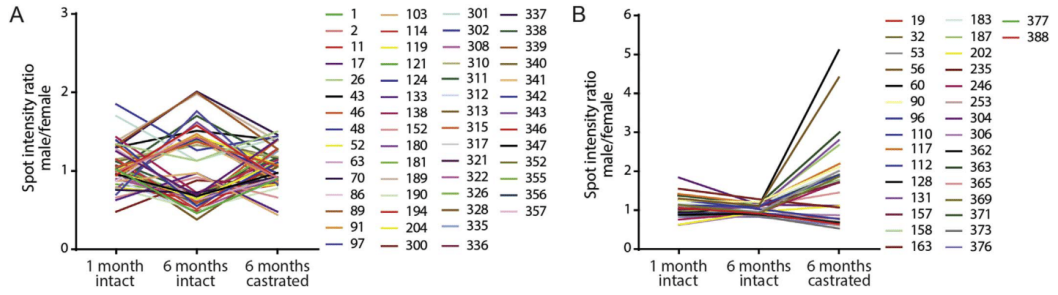

Fig. 4. Ratio of spot intensities between male and female mice of 1 and 6 month intact and 6 month castrated mice. The 90 spots identified in this study were sorted in (A) 58, which restore the ratio to the same level observed before castration and (B) 32, which change more after castration or in the same direction as by aging.

three proteins to speciation analysis using 2D-IB and downstream MS analyses. For ECHA we found 10 reactive species (Fig. 8A, IB001-IB010), while for ECHB we found 7 species (Fig. 8B, IB011-IB17) and for THIM 4 species (Fig. 8C, IB18-IB21) to immunoreact with the antibodies specified in the methods section. Surprisingly spot 100, spot 47 and spots 11–13, previously excised from silver stained gels and identified as ECHA (spot 100), ECHB (spot 47) and THIM (spots 11–13) by MS, were not labeled with the antibodies used here. For completeness, we show in Fig. 8D–F, not only the 21 immunoreactive species IB001-IB021, but additionally the 5 2-DE spots 11–13, 47 and 100. The density

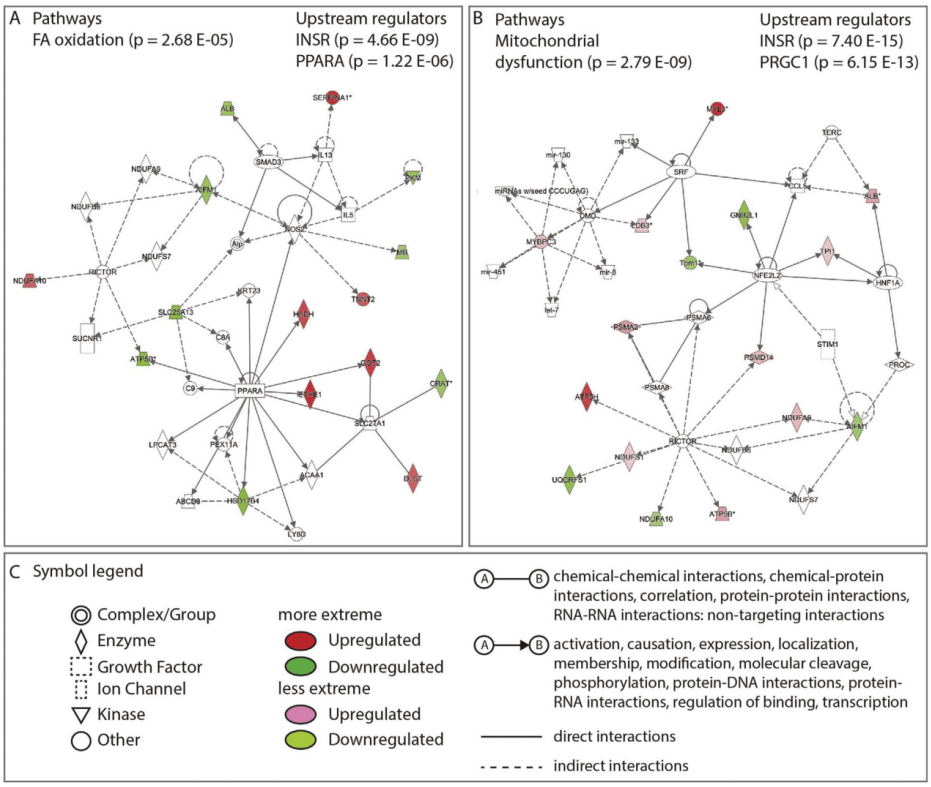

Fig. 5. Top pathways, upstream regulators and networks for sex-related differences in 6 months intact and 6 months castrated mice are shown. The analysis was conducted using IPA tools. (A) For intact mice, the fatty acid (FA) oxidation pathway was found highly regulated (p = 2.68E − 05) between the sexes and is displayed. (B) In castrated mice, the mitochondrial function pathway was significantly differing between male and female mice (p = 2.79E − 09), and is illustrated in the network. The proteins INSR, PPARA and PPAGC1A were found highly significant upstream regulators of the induced changes. INSR: insulin receptor, PPAR: peroxisome proliferator-activated receptor alpha; PRGC1: peroxisome proliferator-activated receptor gamma coactivator 1-alpha.

behavior of these 26 spots is discussed below and herein we will focus solely on sex-related aspects.

3.5. Connecting protein speciation to the regulation of the total protein

The 26 spots stated above were assumed to represent ECHA (Fig. 8D), ECHB (Fig. 8E) and THIM (Fig. 8F). For ECHA 11 species were identified in total, 10 spots by 2D-IB and one spot (ID100) by 2-DE-MS (reported in a previous study, see http://www.mpiib-berlin.mpg.de/2D-PAGE). For ECHB 8 spots were identified in total, 7 based on 2D-IB and 1 based on 2-DE-MS (spot 47, see data base). THIM was found in 7 spots, 4 identified by 2D-IB and 3 by 2-DE-MS (spots 11, 12 and 1, see data base). The optical density of these 26 spots is shown in Fig. 9 for intact (Fig. 9A) and castrated (Fig. 9B) female and male mice.

Total ECHA was significantly decreased in male compared to female mice (all intact), as shown previously in Fig. 7A (see asterisks) and this seems to be due to significant decrease in species IB005 (Fig. 9A, RF = 0.79, p = 0.053). ECHA was also significantly decreased in castrated male compared to castrated female mice at the 1D-protein level (Fig. 7A, see asterisks) and species IB009 was significantly decreased (Fig. 9D, RF = 0.44, p = 0.005), whereas many other ECHA species showed only a tendency for reduction (Fig. 9D, e.g. IB002 and IB008).

In intact mice the 40 and the 50 kDa species of ECHB were not different between the sexes at the 1D protein level (Figs. 7B and 7C) and, accordingly none of the ECHB species was changed (Fig. 9B). In castrated mice, only the 50 kDa species was decreased in male vs. female mice (Fig. 7B, see asterisks), well correlating with the significant reduction of species IB013 (Fig. 9E, RF = 0.60, p = 0.01).

Total THIM was elevated for intact male compared to intact female mice (Fig. 7D, see asterisks), most likely due to increased density of spot 11 (Fig. 9C, RF = 1.58, p = 0.007). In castrated mice, THIM did not show sex-related regulation either at the total protein level (Fig. 7D) or at the single species level (Fig. 9F).

In summary, the results clearly show that single protein species behave differently than in a mixture on a 1D-gel. Nevertheless, we were able to identify species responsible for the regulations observed during 1D protein density examination. It should be mentioned that species showing only a tendency for regulation might also contribute to the observed changes at 1-D levels; however, the summation of spot density is highly disapproved.

3.6. Challenging the specificity of antibodies against ECHA, ECHB and THIM

For the 21 immunoreactive species described above, we relied so far solely on detected immunoreactivity with the antibodies used.

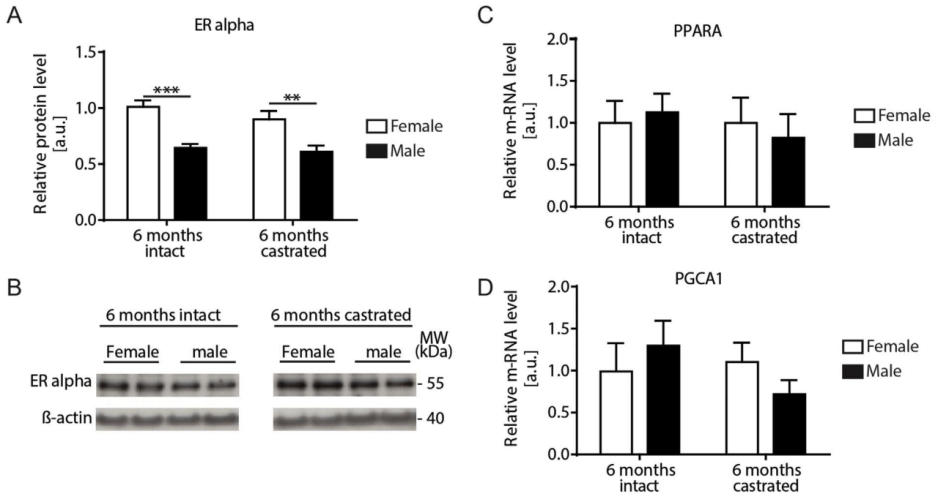

Fig. 6. Quantification of ER alpha, PPAR and PGCA1 for female (white bars) and male (black bars) mice. (A) ER alpha was assessed at the protein level by densitometric quantification of immunoblots, representatively shown in (B). PPARA (C) and PGCA1 (D) were quantified at the m-RNA level. Seven mice per group were analysed and mean values and SEM are plotted. Bonferroni post-test for males vs. females **: $p < 0.01$ and ***: $p < 0.001$.

However, unspecific antibody-binding is an issue not to be underestimated. Therefore, we aimed at verifying this important aspect of antibody specificity and we challenged the identity of immunoreactive spots with MS.

Based on the triangulation principle, all spots assumed to contain ECHA (10 spots), ECHB (7 spots) and THIM (4 spots), which corresponded to the 21 immunoreactive spots described above, were localized on a preparative gel (Fig. 8D–F for the 3 proteins), taken in duplicates and digested with trypsin. One replicate of the tryptic peptides was subjected to FT-ICR, while the second replicate was measured by Q-E-MS.

The MS search results of the FT-ICR are illustrated in Table 1. Based on this mass spectrometer, we found 6 out of 10 spots to contain ECHA (IB001-IB003, IB005, IB008 and IB009), 2 out of 7 spots to contain ECHB (IB011 and IB012) and no THIM was identified in any of the 4 immunoreactive spots examined. Note that in 6 spots (IB015 and IB017-IB021) no proteins were measured at all, presumably due to very low abundance. With the Q-Exactive Orbitrap (Table 2), we found 9 out of

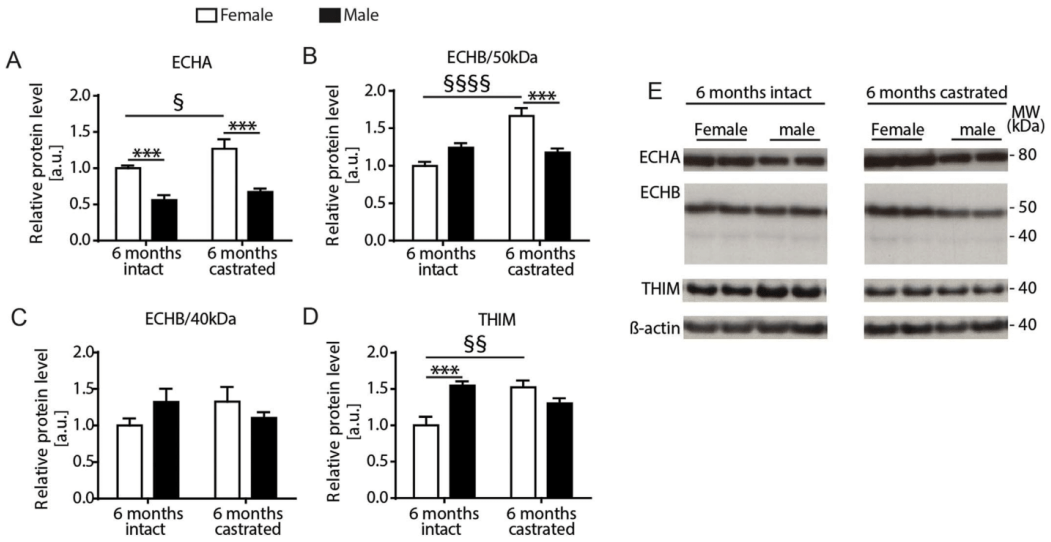

Fig. 7. Quantification of ECHA, ECHB and THIM for female (white bars) and male (black bars) mice. (A) ECHA, (B and C) ECHB and (D) THIM were quantified at the protein level, conducted by densitometric quantification of 1D-immunoblots, representatively shown in (E). Seven mice per group were analysed by 2-DE and ean values and SEM are plotted. Bonferroni post-test for males vs. females *: $p < 0.05$ and ***: $p < 0.001$. Bonferroni post-test for gonadectomy effects §: $p < 0.05$, §§: $p < 0.01$ and §§§§: $p < 0.0001$.

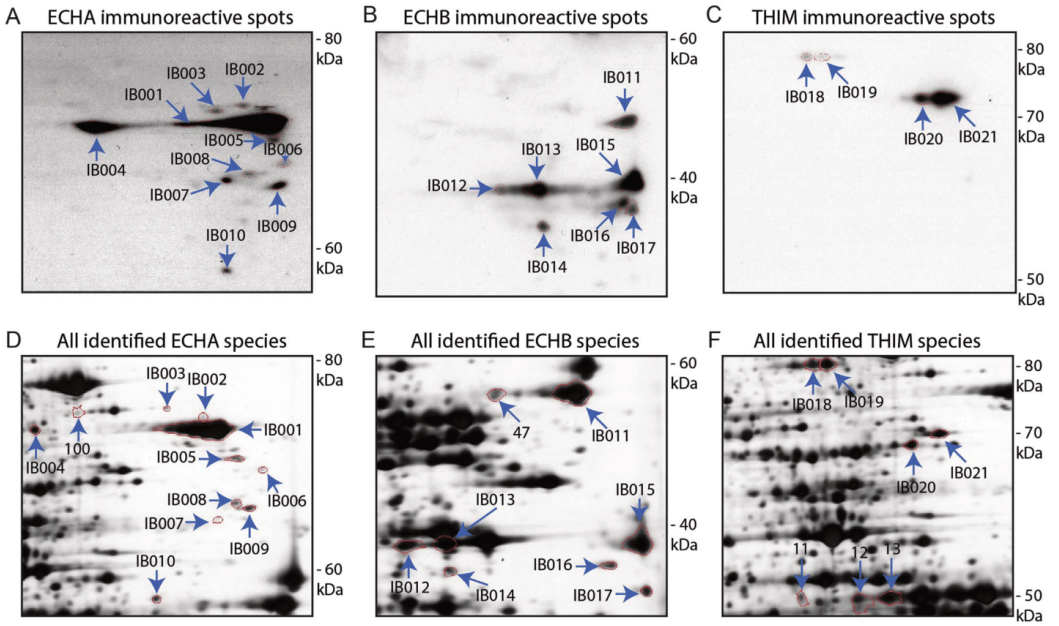

Fig. 8. Speciation of ECHA (A and D), ECHB (B and E) and THIM (C and F), by 2D-IB (A–C) and silver staining (D–F). For 2D-IB (qualitative 2D-IB with one pooled sample per study group) 10 spots were reactive to the antibody against ECHA (A), 7 spots were reactive to the antibody against ECHB (B) and 4 spots were reactive to the antibody against THIM (C). Spots corresponding to those immunoreactive species were taken from preparative gels and analysed by MS. All spots identified as ECHA (D), ECHB (E) and THIM (F) are highlighted in a silver stained 2-DE pattern obtained from urea soluble heart tissue.

10 spots to contain ECHA (IB001 and IB003-IB010), 6 out of 7 spots to contain ECHB (IB011-IB016) and 1 out of 4 spots to contain THIM (IB020).

In summary, we found more matches with the Q-Exactive Orbitrap than with the FT-ICR mass spectrometer, which might be due to superior sensitivity. However, in some spots we did not succeed to identify the proteins of interest and this might be due either to antibody cross-reactivity or to species co-migration, or higher sensitivity of the IB identification compared with the MS identification. For example when a co-migrating species is highly abundant, then it is most likely that spectra of this species are predominantly measured just because these spectra are much more intense.

3.7. Posttranslational modifications as a cause of ECHA, ECHB and THIM speciation

The speciation behavior of our three proteins of interest described above, raised the necessity for assessing their PTM status. When species belonging to the same protein are located at different positions on a 2-DE pattern, PTMs, including any addition of moieties or any degradation events, must be considered as the cause of this speciation behavior. Hence, an error-tolerant search of the Q-Exactive MS data was performed, as more matches were found with this mass spectrometer. As shown in Table 2, IB001 and IB011 were found modified. Modifications for IB001-ECHA species were detected, such as phosphorylation and sulfation, at multiple residues. Furthermore, we found IB011-ECHB species to be phosphorylated, sulfated, carboxylated and acetylated (Table 2). Noteworthy is that IB001 and IB011 were highly abundant, as obvious from 2D-images (see Figs. 8D and 8E), and had the highest unique peptide matches. Taken together, the results underline that improvements are still needed for the measurement of PTMs in complex protein samples, with the protein of interest being of low abundance. A 100% sequence coverage is still a challenge for MS identification of protein species.

4. Discussion

In the current investigation, we used a proteomics approach to identify sexually dimorphic proteins in the myocardium of intact and castrated mice. Mice seemed in good health conditions and, despite gonadectomy procedures, no adverse effects related to hypertrophy were seen. The enlarged cardiomyocyte diameter observed in aging mice is very likely related to normal cardiac aging processes, as it is well known that post-natal cardiac growth is mainly achieved by increasing cardiomyocyte size, because these cells lose their proliferation ability shortly after birth [38]. These first general assessments emphasize normal cardiac function in all mice.

From the 2-DE analysis it seems that many of the sex-related differences are not mediated by gonadal hormones only, as there still are big differences between gonadectomized mice (32 protein species with different abundance pattern), and only a few between male/female mice before sexual maturity (only 8 protein species with a different amount). Our 2-DE-based global protein analysis revealed two prominent protein regulation patterns seen for male/female comparison: proteins probably directly regulated by gonadal hormones, as their regulation follows a V-shaped regulation pattern, and sex-related differences mediated either independently form gonadal hormones or lacking important feedback regulation in their absence. In total, we found most protein changes induced by sexual hormones removed after castration. However, the changes for about 1/3 of the proteins were likely induced by factors other than gonadal hormones.

The most prominent differences between male and female mice in

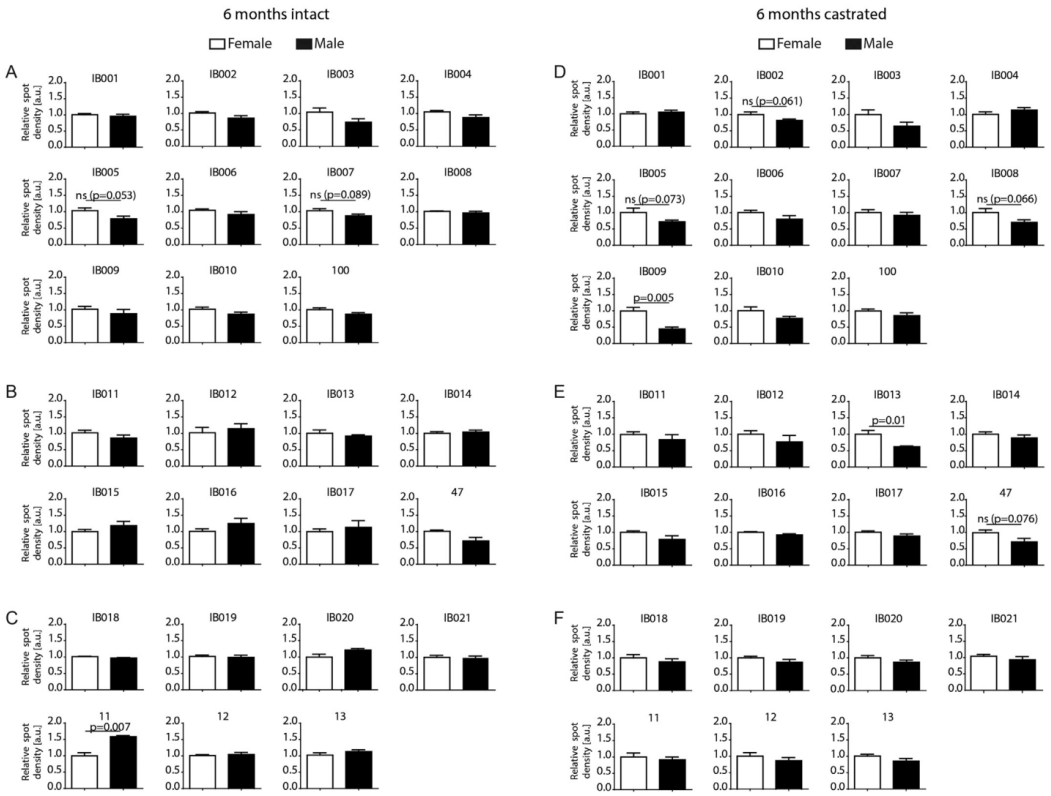

Fig. 9. Relative spot densities for all species identified as ECHA (A and D; IB001-IB010 and spot 100), ECHB (B and E; IB011-IB017 and spot 47) and THIM (C and F; IB018-IB021 and spots 11–13). Spots were identified by 2D-IB (with one pooled sample per study group) and ESI-MS. Relative species intensities for intact (A–C) and castrated (D–F) female (white bars) and male (black bars) mice are displayed. Two-tailed *t*-test for males vs. females *: $p < 0.05$ and ***: $p < 0.001$.

all three conditions compared were found for metabolic proteins (54 out of 90 species). Using the Ingenuity pathway tool we were able to identify the FA metabolism and mitochondrial function being highest ranking. In addition, using the same tool, INSR, PPARA and PRGC1 were predicted to be putative upstream regulators, responsible for inducing the observed changes. Heart function is tightly connected to cardiac energetics [39]. In the healthy myocardium, FA oxidation accounts for up to 90% of total energy supply [40] and many CVDs are now linked to disturbed cardiac metabolism [41–43]. FAs enter cardiomyocytes by the albumin receptor or the FA transport protein and are transformed to long chain acyl-CoA in the cytoplasm [44,45]. They are oxidized by a series of enzymes, including the alpha and beta subunits of the trifunctional enzyme (ECHA and ECHB) and 3-ketoacyl-CoA thiolase (THIM) [40]. The estrogen receptor (ER) alpha and the peroxisome proliferator-activated receptor alpha (PPARA) are known to regulate numerous genes involved in the FA degradation, with the receptors showing a large overlap between the genes they regulate [36]. Peroxisome proliferator-activated receptor gamma coactivator 1-alpha (PRGC1) is an inducible cofactor of ER alpha and PPARA. It is regulated at the transcript level, its activation leads to enhanced abundance of ER alpha and PPARA, which in turn induce transcription of proteins involved in FA oxidation [40,46]. Estrogen is believed to shift the balance between FA/carbohydrate oxidation towards elevated FA metabolism [47–49], while For PPARs such correlation is not yet well established [40,50,51]. In our study, ER alpha was higher in female compared to male mice and remained constant following gonadectomy procedures. Contradictory findings had been reported regarding the influence of steroid hormone deprivation on cardiac estrogen receptor levels. The three proteins ECHA, ECHB and THIM were found elevated upon castration in females only, suggesting a lack of adaptation to deprivation of gonadal hormones in male mice and resulting in a reduced FA capacity in those mice. Normally, reduced FA utilization is connected to a metabolic switch from FAs towards carbohydrates, which is not only associated with hypertension, cardiac hypertrophy and diabetes [41,52] but also with normal physiological conditions [42]. Numerous studies aiming at identifying sexual dimorphism in the cardiovascular system report differences in cardiac energetics, which were observed in diseased conditions or upon diet or exercise manipulation [16,43,53]. Those differences could be simply related to basal male/female differences and interpretation of data might prove difficult. For example, women were shown to have higher muscle content of proteins involved in FA-oxidation than men, while PRGC1 was not different between the groups [50]. Also it was found that estrogen supplementation in healthy men increased the content of FA-oxidizing enzymes in skeletal muscle as compared to control subjects, which might be directly related to enhanced PRGC1 m-RNA content [49]. In the myocardium, oxidation of glucose or fatty acids, mitochondrial oxidative capacity and the performance of the contractile apparatus are tightly regulated [54] and

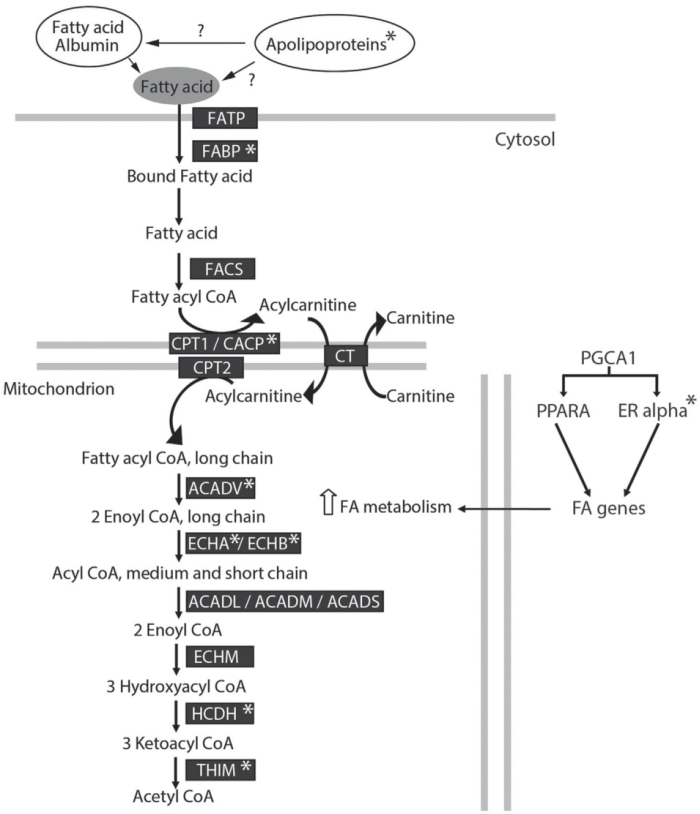

Fig. 10. Overview of FA metabolism. Transporters, enzymes and regulators of the FA metabolism are shown and those varying in this study are labeled with an asterisk. FATP: fatty acid transport protein, FABP: fatty acid binding protein, FACS: fatty acyl CoA synthase, CPT: Carnitine O-palmitoyltransferase, CACP: Carnitine O-acetyltransferase, CT: carnitine transporter, ACADV: Very long-chain specific acyl-CoA dehydrogenase, ACADL: long-chain specific acyl-CoA dehydrogenase, ACADM: medium-chain specific acyl-CoA dehydrogenase, ACADS: short-chain specific acyl-CoA dehydrogenase, ECHEM: Enoyl-CoA hydratase, HCDH: Hydroxyacyl-coenzyme A dehydrogenase.

even small impacts of diet, exercise, hormone removal or hormone substitution would probably cause considerable alterations in the system. However, despite contradictory results, the impact of gonadal hormones and hormone replacement on cardiac energy is still on focus of research and the therapeutic modulation of FA and glucose metabolism has received increasing attention in the last decade [39,55,56]. The efficacy of such modulation is mixed [57], pointing out that cardiac energetics is much more complex and more knowledge about sex differences in cardiac metabolism in health and under deprivation of gonadal hormones will enable a better understanding in disease. An overview of all protein changes found in our study, and which are related to FA metabolism are illustrated in Fig. 10.

Of particular importance in this study was to address the protein speciation issue, often ignored in protein studies, and our experience showed clearly that it cannot be expected that a protein is represented by a single species. A protein is rather represented by more than one species and each of these single protein species may behave differently. In general, we found it difficult to compare between 1D and 2D band/spot pattern. While on the 1D immuno-pattern a prominent 50 kDa and a very weak 40 kDa band were visualized for ECHB, several intense 40 kDa species, beside the 50 kDa species, were seen on the 2D blot. Orbitrap-MS as well identified those intense 40 kDa species from the 2D-IB on the 2-DE gel. In 2-DE gels, the protein is focused in two dimensions, whereas in the 1DE gel the bandwidth is fixed. As a consequence, the low molecular range protein species might have been masked by the presence of other proteins making the antibody-binding epitope inaccessible to the used antibody. Furthermore, challenging the 2D-immunoreactivity results with MS, we found that not each immunoreactive spot was identified as the protein of interest by MS. This can be due to the presence of more than one protein in one spot, with the protein of interest being of low abundance, which is in agreement with observations of Campostrini et al. [58]. They predicted that spots containing only one protein are the minority, rarely exceeding 30% of all spots. Hunsucker and Duncan [59] argued that because of the high dynamic range of protein amounts this should be a rare event. Thiede et al. [24] applying more sensitive mass spectrometry identified up to 22 different proteins in a single Hela 2-DE spot and only about 50% of the spots contained a protein with more than 90% of whole protein amount. Zhan and colleagues applied Orbitrap Velos MS to two different human cancer tissues and found species co-localization with more than 43 different proteins per spot, emphasizing that a much larger number of proteins is accessible by 2-DE than estimated before [60]. It has to be expected that within one spot protein species of the same protein, which have no clear differences in pI and Mr. are migrating on the same position even in high-resolution 2-DE gels. Examples are one-fold phosphorylated protein species modified at different residues or protein species with an exchange of Ile and Leu. Consequently, quantifications by optical density measurements always have to be verified by other methods such as immunoblotting, isotope labeling, or absolute quantification. Another observation was that not each spot initially identified as one of the three proteins stated above could be visualized by the used antibody (e.g. spots 11, 12 and 13 were

not recognized as THIM species, though they were identified as THIM in earlier studies [28]). This might be directly related to PTMs, which can mask antibody-binding sites. In conclusion, MS and immunodectection each have its limitation but in combination, one can detect protein species otherwise missed.

For gel-based proteomics, the strategy to identify only spots with obvious intensity differences between two or more biological situations cannot be recommended, because the complete protein species composition is not unraveled and it is important to know if a rare or a major protein species of a certain protein is present with different amounts between two biological situations. This becomes more evident, if we are able to connect each protein species to a certain function. As long as this is not the case, each protein species can represent the function for which the protein is named, independently of the fact that a spot is a faint or a major one. Here in the comparison of castrated with non-castrated mice we assumed any protein species of a given protein, which is altered in amount, to represent the function of the protein predicted by its name. Surely, this might prove not to be the case for all regulated protein species. Only a complete correlation of each protein species to its biological function will clarify the situation and this proves one of the major challenges of proteomics based on the protein species issue. Profiting from the full resolution power of 2-DE by a complete identification of all spots is a first step to understand the protein species composition. To correlate a spot intensity difference to a protein function, as in this case, is surely a better compromise than mixing up all the protein species as it is usual in bottom-up approaches. The complete acquisition of protein sequence and direct correlation to its function is possible in principal [61], but is difficult in most cases. In the present study, though actual MS technology was used, a complete primary structure characterization was not achieved for all species, which makes it difficult to associate single protein species to a protein function. However, we detected several modifications for one ECHA and one ECHB species. As the other species were seen at different positions on the 2-DE pattern, we assume that they carry modifications as well, which we did not succeed to detect with the protocol we applied.

5. Conclusion

Our results show that the myocardial proteome of castrated male mice still differ considerably from castrated female mice, nearly to the same extent as non-castrated mice do, but to a much higher extent than sexually immature mice. Herein, 2/3 of regulated proteins followed a direct regulation by gonadal hormones, while 1/3 did not. The most prominent differences between male and female mice, regardless of gonadectomy, were found for metabolic proteins, especially for proteins related to FA metabolism and mitochondrial function. The per se differential cardiac energetics in male mice might contribute to the worse outcome in cardiovascular disease models.

Technically, we found that optical quantification might be biased by the presence of more than one protein within a single spot and the high dynamic range of protein species amount in biological samples surely exceeds the resolution power of even large-scale 2-DE. A consequence is that optical quantification of stained spots is not always reliable, which however depends on relative abundance of co-migrating species. This problem could be avoided by quantification at the MS level, where the different protein species are separated by quantification between isotopically labeled peptides or by reducing species overlap by application of narrow-range pH gradient electrophoresis. Verification by further methods such as immunoblotting is necessary. Both, 2-DE-MS and 2-DE-immunoblotting are able to separate and identify protein species as long as the Mr. and the pI are different enough. The advantage of 2-DE immunoblotting is the higher sensitivity of spot detection and the limitation is a potential non-detection, if the protein speciation results in a modification of the epitope, too severe to be still recognized by the antibody. We thus propose for proteomic investigations complementation of 2-DE-MS by 2-DE immunoblotting, to identify/quantify all spots of a 2-DE pattern to obtain information about protein speciation and its potential importance for function and pathology, and to apply MS quantification, for example by isotopic labeling to learn about quantitative changes of all protein species for each protein. Protein speciation is still a perceived issue and therefore, for quantification, preferably all spots of a 2-DE pattern have to be identified and quantified.

Supplementary data to this article can be found online at https://doi.org/10.1016/j.jprot.2017.12.005.

Conflict of interest

The authors have declared no conflict of interest.

References

[1] M.E. Mendelsohn, R.H. Karas, Molecular and cellular basis of cardiovascular gender differences, Science 308 (2005) 1583–1587.
[2] A. Huang, G. Kaley, Gender-specific regulation of cardiovascular function: estrogen as key player, Microcirculation 11 (2004) 9–38.
[3] L. Baker, K.K. Meldrum, M. Wang, R. Sankula, R. Vanam, A. Raiesdana, B. Tsai, K. Hile, J.W. Brown, D.R. Meldrum, The role of estrogen in cardiovascular disease, J. Surg. Res. 115 (2003) 325–344.
[4] H.N. Hodis, Assessing benefits and risks of hormone therapy in 2008: new evidence, especially with regard to the heart, Cleve. Clin. J. Med. 75 (Suppl. 4) (2008) S3–12.
[5] L.A. Leinwand, Sex is a potent modifier of the cardiovascular system, J. Clin. Invest. 112 (2003) 302–307.
[6] R.D. Patten, Models of gender differences in cardiovascular disease, Drug Discov. Today Dis. Model. 4 (2007) 227–232.
[7] D.F. Dai, E.J. Hsieh, T. Chen, L.G. Menendez, N.B. Basisty, L. Tsai, R.P. Beyer, D.A. Crispin, N.J. Shulman, H.H. Szeto, R. Tian, M.J. MacCoss, P.S. Rabinovitch, Global proteomics and pathway analysis of pressure-overload-induced heart failure and its attenuation by mitochondrial-targeted peptides, Circ. Heart Fail. 6 (2013) 1067–1076.
[8] G. Karanigas, D. Fliegner, S. Forler, O. Klein, C. Schubert, J.A. Gustafsson, J. Klose, V. Regitz-Zagrosek, Comparative proteomic analysis reveals sex and estrogen receptor beta effects in the pressure overloaded heart, J. Proteome Res. 13 (2014) 5829–5836.
[9] M. Previlon, G.M. Le, P. Chafey, C. Federeci, M. Pezet, G. Clary, C. Broussard, G. Francois, J.J. Mercadier, P. Rouet-Benzineb, Comparative differential proteomic profiles of nonfailing and failing hearts after in vivo thoracic aortic constriction in mice overexpressing FKBP12.6, Phys. Rep. 1 (2013) e00039.
[10] N. Bousette, T. Kislinger, V. Fong, R. Isserlin, J.A. Hewel, A. Emil, A.O. Gramolini, Large-scale characterization and analysis of the murine cardiac proteome, J. Proteome Res. 8 (2009) 1887–1901.
[11] L. Lam, J. Arthur, C. Semsarian, Proteome map of the normal murine ventricular myocardium, Proteomics 7 (2007) 3629–3633.
[12] K. Raddatz, D. Albrecht, F. Hochgrafe, M. Hecker, M. Gotthardt, A proteome map of murine heart and skeletal muscle, Proteomics 8 (2008) 1885–1897.
[13] B. Chakravarti, M. Oseguera, N. Dalal, P. Fathy, B. Mallik, A. Raval, D.N. Chakravarti, Proteomic profiling of aging in the mouse heart: altered expression of mitochondrial proteins, Arch. Biochem. Biophys. 474 (2008) 22–31.
[14] K. Nishtala, T.Q. Phong, L. Steil, M. Sauter, M.G. Salazar, R. Kandolf, S.B. Felix, U. Volker, K. Klingel, E. Hammer, Proteomic analyses of age related changes in A.BY/SnJ mouse hearts, Proteome Sci. 11 (2013) 29.
[15] M. Diedrich, J. Tadic, L. Mao, M.A. Wacker, G. Nebrich, R. Hetzer, V. Regitz-Zagrosek, J. Klose, Heart protein expression related to age and sex in mice and humans, Int. J. Mol. Med. 20 (2007) 865–874.
[16] A. Foryst-Ludwig, M.C. Kreissl, C. Sprang, B. Thalke, C. Bohm, V. Benz, D. Gurgen, D. Dragun, C. Schubert, K. Mai, P. Stawowy, J. Spranger, V. Regitz-Zagrosek, T. Unger, U. Kintscher, Sex differences in physiological cardiac hypertrophy are associated with exercise-mediated changes in energy substrate availability, Am. J. Physiol. Heart Circ. Physiol. 301 (2011) H115–H122.
[17] J. Kim, A.R. Wende, S. Sena, H.A. Theobald, J. Soto, C. Sloan, B.E. Wayment, S.E. Litwin, M. Holzenberger, D. LeRoith, E.D. Abel, Insulin-like growth factor I receptor signaling is required for exercise-induced cardiac hypertrophy, Mol. Endocrinol. 22 (2008) 2531–2543.
[18] J.P. Konhilas, A.H. Maass, S.W. Luckey, B.L. Stauffer, E.N. Olson, L.A. Leinwand, Sex modifies exercise and cardiac adaptation in mice, Am. J. Physiol. Heart Circ. Physiol. 287 (2004) H2768–H2776.
[19] P. Jungblut, B. Thiede, U. Zimny-Arndt, E.C. Muller, C. Scheler, B. Wittmann-Liebold, A. Otto, Resolution power of two-dimensional electrophoresis and identification of proteins from gels, Electrophoresis 17 (1996) 839–847.
[20] P.R. Jungblut, H.G. Holzhutter, R. Apweiler, H. Schluter, The speciation of the proteome, Chem. Cent. J. 2 (2008) 16.
[21] H. Schluter, R. Apweiler, H.G. Holzhutter, P.R. Jungblut, Finding one's way in proteomics: a protein species nomenclature, Chem. Cent. J. 3 (2009) 11.
[22] B. Macek, M. Mann, J.V. Olsen, Global and site-specific quantitative phosphoproteomics: principles and applications, Annu. Rev. Pharmacol. Toxicol. 49 (2009) 199–221.
[23] P.R. Jungblut, F. Schiele, U. Zimny-Arndt, R. Ackermann, M. Schmid, S. Lange, R. Stein, K.P. Pleissner, Helicobacter pylori proteomics by 2-DE/MS, 1-DE-LC/MS

and functional data mining, Proteomics 10 (2010) 182–193.
[24] B. Thiede, C.J. Koehler, M. Strozynski, A. Treumann, R. Stein, U. Zimny-Arndt, M. Schmid, P.R. Jungblut, High resolution quantitative proteomics of HeLa cells protein species using stable isotope labeling with amino acids in cell culture (SILAC), two-dimensional gel electrophoresis (2DE) and nano-liquid chromatography coupled to an LTQ-OrbitrapMass spectrometer, Mol. Cell. Proteomics 12 (2013) 529–538.
[25] S. Lange, I. Rosenkrands, R. Stein, P. Andersen, S.H. Kaufmann, P.R. Jungblut, Analysis of protein species differentiation among mycobacterial low-Mr-secreted proteins by narrow pH range Immobiline gel 2-DE-MALDI-MS, J. Proteome 97 (2014) 235–244.
[26] E.D. Lekgabe, S.G. Royce, T.D. Hewitson, M.L. Tang, C. Zhao, X.L. Moore, G.W. Tregear, R.A. Bathgate, Du XJ, C.S. Samuel, The effects of relaxin and estrogen deficiency on collagen deposition and hypertrophy of nonreproductive organs, Endocrinology 147 (2006) 5575–5583.
[27] J. Song, C.K. Kost Jr., D.S. Martin, Androgens augment renal vascular responses to ANG II in New Zealand genetically hypertensive rats, Am. J. Phys. Regul. Integr. Comp. Phys. 290 (2006) R1608–R1615.
[28] K. Schwab, B. Neumann, N. Vignon-Zellweger, A. Fischer, R. Stein, P.R. Jungblut, C. Scheler, F. Theuring, Dietary phytoestrogen supplementation induces sex differences in the myocardial protein pattern of mice: a comparative proteomics study, Proteomics 11 (2011) 3887–3904.
[29] J. Heukeshoven, R. Dernick, Simplified method for silver staining of proteins in polyacrylamide gels and the mechanism of silver staining, Electrophoresis 6 (1985) 103–112.
[30] G. Nebrich, M. Herrmann, D. Sagi, J. Klose, P. Giavalisco, High MS-compatibility of silver nitrate-stained protein spots from 2-DE gels using ZipPlates and AnchorChips for successful protein identification, Electrophoresis 28 (2007) 1607–1614.
[31] H. Towbin, T. Staehelin, J. Gordon, Electrophoretic transfer of proteins from polyacrylamide gels to nitrocellulose sheets: procedure and some applications, Biotechnology 24 (1979) 145–149.
[32] H. Schagger, Tricine-SDS-PAGE, Nat. Protoc. 1 (2006) 16–22.
[33] P.R. Jungblut, R. Seifert, Analysis by high-resolution two-dimensional electrophoresis of differentiation-dependent alterations in cytosolic protein pattern of HL-60 leukemic cells, J. Biochem. Biophys. Methods 21 (1990) 47–58.
[34] K. Schwab, B. Neumann, C. Scheler, P.R. Jungblut, F. Theuring, Adaptation of proteomic techniques for the identification and characterization of protein species from murine heart, Amino Acids 41 (2011) 401–414.
[35] X. Zhao, S. Lu, J. Nie, X. Hu, W. Luo, X. Wu, H. Liu, Q. Feng, Z. Chang, Y. Liu, Y. Cao, H. Sun, X. Li, Y. Hu, Z. Yang, Phosphoinositide-dependent kinase 1 and mTORC2 synergistically maintain postnatal heart growth and heart function in mice, Mol. Cell. Biol. 34 (2014) 1966–1975.
[36] J.M. Huss, I.P. Torra, B. Staels, V. Giguere, D.P. Kelly, Estrogen-related receptor alpha directs peroxisome proliferator-activated receptor alpha signaling in the transcriptional control of energy metabolism in cardiac and skeletal muscle, Mol. Cell. Biol. 24 (2004) 9079–9091.
[37] M. Yoon, The role of PPAR alpha in lipid metabolism and obesity: focusing on the effects of estrogen on PPAR alpha actions, Pharmacol. Res. 60 (2009) 151–159.
[38] **Gonzalez-Teran B, Lopez JA, Rodriguez E, Leiva L, Martinez-Martinez S, Bernal JA, Jimenez-Borreguero LJ, Redondo JM, Vazquez J, Sabio G. p38gamma and delta promote heart hypertrophy by targeting the mTOR-inhibitory protein DEPTOR for degradation. Nat. Commun. 2016; 7: 10477.**
[39] W.C. Stanley, M.P. Chandler, Energy metabolism in the normal and failing heart: potential for therapeutic interventions, Heart Fail. Rev. 7 (2002) 115–130.
[40] I.F. Kodde, J. van der S, R.T. Smolenski, J.W. de Jong, Metabolic and genetic regulation of cardiac energy substrate preference, Comp. Biochem. Physiol. A Mol. Integr. Physiol. 146 (2007) 26–39.
[41] M.S. Dodd, D.R. Ball, M.A. Schroeder, L.M. Le Page, H.J. Atherton, L.C. Heather, A.M. Seymour, H. Ashrafian, H. Watkins, K. Clarke, D.J. Tyler, In vivo alterations in cardiac metabolism and function in the spontaneously hypertensive rat heart, Cardiovasc. Res. 95 (2012) 69–76.
[42] L.R. Peterson, P.F. Soto, P. Herrero, K.B. Schechtman, C. Dence, R.J. Gropler, Sex differences in myocardial oxygen and glucose metabolism, J. Nucl. Cardiol. 14 (2007) 573–581.
[43] L.R. Peterson, P.F. Soto, P. Herrero, B.S. Mohammed, M.S. Avidan, K.B. Schechtman, C. Dence, R.J. Gropler, Impact of gender on the myocardial metabolic response to obesity, JACC Cardiovasc. Imaging 1 (2008) 424–433.
[44] D.P. Koonen, J.F. Glatz, A. Bonen, J.J. Luiken, Long-chain fatty acid uptake and FAT/CD36 translocation in heart and skeletal muscle, Biochim. Biophys. Acta 1736 (2005) 163–180.
[45] J.J. Luiken, S.L. Coort, D.P. Koonen, D.J. van der Horst, A. Bonen, A. Zorzano, J.F. Glatz, Regulation of cardiac long-chain fatty acid and glucose uptake by translocation of substrate transporters, Pflugers Arch. 448 (2004) 1–15.
[46] J.C. Corton, H.M. Brown-Borg, Peroxisome proliferator-activated receptor gamma coactivator 1 in caloric restriction and other models of longevity, J. Gerontol. A Biol. Sci. Med. Sci. 60 (2005) 1494–1509.
[47] S.E. Campbell, M.A. Febbraio, Effect of ovarian hormones on mitochondrial enzyme activity in the fat oxidation pathway of skeletal muscle, Am. J. Physiol. Endocrinol. Metab. 281 (2001) E803–E808.
[48] H. Hatta, Y. Atomi, S. Shinohara, Y. Yamamoto, S. Yamada, The effects of ovarian hormones on glucose and fatty acid oxidation during exercise in female ovariectomized rats, Horm. Metab. Res. 20 (1988) 609–611.
[49] A.C. Maher, M. Akhtar, M.A. Tarnopolsky, Men supplemented with 17beta-estradiol have increased beta-oxidation capacity in skeletal muscle, Physiol. Genomics 42 (2010) 342–347.
[50] A.C. Maher, M. Akhtar, J. Vockley, M.A. Tarnopolsky, Women have higher protein content of beta-oxidation enzymes in skeletal muscle than men, PLoS One 5 (2010) e12025.
[51] M. Schupp, U. Kintscher, J. Fielitz, J. Thomas, R. Pregla, R. Hetzer, T. Unger, V. Regitz-Zagrosek, Cardiac PPARalpha expression in patients with dilated cardiomyopathy, Eur. J. Heart Fail. 8 (2006) 290–294.
[52] M. Desrois, R.J. Sidell, D. Gauguier, C.L. Davey, G.K. Radda, K. Clarke, Gender differences in hypertrophy, insulin resistance and ischemic injury in the aging type 2 diabetic rat heart, J. Mol. Cell. Cardiol. 37 (2004) 547–555.
[53] V. Garcia-Rua, M.F. Otero, P.V. Lear, D. Rodriguez-Penas, S. Feijoo-Bandin, T. Noguera-Moreno, M. Calaza, M. Varez-Barredo, A. Mosquera-Leal, J. Parrington, J. Brugada, M. Portoles, M. Rivera, J.R. Gonzalez-Juanatey, F. Lago, Increased expression of fatty-acid and calcium metabolism genes in failing human heart, PLoS One 7 (2012) e37505.
[54] A.V. Kuznetsov, M. Hermann, V. Saks, P. Hengster, R. Margreiter, The cell-type specificity of mitochondrial dynamics, Int. J. Biochem. Cell Biol. 41 (2009) 1928–1939.
[55] J.S. Jaswal, W. Keung, W. Wang, J.R. Ussher, G.D. Lopaschuk, Targeting fatty acid and carbohydrate oxidation—a novel therapeutic intervention in the ischemic and failing heart, Biochim. Biophys. Acta 2011 (1813) 1333–1350.
[56] A.A. Wolff, H.H. Rotmensch, W.C. Stanley, R. Ferrari, Metabolic approaches to the treatment of ischemic heart disease: the clinicians' perspective, Heart Fail. Rev. 7 (2002) 187–203.
[57] V. Lionetti, W.C. Stanley, F.A. Recchia, Modulating fatty acid oxidation in heart failure, Cardiovasc. Res. 90 (2011) 202–209.
[58] N. Campostrini, L.B. Areces, J. Rappsilber, M.C. Pietrogrande, F. Dondi, F. Pastorino, M. Ponzoni, P.G. Righetti, Spot overlapping in two-dimensional maps: a serious problem ignored for much too long, Proteomics 5 (2005) 2385–2395.
[59] S.W. Hunsucker, M.W. Duncan, Is protein overlap in two-dimensional gels a serious practical problem? Proteomics 6 (2006) 1374–1375.
[60] **X. Zhan, H. Yang, F. Peng, J. Li, Y. Mu, Y. Long, T. Cheng, Y. Huang, Z. Li, M. Lu, M. Li, J. Liu, P.R. Jungblut, How many proteins can be identified in a 2-DE gel spot within an analysis of a complex human cancer tissue proteome? Electrophoresis (2017),** http://dx.doi.org/10.1002/elps.201700330 **(ahead of print).**
[61] L.M. Okkels, E.C. Muller, M. Schmid, I. Rosenkrands, S.H. Kaufmann, P. Andersen, Jungblut PR. CFP10 discriminates between nonacetylated and acetylated ESAT-6 of *Mycobacterium tuberculosis* by differential interaction, Proteomics 4 (2004) 2954–2960.

Publikation 2: Differential compartmental processing and phosphorylation of pathogenic human tau and native mouse tau in the Line 66 model of frontotemporal dementia.

JBC ARTICLE

⌘ Author's Choice

Differential compartmental processing and phosphorylation of pathogenic human tau and native mouse tau in the line 66 model of frontotemporal dementia

Received for publication, June 17, 2020, and in revised form, October 9, 2020 Published, Papers in Press, October 30, 2020, DOI 10.1074/jbc.RA120.014890

Nora Lemke[1,2], Valeria Melis[3], Dilyara Lauer[1], Mandy Magbagbeolu[1], Boris Neumann[1,4], Charles R. Harrington[3,5], Gernot Riedel[3], Claude M. Wischik[3,5], Franz Theuring[1], and Karima Schwab[1,*]

From the [1]Charité-Universitätsmedizin Berlin, Berlin, Germany, the [2]Bundesanstalt für Materialforschung und-prüfung, Berlin, Germany, the [3]School of Medicine, Medical Sciences and Nutrition, University of Aberdeen, Foresterhill, Aberdeen, United Kingdom, the [4]Proteome Factory AG, Berlin, Germany, and [5]TauRx Therapeutics Ltd., Aberdeen, United Kingdom

Edited by Paul E. Fraser

Synapse loss is associated with motor and cognitive decline in multiple neurodegenerative disorders, and the cellular redistribution of tau is related to synaptic impairment in tauopathies, such as Alzheimer's disease and frontotemporal dementia. Here, we examined the cellular distribution of tau protein species in human tau overexpressing line 66 mice, a transgenic mouse model akin to genetic variants of frontotemporal dementia. Line 66 mice express intracellular tau aggregates in multiple brain regions and exhibit sensorimotor and motor learning deficiencies. Using a series of anti-tau antibodies, we observed, histologically, that nonphosphorylated transgenic human tau is enriched in synapses, whereas phosphorylated tau accumulates predominantly in cell bodies and axons. Subcellular fractionation confirmed that human tau is highly enriched in insoluble cytosolic and synaptosomal fractions, whereas endogenous mouse tau is virtually absent from synapses. Cytosolic tau was resistant to solubilization with urea and Triton X-100, indicating the formation of larger tau aggregates. By contrast, synaptic tau was partially soluble after Triton X-100 treatment and most likely represents aggregates of smaller size. MS corroborated that synaptosomal tau is nonphosphorylated. Tau enriched in the synapse of line 66 mice, therefore, appears to be in an oligomeric and nonphosphorylated state, and one that could have a direct impact on cognitive function.

Tau proteins belong to the microtubule-associated protein (MAP) family. They play an important role in the assembly of tubulin monomers into microtubules, which constitute the neuronal microtubule network (1). In the 1970s, the microtubule-associated protein tau was identified as a polymerization factor for microtubules, which promotes microtubule assembly and provides axonal stabilization (2). Fragmented tau proteins constitute the major components of intra-neuronal lesions, paired helical filaments (PHFs) characteristic of Alzheimer's disease (AD) brain (3) and other tau-related neurodegenerative disorders referred to as "tauopathies" (4). The human tau gene (*MAPT*) is encoded on chromosome 17 and alternative splicing of exons 2, 3, and 10 of the primary transcript leads to expression of 6 tau isoforms in the central nervous system (CNS) (5). N-terminal projection domains of tau isoforms contain 0, 1, or 2 inserts, and these determine the spacing between microtubules and the diameter of axons (6, 7). The C-terminal microtubule-binding domains contain either 3 or 4 tandem-repeat domains (R1–R4) that serve as regions that interact with microtubules (8, 9). In addition to their role in promoting microtubule stability and organization, tau may also be involved in the regulation of axonal guided transport through interactions with motor proteins and other binding partners (for review see Ref. 10).

In the longest human CNS tau isoform of 441 amino acid residues, more than 85 putative phosphorylation sites have been reported, most of which are located near the microtubule-binding repeat domains (11, 12). Phosphorylation of tau modulates its affinity to microtubules and multiple kinases and phosphatases regulate tau phosphorylation (10, 13–15). Hyperphosphorylation inhibits tau–tubulin binding (16, 17) and has been proposed as being important for tauopathies (18, 19). Other factors, such as glycosylation, caspases, and chaperones may also affect both microtubule assembly and tau aggregation (19, 20). Nevertheless, the relevance of tau phosphorylation in disease progression is uncertain. Phosphorylation of tau inhibits tau–tau binding and is preceded by aggregation of nonphosphorylated tau (16, 17) and the aggregation of nonphosphorylated tau is correlated with the onset of cognitive impairment in mice (21).

Irrespective of its phosphorylation state, high affinity binding through the repeat domain (16) and aggregation of truncated tau to form PHFs (22) can be shown to occur *in vitro* in the absence of phosphorylation. Tau aggregation appears to compromise presynaptic release mechanisms, but has little effect on baseline functions of the post-synaptic and hippocampal pyramidal cells (23) and squid axon (24). These data suggest that tau, in addition to its pathogenic role in axons (25, 26), accumulates in dendrites and synapses (27, 28), where it can promote actin polymerization to cross-link with synaptic vesicles, thus restricting their mobilization and lowering neurotransmitter release (29). These data strengthen the view that different tau protein pools may be compartmentalized into various cell spaces, which may be functionally distinct. Both pre- and post-synaptic tau colocalizes with compartment-specific

This article contains supporting information.

* For correspondence: Karima Schwab, karima.schwab@charite.de.

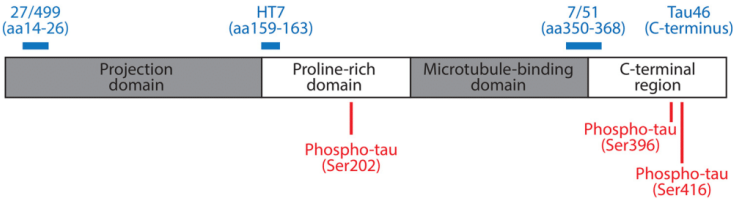

Figure 1. Schematic representation of epitopes of anti-tau antibodies. The epitopes recognized by the different anti-tau antibodies used in this work are indicated with numbering based on the longest human CNS tau isoform (2N4R; 441 amino acids). Detailed description of antibodies, including IgG class and supplier are listed in Table 1.

Table 1

Description of antibodies used in this study, including dilutions used for immunohistochemistry (IHC), immunofluorescence (IF), and immunoblotting (IB)

Antibody[a]	Species/class	Immunogen	Epitope	Supplier (Reference)	Product	Dilution		
						IHC	IF	IB
mAb 7/51	Mouse IgG1κ	PHF-tau	Tau 350-368	TauRx Therapeutics (88)	7/51	1:2,000	NA[b]	1:100
mAb Tau46	Mouse IgG1κ	Bovine tau	Tau carboxyl terminus	Cell Signaling Technology (89)	#4019	1:2,000	NA	1:2,000
mAb 27/499	Mouse IgG2bκ	2N4R tau	Tau 14-26	TauRx Therapeutics (79)	27/499	1:200	NA	NA
mAb HT7	Mouse IgG1κ	Purified human tau	Tau 159-163	Thermo Scientific (90)	MN1000	1:5,000	1:5,000	1:2,000
pAb pSer-202-tau	Rabbit IgG	Synthetic peptide corresponding to residues surrounding Ser-202 of human tau protein	Tau pSer-202	Cell Signaling (91)	#11834	1:500	1:500.	NA
mAb pSer-396-tau	Mouse IgG2b	Purified human tau	Tau pSer-396	Cell Signaling (92)	#9632	1:2,000	1:2,000	NA
mAb pSer-416-tau	Rabbit IgG	Synthetic phosphopeptide corresponding to residues surrounding Ser-416 of human Tau protein	Tau pSer-416	Cell Signaling (93)	#15013	1:500	1:500	NA
pAb β-actin (C-11)	Goat IgG	β-actin	Actin carboxyl-terminus	Santa Cruz Biotechnology	sc-1615	NA	NA	1:1,000
mAb synapsin-1	Mouse IgG1κ	Synapsin-1a and 1b	Synapsin 1 proline-rich D domain	Synaptic Systems (94)	106001	NA	1:2,000	1:10,000
mAb synapsin-2	Rabbit IgG	hSynapsin-2	Synapsin-2 Gly-503	Cell Signaling	#85852	NA	1:2,000	NA
mAb SNAP25	Mouse IgG1	Crude synaptic preparation from the human post-mortem brain	NA	Biolegend (95)	#MMS-614P	NA	NA	1:1,000
mAb syntaxin	Mouse IgG1	Crude synaptic preparation from the human post-mortem brain	Syntaxin 4-190	Abcam	ab112198	NA	NA	1:20,000
mAb PSD95	Rabbit IgG	hPSD95	PSD95 Gln-53	Cell Signaling (96)	#3450	NA	NA	1:500

[a] mAb, monoclonal antibody; pAb, polyclonal antibody.
[b] NA, not applicable for this study.

biomarkers in human AD brain (30–33) indicating that better characterization of the different tau species in these compartments would enable a better understanding of the missorting mechanisms that operate (34, 35). This was examined in our line 66 (L66) mouse as a prototype tauopathy model mimicking frontotemporal dementia (FTD) with parkinsonism overexpressing full-length human tau including mutations P301S and G335D (21).

The focus in this study was on functionally distinct cell compartments, *e.g.* the cytosol and the synapse. In mice, axonal localization of normal tau was confirmed (36, 37), but mislocalization of tau might mediate its pathological propensity (38) with different effects on cell function. Because synapse loss is a good correlate for cognitive capacity in AD (39), we explored how tau localization is affected in these transgenic mice. We report that mutant human tau forms aggregates that do not incorporate endogenous mouse tau and that nonphosphorylated, insoluble human tau protein is enriched in synapses, whereas tau species found in axons and soma are phosphorylated.

Results

We here characterized the cellular compartmentalization of tau protein species in L66 transgenic mice that express full-length mutant human (htau40 with P301S and G335D mutations) under the control of the *Thy1*-regulatory element with an early onset and widely distributed tau pathology. We applied a range of tau antibodies (Fig. 1 and Table 1) to explore (*a*) whether different aggregation products of the transgenic human tau are compartmentalized, and (*b*) whether the phosphorylation state differs between compartments within the same neurons (*i.e.* soma, cytosol, synapse). Initial immunohistochemical findings were then explored and corroborated through subcellular biochemical fractionation.

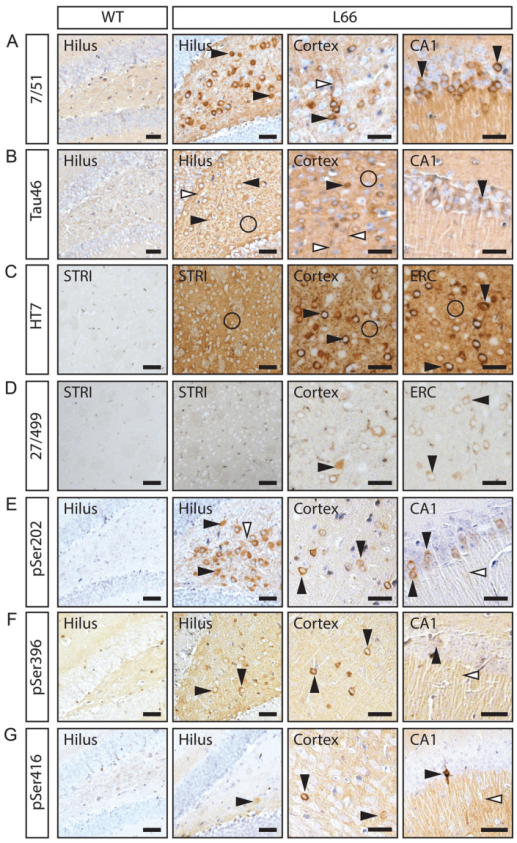

Figure 2. Tau immunohistochemistry in L66 and WT control mice. Tau immunoreactivity with phosphorylation-independent antibodies 7/51 (*A*), Tau46 (*B*), HT7 (*C*), and 27/499 (*D*), and with phosphorylation-specific antibodies pSer-202 (*E*), pSer-396 (*F*), and pSer-416 (*G*) show prominent intraneuronal staining in cortex and hippocampus in L66 brains. Phosphorylation-independent antibodies showed strong synaptic staining mainly in striatum in L66 (*A–D*). Phosphorylation-specific antibodies showed strong staining in cell bodies and axons in L66 (*E–G*). *Black arrowhead,* cytosolic staining in neurons; *white arrowhead,* axonal/dendritic staining; *circle,* synaptic staining. *CA1*, hippocampus subfield CA1; *STRI,* striatum. *Scale bars*, 100 μm. *L66,* line 66 tau transgenic mice.

Histopathological confirmation of hTau in all neuronal compartments

We first established histologically that transgenic human tau accumulates in cell bodies, dendrites, and synapses in L66 mice (Fig. 2 and Fig. S1). Immunopositive labeling was confirmed for all antibodies in cortex, striatum, and hippocampus of L66, whereas sections from WT controls were devoid of tau immunoreactivity with the panel of antibodies we have used spanning a number of domains across the tau molecule (Fig. 1). Labeling with phosphorylation-independent tau antibodies 7/51 (Fig. 2*A*), Tau46 (Fig. 2*B*), and HT7 (Fig. 2*C*) was observed in the somata of pyramidal cells in CA1, hilus of the dentate gyrus, ERC (entorhinal cortex) and cortex (see *black arrowheads*, Fig. 2), but also in cortical and hippocampal dendrites (Fig. 2, *white arrowheads*) and in nerve terminals in cortex and striatum (Fig. 2*C*, *circles*). Human-specific N-terminal tau mAb 27/499 (Fig. 2*D*) showed a similar pattern of labeling. The pattern of labeling seen with phosphorylation-dependent antibodies was distinct. Immunoreactivity for pSer-202 (Fig. 2*E*), pSer-396 (Fig. 2*F*), and pSer-416 (Fig. 2*G*) were seen mainly in cell bodies and axons of principal cells in cortex, the hilus, and CA1, but not in nerve terminals.

Tau accumulation in synapses was verified by double labeling of sections with HT7 (mouse) and the synaptic protein synapsin-2 (rabbit). Because synapsin-1 (used for biochemical assays, see below) and synapsin-2 are distributed similarly within the pre-synapse (40), synpasin-2 was used for double labeling as it was the only synapsin antibody available not raised in mouse. Tau recognized by HT7 was found to be co-localized with synapsin-2, confirming its synaptic localization (Fig. 3). Synaptic tau was seen mainly in striatum, cortex, and stratum radiatum of CA1, but was absent in other hippocampal regions. Phospho-tau was virtually absent from synapses (Fig. S2). These data confirm that transgenic mutant human tau is present in all compartments of the neuron with some region-specific variation in labeling in synaptic endings.

Subcellular fractionation confirms hTau in all compartments of L66 neurons

To characterize better the compartmental localization of human tau in L66 mice, we next applied ultracentrifugation and subcellular fractionation of brain extracts. The procedure for generating the fractions is depicted in Fig. 4. Importantly, P1 and P3 are pellets derived from the soma of cells, whereas P2 is a crude synaptosomal fraction. Further centrifugations of P2 produced LP1 (a mix of pre- and post-synaptic compartments) and LP2 as the enriched synaptic fraction. The cytosol is represented by fractions S1–S3. The LS1 fraction was used as a reference for quantitative comparisons as it had the lowest levels of the proteins of interest (relative protein level (RPL) equals 1).

Synaptic enrichment in fractions LP1 and LP2 was confirmed by enrichment of synapsin-1 and PSD95 proteins (Fig. 5, *A–D*). As expected, synapsin-1 was highly enriched in all pellet fractions (Fig. 5, *A* and *B*; for quantification see Figs. 6*A* and 7*A*) in both WT controls and L66 tissue. Consistent with a previous report (41), the most highly purified synaptic vesicle fraction LP2 and the pre- and postsynaptic membrane fraction LP1 had 40- to 60-fold enrichment of synapsin-1 compared with LS1. PSD95 was found mainly in pellets P1, P2, and in the pre- and postsynaptic membrane fraction LP1 (Fig. 5, *C* and *D*, and Figs. 6*B* and 7*B* for quantification) as reported by others (34, 42).

Murine tau was quantified using mAb Tau46 (Fig. 5, *E* and *F*, *white arrowheads*). Although this antibody labels tau in both WT and L66 brain preparations, murine tau has a gel mobility of 50-55 kDa. There was a 10- to 15-fold enrichment of murine tau in the crude pellet fractions P1 and P3 (quantification in Figs. 6*C* and 7*C*). There was relatively little enrichment of the 50-55–kDa murine tau in LP1 (3.5-fold) and LP2 (2-fold).

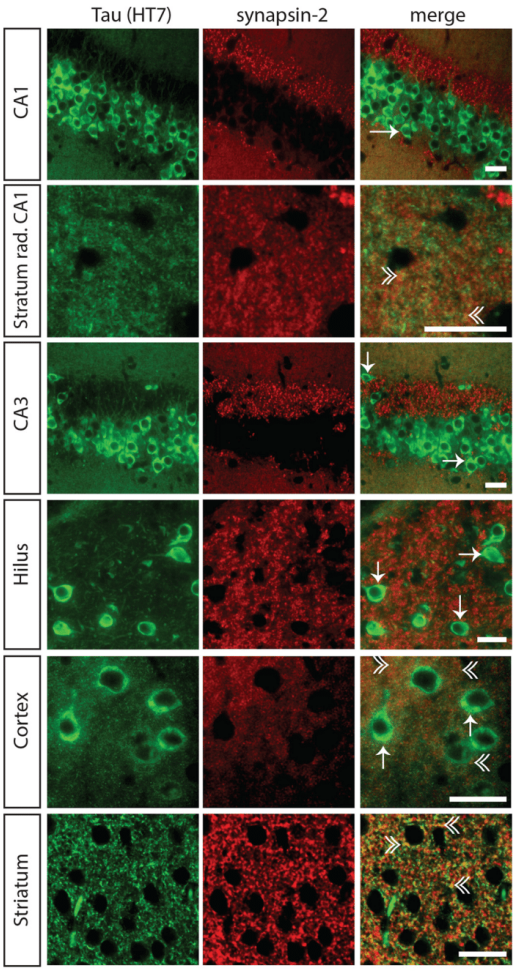

Figure 3. Synaptic localization of tau in L66 using immunofluorescence. Tau immunoreactivity with the phosphorylation-independent antibody HT7 is localized in the neuronal soma (*arrows*), dendrites, and axons of neurons in hippocampal CA1 and CA3, cortex and hilus of the dentate gyrus. Co-localization of HT7-reactive tau and the synaptic marker synapsin-2, seen as yellow puncta in the merged images (*double arrowhead*), confirms the synaptic accumulation of transgenic tau. Synaptic staining of tau is evident mainly in striatum and, to a lesser extent, in cortex and stratum radiatum of the CA1. *Green,* tau; *red,* synapsin-2. *Arrow,* staining in the neuronal soma; *double arrowhead*, synaptic staining. *Scale bars*, 25 μm.

Transgenic mutant tau has a distinct gel mobility of 62 kDa, which could be detected using phosphorylation-independent antibodies 7/51, HT7, and Tau46 (Fig. 5, *E–J, black arrowheads*) and this was seen only in brain tissues from L66 mice and not in WT samples. Transgenic 62-kDa tau was detected in all pellet fractions with antibodies 7/51 (Fig. 7*D*, 10- to 15-fold), as well as with HT7 and Tau46 (Fig. 7, *E* and *F,* 3- to 6-fold). Of particular interest, the co-purification of the 62-kDa human tau with synaptic proteins in the synaptic LP1 and LP2 fractions corroborates the co-localization established by immunohistochemistry (Fig. 3).

Synaptic hTau in L66 is nonphosphorylated

We further explored the phosphorylation status of human and murine tau using MS. This approach was necessary given the large number of phosphorylation sites of tau that have been reported and the limited amounts of tau protein available from LP1 and LP2. Application of MS has the further advantage that it can detect the presence of multiple phosphorylation sites in a single sample run. The 62-kDa tau bands specific to L66 found in the various subcellular extracts (Fig. 5*J*) were excised from silver-stained gels and subjected to Orbitrap LC–MS. Bands were taken in duplicates and digested with either trypsin or thermolysin to increase sequence coverage.

Transgenic mutant human tau was found in all nine fractions (Table 2 and Table S1 and Figs. S3–S7 for detailed MS data) corroborating the results from immunoblotting (Fig. 5). With the PEAKS software, we established phosphorylation of transgenic tau at Thr-181, Ser-199, Ser-202, and Thr-231 (Table 2 and details in Table S2 and Figs. S3–S7) in fractions S1, S2, S3, and LP1. Of particular interest, no phosphorylated residues were identified in fractions LS1, LS2, and LP2. Because these represent the subfractions derived from the crude P2 synaptosomal preparation, this implies that the transgenic human tau found in synapses was not phosphorylated in any of the peptide fragments that were analyzed.

Urea resistance of large hTau aggregates

Given that transgenic mutant human tau differs from native murine tau in terms of compartment distribution and phosphorylation status, we sought to understand better the differences in solubility in 7 M urea, which disrupts membrane interactions and hydrogen bonding (Fig. 8). Tau with 62-kDa gel mobility detected with mAb 7/51 was found in approximately equivalent amounts in the urea supernatant and pellet fractions after low-speed centrifugation (16,000 $\times$ *g* for 45 min). The levels in L66 mice were 4-fold higher in both fractions relative to the 55-kDa murine tau released into the urea supernatant (Fig. 8*A, black* and *white arrowheads,* respectively, and Fig. 8*B* for quantification). By contrast, murine tau was found at a lower level in the urea supernatant from WT mice compared with L66 mice and was largely absent from urea pellet in WT mice (Fig. 8*B*, 1 to 2-fold).

Mutant hTau is partially insoluble in Triton X-100

We used differential centrifugation in the presence or absence of Triton X-100 to compare the distribution of mutant human tau and native murine tau using mAb 7/51 in immunoblots (Fig. 9). As noted above, the 62-kDa tau species was absent in specimens from WT mouse brain, whereas murine tau species with gel mobility in the 50–55 kDa range were present in both L66 and WT specimens. The amounts of 55-kDa tau in the low-speed pellet and supernatant fractions were comparable. Following high-speed centrifugation of the low-speed supernatant, the amounts of 55-kDa tau were again comparable in the high-speed supernatant (FS) and pellet (FP) fractions

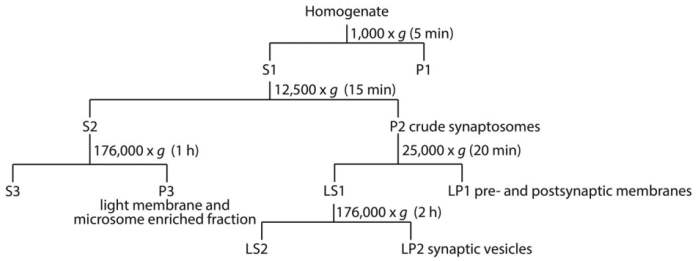

Figure 4. Extraction protocol for subcellular fractionation. Brain tissue homogenate was centrifuged at speeds as indicated in the diagram to allow separation of synaptic from cellular fractions.

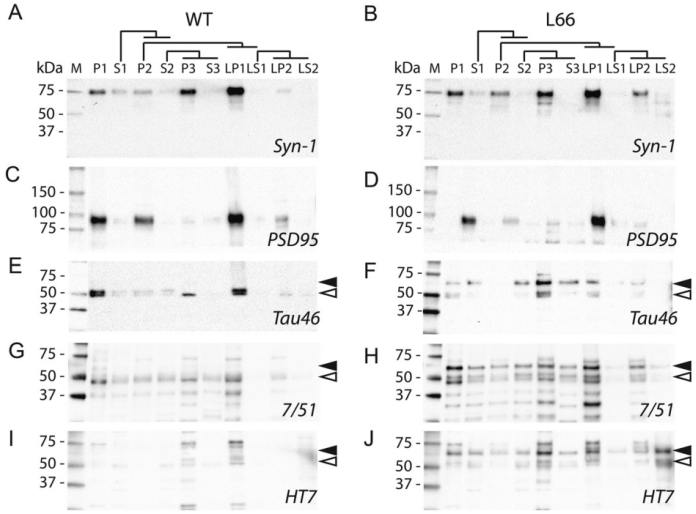

Figure 5. Cellular distribution of tau using subcellular fractionation. Brain tissue from WT controls (*left panel*) and L66 (*right panel*) were subjected to subcellular fractionation as described under "Experimental procedures." Sample fractions (1 μg of total protein) were separated on 4–20% gradient glycine-SDS-PAGE and representative immunoblots are shown. Antibodies against synapsin-1 and PSD95 (*A–D*) were used to confirm synaptic enrichment. Antibodies against tau (*E* and *F* for Tau46, *G* and *H* for 7/51, and *I* and *J* for HT7) were used to quantify tau in the different fractions. Transgenic tau, reactive with 7/51 and HT7 was evident in most fractions of L66 mice, visible as a 62-kDa band (*black arrowheads*), whereas no specific signal for WT mice was seen using either antibody. A tau band at around 50-55 kDa (*white arrowheads*), reactive with the antibody Tau46, showed a similar enrichment pattern for endogenous tau, both in WT controls (*E*) and L66 (*F*). *Black arrowheads,* 62-kDa band, specific to L66 tau-transgenic mice. *White arrowheads,* 50-55-kDa band, murine tau. *L66,* line 66 tau transgenic mice. All 10 bands corresponding to transgenic tau from different fractions were excised from silver-stained glycine gels for downstream MS analyses and results are shown in Table 2 and Tables S1 and S2.

prepared from L66 and WT mice, with the levels in the pellet approximately double those in the supernatant (Fig. 9*F*). When the same procedure was carried out in the presence of Triton X-100 the amounts in the pellet from L66 and WT mice were both substantially reduced in the high-speed pellet (Fig. 9*G*).

Compared with the level of 55-kDa tau in the low-speed pellet, there was 2-fold enrichment of 62-kDa tau in the same pellet and 1.3-fold enrichment in the corresponding supernatant from L66 mice (Fig. 9*D*). Following high-speed centrifugation of the supernatant, the majority of the 62-kDa tau was in the pellet (1.3-fold enrichment) with little remaining in the supernatant (0.4-fold RPL). This distribution was reversed when the same procedure was carried out in the presence of Triton X-100, with the majority now in the high-speed supernatant (1.2-fold), but with a 0.5-fold RPL remaining in the pellet (Fig. 9*E*). Therefore, approximately half of the 62-kDa tau from L66 mice is resistant to solubilization by Triton X-100. Because Triton X-100 would be expected to solubilize any membrane complexes, we interpret this as indicating that the 62-kDa tau sedimenting in these conditions is in the form of oligomeric complexes of molecular mass of at least 500 kDa. Similar findings were seen using HT7 (data not shown).

Soluble hTau is stable to heat denaturation

We further compared the heat stability of mutant human and native murine tau species isolated from the low-speed supernatant in brain extracts from L66 and WT mice. As seen in

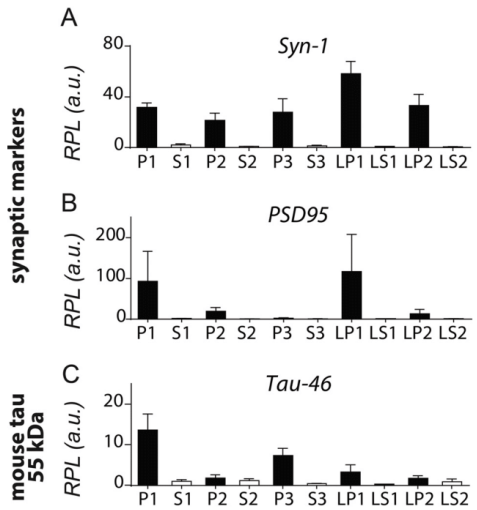

Figure 6. Quantification of synaptic markers and tau after subcellular fractionation in WT mice. Densitometric quantification of synapsin-1 (*A*), PSD95 (*B*), and Tau-46 reactive mouse tau at 50-55 kDa (*C*) was conducted with Image Laboratory using stain-free total protein loading for normalization. Data are expressed as mean ± S.E.

Fig. 10, there is substantial selective enrichment of the 62-kDa tau species in the supernatant following heat treatment for 5 or 30 min at 95°C. There is minimal corresponding enrichment of native murine tau. The results were similar for both phosphorylation-independent antibodies 7/51 and HT7 (Fig. 10*A*, *black arrowheads*). The enrichment of human tau was more than 10-fold compared with that present in the low-speed supernatant (Fig. 10, *B* and *C*). By contrast, β-actin, synapsin-1, PSD95, and syntaxin were completely absent from the heat-stable supernatant (HS) after only 5 min of heat treatment (Fig. 10*A*); the same was the case for synaptophysin and synapsin-2 (data not shown), whereas SNAP25 showed some resistance toward treatment with heat. Therefore, unlike transgenic tau, other membrane-interacting and synaptic proteins are not resistant to heat denaturation.

Discussion

L66 mice overexpress the longest human CNS tau isoform of 441 amino acid residues, which contains the aggregation-promoting mutations P301S and G335D. Expression of mutant human tau is widespread in the brain in this model producing prominent tau aggregates in neurons that can be labeled with Bielschowsky silver and primulin (21). We have now extended the studies in L66 with the aim of understanding better the differential compartmental localization of full-length native mouse and transgenic mutant human tau and how the phosphorylation status of mutant tau varies according to its compartmental localization within neurons. The key novel findings that we report are that although mutant human tau appears to have a wide distribution by immunohistochemistry, biochemical analysis reveals that its compartment distribution differs in a number of respects from that of native tau. Whereas native tau is largely soluble in urea and detergent, a substantial proportion of mutant tau in the brain is insoluble in both. Of particular interest, we report that mutant tau is co-localized with synaptic markers histologically and co-purifies with synaptic proteins in synaptosomal and synaptic vesicle preparations. Immunoblotting and sequence analysis of peptide digests of synaptic mutant tau reveal that it is largely unphosphorylated, whereas it is phosphorylated in cell body and axons (summarized in Table 3). Therefore, the differential neuronal processing of mutant human tau relative to native murine tau, particularly in synapses, may underlie its adverse effects on behavior.

Two basic features have made it possible to differentiate native mouse tau from mutant human tau in the brain. At the histological level, there is no labeling of native tau in WT mouse brain with any of the monoclonal antibodies we have used spanning N-terminal, repeat domain and C-terminal segments of the molecule under the conditions we have used. This is a well-recognized immunohistochemical feature of native tau using conventional tissue processing with formalin fixation (43). By contrast, transgenic mutant tau can be labeled by all the antibodies we have tested, including both phosphorylation-dependent and phosphorylation-independent monoclonal antibodies. Although the reasons for this difference are not yet fully understood at the molecular level, they indicate that the endogenous processing and consequent epitope exposure of mutant tau is fundamentally different from that of native tau. The biochemical characterization of these differences is made possible by the difference in gel mobility between native mouse and transgenic human tau in immunoblots. Most forms of tau protein are well-known to have atypical gel mobility relative to their molecular weight. This has been shown to be due to altered affinity for SDS, which has the effect of retarding their electrophoretic mobility in gels (5, 44). In particular, mouse tau has gel mobility corresponding approximately to 50-55 kDa, whereas mutant human tau has gel mobility corresponding to ~62 kDa. This makes it possible to distinguish the two forms of tau in immunoblots despite using monoclonal antibodies, which are not inherently discriminatory.

We first show that mutant human tau co-localizes immunohistochemically with synapsin-2. This was seen mainly in striatum, and to a lesser extent in cortex and stratum radiatum of CA1. We then used biochemical fractionation to determine whether mutant tau co-purifies with pre- and post-synaptic markers (synapsin-1 and PSD95, respectively). Synaptic proteins were found in crude fractions pelleting with sedimentation limits corresponding to a particle of size 95 nm (crude synaptosomal fraction P2 and the LP1 fraction containing pre- and post-synaptic membranes). These were further enriched in the preparations with particle sedimentation limits corresponding to 21 nm (microsomal fraction P3) and 15 nm (synaptic vesicle fraction LP2). Mutant tau protein recognized by the repeat-domain marker (mAb 7/51; residues 350-368) was found to be enriched in the smallest particle fractions P3 (21 nm) and LP2 (15 nm). The same was true to a somewhat lesser extent using more N-terminal (HT7; residues 159-163) and C-terminal (Tau46; residues 404-441) antibodies. Sequencing of peptides from the 62-kDa tau protein co-purifying with synapsin-1 in

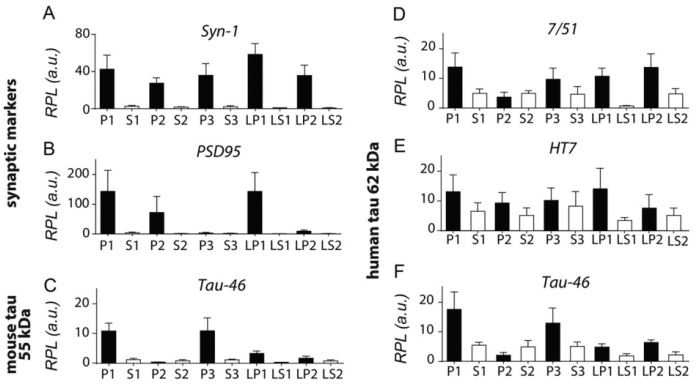

Figure 7. Quantification of synaptic markers and tau after subcellular fractionation in L66 mice. Densitometric quantification of synapsin-1 (*A*), PSD95 (*B*), Tau-46 reactive mouse tau at 50-55 kDa (*C*), as well as transgenic human tau at 62 kDa reactive with 7/51 (*D*), HT7 (*E*), and Tau-46 (*F*) was conducted with Image Laboratory using stain-free total protein loading for normalization. Data are expressed as mean ± S.E.

Table 2

Subcellular fractions (see Fig. 4 for fractions) probed by Orbitrap LC-MS and identified by Mascot and PEAKS search engines

Phosphorylated tau peptides were identified by PEAKS. Only the transgenic human tau isoform Tau-X is shown. For detailed MS results, see Tables S1 and S2.

Subcellular Fraction	Number of peptides matched (Mascot/PEAKS)	Number of phosphorylated peptides	Phosphorylation sites
S1	18/21	4	Thr-181, Ser-202, Thr-231
P2	4/5	None	-
S2	17/28	6	Thr-181, Ser-199, Ser-202, Thr-231
P3	14/14	None	-
S3	16/22	4	Thr-181, Thr-231
LP1	13/20	4	Thr-181, Ser-202, Thr-231
LS1	6/6	None	-
LP2	3/2	None	-
LS2	1/1	None	-

these fractions identified tau fragments spanning residues 195 to 369 by MS sequence analysis. Although small amounts of native mouse tau were also identified in these fractions, these were present at levels ~20% of the levels of mutant human tau. Therefore, we have established that soluble tau species from mutant human tau co-localize with synapses and co-purify with synaptic proteins in crude synaptosomal and enriched synaptic vesicle extracts in the L66 model of FTD.

When the phosphorylation status of transgenic human tau was examined further, we found that none of the phosphorylation-dependent monoclonal antibodies co-labeled with synapses. The labeling seen with these antibodies was restricted mainly to the cell bodies and axons of principal cells in cortex and hilus and CA1 of hippocampus. This was confirmed biochemically. Phosphorylated transgenic tau was found predominantly in low-speed supernatant fractions and remained in the supernatant following high-speed centrifugation. This was confirmed by MS sequence analysis, which identified peptides phosphorylated at Thr-181, Ser-199, Ser-202, and Thr-231 in these fractions. Of particular note, none of the peptides isolated from transgenic tau and co-purifying with synapsin-1 was found to be phosphorylated. The only exception to this was in the fraction containing crude synaptosomal constituents that sedimented with particles of size greater than 95 nm. We therefore conclude that the transgenic mutant human tau that accumulates in synapses is predominantly unphosphorylated. This protein sediments as a particle having a molecular mass of at least 200 kDa corresponding to trimeric or larger, low-order oligomers. By contrast, the aggregated tau protein found in cell bodies is largely filamentous and is found in the higher order tangle-like structures that can be labeled with Bielschowsky silver and primulin. Having this information, further immunoelectron microscopy studies may reveal more detail on the process of oligomer and filament assembly within the neuron and, particularly at the synapse.

Consistent with our findings, an association between mutant tau and synaptic vesicles has been reported previously in both *Drosophila* and rat neurons (23, 29). These vesicle-tau interactions hamper transmitter release through polymerization of N-terminal tau domains linking presynaptic F-actin with vesicle membranes, thereby making the presynaptic compartment more rigid (29). That the respective tau species destined for the presynaptic compartment can be oligomeric and nonphosphorylated was established by micropipette administration of tau through the patch pipette while recording from affected cells in the whole cell configuration (23). Voltage recordings revealed strongly reduced action potential amplitudes and slowed action potential rise and decay kinetics. Pre-synaptically, tau increased the run-down or unitary responses suggesting either reduced availability of vesicular release (29) or

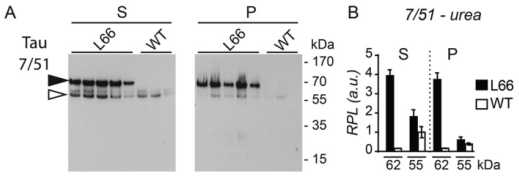

Figure 8. Urea solubility of tau species. Brain tissue from L66 and WT control mice (n = 5 and 3, respectively) was subjected to urea protein extraction and supernatant (*S*) and soluble pellet (*P*) fractions were obtained by low-speed centrifugation (16,000 × *g* for 45 min). Protein extracts (20 μg) were separated on 10% Tricine-SDS-PAGE and the immunoreactivity of the fractions was probed using mAb 7/51 as shown in immunoblots (*A*). Densitometric quantification of the blots revealed 7/51-reactive tau specific to L66 (62-kDa bands, *black arrowhead*) accumulated in P and S nearly to the same extent, emphasizing that some of the transgenic tau was resistant to urea solubilization (*B*). Murine tau detected at 55 kDa (*white arrowhead*) was almost completely depleted from the pellet P after addition of urea. Densitometric quantification was conducted with AlphaEase using the 55 kDa band in S from WT for normalization. Values are expressed as mean ± S.E.

lowered re-uptake of transmitter in synaptic vesicles due to inhibition of P-type Ca^{2+}-ATPases by tau (45, 46). At physiological pH and under challenge, these Ca^{2+} ATPases promote Ca^{2+}/H^{+} exchange activity at the vesicular membrane and Ca^{2+} uptake into the vesicle (47). Neighboring cells were not affected by this treatment. Furthermore, transfection of full-length tau into neurons was associated with decreased expression of synaptic markers and reduced transport of these proteins into the presynapse (48), as well as with Ca^{2+} dysregulation (49). An association between vesicles and actin promoted through the N-terminal domain of tau (29) could contribute both to the insolubility of tau and increased rigidity in the synaptosomal compartment. Accumulation of tau in the cytoplasm is thought to interfere with a range of normal physiological processes (for review see Ref. 50). The accumulation of tau aggregates in the cytosol in L66 mice was a feature also observed in JNPL3 mice (P301L mutation). As in our L66 model, the overexpressed mutant tau led to the formation of cytoplasmic tau aggregates, neuronal loss, and motor deficits (21, 51, 52), and is consistent with what is observed in tauopathies (for review see Ref. 53).

That soluble tau species can modulate the post-synaptic compartment was suggested through the administration of intracerebroventricular recombinant or AD tau aggregates (38, 54). These investigators reported deficits in hippocampal long-term potentiation, but no deficits in paired pulse inhibition ratios. This is in line with our labeling of tau protein in fraction LP1, which contained both presynaptic (synapsin) and post-synaptic elements (PSD95). As is confirmed here for L66, these tau species are in both phosphorylated and nonphosphorylated states and require the C-terminal domain of the tau molecule (55). Some of the phosphorylation sites identified in L66 mice were also seen in WT control mice and have also been described in postmortem brain tissue of cognitively normal people, suggesting the existence of selective phosphorylation states under physiological conditions (12, 56) and are likely not related to pathological processing of tau.

The cellular distribution of different tau pools might be attributed to specific localization-dependent post-transcriptional regulation events. For example, several kinases have been described that phosphorylate tau (13, 14, 57). In addition, it has been reported that both phosphatases and kinases are also compartmentalized, and that synaptic phosphorylation activates a number of proteins (for review see Refs. 58 and 59). Therefore, it seems likely that tau undergoes compartment-specific modification and aggregation processes. A brain region-specific increase in phospho-tau-positive synaptosomes in AD patients has been reported using crude cortical synaptosomal preparations (30), similar to our MS findings in the crude P2 and LP1 factions from L66 brain tissues. Others have also reported that synaptic tau extracted from AD brain tissues is oligomeric and hyperphosphorylated (30, 31) but this has not been confirmed. Sokolow and colleagues (33) labeled the majority of synaptic terminals with HT7 (not specific for phosphorylated tau) in both AD and control subjects and found an increase in a truncated 20-kDa tau fragment lacking a C terminus and appearing as dimers in immunoblots from AD samples.

Mutant human tau was equally enriched in both supernatant and pellet after addition of urea, whereas murine tau was almost completely depleted in the urea pellet (summarized in Table 4). The urea-resistant human tau species are less likely to be membrane bound, as urea disrupts these membrane associations and hydrogen bonding within tau protein aggregates (60). Mouse tau is not insoluble in urea and remains in the supernatant. This is consistent with the observation in JNPL3 mice expressing the P301L mutation (61). The sarkosyl-insoluble preparation of tau in this model was found to be largely human and only became filamentous in older animals. It appears that the progression of tau aggregation pathology is more advanced in our L66 mice to such an extent that the filamentous state was already established at 7 months of age (21). In addition, native mouse tau was largely absent from the high-speed Triton X-100 pellet, supporting its inability to assemble into aggregates. However, it is not possible to determine from the data currently available whether there is some degree of recruitment of mouse tau into the Triton- and urea-insoluble aggregates. The mutant tau protein in the low-speed Triton X-100 supernatant was found to remain heat stable even after lengthy exposure to heat. It was also found to be stable when purified using TCA (data not shown) (62). Heat stability is an inherent property of tau as an aggregation-prone and intrinsically unstructured protein without a hydrophobic core (63–65) and is widely used as a method for separation of tau from other abundant proteins (2, 63, 64). In contrast to tau, other synaptic proteins were not heat stable. Increasing concentrations of insoluble tau have been reported to lead to formation of filamentous tau aggregates in elderly transgenic P301L tau mice (66). Triton-insoluble filamentous tau species enriched from P301S mice have a greater seeding potential *in vitro* (67) and have higher toxicity (68). However, we have reported recently that the toxicity of filamentous tau can be dissociated from the ability of truncated oligomers to induce abnormal phosphorylation of endogenous tau (69). At present, the molecular mechanism of aggregation of full-length mutant human tau remains unknown.

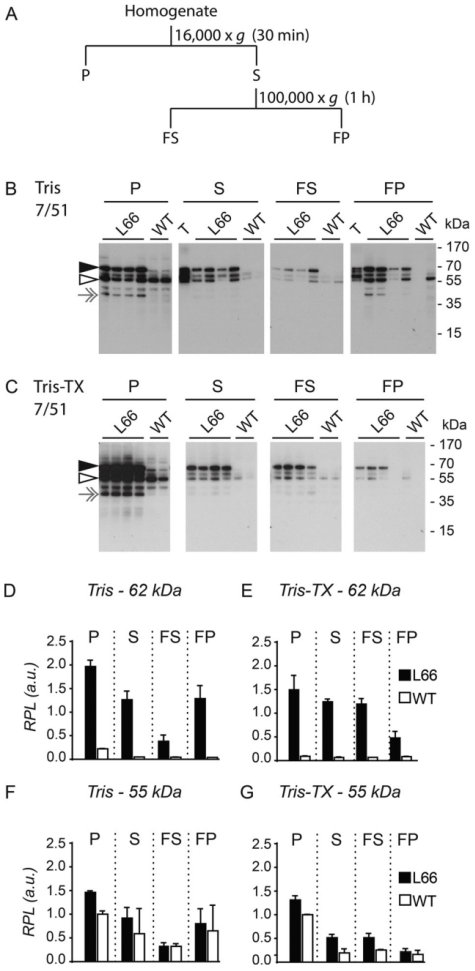

Figure 9. Tau protein solubility with and without Triton X-100. (*A*) Extraction scheme for low- and high-speed extraction of brain tissue from L66 tau transgenic and WT control mice; tissue was subjected to extraction with either Tris (*B*) or Tris-Triton X-100 (*C*). Pellet (*P*) and supernatant (*S*) fractions were obtained by low-speed centrifugation at 16,000 × *g* for 30 min, whereas the fast pellet (*FP*) and the fast supernatant (*FS*) fractions were obtained by high-speed centrifugation of S at 100,000 × *g* for 1 h. Samples (15 μg of protein) were separated by 10% tricine-SDS-PAGE and immunoblots are shown. The immunoreactivity of the fractions was probed using the phosphorylation-independent anti-tau antibody 7/51. Densitometric quantification of the blots revealed 7/51-reactive tau (62-kDa bands) accumulated in P, S, and FP fractions. After the addition of Triton X-100, some of 7/51-reactive tau in FP fraction was solubilized and found in the FS fraction. Densitometric quantification was conducted with AlphaEase using the 55-kDa band in P from WT for normalization. Values are expressed as mean ± S.E. *T*, tau ladder. *Black arrowheads*, 62-kDa human tau, and *white arrowheads*, 55-kDa mouse tau. *Gray arrows*, 37-kDa band, non-tau nonspecific labeling.

Although our data provide strong evidence that the mutant human tau that aggregates in the synaptic compartment is nonphosphorylated, this is at odds with some other reports. For example, Kimura and co-workers (66) suggest that phosphorylation is crucial for the development of synaptic tau toxicity and synapse loss in P301L mice. By contrast, Zhou *et al.* (29) reported data more in line with those reported here, confirming that synaptic function is compromised using both pathogenic human tau mutants and phosphomimetic tau species devoid of 14 putative phosphor-serine/threonine residues (changed to glutamate residues). These data are consistent with evidence showing that tau aggregation and toxicity can both occur in the absence of any phosphorylation (16, 22, 69). Phosphorylation of tau inhibits tau–tau binding (16, 17) and might play a protective role against its toxicity (17, 70–73). Consistent with this, aggregation of nonphosphorylated tau correlates with the onset and extent of cognitive impairment in mice (21) and humans (74, 75), whereas phospho-tau pathology appears to be a late stage event in the disease progression (74). It is not known at present what triggers pathological compartmentalization of tau and how specifically this affects synaptic membranes or vesicles.

Although we have gone some way toward defining the abnormal compartmentalization of transgenic human tau in a mouse model of FTD, there are important limitations in the work to date. The tau protein accumulating in the core of the tau filaments found in FTD brain tissues is restricted to the repeat region similar to that found in the core of the PHF in AD (3, 76, 77), albeit with a different fold (78). This core is proteolytically stable and propagates the aggregation cascade via a high affinity tau–tau binding interaction (16, 79). The present study has focused on the soluble transgenic mutant tau species that can be isolated from mouse brain. The tau protein that remains insoluble after urea and/or Triton X-100 treatment needs to be characterized further with a view to determining the identity of any proteolytically stable and insoluble tau species generated in this model. In L66 mice, the human tau is expressed in a form that readily forms insoluble aggregates that do not incorporate endogenous murine tau. Evidence for incorporation of endogenous tau into tau aggregates in mice expressing different isoforms of human tau is variable. Although no co-aggregation was seen in similar tau P301L mice (28, 61, 80), others have reported such co-aggregation, *e.g.* in TauΔK280 mice (81–84). Further models, such as those expressing 3R isoforms, may differ and remain to be tested.

In summary, we here present an attempt to determine the physicochemical changes of tau protein in different cellular compartments in the L66 mouse model for FTD. We show that transgenic mutant human tau form distinct insoluble aggregates that do not incorporate endogenous mouse tau. The 62-kDa human tau forms larger aggregates that are resistant to urea and Triton X-100. Other species, oligomers of smaller size that were sedimented at higher speed, were partially soluble after Triton X-100 treatment. The tau species that concentrate in synapses are in a nonphosphorylated form. Another pool of tau, which is in part Triton X-100–soluble, is heat stable, phosphorylated, and presumably cytosolic. Native mouse tau, on the other hand, does not accumulate in synaptic fractions and is neither urea/Triton X-100–resistant nor heat stable. The analyses presented here for an FTD model, when compared with physiologically appropriate AD models, will shed light on how

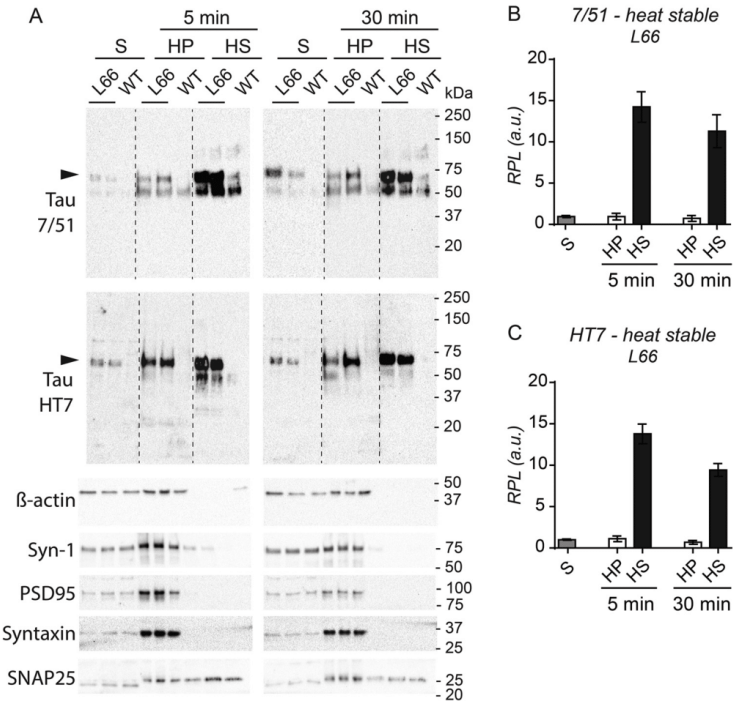

Figure 10. Heat stability of Tris-soluble tau. Tris-soluble fractions (see Fig. 9, S fractions) were heated at 95 °C for 5 or 30 min and 2 μg of total protein of original supernatant (S), the heat-stable supernatant (HS), and precipitated pellet fractions (HP) were subjected to 4–15% glycine SDS-PAGE and subsequent immunoblotting using the phosphorylation-independent anti-tau antibodies 7/51 and HT7 as shown in representative immunoblots (*A*). With both antibodies, heat-treated tau was mainly found in the supernatant fraction HS, and only a small subset of tau was found in the pellet HP. β-Actin and several synaptic proteins were solely found in HP after only 5 min heat treatment. *Dotted lines* indicate where fractions from one brain were excised due to sample smearing. The quantification in *panels B* and *C* represent data obtained from (*A*) and from further samples. Synapsin-1, PSD95, and syntaxin were not heat stable, whereas SNAP25 was partially stable toward heat treatment, as some of it remained soluble in the supernatant HS after 5 min of boiling. Densitometric quantification for 7/51 (*B*) and HT7 (*C*) conducted with Image Laboratory using stain-free total protein loading for normalization confirmed the findings for transgenic tau, emphasizing the thermal stability of tau. Values are expressed as mean ± S.E. *Black arrowheads*, 62-kDa human tau.

different tau conformations develop. This may help understand the distinct pathologies observed for different tauopathies and provide new therapeutic targets that may be either shared between tauopathies or unique to individual disorders.

Experimental procedures

Animals

Tau transgenic L66 and NMRI WT control mice were used in this study and have been described in detail previously (21). L66 mice overexpress the longest human tau isoform (2N4R) with 441 amino acid residues, under control of the mouse *Thy1*-promoter. Two aggregation-promoting mutations, P301S and G335D in the repeat domain, were inserted into the tau cDNA and this mutated isoform is hereafter termed Tau-X. Female homozygous transgenic L66 (n = 15) and WT litters (n = 12) were bred commercially (Charles River Laboratories, UK) in isolators and delivered by truck to Aberdeen at least 10 days before experimental work commenced. They were housed by genotype in small colonies up to 5 animals in open housing (Macrolon III) with corncob bedding and paper strips and cardboard tubes as enrichment (cleaning rota once per week). Holding rooms were on constant temperature (20-22° C), humidity (60–65%), and air exchange rate (17-20 changes/h) with 12 h light/dark cycle (lights on at 6 am, simulated dawn). Animals had free access to food and water and were aged 6-7 months when sacrificed by cervical dislocation. Brains were rapidly extracted and snap frozen in liquid nitrogen for protein studies or fixed for 24 h in formalin and embedded in paraffin for histopathology. There was no blinding or randomization at this stage of the experiment. All animal experiments were performed in accordance with the European Communities Council Directive (63/2010/EU) and a project license with local ethical approval under the UK Animals (Scientific Procedures) Act (1986). Brains were sent to Berlin via courier on dry ice.

Immunohistochemistry and immunofluorescence

Five-μm coronal sections were collected at desired brain areas (corresponding to sections Bregma −3.8 mm for

Table 3

Summary for subcellular distribution of tau and its phosphorylation status using mmunohistochemistry, immunofluorescence, subcellular fractionation and MS (see Figs. 2–6 and Table 2)

The following designations were used: S1-S3, LS1, LS2: supernatants; P1, nuclei and debris; P2, crude synaptosomes; P3, light membrane/microsomes; LP1, pre- and post-synaptic membranes, LP2, synaptic vesicles.

				Cellular compartment/fraction									
Method	Protein	Antibody	Genotype	Cell body					Puncta				
Immunohistochemistry	Tau	7/51	L66	+					2+				
			WT	−					+				
		HT7	L66	+					3+ (co-localization with synapsin-2)				
			WT	−					−				
		Tau46	L66	+					2+				
			WT	−					+				
		27/499	L66	+					−				
			WT	−					−				
		pSer-202	L66	+					+				
			WT	−					−				
		pSer-396	L66	+					+				
			WT	−					+				
		pSer-416	L66	+					+				
			WT	−					+				
				S1	P1	S2	S3	P3	P2	LS1	LP1	LS2	LP2
Subcellular fractionation	Synaptic markers	Syn1	L66	−	2+	−	−	2+	2+	−	2+	−	2+
			WT	−	2+	−	−	2+	2+	−	2+	−	2+
		PSD95	L66	−	2+	−	−	−	2+	−	2+	−	−
			WT	−	2+	−	−	−	2+	−	2+	−	−
	Human tau (62 kDa)	7/51	L66	2+	2+	2+	2+	2+	2+	+	2+	2+	2+
			WT	−	−	−	−	−	−	−	−	−	−
		HT7	L66	2+	2+	2+	2+	2+	2+	+	2+	2+	2+
			WT	−	−	−	−	−	−	−	−	−	−
		Tau46	L66	2+	2+	2+	2+	2+	+	+	2+	+	2+
			WT	−	−	−	−	−	−	−	−	−	−
	Mouse tau (55 kDa)	Tau46	L66	−	2+	−	−	2+	−	−	+	−	+
			WT	−	2+	−	−	2+	+	−	+	−	+
MS	Phosphorylated human tau	Silver gel (62 kDa)	L66	2+	−	2+	2+	−	−	−	2+	−	−

Table 4

Summary for urea/Triton X-100 solubility and heat stability of tau (see Figs. 7–9)

Experiment	Antibody	Tau Isoform	Genotype	P	S	FS[a]	FP	HP	HS
Urea	7/51	Human tau (62 kDa)	L66	2+	2+				
			WT	−	−				
		Mouse tau (55 kDa)	L66	+	2+				
			WT	+	2+				
Tris	7/51	Human tau (62 kDa)	L66	2+	2+	+	2+		
			WT	−	−	−	−		
		Mouse tau (55 kDa)	L66	2+	2+	+	2+		
			WT	2+	2+	+	2+		
Tris-Triton X-100	7/51	Human tau (62 kDa)	L66	2+	2+	2+	+		
			WT	−	−	−	−		
		Mouse tau (55 kDa)	L66	2+	+	+	+		
			WT	2+	+	+	+		
Heat stability	7/51	Human tau (62 kDa)	L66		+			+	3+
			WT		−			−	−
	HT7	Human tau (62 kDa)	L66		+			+	3+
			WT		−			−	−

[a] Empty cells, not applicable.

hippocampus and auditory/visual cortices and Bregma +0.74 mm for striatum and motor/entorhinal cortices of the mouse brain atlas (85)) from randomly chosen L66 (n = 5) and WT (n = 5) mice, de-waxed, boiled in 10 mM citrate buffer, and further processed for immunohistochemistry or immunofluorescence as described below.

For immunohistochemistry, sections were boiled in 10 mM citric buffer, incubated in hydrogen peroxidase solution (0.3% (v/v)) for 10 min, and then for 20 min in blocking buffer (0.1% (w/v) BSA in PBS). Sections were incubated in primary and secondary antibodies diluted in blocking buffer, each for 1 h at room temperature with 3× 10 min PBS-washing steps after each antibody. Sections were developed with diaminobenzidine solution (Dako, Denmark) and embedded in Neo-Mount® (Merck Millipore, Germany). Anti-tau antibodies directed against both phosphorylated and nonphosphorylated tau protein, and with epitopes in N- and C-terminal domains were used: mAb 7/51, Tau46, HT7, mAb 27/499, pSer-202, pSer-396, and pSer-416. The epitopes recognized by these antibodies are illustrated in Fig. 1 and their details listed in Table 1.

For immunofluorescence, sections were blocked for 1 h in blocking buffer (5% (v/v) normal goat serum in PBS containing 0.3% (v/v) Triton X-100) and incubated overnight at 4 °C in primary antibody mixture (HT7 and synapsin-2; pSer-202 and

synapsin-2, pSer-396 and synapsin-1 as well as pSer-416 and synapsin-2, see Table 1 for dilutions) diluted in blocking buffer. The next day, sections were washed 3× 10 min with PBS, incubated for 1.5 h in fluorochrome-conjugated secondary antibodies (Alexa Fluor® 488-conjugated donkey anti-mouse IgG and Alexa Fluor® 568-conjugated goat anti-rabbit IgG, Life Technologies, USA; both diluted 1:500 in blocking buffer), washed again 3× 10 min with PBS, covered with DAPI Gold Antifade Reagent (Cell Signaling Technology, MA, USA), and examined using a microscope equipped for fluorescence (Carl Zeiss, Jena, Germany).

Subcellular fractionation of brain tissues

Subcellular fractionation was conducted as described before (34) and the workflow is shown in Fig. 4. Randomly selected brains from L66 (n = 5) and WT (n = 4) mice were used. Briefly, 10 volumes of Tris buffer (25 mM, pH 7.4) containing 9% sucrose, 2 mM EDTA, 5 mM DTT and protease and phosphatase inhibitors were added to crushed frozen brain tissues (pulverized using a pestle and mortar with liquid nitrogen) and repeatedly pipetted up and down. The homogenate was centrifuged for 5 min at 4 °C and 1,000 × g to obtain a supernatant (S1) and pellet (P1, containing nuclei and large debris). S1 was centrifuged for 15 min at 4 °C and 12,500 × g to obtain a further supernatant (S2, see below) and a crude synaptosomal fraction pellet (P2). P2 was subsequently lysed in ice-cold water and the lysate adjusted to 25 mM Tris and incubated for 30 min at 4 °C. Thereafter, P2 was centrifuged at 25,000 × g for 20 min at 4 °C to pellet a pre- and postsynaptic membrane fraction (LP1). The supernatant fraction (LS1) was further centrifuged for 2 h at 4 °C and 176,000 × g to obtain a synaptic vesicle pellet fraction (LP2) and a supernatant fraction (LS2). The S2 fraction from above was centrifuged at 176,000 × g for 1 h at 4 °C to obtain a cytosolic fraction (S3) and a light membrane/microsome-enriched pellet fraction (P3). The pellets (P1, P3, LP1, and LP2) were each suspended in 1 volume of reducing Laemmli buffer (125 mM Tris-HCl, pH 7.0, 0.8% (w/v) SDS, 20% (v/v) glycerol, and 10% (v/v) 2-mercaptoethanol). Protein concentration was determined using the Bradford reagent (Carl Roth, Karlsruhe, Germany), according to the manufacturer's recommendations.

Protein extraction from brain tissue using urea

Crushed frozen brain tissue from L66 (n = 5) and WT (n = 3) mice was incubated for 45 min at room temperature in 6 volumes of urea extraction buffer (7 M urea, 2 M thiourea, 2% ampholyte 2-4, 70 mM DTT, 25 mM Tris/HCl, pH 8.0, 50 mM KCl, 3 mM EDTA, 2.9 mM benzamidine, and 2.1 μM leupeptin) and separated by centrifugation at 16,000 × g for 45 min at room temperature. The supernatant (S) was transferred to new tubes. The pellet was mixed with 1 volume of reducing Laemmli buffer, boiled for 5 min at 95 °C, and the soluble pellet (P) was retained for later analysis. Both S and P fractions were used for tau characterization. The protein concentration of all fractions was determined as stated above.

Protein extraction from brain tissue with and without detergent

Five volumes of Tris extraction buffer (30 mM Tris, pH 7.4, containing cOmplete™ protease inhibitor and PhosStop™ phosphatase inhibitor mixture tablets from Roche), with or without the addition of Triton X-100 (0.1% (v/v)), were added to crushed frozen tissue (5 L66 and 3 WT brains pulverized using pestle and mortar with liquid nitrogen), repeatedly pipetted up and down for homogenization and incubated for 30 min at 4 °C. The extraction procedure is shown in Fig. 9*A*. The homogenate was centrifuged for 30 min at 16,000 × g and 4 °C. The supernatant (S) was transferred to a new tube and the pellet (P) suspended in 1 volume of reducing Laemmli buffer. Some of the supernatant (S) was retained for analysis, whereas the remaining supernatant was centrifuged for 1 h at 100,000 × g and 4 °C. The resulting high-speed supernatant (FS) was transferred into a new tube and the high-speed pellet (FP) mixed with 1 volume of reducing Laemmli buffer.

Heat denaturation

For heat denaturation, low-speed supernatant (S) from the above-mentioned Tris extraction, was boiled for either 5 or 30 min at 95 °C and the reaction stopped by transfer to ice. The boiled mixture was subjected to centrifugation at 16,000 × g for 5 min to separate supernatant fraction (HS, which is heat-stable) from heat-pelleted fraction (HP) and the latter was suspended with 1 volume of reducing Laemmli buffer. The protein concentration of all fractions was determined using the Bradford method.

One-dimensional electrophoresis

Samples derived from urea extraction, detergent extraction, heat denaturation, and subcellular fractionation were subjected to Tricine or glycine one-dimensional electrophoresis. Loading details are given in the legends of Figs. 5–10. The Tricine gels (10%) were run using a discontinuous buffer. The cathode buffer consisted of 100 mM Tris, 100 mM Tricine, and 1% (w/v) SDS and the anode buffer contained 100 mM Tris and 0.07% (v/v) HCl. The glycine gels (10% gels or commercial gradient gels from 4–15 or 4–20%, Bio-Rad Laboratories, USA) were run in Tris glycine buffer containing 192 mM glycine, 25 mM Tris, and 0.9% (w/v) SDS.

MS compatible silver staining

Gels were fixed overnight in 50% (v/v) ethanol, 10% (v/v) acetic acid and thereafter silver stained according to standard procedures (86). Briefly, gels were rinsed for 10 min in 20% (v/v) ethanol, incubated for 1 min in 0.02% (w/v) sodium thiosulfate solution, and rinsed twice in water. Then gels were incubated for 30 min in 0.1% (w/v) silver nitrate solution, rinsed for 1 min in water followed by 3-6 min incubation in developing solution (2.5% (w/v) sodium carbonate, 0.02% (v/v) formaldehyde, 0.025% (w/v) thimerosal). The reaction was stopped by 2× 10 min incubation in 1.85% (w/v) EDTA disodium salt dihydrate, Titration complex III. These gels were used to excise spots for MS analysis.

Protein immunoblotting

Proteins from glycine gels were transferred to polyvinylidene difluoride membranes at U_{const} = 5 V in Towbin transfer buffer (25 mM Tris, 200 mM glycine, 0.1% (w/v) SDS, and 20% (v/v) ethanol) for 30 min, whereas proteins from tricine electrophoresis were transferred to polyvinylidene difluoride at 4 °C and I_{const} = 0.4 mA/cm^2 in tricine transfer buffer (300 mM tricine, 6% (v/v) acetic acid, pH 8.6) overnight. Afterward, membranes were blocked for 1 h in blocking solution (4% (w/v) BSA in TBS with 0.2% (v/v) Tween-20), incubated overnight at 4 °C in primary antibody, diluted in blocking solution, washed 3 times in TBS-T (TBS with 0.2% (v/v) Tween-20), and incubated for 1 h in secondary antibody (Dako, Denmark), diluted 1:5,000 in blocking solution. After washing 3 more times in TBS-T, membranes were overlaid with ECL solution (100 mM Tris, pH 8.5, 1.25 mM luminol, 200 μM *p*-coumaric acid, 0.01% (v/v) H_2O_2) and chemiluminescence signals were detected on hyper-films (GE Healthcare, USA) or by the ChemiDoc Imaging System (Bio-Rad Laboratories, USA). All incubations were conducted at room temperature, unless otherwise stated. The antibodies tested were mAb 7/51, HT7, Tau46, β-actin, SNAP25, synapsin-1, syntaxin-1, and PSD95 and details are given in Table 1. A tau ladder (T7951, Sigma, USA) comprising all six human tau isoforms was included as control for anti-tau immunoreactivity. Signals were densitometrically quantified using the AlphaEase software version 3.1.2 (Alpha Innotech Corporation, USA) or Image Laboratory software version 5.0 (Bio-Rad Laboratories, USA) and values plotted as group mean ± S.E., without intention to perform statistical analyses.

MS analysis and protein identification criteria

Spots of interest were excised from silver-stained gels and excised gel bands were prepared for enzymatic cleavage by 3 times swelling/shrinking in 100 mM aqueous tetraethylammonium bicarbonate solution or 50 mM tetraethylammonium bicarbonate in 60% acetonitrile, respectively. For reduction and alkylation of cysteine residues, the bands were treated with tris (2-carboxyethyl)phosphine (5 mM final) and iodoacetamide (5 mM final) during consecutive swelling steps. Each step was carried out for 30 min at room temperature. After the last shrinking step, the gel slices were dried for 5 min in open Eppendorf tubes. Proteolysis was conducted by addition of trypsin or thermolysin (200 ng/spot) and overnight incubation at 37 °C. The resulting peptides were acidified with formic acid (0.5% (v/v) final concentration) prior to mass spectrometric analysis. Peptides were analyzed by nanoLC-ESI-MS/MS. The LC–MS system consisted of an Agilent 1100 nanoHPLC system (Agilent, Germany), a PicoTip electrospray emitter (New Objective, USA) and an Orbitrap XL mass spectrometer (ThermoFisher, Bremen, Germany). After trapping and desalting the peptides on a Zorbax 300SB-C18 enrichment column (0.3 mm × 5 mm, Agilent, Germany) for 5 min using 0.5% (v/v) formic acid solution, peptides were separated on a Zorbax 300-SB-C18 column (75 μM × 150 mm, Agilent, Germany) within 35 min using an acetonitrile, 0.1% formic acid gradient from 15 to 40% acetonitrile. The Orbitrap instrument was operated in a data-dependent mode by subjecting the 10 most abundant ions of each survey spectrum (nominal resolution 35,000) to CID fragmentation, with a normalized collision energy set at 35%. MGF files were generated by DTA SuperCharge (version 2.0, RRID:SCR_019206) and the MS/MS Mascot search engine version 2.2 (Matrix Science, UK) was used for protein identification. A custom protein database was used comprising a complete UniProtKB *Mus musculus* protein database (with 24728 entries, downloaded from RRID:SCR_002380 on December 2015), into which we introduced the 6 human WT tau isoforms Tau-A to Tau-F (downloaded from RRID:SCR_002380 on December 2015) and the mutant tau isoform from L66 mice, named Tau-X (equivalent to Tau-F (2R4N) with the addition of P301S and G335D mutations). The following search parameters for Mascot were used and no additional threshold was applied (all significant hits with $p < 0.05$ were considered): (i) instrument: ion trap: (ii) enzyme: trypsin and thermolysin, 2 missed cleavages allowed; (iii) variable modifications: acetyl (N-term), oxidation (M), and deamidation (NQ); (iv) fixed modifications: carbamidomethyl (C); (v) mass values: monoisotopic; (vi) fragment search tolerance: 2 ppm for peptide mass and 0.5 Da; (vii) peptide charge: 1+, 2+ and 3+. For identification of phosphorylated Tau-X species, PEAKS software (version 8.0, Bioinformatics Solutions Inc.) was used with the following settings: variable modifications: carbamidomethylation, propionamide, oxidation (M), deamidation (NQ), and phosphorylation (STY), precursor ion tolerance: 3 ppm, fragment ion tolerance: 0.6 Da, peptide hit threshold (-10 logP) $\geq$ 20.0, FDR $<$ 0.1% (FDR was calculated by the decoy fusion method as described in Zhang (87)), and maximum number of PTMs: 5.

Data availability

All data are provided within the manuscript and under the Supporting information. Raw MS files are the accessible on the MassIVE database, accession number MSV000085945.

Funding and additional information—This work was supported by EMPIR programme in Research Project 15HLT02 ReMiND co-financed by the Participating States and the European Union's Horizon 2020 research and innovation programme (to N. L.). Work was also supported by WisTa Laboratories Ltd. (to V. M., D. L., M. M., C. R. H., G. R., C. M. W., F. T., and K. S.).

Conflict of interest—This work was sponsored by WisTa Laboratories Ltd., an affiliate of TauRx Therapeutics Ltd. C. R. H. and C. M. W. are employees and officers of TauRx Therapeutics Ltd.

Abbreviations—The abbreviations used are: MAP, microtubule-associated protein; CNS, central nervous system; FTD, frontotemporal dementia; ERC, entorhinal cortex; FP, fast pellet; FS, fast supernatant; HP, heat pellet; HS, heat-stable supernatant; htau40, human tau with 441 amino acids; LP1, pre- and postsynaptic membrane fraction; LP2, synaptic vesicle fraction; LS1, synaptosomal fraction; LS2, soluble synaptosomal fraction; P, pellet; P1, nuclear pelleted debris fraction; P2, crude synaptosomal fraction; P3, light membrane/microsome-enriched fraction; pAb, polyclonal antibody; PTM, post-translational modification; RPL, relative protein level; S, supernatant; S1 and S2, soluble fractions; S3, cytosolic

fraction; Tau-X, 2N4R tau with P301S and G335D mutations; L66, line 66 tau transgenic mice; PHF, paired helical filament; AD, Alzheimer's disease; Tricine, N-[2-hydroxy-1,1-bis(hydroxymethyl) ethyl]glycine.

References

1. Maccioni, R. B., and Cambiazo, V. (1995) Role of microtubule-associated proteins in the control of microtubule assembly. *Physiol. Rev.* **75,** 835–864 CrossRef Medline
2. Weingarten, M. D., Lockwood, A. H., Hwo, S. Y., and Kirschner, M. W. (1975) A protein factor essential for microtubule assembly. *Proc. Natl. Acad. Sci. U. S. A.* **72,** 1858–1862 CrossRef Medline
3. Wischik, C. M., Novak, M., Thøgersen, H. C., Edwards, P. C., Runswick, M. J., Jakes, R., Walker, J. E., Milstein, C., Roth, M., and Klug, A. (1988) Isolation of a fragment of tau derived from the core of the paired helical filament of Alzheimer disease. *Proc. Natl. Acad. Sci. U. S. A.* **85,** 4506–4510 CrossRef Medline
4. Goedert, M., and Spillantini, M. G. (2017) Propagation of tau aggregates. *Mol. Brain* **10,** 18 CrossRef Medline
5. Goedert, M., Spillantini, M. G., Jakes, R., Rutherford, D., and Crowther, R. A. (1989) Multiple isoforms of human microtubule-associated protein tau: sequences and localization in neurofibrillary tangles of Alzheimer's disease. *Neuron* **3,** 519–526 CrossRef Medline
6. Chen, J., Kanai, Y., Cowan, N. J., and Hirokawa, N. (1992) Projection domains of MAP2 and tau determine spacings between microtubules in dendrites and axons. *Nature* **360,** 674–677 CrossRef Medline
7. Kanai, Y., Chen, J., and Hirokawa, N. (1992) Microtubule bundling by tau proteins *in vivo*: Analysis of functional domains. *EMBO J.* **11,** 3953–3961 CrossRef Medline
8. Buée, L., Bussière, T., Buée-Scherrer, V., Delacourte, A., and Hof, P. R. (2000) Tau protein isoforms, phosphorylation and role in neurodegenerative disorders. *Brain Res. Rev.* **33,** 95–130 CrossRef Medline
9. Lee, G., Neve, R. L., and Kosik, K. S. (1989) The microtubule binding domain of tau protein. *Neuron* **2,** 1615–1624 CrossRef Medline
10. Mietelska-Porowska, A., Wasik, U., Goras, M., Filipek, A., and Niewiadomska, G. (2014) Tau protein modifications and interactions: Their role in function and dysfunction. *Int. J. Mol. Sci.* **15,** 4671–4713 CrossRef Medline
11. Pierre, M., and Nunez, J. (1983) Multisite phosphorylation of τ proteins from rat brain. *Biochem. Biophys. Res. Commun.* **115,** 212–219 CrossRef Medline
12. Šimić, G., Babić Leko, M., Wray, S., Harrington, C., Delalle, I., Jovanov-Milošević, N., Bažadona, D., Buée, L., de Silva, R., Di Giovanni, G., Wischik, C., and Hof, P. R. (2016) Tau protein hyperphosphorylation and aggregation in Alzheimer's disease and other tauopathies, and possible neuroprotective strategies. *Biomolecules* **6,** 6–28 CrossRef Medline
13. Billingsley, M. L., and Kincaid, R. L. (1997) Regulated phosphorylation and dephosphorylation of tau protein: Effects on microtubule interaction, intracellular trafficking and neurodegeneration. *Biochem. J.* **323,** 577–591 CrossRef
14. Dolan, P. J., and Johnson, G. V. (2010) The role of tau kinases in Alzheimer's disease. *Curr. Opin. Drug Discov. Devel.* **13,** 595–603 Medline
15. Johnson, G. V. W., and Stoothoff, W. H. (2004) Tau phosphorylation in neuronal cell function and dysfunction. *J. Cell Sci.* **117,** 5721–5729 CrossRef Medline
16. Lai, R. Y. K., Harrington, C. R., and Wischik, C. M. (2016) Absence of a role for phosphorylation in the tau pathology of Alzheimer's disease. *Biomolecules* **6,** 19 CrossRef
17. Schneider, A., Biernat, J., Von Bergen, M., Mandelkow, E., and Mandelkow, E. M. (1999) Phosphorylation that detaches tau protein from microtubules (Ser262, Ser214) also protects it against aggregation into Alzheimer paired helical filaments. *Biochemistry* **38,** 3549–3558 CrossRef Medline
18. Iqbal, K., Alonso, A. D., Chen, S., Chohan, M. O., El-Akkad, E., Gong, C. X., Khatoon, S., Li, B., Liu, F., Rahman, A., Tanimukai, H., and Grundke-Iqbal, I. (2005) Tau pathology in Alzheimer disease and other tauopathies. *Biochim. Biophys. Acta* 210 CrossRef Medline
19. Iqbal, K., Liu, F., Gong, C. X., Alonso, A. D., and Grundke-Iqbal, I. (2009) Mechanisms of tau-induced neurodegeneration. *Acta Neuropathol.* **118,** 53–69 CrossRef Medline
20. Fontaine, S. N., Sabbagh, J. J., Baker, J., Martinez-Licha, C. R., Darling, A., and Dickey, C. A. (2015) Cellular factors modulating the mechanism of tau protein aggregation. *Cell. Mol. Life Sci.* **72,** 1863–1879 CrossRef Medline
21. Melis, V., Zabke, C., Stamer, K., Magbagbeolu, M., Schwab, K., Marschall, P., Veh, R. W., Bachmann, S., Deiana, S., Moreau, P. H., Davidson, K., Harrington, K. A., Rickard, J. E., Horsley, D., Garman, R., *et al.* (2015) Different pathways of molecular pathophysiology underlie cognitive and motor tauopathy phenotypes in transgenic models for Alzheimer's disease and frontotemporal lobar degeneration. *Cell. Mol. Life Sci.* **72,** 2199–2222 CrossRef Medline
22. Al-Hilaly, Y. K., Pollack, S. J., Vadukul, D. M., Citossi, F., Rickard, J. E., Simpson, M., Storey, J. M. D., Harrington, C. R., Wischik, C. M., and Serpell, L. C. (2017) Alzheimer's disease-like paired helical filament assembly from truncated tau protein is independent of disulfide crosslinking. *J. Mol. Biol.* **429,** 3650–3665 CrossRef Medline
23. Hill, E., Karikari, T. K., Moffat, K. G., Richardson, M. J. E., and Wall, M. J. (2019) Introduction of tau oligomers into cortical neurons alters action potential dynamics and disrupts synaptic transmission and plasticity. *eNeuro* **6,** ENEURO.0166-19.2019 CrossRef
24. Moreno, H., Morfini, G., Buitrago, L., Ujlaki, G., Choi, S., Yu, E., Moreira, J. E., Avila, J., Brady, S. T., Pant, H., Sugimori, M., and Llinás, R. R. (2016) Tau pathology-mediated presynaptic dysfunction. *Neuroscience* **325,** 30–38 CrossRef Medline
25. Probst, A., Tolnay, M., Mistl, C., Götz, J., Wiederhold, K. H., Jaton, A. L., Hong, M., Ishihara, T., Lee, V. M. Y., Trojanowski, J. Q., Jakes, R., Crowther, R. A., Goedert, M., Spillantini, M. G., and Bürki, K. (2000) Axonopathy and amyotrophy in mice transgenic for human four-repeat tau protein. *Acta Neuropathol.* **99,** 469–481 CrossRef Medline
26. Spittaels, K., Van Den Haute, C., Van Dorpe, J., Bruynseels, K., Vandezande, K., Laenen, I., Geerts, H., Mercken, M., Sciot, R., Van Lommel, A., Loos, R., and Van Leuven, F. (1999) Prominent axonopathy in the brain and spinal cord of transgenic mice overexpressing four-repeat human tau protein. *Am. J. Pathol.* **155,** 2153–2165 CrossRef Medline
27. Ittner, L. M., Ke, Y. D., Delerue, F., Bi, M., Gladbach, A., van Eersel, J., Wölfing, H., Chieng, B. C., Christie, M. J., Napier, I. A., Eckert, A., Staufenbiel, M., Hardeman, E., and Götz, J. (2010) Dendritic function of tau mediates amyloid-β toxicity in Alzheimer's disease mouse models. *Cell* **142,** 387–397 CrossRef Medline
28. Yoshiyama, Y., Higuchi, M., Zhang, B., Huang, S. M., Iwata, N., Saido, T. C. C., Maeda, J., Suhara, T., Trojanowski, J. Q., and Lee, V. M. Y. (2007) Synapse loss and microglial activation precede tangles in a P301S tauopathy mouse model. *Neuron* **53,** 337–351 CrossRef Medline
29. Zhou, L., McInnes, J., Wierda, K., Holt, M., Herrmann, A. G., Jackson, R. J., Wang, Y. C., Swerts, J., Beyens, J., Miskiewicz, K., Vilain, S., Dewachter, I., Moechars, D., Strooper, B. D., Spires-Jones, T. L., *et al.* (2017) Tau association with synaptic vesicles causes presynaptic dysfunction. *Nat. Commun.* **8,** 15295 CrossRef Medline
30. Fein, J. A., Sokolow, S., Miller, C. A., Vinters, H. V., Yang, F., Cole, G. M., and Gylys, K. H. (2008) Co-localization of amyloid beta and tau pathology in Alzheimer's disease synaptosomes. *Am. J. Pathol.* **172,** 1683–1692 CrossRef
31. Henkins, K. M., Sokolow, S., Miller, C. A., Vinters, H. V., Poon, W. W., Cornwell, L. B., Saing, T., and Gylys, K. H. (2012) Extensive p-Tau pathology and SDS-stable p-Tau oligomers in Alzheimer's cortical synapses. *Brain Pathol.* **22,** 826–833 CrossRef Medline
32. Tai, H. C., Serrano-Pozo, A., Hashimoto, T., Frosch, M. P., Spires-Jones, T. L., and Hyman, B. T. (2012) The synaptic accumulation of hyperphosphorylated tau oligomers in Alzheimer disease is associated with dysfunction of the ubiquitin-proteasome system. *Am. J. Pathol.* **181,** 1426–1435 CrossRef Medline
33. Sokolow, S., Henkins, K. M., Bilousova, T., Gonzalez, B., Vinters, H. V., Miller, C. A., Cornwell, L., Poon, W. W., and Gylys, K. H. (2015) Pre-

synaptic C-terminal truncated tau is released from cortical synapses in Alzheimer's disease. *J. Neurochem.* **133,** 368–379 CrossRef Medline
34. Sahara, N., Murayama, M., Higuchi, M., Suhara, T., and Takashima, A. (2014) Biochemical distribution of tau protein in synaptosomal fraction of transgenic mice expressing human P301L tau. *Front. Neurol.* **5,** 26 CrossRef Medline
35. Harris, J. A., Koyama, A., Maeda, S., Ho, K., Devidze, N., Dubal, D. B., Yu, G. Q., Masliah, E., and Mucke, L. (2012) Human P301L-mutant tau expression in mouse entorhinal-hippocampal network causes tau aggregation and presynaptic pathology but no cognitive deficits. *PLoS ONE* **7,** e45881 CrossRef Medline
36. Binder, L. I., Frankfurter, A., and Rebhun, L. I. (1985) The distribution of tau in the mammalian central nervous central nervous. *J. Cell Biol.* **101,** 1371–1378 CrossRef Medline
37. Kubo, A., Misonou, H., Matsuyama, M., Nomori, A., Wada-Kakuda, S., Takashima, A., Kawata, M., Murayama, S., Ihara, Y., and Miyasaka, T. (2019) Distribution of endogenous normal tau in the mouse brain. *J. Comp. Neurol.* **527,** 985–998 CrossRef Medline
38. Hoover, B. R., Reed, M. N., Su, J., Penrod, R. D., Kotilinek, L. A., Grant, M. K., Pitstick, R., Carlson, G. A., Lanier, L. M., Yuan, L. L., Ashe, K. H., and Liao, D. (2010) Tau mislocalization to dendritic spines mediates synaptic dysfunction independently of neurodegeneration. *Neuron* **68,** 1067–1081 CrossRef Medline
39. Serrano-Pozo, A., Frosch, M. P., Masliah, E., and Hyman, B. T. (2011) Neuropathological alterations in Alzheimer disease. *Cold Spring Harb. Perspect. Med* **1,** a006189 CrossRef Medline
40. Thiel, G. (1993) Synapsin I, synapsin II, and synaptophysin: marker proteins of synaptic vesicles. in. *Brain Pathol.* **3,** 87–95 CrossRef Medline
41. Huttner, W. B., Schiebler, W., Greengard, P., and De Camilli, P. (1983) Synapsin I (protein I), a nerve terminal-specific phosphoprotein. III. Its association with synaptic vesicles studied in a highly purified synaptic vesicle preparation. *J. Cell Biol.* **96,** 1374–1388 CrossRef Medline
42. Mizuno, M., Kato, D., Kanamori, T., Toyoda, T., Suzuki, T., Ojika, K., and Matsukawa, N. (2013) Phosphorylation of collapsin response mediator protein-2 regulates its localization and association with hippocampal cholinergic neurostimulating peptide precursor in the hippocampus. *Neurosci. Lett.* **535,** 122–127 CrossRef Medline
43. Pollock, N. J., and Wood, J. G. (1988) Differential sensitivity of the microtubule-associated protein, tau, in Alzheimer's disease tissue to formalin fixation. *J. Histochem. Cytochem.* **36,** 1117–1121 CrossRef Medline
44. Goedert, M., and Jakes, R. (1990) Expression of separate isoforms of human tau protein: Correlation with the tau pattern in brain and effects on tubulin polymerization. *EMBO J.* **9,** 4225–4230 CrossRef Medline
45. Berrocal, M., Marcos, D., Sepúlveda, M. R., Pérez, M., Ávila, J., and Mata, A. M. (2009) Altered Ca^{2+} dependence of synaptosomal plasma membrane Ca^{2+}-ATPase in human brain affected by Alzheimer's disease. *FASEB J.* **23,** 1826–1834 CrossRef Medline
46. Berrocal, M., Caballero-Bermejo, M., Gutierrez-Merino, C., and Mata, A. M. (2019) Methylene blue blocks and reverses the inhibitory effect of tau on PMCA function. *Int. J. Mol. Sci.* **20,** 3521 CrossRef
47. Ono, Y., Mori, Y., Egashira, Y., Sumiyama, K., and Takamori, S. (2019) Expression of plasma membrane calcium ATPases confers Ca^{2+}/H^{+} exchange in rodent synaptic vesicles. *Sci. Rep.* **9,** 4289 CrossRef Medline
48. Thies, E., and Mandelkow, E. M. (2007) Missorting of tau in neurons causes degeneration of synapses that can be rescued by the kinase MARK2/Par-1. *J. Neurosci.* **27,** 2896–2907 CrossRef Medline
49. Decker, J. M., Krüger, L., Sydow, A., Zhao, S., Frotscher, M., Mandelkow, E., and Mandelkow, E. M. (2015) Pro-aggregant Tau impairs mossy fiber plasticity due to structural changes and Ca^{++} dysregulation. *Acta Neuropathol. Commun.* **3,** 23 CrossRef Medline
50. Bodea, L. G., Eckert, A., Ittner, L. M., Piguet, O., and Götz, J. (2016) Tau physiology and pathomechanisms in frontotemporal lobar degeneration. *J. Neurochem.* **138,** 71–94 CrossRef
51. Götz, J., Chen, F., Barmettler, R., and Nitsch, R. M. (2001) Tau filament formation in transgenic mice expressing P301L tau. *J. Biol. Chem.* **276,** 529–534 CrossRef Medline
52. Lewis, J., McGowan, E., Rockwood, J., Melrose, H., Nacharaju, P., Van Slegtenhorst, M., Gwinn-Hardy, K., Murphy, M. P., Baker, M., Yu, X., Duff, K., Hardy, J., Corral, A., Lin, W. L., Yen, S. H., *et al.* (2000) Neurofibrillary tangles, amyotrophy and progressive motor disturbance in mice expressing mutant (P301L)tau protein. *Nat. Genet.* **25,** 402–405 CrossRef Medline
53. Goedert, M., Ghetti, B., and Spillantini, M. G. (2012) Frontotemporal dementia: Implications for understanding Alzheimer disease. *Cold Spring Harb. Perspect. Med.* **2,** a006254 CrossRef Medline
54. Ondrejcak, T., Klyubin, I., Corbett, G. T., Fraser, G., Hong, W., Mably, A. J., Gardener, M., Hammersley, J., Perkinton, M. S., Billinton, A., Walsh, D. M., and Rowan, M. J. (2018) Cellular prion protein mediates the disruption of hippocampal synaptic plasticity by soluble tau *in vivo*. *J. Neurosci.* **38,** 10595–10606 CrossRef Medline
55. Tamagnini, F., Walsh, D. A., Brown, J. T., Bondulich, M. K., Hanger, D. P., and Randall, A. D. (2017) Hippocampal neurophysiology is modified by a disease-associated C-terminal fragment of tau protein. *Neurobiol. Aging* **60,** 44–56 CrossRef Medline
56. Morris, M., Knudsen, G. M., Maeda, S., Trinidad, J. C., Ioanoviciu, A., Burlingame, A. L., and Mucke, L. (2015) Tau post-translational modifications in wild-type and human amyloid precursor protein transgenic mice. *Nat. Neurosci.* **18,** 1183–1189 CrossRef Medline
57. Hanger, D. P., Betts, J. C., Loviny, T. L. F., Blackstock, W. P., and Anderton, B. H. (1998) New phosphorylation sites identified in hyperphosphorylated tau (paired helical filament-tau) from Alzheimer's disease brain using nanoelectrospray mass spectrometry. *J. Neurochem.* **71,** 2465–2476 CrossRef Medline
58. Micheau, J., and Riedel, G. (1999) Protein kinases: Which one is the memory molecule? *Cell. Mol. Life Sci.* **55,** 534–548 CrossRef Medline
59. Riedel, G. (1999) If phosphatases go up, memory goes down. *Cell. Mol. Life Sci.* **55,** 549–553 CrossRef Medline
60. Roman, E. A., and González Flecha, F. L. (2014) Kinetics and thermodynamics of membrane protein folding. *Biomolecules* **4,** 354–373 CrossRef Medline
61. Sahara, N., Lewis, J., DeTure, M., McGowan, E., Dickson, D. W., Hutton, M., and Yen, S.-H. (2002) Assembly of tau in transgenic animals expressing P301L tau: Alteration of phosphorylation and solubility. *J. Neurochem.* **83,** 1498–1508 CrossRef Medline
62. Lindwall, G., and Cole, R. D. (1984) The purification of tau protein and the occurrence of two phosphorylation states of tau in brain. *J. Biol. Chem.* **259,** 12241–12245 Medline
63. Greenberg, S. G., Davies, P., Schein, J. D., and Binder, L. I. (1992) Hydrofluoric acid-treated τ_{PHF} proteins display the same biochemical properties as normal τ. *J. Biol. Chem.* **267,** 564–569 Medline
64. Grundke-Iqbal, I., Iqbal, K., Quinlan, M., Tung, Y. C., Zaidi, M. S., and Wisniewski, H. M. (1986) Microtubule-associated protein tau: A component of Alzheimer paired helical filaments. *J. Biol. Chem.* **261,** 6084–6089 Medline
65. Tompa, P. (2002) Intrinsically unstructured proteins. *Trends Biochem. Sci.* **27,** 527–533 CrossRef Medline
66. Kimura, T., Fukuda, T., Sahara, N., Yamashita, S., Murayama, M., Mizoroki, T., Yoshiike, Y., Lee, B., Sotiropoulos, I., Maeda, S., and Takashima, A. (2010) Aggregation of detergent-insoluble tau is involved in neuronal loss but not in synaptic loss. *J. Biol. Chem.* **285,** 38692–38699 CrossRef Medline
67. Falcon, B., Cavallini, A., Angers, R., Glover, S., Murray, T. K., Barnham, L., Jackson, S., O'Neill, M. J., Isaacs, A. M., Hutton, M. L., Szekeres, P. G., Goedert, M., and Bose, S. (2015) Conformation determines the seeding potencies of native and recombinant Tau aggregates. *J. Biol. Chem.* **290,** 1049–1065 CrossRef Medline
68. Jiang, L., Ash, P. E. A., Maziuk, B. F., Ballance, H. I., Boudeau, S., Abdullatif, A. A., Orlando, M., Petrucelli, L., Ikezu, T., and Wolozin, B. (2019) TIA1 regulates the generation and response to toxic tau oligomers. *Acta Neuropathol.* **137,** 259–277 CrossRef Medline
69. Pollack, S. J., Trigg, J., Khanom, T., Biasetti, L., Marshall, K. E., Al-Hilaly, Y. K., Rickard, J. E., Harrington, C. R., Wischik, C. M., and Serpell, L. C. (2020) Paired helical filament-forming region of tau(297–391) influences endogenous tau protein and accumulates in acidic compartments in human neuronal cells. *J. Mol. Biol.* **432,** 4891–4907 CrossRef Medline

70. Arendt, T., Stieler, J., Strijkstra, A. M., Hut, R. A., Rüdiger, J., Van der Zee, E. A., Harkany, T., Holzer, M., and Härtig, W. (2003) Reversible paired helical filament-like phosphorylation of tau is an adaptive process associated with neuronal plasticity in hibernating animals. *J. Neurosci.* **23,** 6972–6981 CrossRef Medline
71. Bretteville, A., and Planel, E. (2008) Tau aggregates: Toxic, inert, or protective species? *J. Alzheimer's Dis.* **14,** 431–436 CrossRef
72. Flores-Rodríguez, P., Ontiveros-Torres, M. A., Cárdenas-Aguayo, M. C., Luna-Arias, J. P., Meraz-Ríos, M. A., Viramontes-Pintos, A., Harrington, C. R., Wischik, C. M., Mena, R., Florán-Garduño, B., and Luna-Muñoz, J. (2015) The relationship between truncation and phosphorylation at the C-terminus of tau protein in the paired helical filaments of Alzheimer's disease. *Front. Neurosci.* **9,** 33 CrossRef Medline
73. Goedert, M., Jakes, R., Crowther, R. A., Six, J., Lubke, U., Vandermeeren, M., Cras, P., Trojanowski, J. Q., and Lee, V. M. Y. (1993) The abnormal phosphorylation of tau protein at Ser-202 in Alzheimer disease recapitulates phosphorylation during development. *Proc. Natl. Acad. Sci. U.S.A.* **90,** 5066–5070 CrossRef Medline
74. Mukaetova-Ladinska, E. B., Garcia-Siera, F., Hurt, J., Gertz, H. J., Xuereb, J. H., Hills, R., Brayne, C., Huppert, F. A., Paykel, E. S., McGee, M., Jakes, R., Honer, W. G., Harrington, C. R., and Wischik, C. M. (2000) Staging of cytoskeletal and β-amyloid changes in human isocortex reveals biphasic synaptic protein response during progression of Alzheimer's disease. *Am. J. Pathol.* **157,** 623–636 CrossRef Medline
75. Nagy, Z., Hindley, N. J., Braak, H., Braak, E., Yilmazer-Hanke, D. M., Schultz, C., Barnetson, L., King, E. M. F., Jobst, K. A., and Smith, A. D. (1999) The progression of Alzheimer's disease from limbic regions to the neocortex: Clinical, radiological and pathological relationships. *Dement. Geriatr. Cogn. Disord.* **10,** 115–120 CrossRef Medline
76. Novak, M., Jakes, R., Edwards, P. C., Milstein, C., and Wischik, C. M. (1991) Difference between the tau protein of Alzheimer paired helical filament core and normal tau revealed by epitope analysis of monoclonal antibodies 423 and 7.51. *Proc. Natl. Acad. Sci. U. S. A.* **88,** 5837–5841 CrossRef Medline
77. Novak, M., Kabat, J., and Wischik, C. M. (1993) Molecular characterization of the minimal protease resistant tau unit of the Alzheimer's disease paired helical filament. *EMBO J.* **12,** 365–370 CrossRef Medline
78. Falcon, B., Zhang, W., Schweighauser, M., Murzin, A. G., Vidal, R., Garringer, H. J., Ghetti, B., Scheres, S. H. W., and Goedert, M. (2018) Tau filaments from multiple cases of sporadic and inherited Alzheimer's disease adopt a common fold. *Acta Neuropathol.* **136,** 699–708 CrossRef Medline
79. Wischik, C. M., Edwards, P. C., Lai, R. Y. K., Roth, M., and Harrington, C. R. (1996) Selective inhibition of Alzheimer disease-like tau aggregation by phenothiazines. *Proc. Natl. Acad. Sci. U. S. A.* **93,** 11213–11218 CrossRef Medline
80. Yanamandra, K., Kfoury, N., Jiang, H., Mahan, T. E., Ma, S., Maloney, S. E., Wozniak, D. F., Diamond, M. I., and Holtzman, D. M. (2013) Anti-tau antibodies that block tau aggregate seeding invitro markedly decrease pathology and improve cognition *in vivo*. *Neuron* **80,** 402–414 CrossRef Medline
81. Hochgräfe, K., Sydow, A., and Mandelkow, E. M. (2013) Regulatable transgenic mouse models of Alzheimer disease: Onset, reversibility and spreading of tau pathology. *FEBS J.* **280,** 4371–4381 CrossRef Medline
82. Sydow, A., Van Der Jeugd, A., Zheng, F., Ahmed, T., Balschun, D., Petrova, O., Drexler, D., Zhou, L., Rune, G., Mandelkow, E., D'Hooge, R., Alzheimer, C., and Mandelkow, E.-M. (2011) Reversibility of Tau-related cognitive defects in a regulatable FTD mouse model. *J. Mol. Neurosci.* **45,** 432–437 CrossRef
83. Van der Jeugd, A., Hochgräfe, K., Ahmed, T., Decker, J. M., Sydow, A., Hofmann, A., Wu, D., Messing, L., Balschun, D., D'Hooge, R., and Mandelkow, E.-M. (2012) Cognitive defects are reversible in inducible mice expressing pro-aggregant full-length human Tau. *Acta Neuropathol.* **123,** 787–805 CrossRef Medline
84. Mocanu, M. M., Nissen, A., Eckermann, K., Khlistunova, I., Biernat, J., Drexler, D., Petrova, O., Schönig, K., Bujard, H., Mandelkow, E., Zhou, L., Rune, G., and Mandelkow, E.-M. (2008) The potential for β-structure in the repeat domain of tau protein determines aggregation, synaptic decay, neuronal loss, and coassembly with endogenous tau in inducible mouse models of tauopathy. *J. Neurosci.* **28,** 737–748 CrossRef Medline
85. Paxinos, G., and Franklin, K. B. J. (2012) *The mouse brain in stereotaxic coordinates*, Compact 4th Edition, Academic Press, New York
86. Nebrich, G., Herrmann, M., Sagi, D., Klose, J., and Giavalisco, P. (2007) High MS-compatibility of silver nitrate-stained protein spots from 2-DE gels using ZipPlates and AnchorChips for successful protein identification. *Electrophoresis* **28,** 1607–1614 CrossRef Medline
87. Zhang, J., Xin, L., Shan, B., Chen, W., Xie, M., Yuen, D., Zhang, W., Zhang, Z., Lajoie, G. A., and Ma, B. (2012) PEAKS DB: *de novo* sequencing assisted database search for sensitive and accurate peptide identification. *Mol. Cell. Proteomics* **11,** M111.010587 CrossRef Medline
88. Harrington, C. R., Edwards, P. C., and Wischik, C. M. (1990) Competitive ELISA for the measurement of tau protein in Alzheimer's disease. *J. Immunol. Meth.* **134,** 261–271 CrossRef
89. Fan, R., Schrott, L. M., Arnold, T., Snelling, S., Rao, M., Graham, D., Cornelius, A., and Korneeva, N. L. (2018) Chronic oxycodone induces axonal degeneration in rat brain. *BMC Neurosci.* **19,** 15 CrossRef Medline
90. Bodea, L. G., Evans, H. T., Van der Jeugd, A., Ittner, L. M., Delerue, F., Kril, J., Halliday, G., Hodges, J., Kiernan, M. C., and Götz, J. (2017) Accelerated aging exacerbates a pre-existing pathology in a tau transgenic mouse model. *Aging Cell* **16,** 377–386 CrossRef
91. Dengler-Crish, C. M., Smith, M. A., and Wilson, G. N. (2017) Early evidence of low bone density and decreased serotonergic synthesis in the dorsal Raphe of a tauopathy model of Alzheimer's disease. *J. Alzheimer's Dis.* **55,** 1605–1619 CrossRef Medline
92. Sun, W., Lee, S., Huang, X., Liu, S., Inayathullah, M., Kim, K. M., Tang, H., Ashford, J. W., and Rajadas, J. (2016) Attenuation of synaptic toxicity and MARK4/PAR1-mediated Tau phosphorylation by methylene blue for Alzheimer's disease treatment. *Sci. Rep.* **6,** 34784 CrossRef Medline
93. Mengke, N. S., Hu, B., Han, Q. P., Deng, Y. Y., Fang, M., Xie, D., Li, A., and Zeng, H. K. (2016) Rapamycin inhibits lipopolysaccharide-induced neuroinflammation in vitro and in vivo. *Mol. Med. Rep.* **14,** 4957–4966 CrossRef Medline
94. Birnbaum, J. H., Wanner, D., Gietl, A. F., Saake, A., Kündig, T. M., Hock, C., Nitsch, R. M., and Tackenberg, C. (2018) Oxidative stress and altered mitochondrial protein expression in the absence of amyloid-β and tau pathology in iPSC-derived neurons from sporadic Alzheimer's disease patients. *Stem Cell Res.* **27,** 121–130 CrossRef Medline
95. Brinkmalm, A., Brinkmalm, G., Honer, W. G., Frölich, L., Hausner, L., Minthon, L., Hansson, O., Wallin, A., Zetterberg, H., Blennow, K., and Öhrfelt, A. (2014) SNAP-25 is a promising novel cerebrospinal fluid biomarker for synapse degeneration in Alzheimer's disease. *Mol. Neurodegener.* **9,** 53 CrossRef
96. Barfield, E. T., Gerber, K. J., Zimmermann, K. S., Ressler, K. J., Parsons, R. G., and Gourley, S. L. (2017) Regulation of actions and habits by ventral hippocampal trkB and adolescent corticosteroid exposure. *PLos Biol.* **15,** e2003000 CrossRef Medline

Supporting Information

Differential compartmental processing and phosphorylation of pathogenic human tau and native mouse tau in the Line 66 model of frontotemporal dementia

Nora Lemke[1,2], Valeria Melis[3], Dilyara Lauer[1], Mandy Magbagbeolu[1], Boris Neumann[1,4], Charles R. Harrington[3,5], Gernot Riedel[3], Claude M. Wischik[3,5], Franz Theuring[1], Karima Schwab[1*]

[1] Charité - Universitätsmedizin Berlin, Hessische Str. 3-4, 10115 Berlin, Germany

[2] Bundesanstalt für Materialforschung und-prüfung, Richard-Willstätter-Str. 11, 12489 Berlin, Germany

[3] School of Medicine, Medical Sciences and Nutrition, University of Aberdeen, Foresterhill, Aberdeen, AB25 2ZD, UK

[4] Proteome Factory AG, Magnusstr. 11, 12489 Berlin, Germany

[5] TauRx Therapeutics Ltd., 395 King Street, Aberdeen, AB24 5RP, UK

*Corresponding author: Karima Schwab

Email: karima.schwab@charite.de

Supplementary Tables

Table S1: : Identification of immuno-reactive species S1, P2, S2, P3, S3, LP1, LS1, LP2 and LS2 by Orbitrap LC-MS and Mascot search engine. The bands at a size of around 62 kDa were excised from preparative silver gels (see Fig. 5 for fractions). MAPT: microtubule-associated protein tau. Human tau isoforms (Tau-A to Tau-F) were identified by database search, nomenclature according to UniProt database. Although high sequence homology does not permit excluding mouse tau from the table, mouse species are not shown here as mouse tau is present at 55 kDa and not at 62 kDa. Furthermore, due to the high sequence homology, transgenic tau isoform Tau-X was only identified unequivocally when the sequence coverage was high enough. Peptide and protein score (-10Log(p)) is the measure of significance. Peptide mass error: deviation of the measured peptide mass from the theoretical peptide mass. ppm: parts per million. Regular font: peptides derived from tryptic digest, italics: peptides derived from thermolysin digest, double dagger (‡): thermolysin peptide which was also identified in tryptic digest.

Fraction	Position of tau in hit list	Protein isoform (Sequence coverage)	Number of AA	Protein score	Number of peptides matched	Matched peptide	m/z	Pre-cursor charge	Peptide score	Peptide mass error [ppm]	Number of missed peptide cleavages
S1	15	Tau-X (49%)	441	809	18	LDLSNVQSK	502.2762	+2	52	3.27	0
						TPSLPTPPTR	533.7976	+2	31	-1.14	0
						KLDLSNVQSK	566.3218	+2	71	-0.36	1
						SEKLDFKDR	379.8684	+3	28	0.81	2
						LQTAPVPMPDLK	655.3640	+2	56	1.73	0
						SGYSSPGSPGTPGSR	697.3212	+2	80	0.65	0
						TPSLPTPPTREPK	710.8942	+2	42	1.12	1
						IGSLDNITHVPGGGNK	526.9476	+3	40	3.13	0
						VAVVRTPPKSPSSAK	535.2905	+3	33	0.12	2
						TPPAPKTPPSSGEPPK	556.6054	+3	42	-1.5	1
						IGSLDNITHVPGGGNKK	569.6445	+3	36	0.29	1
						STPTAEDVTAPLVDEGAPGK	977.9868	+2	67	3.06	0
						HVSGGGSVQIVYKPVDLSK	657.3614	+3	57	-0.44	0
						CGSLGNIHHKPGGDQVEVK	678.0048	+3	33	-1.53	0
						QEFEVMEDHAGTYGLGDR	685.3001	+3	48	-3.09	0
						TPPAPKTPPSSGEPPKSGDR	695.0000	+3	32	-0.08	2
						HLSNVSSTGSIDMVDSPQLATLADEVSASLAK	1087.2088	+3	63	3.71	0
						‡ LQTAPVPMPDLK	*655.3627*	*+2*	*64*	*-0.19*	*3*
						LDNITHVPGGGNKK	*483.9317*	*+3*	*37*	*-0.25*	*4*
P2	31	Tau-X (12%)	441	237	4	KLDLSNVQSK	566.3206	+2	52	-2.57	1
		Tau-D (17%)	383			LQTAPVPMPDLK	655.3635	+2	56	1.06	0
		Tau-E (16%)	412			SGYSSPGSPGTPGSR	697.3198	+2	88	-1.33	0
		Tau-F (14%)	441			IGSLDNITHVPGGGNK	526.9461	+3	43	0.28	0
S2	20	Tau-X (45%)	441	777	17	LDLSNVQSK	502.2754	+2	55	1.7	0
						TPSLPTPPTR	533.7975	+2	46	-1.41	0
						KLDLSNVQSK	566.3227	+2	74	1.21	1
						SEKLDFKDR	379.8688	+3	40	1.89	2
						LQTAPVPMPDLK	663.3599	+2	54	-0.65	0
						SGYSSPGSPGTPGSR	697.3209	+2	94	0.19	0
						TPSLPTPPTREPK	474.2649	+3	30	0.49	1
						IGSLDNITHVPGGGNK	526.9470	+3	37	1.87	0
						TPPAPKTPPSSGEPPK	556.6059	+3	33	-0.48	1
						IGSLDNITHVPGGGNKK	569.6441	+3	37	-0.34	1
						STPTAEDVTAPLVDEGAPGK	977.9851	+2	82	1.3	0
						HVSGGGSVQIVYKPVDLSK	657.3619	+3	38	0.35	0
						CGSLGNIHHKPGGDQVEVK	678.0058	+3	31	-0.08	0
						QEFEVMEDHAGTYGLGDR	685.3035	+3	54	1.87	0
						HLSNVSSTGSIDMVDSPQLATLADEVSASLAK	1087.2060	+3	74	1.13	0
						‡ LQTAPVPMPDLK	*655.3623*	*+2*	*63*	*-0.78*	*3*
						FEVMEDHAGTYG	*686.2813*	*+2*	*44*	*2.28*	*2*
						IGDTPSLEDEAAGH	*706.3202*	*+2*	*74*	*-0.36*	*3*
P3	21	Tau-X (41%)	441	782	14	LDLSNVQSK	502.2768	+2	41	4.52	0
						KLDLSNVQSK	566.3233	+2	72	2.15	1
						SEKLDFKDR	379.8679	+3	39	-0.5	2
						LQTAPVPMPDLK	663.3611	+2	57	1.12	0
						SGYSSPGSPGTPGSR	697.3212	+2	84	0.55	0
						TPSLPTPPTREPK	474.2662	+3	30	3.34	1
						IGSLDNITHVPGGGNK	526.9470	+3	54	1.89	0
						IGSLDNITHVPGGGNKK	569.6427	+3	42	-2.9	1
						STPTAEDVTAPLVDEGAPGK	977.9867	+2	84	2.93	0
						HVSGGGSVQIVYKPVDLSK	657.3623	+3	62	0.97	0
						CGSLGNIHHKPGGDQVEVK	678.0070	+3	41	1.74	0
						QEFEVMEDHAGTYGLGDR	685.3018	+3	45	-0.51	0
						QEFEVMEDHAGTYGLGDRK	546.2526	+4	37	0.8	1
						HLSNVSSTGSIDMVDSPQLATLADEVSASLAK	1087.2063	+3	96	1.36	0
						‡ LQTAPVPMPDLK	*655.3633*	*+2*	*53*	*0.75*	*3*
S3	20	Tau-X (45%)	441	782	16	LDLSNVQSK	502.2757	+2	61	2.3	0
						TPSLPTPPTR	533.7997	+2	31	2.88	0
						KLDLSNVQSK	566.3230	+2	67	1.73	1

						SEKLDFKDR	379.8685	+3	30	0.88	2
						LQTAPVPMPDLK	663.3599	+2	63	-0.67	0
						SGYSSPGSPGTPGSR	697.3206	+2	79	-0.19	0
						IGSLDNITHVPGGGNK	526.9471	+3	53	2.12	0
						TPPAPKTPPSSGEPPK	556.6057	+3	37	-0.95	1
						IGSLDNITHVPGGGNKK	569.6453	+3	45	1.64	1
						STPTAEDVTAPLVDEGAPGK	977.9855	+2	77	1.74	0
						HVSGGGSVQIVYKPVDLSK	657.3623	+3	52	0.85	0
						CGSLGNIHHKPGGDQVEVK	678.0057	+3	35	-0.19	0
						QEFEVMEDHAGTYGLGDR	685.3022	+3	67	0.05	0
						TPPAPKTPPSSGEPPKSGDR	694.9981	+3	31	-2.72	2
						HLSNVSSTGSIDMVDSPQLATLADEVSASLAK	1087.2050	+3	55	0.22	0
						‡ LQTAPVPMPDLK	*655.3624*	*+2*	*54*	*-0.69*	*3*
						FEVMEDHAGTYG	*686.2808*	*+2*	*48*	*1.54*	*2*
LP1	21	Tau-X (35%)	441	625	13	LDLSNVQSK	502.2742	+2	52	-0.65	0
						TPSLPTPPTR	533.7994	+2	29	2.16	0
						KLDLSNVQSK	566.3227	+2	46	1.1	1
						LQTAPVPMPDLK	663.3607	+2	66	0.59	0
						SGYSSPGSPGTPGSR	697.3201	+2	76	-1.01	0
						IGSLDNITHVPGGGNK	526.9467	+3	54	1.4	0
						TPPAPKTPPSSGEPPK	556.6054	+3	41	-1.5	1
						IGSLDNITHVPGGGNKK	569.6443	+3	42	0.02	1
						STPTAEDVTAPLVDEGAPGK	977.9810	+2	91	-2.95	0
						HVSGGGSVQIVYKPVDLSK	657.3616	+3	39	-0.15	0
						CGSLGNIHHKPGGDQVEVK	678.0059	+3	36	0.07	0
						QEFEVMEDHAGTYGLGDR	685.3023	+3	53	0.2	0
						‡ LQTAPVPMPDLK	*663.3608*	*+2*	*49*	*0.79*	*3*
						FEVMEDHAGTYG	*686.2797*	*+2*	*45*	*-0.06*	*2*
LS1	30	Tau-X (14%)	441	330	6	LDLSNVQSK	502.2749	+2	43	0.68	0
		Tau-D (16%)	383			TPSLPTPPTR	533.7988	+2	36	1.18	0
		Tau-E (15%)	412			KLDLSNVQSK	566.3224	+2	67	0.58	1
		Tau-F (14%)	441			LQTAPVPMPDLK	655.3634	+2	66	0.78	0
						SGYSSPGSPGTPGSR	697.3205	+2	73	-0.41	0
						IGSLDNITHVPGGGNK	526.9459	+3	47	-0.2	0
LP2	43	Tau-X (9%)	441	149	3	LQTAPVPMPDLK	655.3626	+2	51	-0.39	0
		Tau-Fetal (12%)	352			SGYSSPGSPGTPGSR	697.3204	+2	63	-0.55	0
		Tau-A (13%)	316			IGSLDNITHVPGGGNK	526.9457	+3	37	-0.5	0
		Tau-B (11%)	381								
		Tau-C (10%)	410								
		Tau-D (11%)	383								
		Tau-E (10%)	412								
		Tau-F (9%)	441								
LS2	59	Tau-X (3%)	441	61	1	SGYSSPGSPGTPGSR	697.3205	+2	61	-0.37	0
		Tau-Fetal (4%)	352								
		Tau-A (4%)	316								
		Tau-B (3%)	381								
		Tau-C (3%)	410								
		Tau-D (3%)	383								
		Tau-E (3%)	412								
		Tau-F (3%)	441								

Table S2: Identification of phosphorylated Tau-X species derived from subcellular fractionation (see Fig. 5) by Orbitrap LC-MS and PEAKS software analysis. Peptide score (-10Log(p)) is the measure of significance. Peptide mass error: deviation of the measured peptide mass from the theoretical peptide mass. ppm: parts per million, AA: amino acid, S: Serine, T: Threonine, +79.97: mass of phosphorylation (monoisotopic).

Fraction	Number of peptides matched (PEAKS)	Sequence coverage	Number of phospho-peptides matched	Matched phosphorylated peptide	Position of phosphorylation (AA)	Peptide score (-10log(p))	Peptide mass	Peptide mass error (ppm)
S1	21	45%	4	SGYSSPGS(+79.97)PGTPGSR	S202	55.03	1472.5933	-0.2
				TPPAPKT(+79.97)PPSSGEPPK	T181	47.11	1666.7966	-0.5
				TPPAPKT(+79.97)PPSSGEPPKSGDR	T181	37.04	2081.9783	-0.9
				VAVVRT(+79.97)PPKSPSSAK	T231	27.30	1602.8494	-0.3
P2	5		no phosphorylated tau peptides found					
S2	28	53%	6	SGYSSPGS(+79.97)PGTPGSR	S202	56.04	1472.5933	-0.8
				SGYSS(+79.97)PGSPGTPGSR	S399	54.98	1472.5933	0.6
				TPPAPKT(+79.97)PPSSGEPPK	T181	52.52	1666.7966	1.1
				TPPAPKT(+79.97)PPSSGEPPKSGDR	T181	42.53	2081.9783	-0.8
				VAVVRT(+79.97)PPKSPSSAK	T231	32.59	1602.8494	-1.0
				KVAVVRT(+79.97)PPKSPSSAK	T231	29.68	1730.9443	-0.2
P3	14	42%	no phosphorylated tau peptides found					
S3	22	50%	4	TPPAPKT(+79.97)PPSSGEPPK	T181	45.13	1666.7966	0.3
				TPPAPKT(+79.97)PPSSGEPPKSGDR	T181	41.25	2081.9783	-1.5
				VAVVRT(+79.97)PPKSPSSAK	T231	27.96	1602.8494	-0.2
				KVAVVRT(+79.97)PPKSPSSAK	T231	26.61	1730.9443	0.0
LP1	20	32%	4	SGYSSPGS(+79.97)PGTPGSR	S202	47.03	1472.5933	-0.4
				TPPAPKT(+79.97)PPSSGEPPK	T181	28.49	1666.7966	-0.7
				KVAVVRT(+79.97)PPKSPSSAK	T231	25.22	1730.9443	0.0
				TPPAPKT(+79.97)PPSSGEPPKSGDR	T181	23.01	2081.9783	-1.4
LS1	6	11%	no phosphorylated tau peptides found					
LP2	2	6%	no phosphorylated tau peptides found					
LS2	1	3%	no phosphorylated tau peptides found					

Supplementary Figures

Figure S1: Tau immunohistochemistry in L66 and WT control mice. Tau immunoreactivity with phosphorylation-independent antibodies 7/51 (A), Tau46 (B), HT7 (C) and 27/499 (D), and with phosphorylation-specific antibodies pSer202 (E), pSer396 (F) and pSer416 (G) show prominent intraneuronal staining in cortex and hippocampus in L66 brains. Phosphorylation-independent antibodies showed strong synaptic staining mainly in striatum in L66 (A-D). Phosphorylation-specific antibodies showed strong staining in cell bodies and axons in L66 (E-G). Black arrowhead: cytosolic staining in neurons, white arrowhead: axonal/dendritic staining, circle: synaptic staining. CA1: hippocampus subfield CA1, STRI: striatum, ERC: entorhinal cortex. Scale bars, 100 µm. L66: Line 66 tau transgenic mice. WT: wild-type mice.

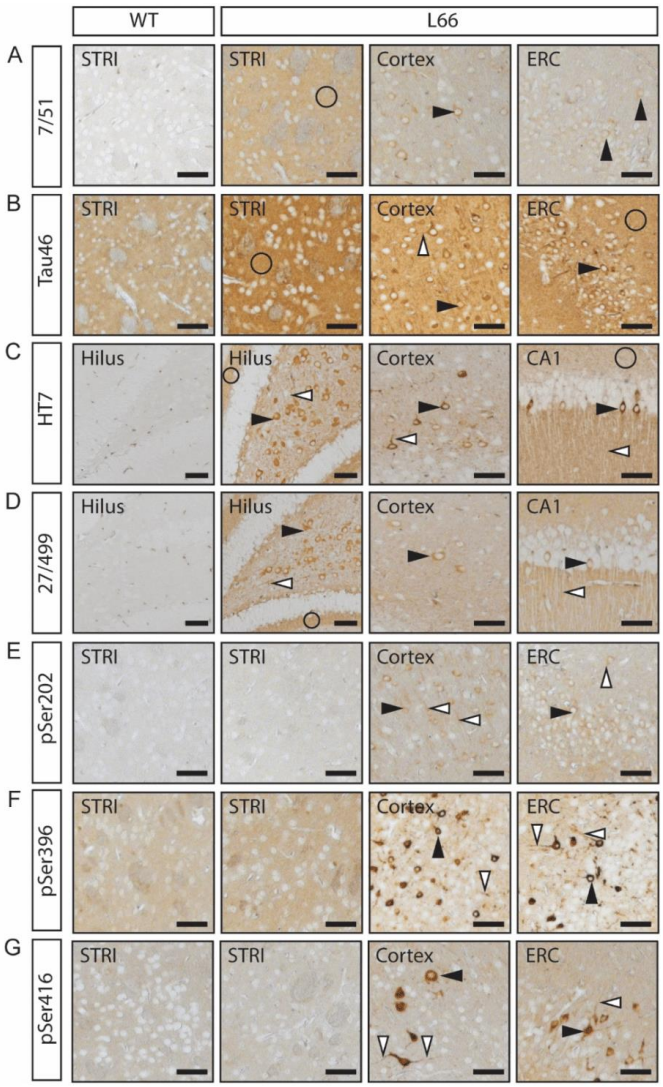

Figure S2: Co-staining for synapsin and phospho-tau in L66 mice, using immunofluorescence. Tau immunoreactivity with the phosphorylation-dependent antibodies pSer202, pSer396 or pSer416 (green) with synapsin-1 or synapsin-2 (red). In the merged panels on the right: arrows indicate tau staining in the neuronal soma; double arrowheads, synaptic tau. Scale bars, 25 µm. Phospho-tau is present in the cell soma but is virtually absent from synapses.

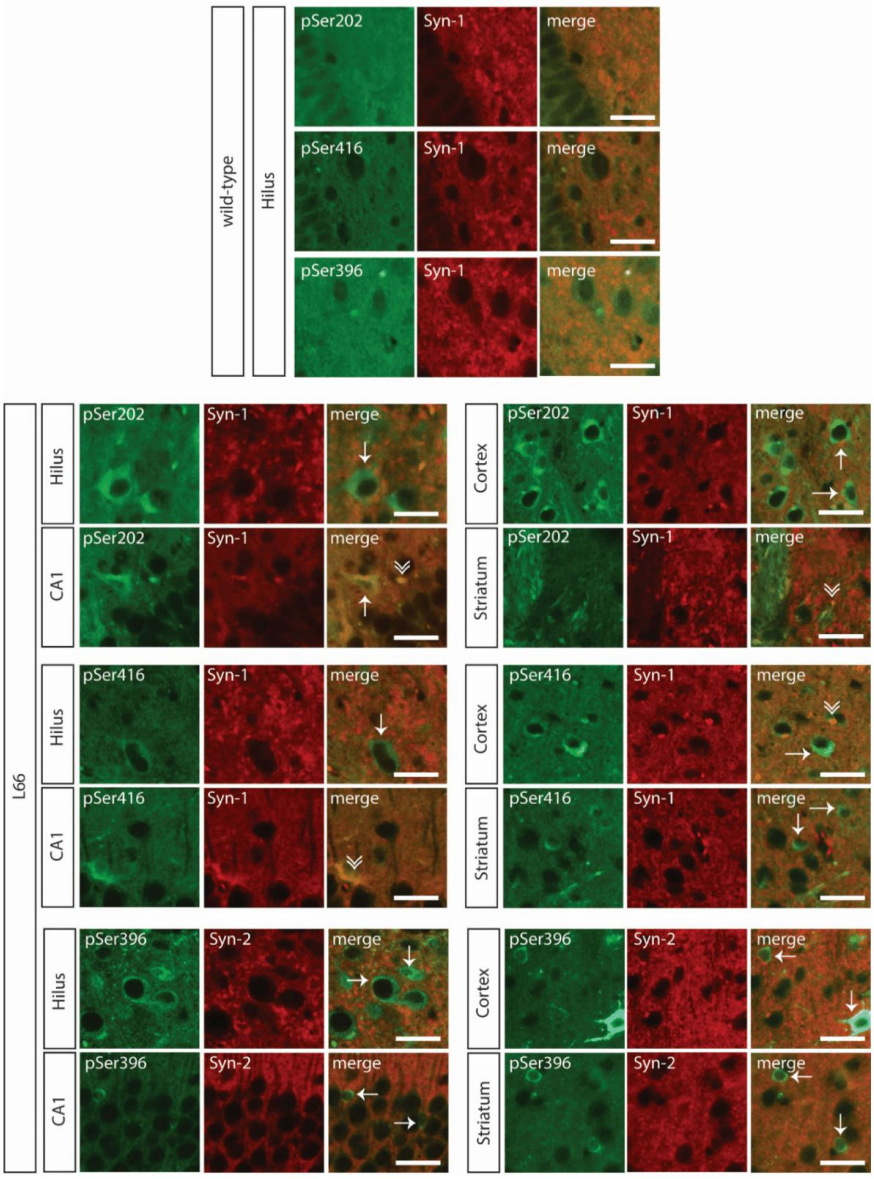

Figure S3: Annotated MS/MS spectrum of single peptide identification of Tau-X species derived from subcellular fractionation in fraction LS2 (see Table S1) by Orbitrap LC-MS and Mascot software analysis. Peptide SGYSSPGSPGTPGSR, mass 1392.5933

Annotated spectrum with alignment

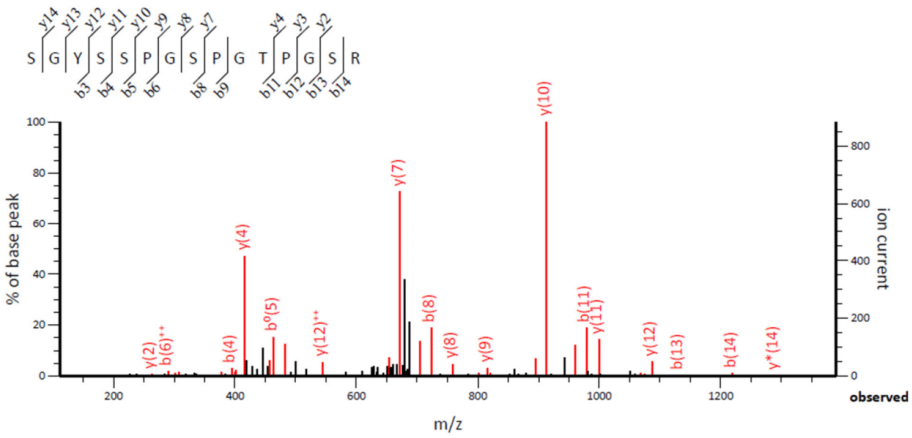

Ion table and mass error map

#	b	b^{++}	b^{0}	b^{0++}	Seq.	y	y^{++}	y^{*}	y^{*++}	y^{0}	y^{0++}	#
1	88.0393	44.5233	70.0287	35.5180	S							15
2	145.0608	73.0340	127.0502	64.0287	G	1306.6022	**653.8047**	1289.5757	645.2915	1288.5917	644.7995	14
3	***308.1241***	154.5657	290.1135	145.5604	Y	1249.5808	625.2940	1232.5542	616.7807	1231.5702	616.2887	13
4	***395.1561***	198.0817	377.1456	189.0764	S	***1086.5174***	**543.7624**	1069.4909	535.2491	1068.5069	534.7571	12
5	***482.1882***	241.5977	464.1776	232.5924	S	***999.4854***	500.2463	982.4588	491.7331	981.4748	491.2411	11
6	579.2409	290.1241	561.2304	281.1188	P	***912.4534***	**456.7303**	895.4268	448.2170	894.4428	447.7250	10
7	636.2624	318.6348	618.2518	309.6295	G	***815.4006***	408.2039	798.3741	399.6907	797.3900	399.1987	9
8	***723.2944***	362.1508	705.2838	353.1456	S	***758.3791***	379.6932	741.3526	371.1799	740.3686	370.6879	8
9	***820.3472***	410.6772	802.3366	401.6719	P	***671.3471***	336.1772	654.3206	327.6639	653.3365	327.1719	7
10	877.3686	439.1880	859.3581	430.1827	G	574.2944	287.6508	557.2678	279.1375	556.2838	278.6455	6
11	***978.4163***	489.7118	960.4058	480.7065	T	517.2729	259.1401	500.2463	250.6268	499.2623	250.1348	5
12	***1075.4691***	538.2382	1057.4585	529.2329	P	***416.2252***	208.6162	399.1987	200.1030	398.2146	199.6110	4
13	***1132.4905***	566.7489	1114.4800	557.7436	G	319.1724	160.0899	302.1459	151.5766	301.1619	151.0846	3
14	***1219.5226***	610.2649	1201.5120	601.2596	S	***262.1510***	131.5791	245.1244	123.0659	244.1404	122.5738	2
15					R	175.1190	88.0631	158.0924	79.5498			1

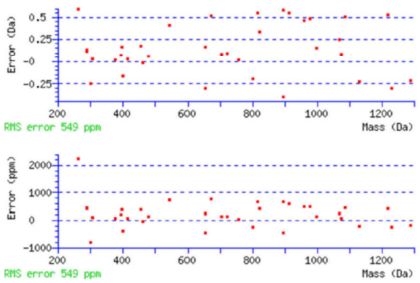

Figure S4: Annotated MS/MS spectra of phosphorylated Tau-X species derived from subcellular fractionation in fraction S1 (see Table S2) by Orbitrap LC-MS and PEAKS software analysis.

S4.A: peptide SGYSSPGS(+79.97)PGTPGSR, mass 1472.5933

Annotated spectrum with alignment

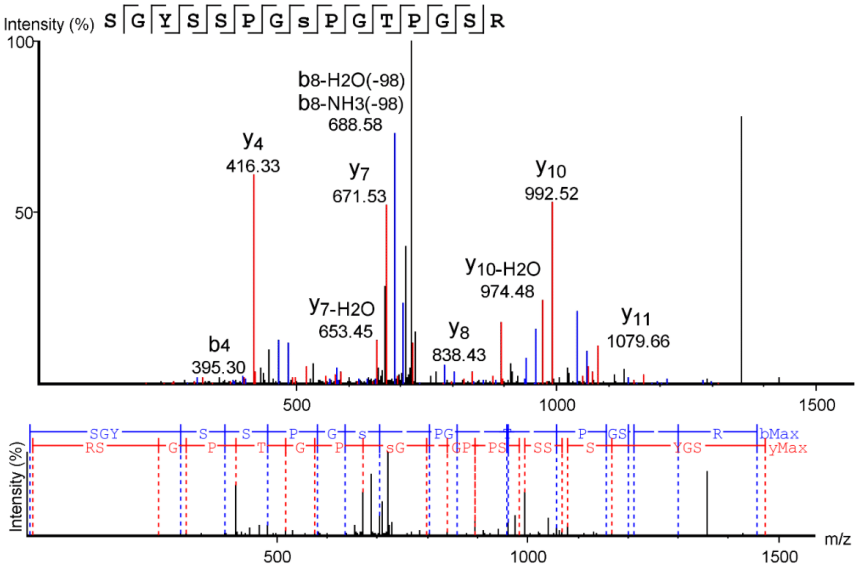

Ion table and mass error map

#	b	b-H2O	b-NH3	b (2+)	Seq	y	y-H2O	y-NH3	y (2+)	#
1	88.04	70.03	71.01	44.52	S					15
2	145.06	127.05	128.03	73.03	G	1386.57	1368.56	1369.54	693.20	14
3	308.09	289.67	291.10	154.56	Y	1329.55	1311.41	1312.52	665.27	13
4	395.30	377.23	378.45	198.08	S	1166.54	1148.47	1150.00	583.87	12
5	482.29	464.36	465.16	241.59	S	1079.66	1061.58	1062.42	540.23	11
6	579.36	561.25	562.24	289.67	P	992.52	974.48	975.39	496.89	10
7	636.36	618.63	619.37	318.72	G	895.11	877.63	878.34	448.18	9
8	802.96	785.38	786.23	402.13	S(+79.97)	838.43	820.73	820.73	419.32	8
9	900.31	882.65	883.43	450.66	P	671.53	653.45	654.32	335.58	7
10	957.30	939.21	940.51	479.17	G	574.45	556.62	557.27	287.65	6
11	1058.42	1040.47	1041.36	529.69	T	517.23	499.26	500.25	259.65	5
12	1155.60	1137.53	1138.41	577.65	P	416.33	398.30	399.51	209.07	4
13	1212.58	1194.45	1195.12	606.73	G	319.45	301.21	302.15	160.09	3
14	1299.64	1281.17	1282.62	650.41	S	262.18	244.09	245.12	131.58	2
15					R	175.12	157.11	158.09	88.06	1

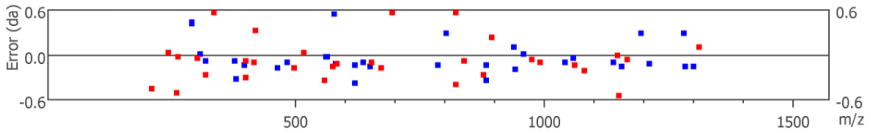

8

S4.B: peptide TPPAPKT(+79.97)PPSSGEPPK, mass 1666.7966

Annotated spectrum with alignment

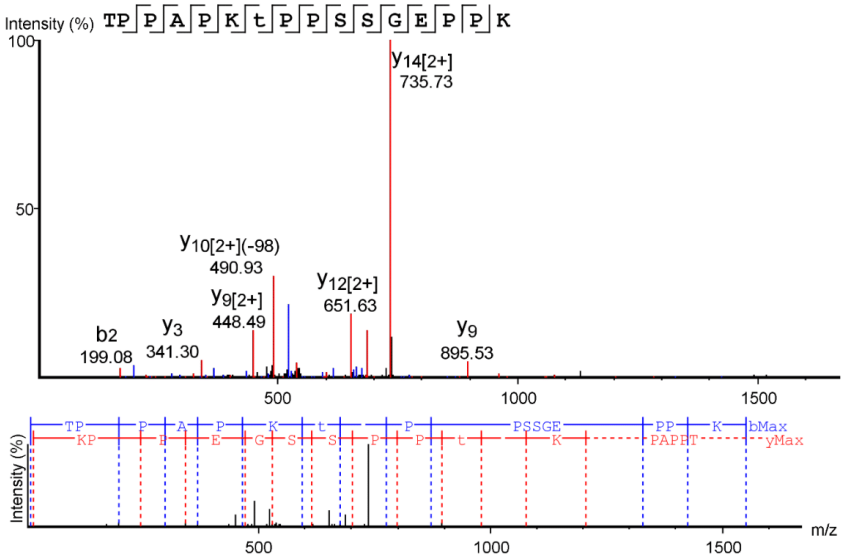

Ion table and mass error map

#	b	b-H2O	b-NH3	b (2+)	Seq	y	y-H2O	y-NH3	y (2+)	#
1	102.06	84.04	85.03	51.53	T					20
2	199.03	181.10	182.08	100.05	P	1981.94	1963.93	1964.91	991.47	19
3	296.25	278.30	279.13	148.58	P	1884.89	1866.87	1867.86	943.00	18
4	367.34	349.22	350.17	184.10	A	1787.83	1769.82	1770.81	894.30	17
5	464.25	446.24	447.22	232.63	P	1716.80	1698.78	1699.77	859.27	16
6	591.92	574.17	575.32	296.25	K	1619.74	1601.73	1602.72	810.81	15
7	773.44	755.35	756.45	387.18	T(+79.97)	1491.83	1473.64	1474.62	746.32	14
8	870.41	852.40	853.39	435.51	P	1310.72	1292.99	1293.61	655.82	13
9	967.47	949.45	950.44	484.23	P	1213.70	1195.57	1196.55	607.76	12
10	1054.50	1036.49	1037.47	528.08	S	1117.05	1098.52	1099.50	558.76	11
11	1141.53	1123.52	1124.50	571.41	S	1029.64	1011.49	1012.47	515.56	10
12	1198.55	1180.49	1181.52	599.37	G	943.00	924.82	925.44	471.73	9
13	1327.76	1309.73	1310.72	664.30	E	885.51	867.27	868.42	443.22	8
14	1424.65	1406.64	1407.62	712.82	P	756.45	738.39	739.59	378.99	7
15	1521.70	1503.69	1504.67	761.35	P	659.59	641.85	641.85	330.62	6
16	1649.79	1631.78	1632.77	825.40	K	562.52	544.28	545.27	281.27	5
17	1736.83	1718.82	1719.80	868.91	S	434.51	416.57	416.57	217.60	4
18	1793.85	1775.84	1776.82	897.11	G	347.17	329.16	330.62	174.08	3
19	1908.87	1890.86	1891.85	955.39	D	290.15	272.14	273.12	145.57	2
20					R	175.12	157.11	158.09	88.06	1

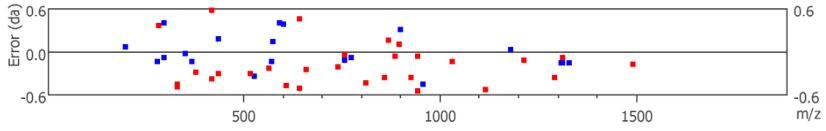

S4.C: peptide TPPAPKT(+79.97)PPSSGEPPKSGDR, mass 2081.9783

Annotated spectrum with alignment

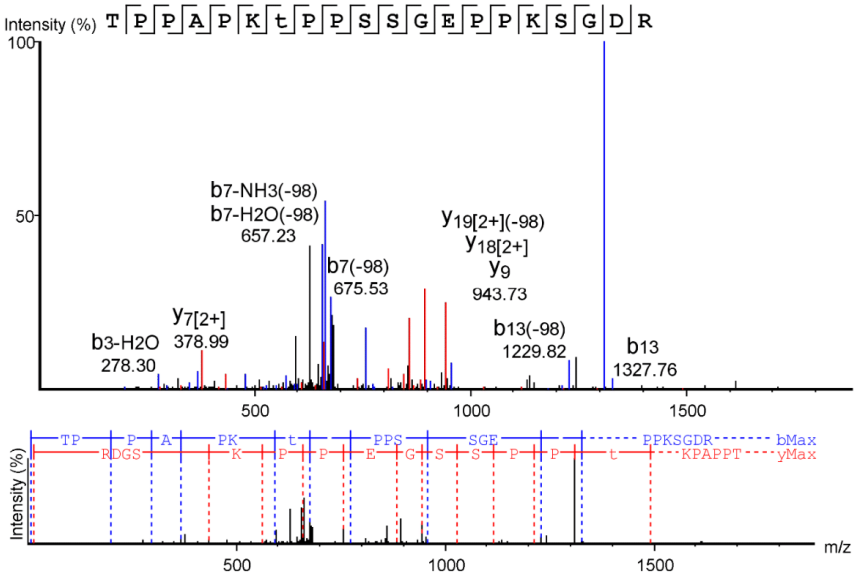

Ion table and mass error map

#	b	b-H2O	b-NH3	b (2+)	Seq	y	y-H2O	y-NH3	y (2+)	#
1	102.06	84.04	85.03	51.53	T					16
2	199.08	181.13	182.24	100.05	P	1566.76	1548.75	1549.73	783.88	15
3	296.37	278.24	279.13	148.58	P	1469.70	1451.69	1452.68	735.73	14
4	367.30	349.18	350.17	184.10	A	1372.65	1354.64	1355.62	686.82	13
5	464.29	446.24	447.22	232.19	P	1301.61	1283.89	1284.59	651.63	12
6	592.67	574.58	575.31	296.37	K	1204.25	1186.55	1187.53	602.67	11
7	773.40	755.35	756.03	387.18	T(+79.97)	1076.58	1058.33	1059.11	538.43	10
8	870.64	852.45	853.39	435.71	P	895.53	877.54	878.43	448.49	9
9	967.47	949.45	950.44	484.23	P	798.73	780.77	781.37	399.59	8
10	1054.50	1036.49	1037.47	527.68	S	701.64	683.34	684.07	351.23	7
11	1141.53	1123.52	1124.50	570.80	S	614.28	596.27	597.64	307.78	6
12	1198.55	1180.54	1181.52	599.78	G	527.68	509.68	509.68	264.27	5
13	1327.86	1309.58	1310.57	664.59	E	470.48	452.52	453.23	235.40	4
14	1424.65	1406.64	1407.62	712.82	P	341.30	323.24	324.57	171.05	3
15	1521.70	1503.69	1504.67	761.29	P	244.22	226.23	226.95	122.58	2
16					K	147.11	129.10	130.09	74.06	1

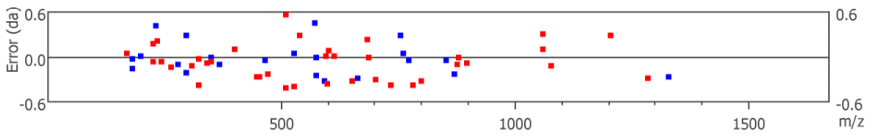

S4.D: peptide VAVVRT(+79.97)PPKSPSSAK, mass 1602.8494

Annotated spectrum with alignment

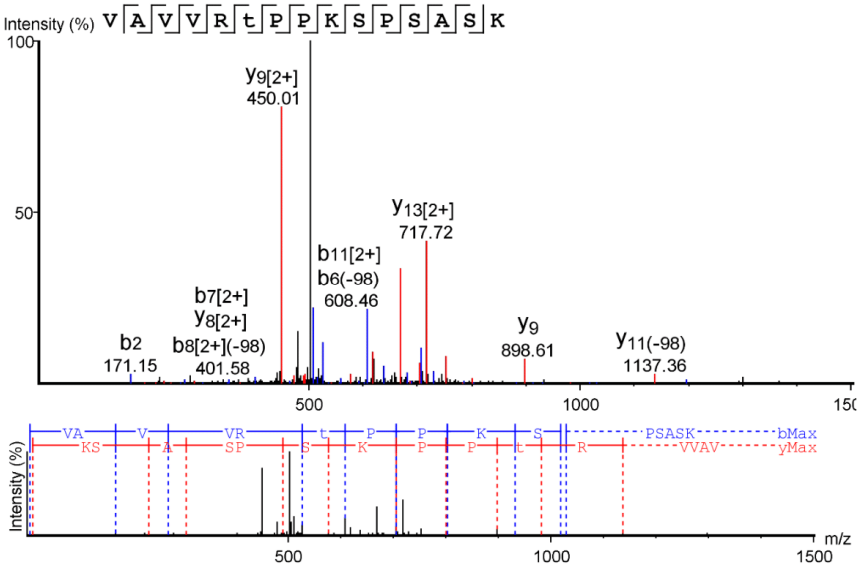

Ion table and mass error map

#	b	b-H2O	b-NH3	b (2+)	Seq	y	y-H2O	y-NH3	y (2+)	#
1	100.08	82.07	83.05	50.54	V					15
2	171.15	153.10	154.09	86.06	A	1504.79	1486.78	1487.76	753.15	14
3	270.23	252.17	253.15	135.59	V	1433.75	1415.74	1416.72	717.72	13
4	369.25	350.87	351.77	185.13	V	1334.68	1316.67	1317.66	668.31	12
5	525.33	507.02	508.79	262.64	R	1235.61	1217.60	1218.59	618.78	11
6	706.46	688.27	689.57	353.42	T(+79.97)	1079.51	1061.50	1062.49	539.97	10
7	803.54	785.14	786.32	402.27	P	898.61	880.49	881.28	450.01	9
8	900.47	882.69	883.59	450.74	P	801.39	783.32	784.42	401.58	8
9	1028.93	1010.56	1011.54	514.67	K	704.24	686.82	686.82	352.70	7
10	1115.60	1097.59	1098.57	558.45	S	576.36	558.45	559.27	289.11	6
11	1212.65	1194.69	1195.62	606.34	P	489.46	471.26	472.24	245.38	5
12	1299.68	1281.67	1282.66	650.34	S	392.21	373.92	375.19	197.19	4
13	1370.72	1352.71	1353.69	685.86	A	305.24	287.17	288.15	153.09	3
14	1457.75	1439.74	1440.72	729.69	S	234.11	216.13	217.07	117.57	2
15					K	147.11	129.10	130.09	74.06	1

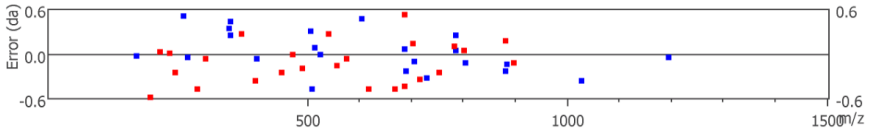

Figure S5: Annotated MS/MS spectra of phosphorylated Tau-X species derived from subcellular fractionation in fraction S2 (see Table S2) by Orbitrap LC-MS and PEAKS software analysis.

S5.A: peptide SGYSSPGS(+79.97)PGTPGSR, mass 1472.5933

Annotated spectrum with alignment

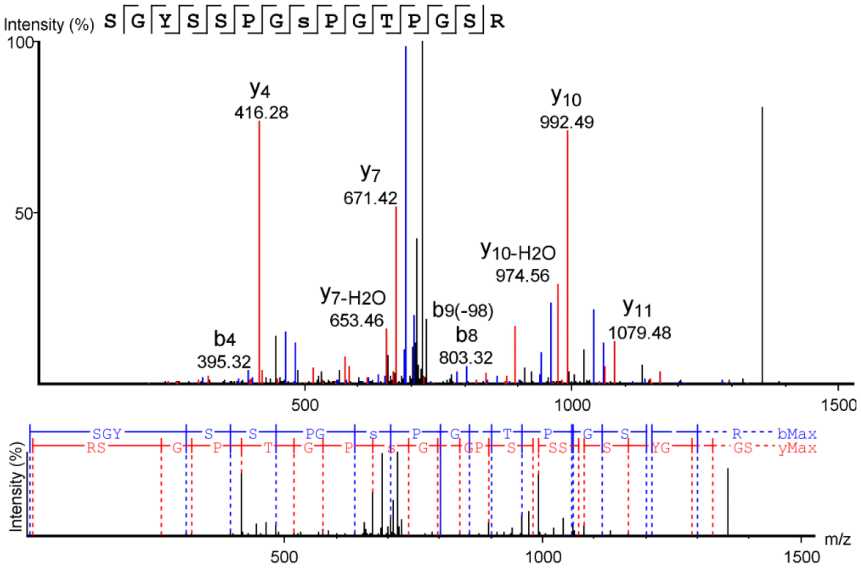

Ion table and mass error map

#	b	b-H2O	b-NH3	b (2+)	Seq	y	y-H2O	y-NH3	y (2+)	#
1	88.04	70.03	71.01	44.52	S					15
2	145.06	127.05	128.03	73.03	G	1386.57	1368.56	1369.54	693.78	14
3	308.21	290.21	291.37	154.56	Y	1329.45	1311.54	1312.52	665.37	13
4	395.32	377.20	378.50	198.08	S	1166.51	1148.61	1149.45	584.02	12
5	482.32	464.19	465.16	241.59	S	1079.48	1061.50	1062.42	540.23	11
6	579.24	561.34	562.47	290.21	P	992.49	974.56	975.39	496.71	10
7	636.82	618.45	619.24	318.63	G	895.37	877.58	878.34	448.40	9
8	803.32	785.29	786.23	402.48	S(+79.97)	838.42	820.30	821.53	419.28	8
9	900.62	882.04	883.51	450.66	P	671.42	653.46	654.32	336.17	7
10	957.34	939.41	940.31	478.64	G	574.51	556.28	557.13	287.65	6
11	1058.44	1040.34	1041.52	529.69	T	517.40	499.34	500.79	259.27	5
12	1155.44	1137.29	1138.23	578.53	P	416.28	398.32	399.43	209.11	4
13	1212.65	1194.60	1195.43	606.28	G	319.30	300.98	302.22	160.09	3
14	1299.81	1281.48	1282.12	650.06	S	262.26	244.20	245.24	131.58	2
15					R	175.12	157.11	158.09	88.06	1

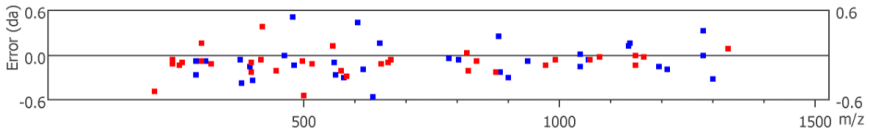

5.B: peptide SGYSS(+79.97)PGSPGTPGSR, mass 1472.5933

Annotated spectrum with alignment

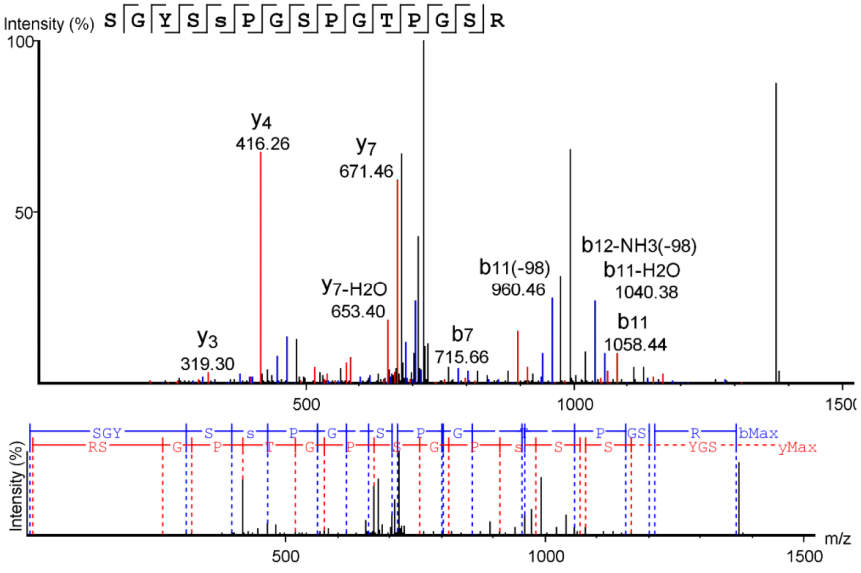

Ion table and mass error map

#	b	b-H2O	b-NH3	b (2+)	Seq	y	y-H2O	y-NH3	y (2+)	#
1	88.04	70.03	71.01	44.52	S					15
2	145.06	127.05	128.03	73.03	G	1386.57	1368.56	1369.54	694.10	14
3	308.21	290.25	291.10	154.56	Y	1329.55	1311.54	1312.98	665.40	13
4	395.20	377.24	378.13	198.08	S	1166.62	1148.60	1149.46	583.86	12
5	562.48	544.14	545.20	281.58	S(+79.97)	1079.52	1061.53	1062.70	540.31	11
6	659.09	641.20	642.18	329.54	P	912.68	894.58	895.43	456.73	10
7	715.66	698.19	698.97	358.06	G	815.77	797.50	798.37	408.20	9
8	803.32	785.54	786.23	402.13	S	758.66	740.39	741.94	379.69	8
9	900.31	882.30	883.78	450.29	P	671.46	653.40	654.32	336.17	7
10	957.20	939.71	939.71	479.17	G	574.78	556.23	557.27	287.65	6
11	1058.44	1040.38	1041.36	529.15	T	517.41	499.26	500.25	259.19	5
12	1155.86	1137.71	1138.41	578.22	P	416.26	398.29	399.20	209.10	4
13	1212.82	1194.45	1195.05	606.73	G	319.30	301.19	302.15	160.09	3
14	1299.49	1281.46	1282.77	649.72	S	262.09	244.08	245.12	131.58	2
15					R	175.12	157.11	158.09	88.06	1

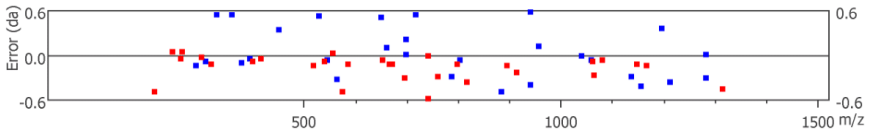

S5.C: peptide TPPAPKT(+79.97)PPSSGEPPK, mass 1666.7966

Annotated spectrum with alignment

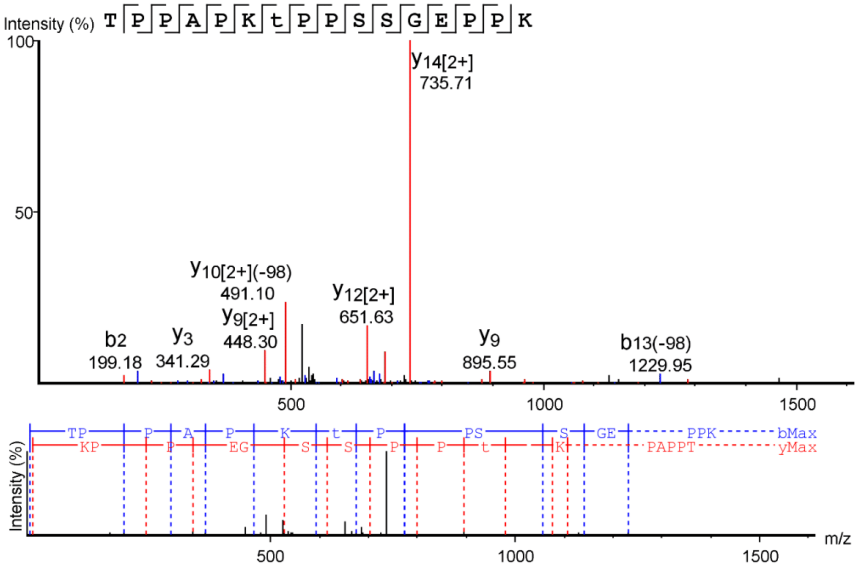

Ion table and mass error map

#	b	b-H2O	b-NH3	b (2+)	Seq	y	y-H2O	y-NH3	y (2+)	#
1	102.06	84.04	85.03	51.53	T					16
2	199.18	181.10	182.08	100.05	P	1566.76	1548.75	1549.73	784.28	15
3	296.26	278.22	279.13	148.58	P	1469.70	1451.69	1452.68	735.71	14
4	367.35	349.28	350.17	184.10	A	1372.65	1354.64	1355.62	686.85	13
5	463.88	446.24	447.22	232.63	P	1301.61	1283.82	1284.59	651.63	12
6	592.37	574.34	575.32	296.26	K	1204.56	1186.55	1187.74	602.40	11
7	773.49	755.60	756.91	387.21	T(+79.97)	1076.64	1058.84	1059.83	538.73	10
8	870.41	851.82	853.39	435.71	P	895.55	877.58	878.39	448.30	9
9	967.47	949.45	950.44	484.67	P	798.61	780.39	781.58	399.70	8
10	1054.67	1036.49	1037.47	527.67	S	701.36	683.33	684.32	351.17	7
11	1141.52	1123.52	1124.50	571.26	S	614.46	596.50	597.86	308.19	6
12	1198.55	1180.54	1181.52	599.58	G	527.67	509.55	510.26	264.42	5
13	1327.59	1309.58	1310.57	664.59	E	470.26	452.45	453.23	235.63	4
14	1424.65	1406.64	1407.62	712.44	P	341.29	323.36	324.19	171.19	3
15	1521.70	1503.69	1504.67	761.35	P	244.33	226.19	227.14	122.58	2
16					K	147.11	129.10	130.09	74.06	1

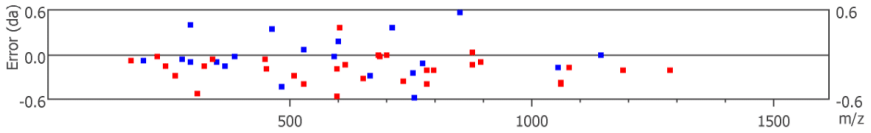

S5.D: peptide TPPAPKT(+79.97)PPSSGEPPKSGDR, mass 2081.9783

Annotated spectrum with alignment

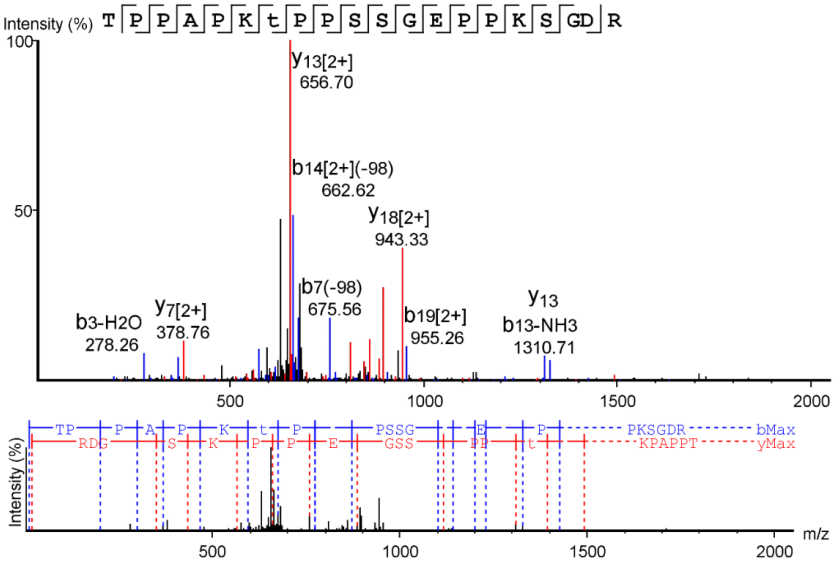

Ion table and mass error map

#	b	b-H2O	b-NH3	b (2+)	Seq	y	y-H2O	y-NH3	y (2+)	#
1	102.06	84.04	85.03	51.53	T					20
2	199.28	181.10	182.08	100.05	P	1981.94	1963.93	1964.91	991.90	19
3	296.08	278.26	279.13	148.58	P	1884.89	1866.87	1867.86	943.33	18
4	367.35	349.17	350.44	184.10	A	1787.83	1769.82	1770.81	894.41	17
5	464.44	446.24	447.32	233.14	P	1716.80	1698.78	1699.77	859.01	16
6	592.47	574.38	575.32	296.08	K	1619.74	1601.73	1602.72	810.75	15
7	773.47	755.43	756.53	387.18	T(+79.97)	1491.72	1473.64	1474.62	746.54	14
8	870.80	852.40	853.39	435.71	P	1310.71	1292.37	1293.72	655.98	13
9	967.47	949.45	950.76	484.23	P	1213.58	1195.57	1196.55	606.76	12
10	1054.50	1035.97	1037.47	527.53	S	1116.68	1098.77	1099.50	558.94	11
11	1141.85	1123.06	1124.50	571.26	S	1029.50	1011.49	1012.47	514.66	10
12	1198.55	1180.58	1181.52	600.13	G	942.46	924.02	925.61	471.86	9
13	1327.71	1309.17	1310.71	664.13	E	885.34	867.71	868.51	443.22	8
14	1424.51	1406.64	1407.62	712.82	P	756.53	738.39	739.57	378.76	7
15	1521.70	1503.69	1505.21	760.77	P	659.54	641.63	642.43	330.55	6
16	1649.79	1631.78	1632.97	825.23	K	562.49	543.74	545.72	281.65	5
17	1736.83	1718.82	1719.80	868.51	S	434.42	416.43	417.17	218.17	4
18	1793.85	1775.84	1776.82	897.42	G	347.50	329.16	330.55	174.08	3
19	1908.87	1890.86	1891.85	955.26	D	290.15	272.14	273.12	145.57	2
20					R	175.12	157.11	158.09	88.06	1

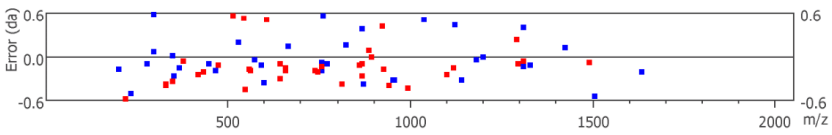

S5.E: peptide VAVVRT(+79.97)PPKSPSSAK, mass 1602.8494

Annotated spectrum with alignment

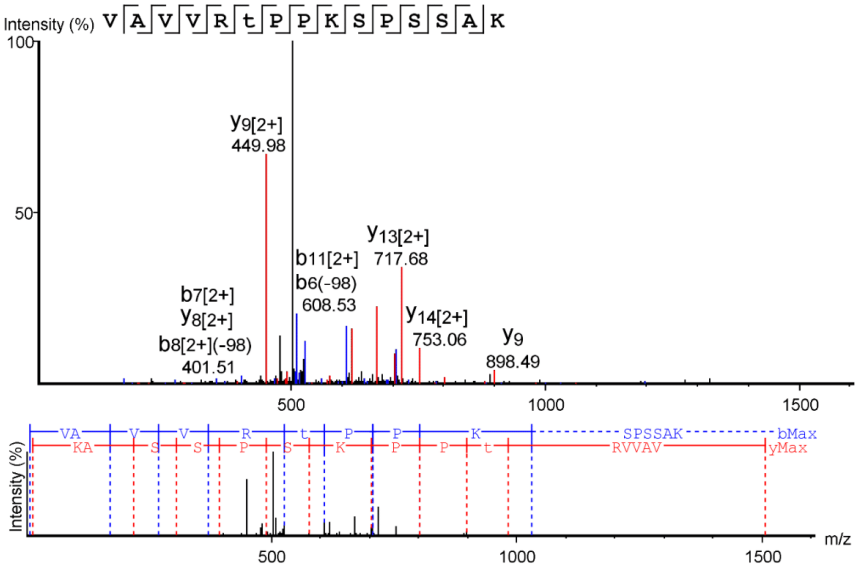

Ion table and mass error map

#	b	b-H2O	b-NH3	b (2+)	Seq	y	y-H2O	y-NH3	y (2+)	#
1	100.08	82.07	83.05	50.54	V					15
2	171.00	153.10	154.09	86.06	A	1504.79	1486.78	1487.76	753.06	14
3	270.24	252.34	253.15	135.59	V	1433.75	1415.74	1416.72	717.68	13
4	369.33	351.24	352.22	185.13	V	1334.68	1316.67	1317.66	668.37	12
5	525.56	507.05	508.22	263.18	R	1235.61	1217.60	1218.59	618.31	11
6	706.49	688.54	689.85	353.67	T(+79.97)	1079.51	1061.43	1062.49	540.53	10
7	803.42	785.41	786.08	402.41	P	898.49	880.46	881.58	449.98	9
8	900.47	882.55	883.92	450.74	P	801.43	783.76	784.42	401.51	8
9	1029.12	1010.56	1011.54	514.79	K	704.22	686.43	687.37	352.88	7
10	1115.60	1097.59	1098.57	558.34	S	576.39	558.34	559.27	288.90	6
11	1212.65	1194.64	1195.40	607.39	P	489.29	471.34	472.24	245.13	5
12	1299.68	1281.67	1282.66	649.99	S	392.13	374.20	375.19	197.02	4
13	1386.71	1368.70	1369.69	693.86	S	304.77	287.17	288.14	153.09	3
14	1457.75	1439.74	1440.72	729.62	A	218.53	200.34	201.12	109.57	2
15					K	147.11	129.10	130.09	74.06	1

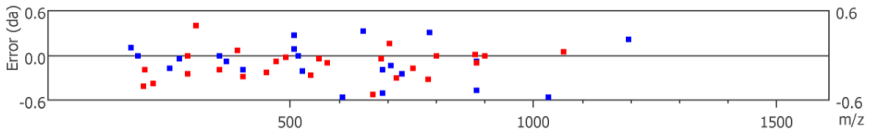

S5.F: peptide KVAVVRT(+79.97)PPKSPSSAK, mass 1730.9443

Annotated spectrum with alignment

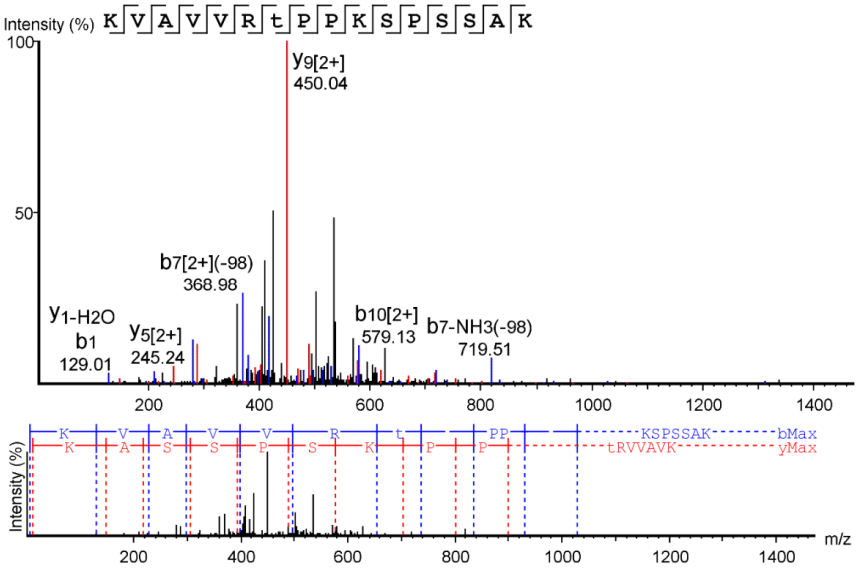

Ion table and mass error map

#	b	b-H2O	b-NH3	b (2+)	Seq	y	y-H2O	y-NH3	y (2+)	#
1	129.01	111.09	112.08	65.05	K					16
2	228.32	210.15	211.21	114.59	V	1603.86	1585.85	1586.83	802.43	15
3	299.03	280.89	282.16	150.17	A	1504.79	1486.78	1487.76	752.94	14
4	398.61	380.52	381.34	199.24	V	1433.75	1415.74	1416.72	717.70	13
5	496.90	479.51	480.48	249.04	V	1334.68	1316.67	1317.66	668.27	12
6	653.37	635.26	636.53	327.22	R	1235.61	1217.60	1218.59	618.66	11
7	834.65	816.40	817.67	417.95	T(+79.97)	1079.51	1061.50	1062.88	540.26	10
8	931.23	913.50	914.75	466.36	P	898.09	880.49	881.47	450.04	9
9	1028.83	1010.56	1011.54	514.93	P	801.54	782.86	784.42	401.52	8
10	1156.66	1138.65	1139.63	579.13	K	704.03	686.40	687.57	352.84	7
11	1243.69	1225.68	1226.67	622.35	S	576.40	558.58	559.27	288.92	6
12	1340.75	1322.73	1323.72	670.39	P	489.34	471.04	471.77	245.24	5
13	1427.78	1409.77	1410.75	714.93	S	392.37	373.75	375.48	197.14	4
14	1514.81	1496.80	1497.78	757.90	S	305.34	287.17	288.15	153.09	3
15	1585.85	1567.84	1568.82	793.42	A	218.12	200.25	201.17	109.57	2
16					K	147.12	129.01	130.09	74.06	1

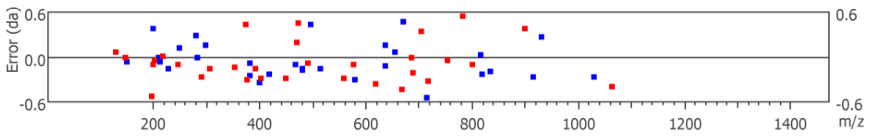

Figure S6: Annotated MS/MS spectra of phosphorylated Tau-X species derived from subcellular fractionation in fraction S3 (see Table S2) by Orbitrap LC-MS and PEAKS software analysis.

S6.A: peptide TPPAPKT(+79.97)PPSSGEPPK, mass 1666.7966

Annotated spectrum with alignment

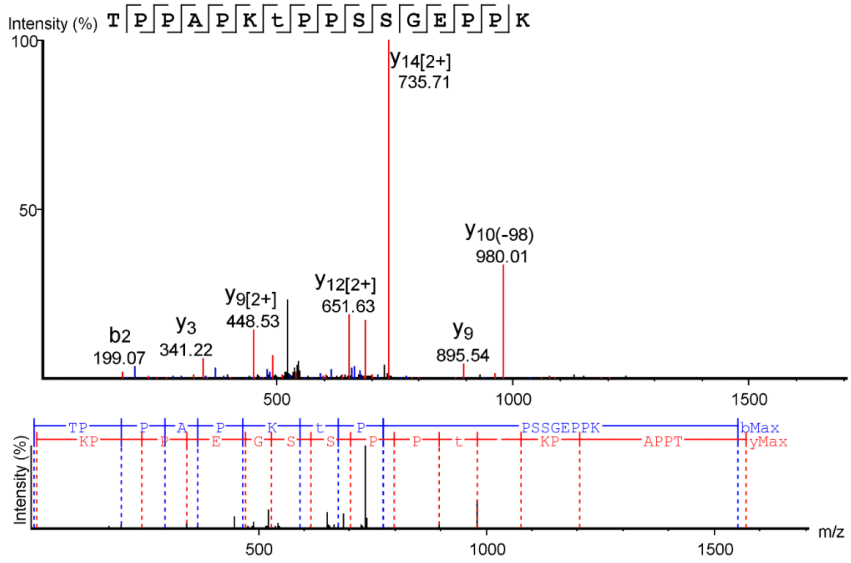

Ion table and mass error map

#	b	b-H2O	b-NH3	b (2+)	Seq	y	y-H2O	y-NH3	y (2+)	#
1	102.06	84.04	85.03	51.53	T					16
2	199.07	181.10	182.10	100.05	P	1566.76	1548.75	1549.73	783.78	15
3	296.24	277.85	279.40	148.58	P	1469.70	1451.69	1452.68	735.71	14
4	367.27	349.13	350.33	184.10	A	1372.65	1354.64	1355.62	686.82	13
5	464.21	445.96	447.22	232.33	P	1301.61	1283.60	1284.59	651.63	12
6	592.44	573.96	575.32	296.24	K	1204.56	1186.55	1187.52	602.87	11
7	773.45	755.35	756.33	387.07	T(+79.97)	1076.56	1058.85	1058.85	538.53	10
8	870.41	852.40	853.39	435.49	P	895.54	877.70	878.42	448.53	9
9	967.47	949.45	950.44	483.79	P	798.46	780.39	781.37	400.25	8
10	1054.50	1036.68	1037.47	527.61	S	701.33	683.31	684.59	351.22	7
11	1141.53	1123.52	1124.50	571.26	S	614.28	596.58	597.29	307.66	6
12	1198.55	1180.54	1181.52	599.84	G	527.61	509.79	509.79	264.35	5
13	1327.59	1309.58	1310.57	664.49	E	470.25	452.42	453.13	235.63	4
14	1424.65	1406.64	1407.62	712.24	P	341.22	323.42	324.19	171.18	3
15	1521.70	1503.69	1504.67	761.82	P	244.31	226.20	227.14	122.58	2
16					K	147.11	129.10	130.09	74.06	1

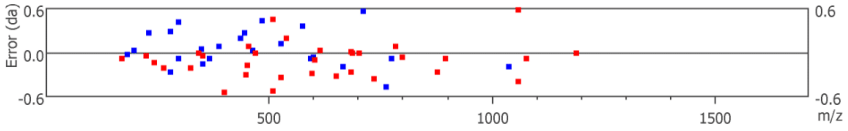

S6.B: peptide TPPAPKT(+79.97)PPSSGEPPKSGDR, mass 2081.9783

Annotated spectrum with alignment

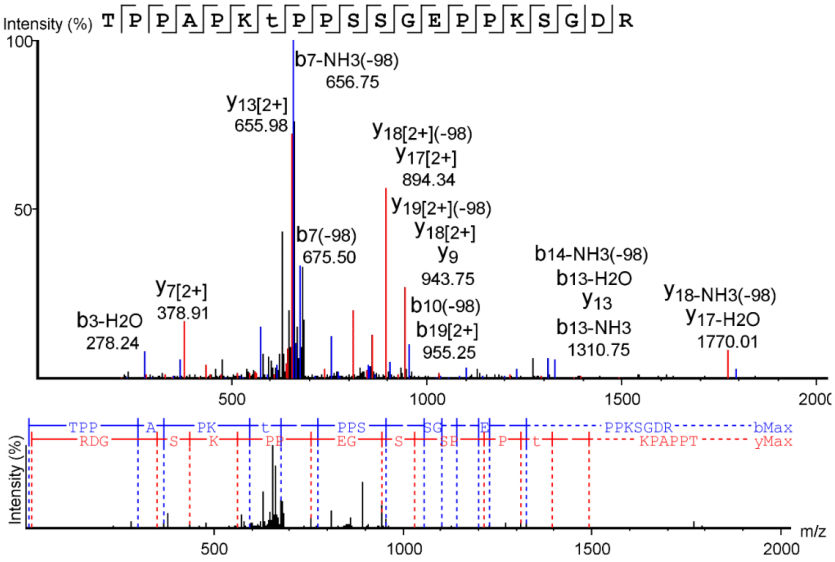

Ion table and mass error map

#	b	b-H2O	b-NH3	b (2+)	Seq	y	y-H2O	y-NH3	y (2+)	#
1	102.06	84.04	85.03	51.53	T					20
2	199.11	181.10	182.08	100.05	P	1981.94	1963.93	1964.91	991.47	19
3	296.32	278.24	279.13	148.58	P	1884.89	1866.87	1867.86	942.93	18
4	367.20	349.15	350.17	184.10	A	1787.83	1770.01	1770.81	894.34	17
5	464.25	446.24	447.22	232.18	P	1716.80	1698.78	1699.77	859.32	16
6	592.39	574.34	575.12	296.32	K	1619.74	1601.73	1602.72	810.23	15
7	773.47	754.96	756.48	387.18	T(+79.97)	1491.42	1473.64	1474.62	746.32	14
8	870.41	852.40	853.51	435.43	P	1310.75	1292.88	1293.61	655.98	13
9	967.47	949.45	950.44	484.26	P	1213.51	1195.57	1196.55	607.78	12
10	1054.85	1036.51	1037.47	527.35	S	1116.53	1098.52	1099.50	558.74	11
11	1141.56	1123.52	1124.50	571.26	S	1029.79	1011.49	1012.47	515.31	10
12	1198.76	1180.54	1181.52	599.78	G	942.93	924.45	925.41	472.03	9
13	1327.75	1309.73	1310.75	664.61	E	885.44	867.60	868.39	443.34	8
14	1424.65	1406.64	1407.62	712.82	P	756.48	738.22	739.80	378.91	7
15	1521.70	1503.69	1504.67	761.35	P	659.35	641.07	642.58	330.30	6
16	1649.79	1631.78	1632.77	825.40	K	562.49	544.28	545.00	281.99	5
17	1736.83	1718.82	1719.80	868.39	S	434.20	416.36	417.17	218.07	4
18	1793.85	1775.84	1776.82	897.42	G	347.27	329.16	330.30	174.08	3
19	1908.87	1890.86	1891.85	955.25	D	290.15	272.14	273.12	145.57	2
20					R	175.12	157.11	158.09	88.06	1

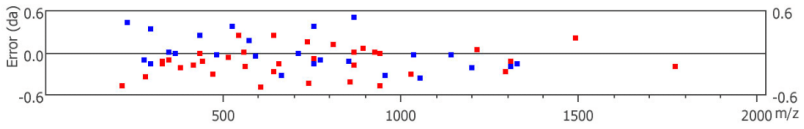

S6.C: peptide VAVVRT(+79.97)PPKSPSSAK, mass 1602.8494

Annotated spectrum with alignment

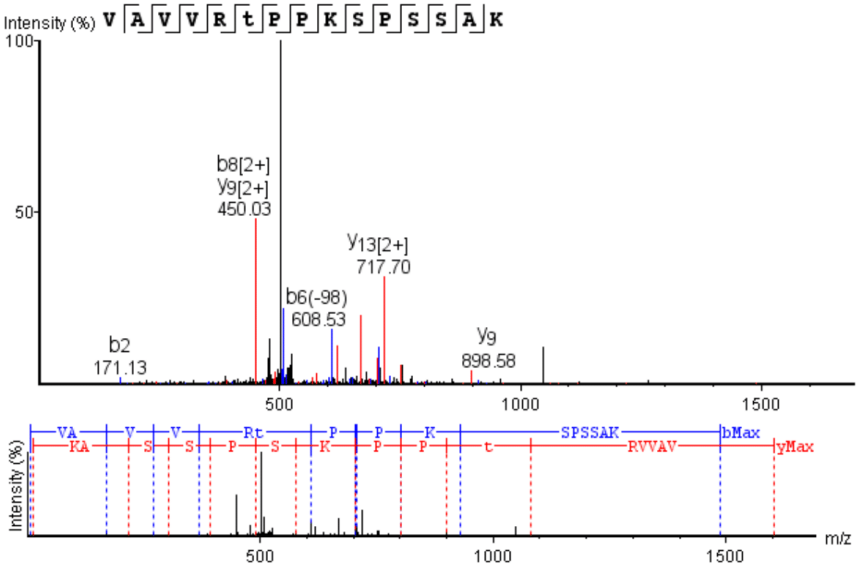

Ion table and mass error map

#	b	b-H2O	b-NH3	b (2+)	Seq	y	y-H2O	y-NH3	y (2+)	#
1	100.08	82.07	83.05	50.54	V					15
2	171.13	153.10	154.09	86.06	A	1504.79	1487.06	1487.76	752.91	14
3	270.07	252.32	253.15	135.59	V	1433.75	1415.74	1416.72	717.70	13
4	369.12	351.28	352.73	185.13	V	1334.68	1316.67	1317.66	668.38	12
5	525.35	506.76	508.04	263.18	R	1235.61	1217.60	1219.03	618.31	11
6	706.45	688.32	689.52	353.59	T(+79.97)	1079.67	1061.50	1062.49	540.50	10
7	803.42	785.78	786.62	402.21	P	898.58	880.72	881.47	450.03	9
8	900.47	882.46	883.44	451.07	P	801.51	783.58	784.42	401.53	8
9	1028.57	1010.56	1011.54	514.67	K	704.28	686.47	687.60	352.73	7
10	1115.60	1097.59	1098.57	558.46	S	576.48	558.46	559.27	288.73	6
11	1212.65	1194.64	1195.62	606.83	P	489.38	471.20	472.15	245.43	5
12	1299.68	1281.67	1282.66	650.40	S	392.20	374.20	375.43	196.22	4
13	1386.71	1368.70	1369.69	693.86	S	305.26	287.17	288.73	153.09	3
14	1457.75	1439.74	1440.72	729.59	A	218.20	200.14	201.12	109.57	2
15					K	147.11	129.10	130.09	74.06	1

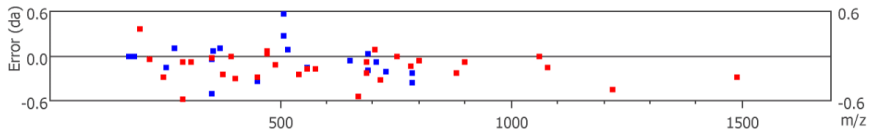

S6.D: peptide KVAVVRT(+79.97)PPKSPSSAK, mass 1730.9443

Annotated spectrum with alignment

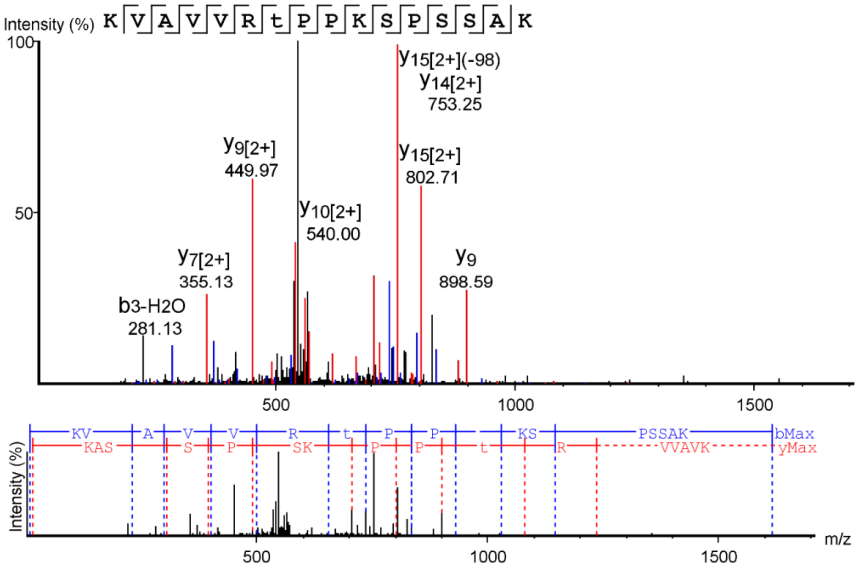

Ion table and mass error map

#	b	b-H2O	b-NH3	b (2+)	Seq	y	y-H2O	y-NH3	y (2+)	#
1	129.10	111.09	112.08	65.05	K					16
2	228.13	210.33	211.21	114.59	V	1603.86	1585.85	1586.83	802.71	15
3	299.30	281.13	282.18	150.10	A	1504.79	1486.78	1487.76	753.25	14
4	398.48	380.27	381.28	200.23	V	1433.75	1415.74	1416.72	717.26	13
5	497.36	479.33	480.01	248.96	V	1334.68	1316.67	1317.66	668.11	12
6	653.54	635.44	636.42	327.22	R	1235.89	1217.60	1218.59	618.78	11
7	834.54	816.45	817.56	418.05	T(+79.97)	1079.90	1062.08	1062.08	540.00	10
8	931.51	913.50	914.49	466.26	P	898.59	880.58	881.47	449.97	9
9	1028.58	1010.56	1011.85	514.78	P	801.39	783.48	784.49	401.26	8
10	1156.66	1138.65	1139.63	578.83	K	704.20	686.31	687.68	353.09	7
11	1243.69	1225.68	1226.67	622.03	S	576.30	558.52	559.49	288.65	6
12	1340.75	1322.73	1323.72	670.52	P	489.10	471.26	472.30	245.10	5
13	1427.78	1409.77	1410.75	714.39	S	392.37	374.46	375.21	197.16	4
14	1514.81	1496.80	1497.78	758.15	S	305.29	287.17	287.90	153.09	3
15	1585.85	1567.84	1568.82	793.60	A	218.15	200.23	201.24	109.57	2
16					K	147.11	129.10	130.09	74.06	1

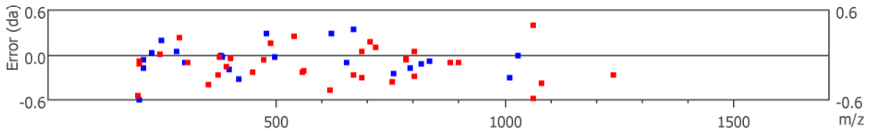

Figure S7: Annotated MS/MS spectra of phosphorylated Tau-X species derived from subcellular fractionation in fraction LP1 (see Table S2) by Orbitrap LC-MS and PEAKS software analysis.

S7.A: peptide SGYSSPGS(+79.97)PGTPGSR, mass 1472.5933

Annotated spectrum with alignment

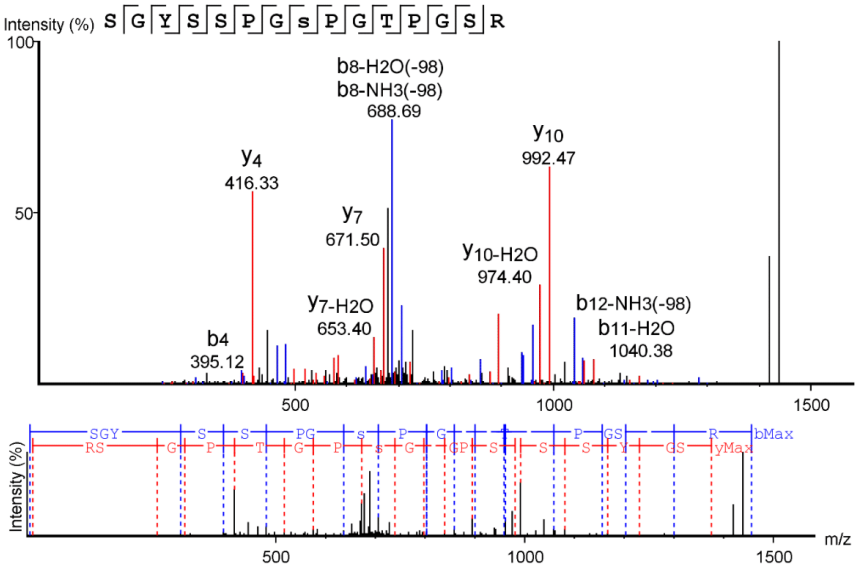

Ion table and mass error map

#	b	b-H2O	b-NH3	b (2+)	Seq	y	y-H2O	y-NH3	y (2+)	#
1	88.04	70.03	71.01	44.52	S					15
2	145.06	127.05	128.03	73.03	G	1386.57	1368.56	1369.54	693.74	14
3	308.07	290.23	291.10	154.56	Y	1329.55	1311.54	1312.52	665.70	13
4	395.12	377.24	378.13	198.08	S	1166.55	1148.45	1149.27	584.01	12
5	482.22	464.27	465.16	242.12	S	1079.52	1061.42	1062.42	540.45	11
6	579.24	561.23	561.98	290.23	P	992.47	974.40	975.39	496.86	10
7	636.25	618.42	619.24	319.07	G	895.37	877.49	878.34	448.18	9
8	803.29	784.90	786.58	402.13	S(+79.97)	838.45	820.53	821.60	419.30	8
9	899.93	882.30	883.08	451.18	P	671.50	653.40	654.32	336.17	7
10	957.42	939.15	939.97	478.67	G	574.75	556.40	557.27	287.35	6
11	1058.35	1040.38	1041.36	529.69	T	517.49	499.26	500.25	259.30	5
12	1155.53	1137.19	1137.82	578.22	P	416.33	398.24	399.20	208.61	4
13	1212.46	1194.57	1195.23	606.73	G	319.07	301.11	302.32	160.09	3
14	1299.60	1281.53	1282.46	650.20	S	262.07	244.11	245.36	131.58	2
15					R	175.12	157.11	158.09	88.06	1

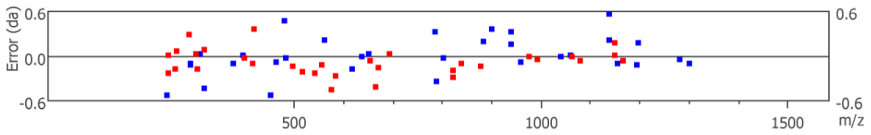

S7.B: peptide TPPAPKT(+79.97)PPSSGEPPK, mass 1666.7966

Annotated spectrum with alignment

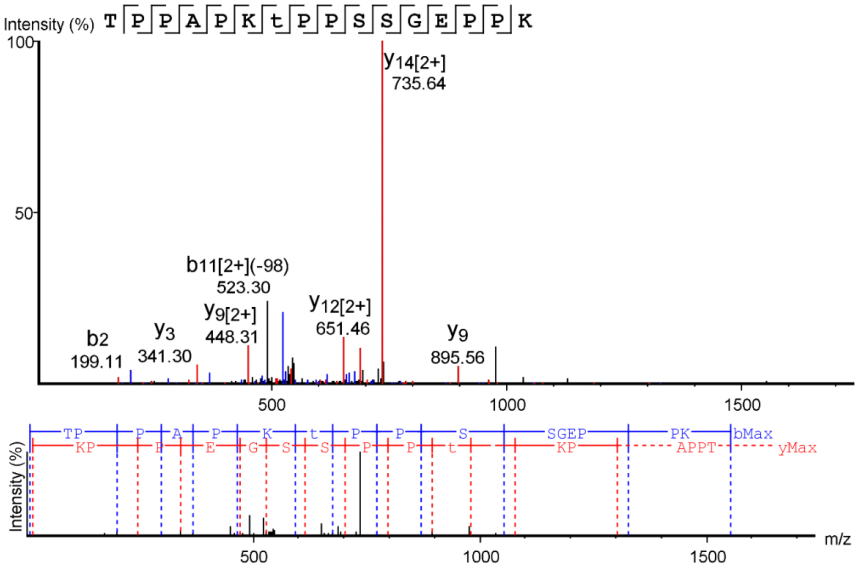

Ion table and mass error map

#	b	b-H2O	b-NH3	b (2+)	Seq	y	y-H2O	y-NH3	y (2+)	#
1	102.06	84.04	85.03	51.53	T					16
2	199.11	181.13	182.08	100.05	P	1566.76	1548.75	1549.73	783.43	15
3	296.24	278.32	279.13	148.58	P	1469.70	1451.69	1452.68	735.64	14
4	367.26	349.04	350.17	184.10	A	1372.65	1354.64	1355.62	686.77	13
5	463.90	446.24	447.22	232.22	P	1301.92	1283.60	1284.59	651.46	12
6	592.48	574.32	575.32	296.24	K	1204.56	1186.55	1187.53	602.51	11
7	773.54	755.46	756.33	387.18	T(+79.97)	1076.53	1058.60	1059.83	539.10	10
8	870.77	852.40	853.39	435.52	P	895.56	877.59	878.35	448.31	9
9	967.47	949.45	950.36	484.63	P	798.41	779.86	781.51	399.95	8
10	1054.55	1036.49	1037.47	527.56	S	701.62	683.34	684.32	351.46	7
11	1141.53	1123.52	1124.50	571.28	S	614.49	596.30	597.56	307.66	6
12	1198.55	1180.54	1181.52	600.17	G	527.56	508.93	509.91	264.14	5
13	1327.59	1309.58	1310.57	664.53	E	470.79	452.49	453.23	235.63	4
14	1424.65	1406.64	1407.62	713.09	P	341.30	323.32	324.19	171.12	3
15	1521.70	1503.69	1504.67	761.78	P	244.21	226.25	227.14	122.58	2
16					K	147.11	129.10	130.09	74.06	1

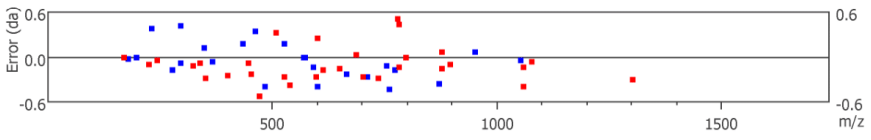

S7.C: peptide KVAVVRT(+79.97)PPKSPSSAK, mass 1730.9443

Annotated spectrum with alignment

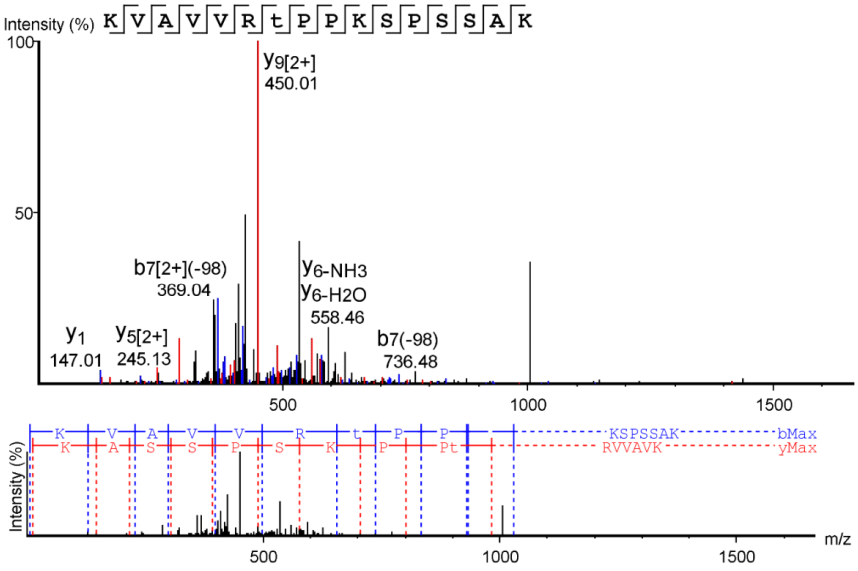

Ion table and mass error map

#	b	b-H2O	b-NH3	b (2+)	Seq	y	y-H2O	y-NH3	y (2+)	#
1	129.14	111.09	112.08	65.05	K					16
2	228.25	210.01	211.14	114.59	V	1603.86	1585.85	1586.83	802.32	15
3	299.36	281.20	282.27	150.10	A	1504.79	1486.78	1487.76	753.21	14
4	398.41	379.89	380.97	199.64	V	1433.75	1415.99	1416.72	717.89	13
5	497.29	478.75	480.34	249.19	V	1334.68	1316.67	1317.66	668.00	12
6	653.86	635.53	636.42	327.24	R	1235.61	1217.60	1218.59	618.65	11
7	834.51	816.45	817.65	418.11	T(+79.97)	1079.51	1061.50	1062.49	540.71	10
8	931.78	913.50	914.68	466.47	P	898.50	880.49	881.47	450.01	9
9	1028.77	1010.56	1011.54	514.92	P	801.59	783.44	785.01	401.55	8
10	1156.66	1138.51	1139.63	578.77	K	704.39	686.91	686.91	352.48	7
11	1243.69	1225.68	1226.67	622.62	S	576.45	558.46	559.75	288.87	6
12	1340.75	1322.73	1323.72	671.17	P	489.32	471.45	472.38	245.13	5
13	1427.78	1409.77	1410.75	714.43	S	392.22	374.29	375.44	196.61	4
14	1514.81	1496.80	1497.78	758.35	S	305.36	287.25	288.15	153.09	3
15	1585.85	1567.84	1568.82	793.42	A	218.16	200.44	201.12	109.57	2
16					K	147.01	129.14	130.05	74.06	1

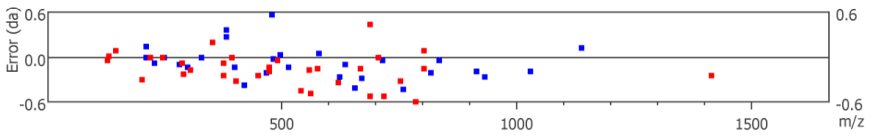

S7.D: peptide TPPAPKT(+79.97)PPSSGEPPKSGDR, mass 2081.9783

Annotated spectrum with alignment

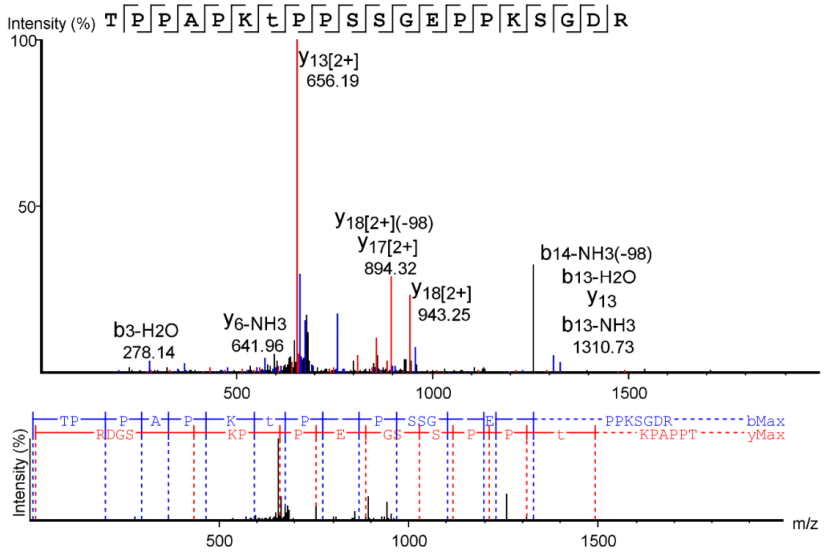

Ion table and mass error map

#	b	b-H2O	b-NH3	b (2+)	Seq	y	y-H2O	y-NH3	y (2+)	#
1	102.06	84.04	85.03	51.53	T					20
2	199.08	181.10	182.08	100.05	P	1981.94	1963.93	1964.91	991.67	19
3	296.38	278.14	279.13	148.58	P	1884.89	1866.87	1867.86	943.25	18
4	367.16	349.32	350.17	184.10	A	1787.83	1769.82	1770.81	894.32	17
5	464.54	446.78	446.78	232.63	P	1716.80	1698.78	1699.77	858.92	16
6	592.28	574.47	575.32	296.38	K	1619.74	1601.73	1602.72	810.09	15
7	773.32	755.61	756.63	387.18	T(+79.97)	1492.07	1473.75	1474.62	746.67	14
8	870.31	852.40	853.77	435.71	P	1310.73	1292.74	1293.60	656.19	13
9	967.06	949.25	950.44	483.69	P	1213.63	1195.66	1196.55	607.63	12
10	1054.50	1036.49	1037.47	528.34	S	1116.31	1098.52	1099.68	558.96	11
11	1141.53	1123.52	1124.50	570.99	S	1029.33	1011.27	1012.50	515.59	10
12	1198.63	1180.54	1181.82	599.79	G	942.46	924.99	924.99	471.29	9
13	1327.82	1309.52	1310.73	664.59	E	885.74	867.49	868.42	443.22	8
14	1424.65	1406.64	1407.62	712.82	P	756.63	738.55	739.67	378.70	7
15	1521.70	1503.69	1504.67	761.35	P	659.58	641.34	641.96	330.77	6
16	1649.79	1631.78	1632.77	825.40	K	562.29	544.75	544.75	281.38	5
17	1736.83	1718.82	1719.80	868.91	S	434.13	416.19	417.61	217.60	4
18	1793.85	1775.84	1776.82	897.27	G	347.17	329.11	330.14	174.08	3
19	1908.87	1890.86	1891.85	955.29	D	290.15	272.14	273.20	145.57	2
20					R	175.12	157.11	158.09	88.06	1

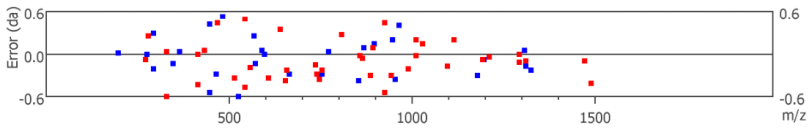

Publikation 3: Development of a calibration and standardization procedure for LA-ICP-MS using a conventional ink-jet printer for quantification of proteins in electro- and Western-blot assays

JAAS

PAPER

Development of a calibration and standardization procedure for LA-ICP-MS using a conventional ink-jet printer for quantification of proteins in electro- and Western-blot assays†

Simone Hoesl,‡[ad] Boris Neumann,‡*[bc] Sandra Techritz,[a] Michael Linscheid,[d] Franz Theuring,[c] Christian Scheler,[b] Norbert Jakubowski[a] and Larissa Mueller[a]

Cite this: *J. Anal. At. Spectrom.*, 2014, **29**, 1282

Received 13th February 2014
Accepted 2nd April 2014

DOI: 10.1039/c4ja00060a

www.rsc.org/jaas

We developed new procedures for internal standardization and calibration to be used for laser ablation inductively coupled plasma mass spectrometry (LA-ICP-MS) for elemental micro mapping imaging of biological samples like Western blot membranes and tissue sections. These procedures are based on printing of metal spiked inks onto the top of thin layer samples for simultaneous internal standardization and calibration of LA-ICP-MS. In the case of internal standardization the ink is spiked with indium as an internal standard and homogenously printed over the entire membrane (size 56 cm^2) prior to LA-ICP-MS detection, a standard deviation (RSD) value of 2% was achieved. In the second approach the metal content of lanthanide tagged proteins and antibodies after biological work flows was quantified by LA-ICP-MS on nitro-cellulose membranes. In this case the inks spiked with varying metals were printed with different densities on the same nitrocellulose membranes in well-defined squares to produce matrix-matched calibration standards. For validation and calibration the ink squares were excised and the specific metal content was measured by liquid ICP-MS after solubilization of the membrane slice. For the printed calibration standard limits of detection (LOD) of <4 fmol for different metals and relative process standard deviations of 1–2% only were determined *via* LA-ICP-MS.

1. Introduction

LA-ICP-MS is a technique for direct analysis with little or no additional sample preparation. Thus it looks promising for combinations with medical and biochemical workflows such as Western blot immunoassays or immuno-histological staining.[1] So far, endogenously incorporated metals, non-metals[2] and synthetic modifications in biological samples or proteins have been detected. LA-ICP-MS offers high sensitivity, spatial resolution in the µm range, large dynamic range (9 orders of magnitude)[3–5] and multi-elemental capability, which allows the detection of most elements of the periodic table.[6] However, it is still limited by the fact that so far no straightforward procedure is available – for internal standardization and quantification and by the lack of standards for calibration that additionally complicates the validation of the method.

In some most recent applications of clinical and biological relevance proteins are indirectly detected by biomolecular markers such as metal tagged antibodies. The first immunoassays using metal tagged antibodies in combination with LA-ICP-MS as the detection process were applied by Hutchinson *et al.*[7] and Müller *et al.*[8] These applications resulted in a fast improvement in sensitivity using numerous tagging reagents for detection of low abundance proteins. Concerning these reagents, the first use based on a linear chain chelate with ICP-MS detection was discussed by Zhang *et al.*[9] who applied a biotinylated monoclonal antibody conjugated with europium using SCN-DTTA (*N*′-(*p*-isothiocyanatobenzyl)-diethylenetriamine-*N*1,*N*2,*N*3,*N*3-tetraacetate-Eu^{3+}) as a chelating compound. This approach enables the analysis of complex serum samples in a multiplex assay. More recently, Waentig *et al.* established a labelling technique for primary antibodies by using *p*-SCN-Bn-DOTA (2-(4-isothiocyanatobenzyl)-1,4,7,10-tetraazacyclod-odecane-1,4,7,10-tetraacetic acid)[10,11] for studying the chemical induced expression of cytochrome P450 (CYP) in multiplex Western blot immunoassays.[12] A similar principle was also used by de Bang *et al.* for analyzing multiple plant proteins in a

[a]*BAM Federal Institute for Materials Research and Testing, Richard-Willstaetter-Str. 11, 12489 Berlin, Germany. E-mail: simone.hoesl@bam.de*

[b]*Proteome Factory AG, Magnusstraße 11, 12489 Berlin, Germany. E-mail: neumann@proteomefactory.com; Fax: +49 (0)30 2061 6267; Tel: +49 (0)30 2061 6265*

[c]*Charité-Universitätmedizin Berlin, Institute of Pharmacology, Hessische Straße 3-4, 10115 Berlin, Germany*

[d]*Humboldt Universität zu Berlin, Department of Chemistry, Brook-Taylor-Straße 2, 12489 Berlin, Germany*

† Electronic supplementary information (ESI) available. See DOI: 10.1039/c4ja00060a

‡ These authors contributed equally to this work.

Western blot immunoassay.[13] To improve sensitivity a novel polymer-based elemental tagging kit was developed by Lou *et al.*[14] which is used to tag various antibodies for detection of leukemia cells. Currently, a commercially available tagging reagent for proteins called MeCAT (metal coded tag)[15,16] was optimized for the tagging of antibodies and successfully applied in LA-ICP-MS based Western blot immunoassays.[17]

Presently, LA-ICP-MS detection is mainly used as a qualitative imaging method. The development of suitable calibration standards, internal standards for standardization and improvement of reproducibility and accuracy are still under investigation.[6] In liquid analysis the internal standard is used for calibration and thus is required to have similar physical and chemical properties to the analyte during the nebulization process, transport, ionization and transmission into the ICP-MS. In laser ablation it should correct for differences in the ablation process due to laser instabilities or changes of sample properties by compensating variations or drift effects during the LA process.[18]

For internal standardization elements such as ^{13}C in NC membranes,[19] iodination of intact proteins[20] or gold deposition on sample surfaces[21] are used for signal normalization but cannot be used for the development of quantification schemes.

Several calibration methods are described in the literature. Matrix matched in-house standards are used in order to account for matrix effects as well as variations in ablated and transported mass, and instrumental drift.[22] Examples are given for metal spiked homogenized tissue,[23,24] cellulose or pellets[25] and external on-line solution-based standardization was also used for calibration.[26,27]

Various normalization approaches and quantification strategies addressing these critical properties are described in detail in the reviews from Konz *et al.*[18] and Hare *et al.*[6]

Feldmann *et al.*[28] used an ink jet pattern to optimize the wash out of a laser ablation cell for detection of hetero-elements in proteins blotted onto the membrane by LA-ICP-MS while Bellis *et al.*[29] used commercial inks with ordinary copper content as a reference for biological samples in LA-ICP-MS.

In the study we employed first proof-of-principle experiments to investigate a new approach using inks, which are spiked with different elements, printed onto the top of a sample for internal standardization and calibration in LA-ICP-MS. Two different types of inks were spiked with characteristic metal contents. The first set of ink contains indium as an internal standard whereas the second ink contains multiple lanthanide metals for calibration of metal tagged proteins and antibodies detected by LA-ICP-MS. The approach was tested in a model investigation using proteins separated by SDS-PAGE and electro-blotted onto a NC membrane.

2. Experimental

2.1. Chemicals

All solutions were prepared using ultrapure water (Milli-Q water purification system, Millipore, Bedford, MA). The following chemicals were used: indium standard (CertiPUR, Merck Millipore, Darmstadt, Germany); multi lanthanide standard and erbium (Er) and praseodymium (Pr) standard (Alfa Aesar, Karlsruhe, Germany); printer ink (Proteome Factory AG, Germany); MeCAT kit loaded with erbium, praseodymium (Proteome Factory, Berlin, Germany); Bradford reagent (Proteome Factory, Berlin, Germany), tris(hydroxymethyl)aminomethane (Tris), Tween 20, acrylamide solution (30%), 1,4-dithio-DL-threitol (DTT) (all from Applichem, Darmstadt, Germany); glycerol, HNO_3 ultra-pure, sodium dodecyl sulfate (SDS) (ROTH, Karlsruhe, Germany); tris(2-carboxylethyl)phosphine·HCl (TCEP) (PIERCE, Thermo Fisher Scientific, Schwerte, Germany).

2.2. Proteins and antibodies

Lysozyme from chicken egg, bovine serum albumin (BSA), and ovalbumin from chicken egg were supplied from Sigma Aldrich (Taufkirchen, Germany). The polyclonal antibody rabbit anti-chicken lysozyme was purchased from Dunn Labortechnik (Asbach, Germany).

2.3. Protein determination

The concentrations of tagged proteins were determined by a micro plate spectrophotometer Spectramax Plus 384 (Molecular Devices, Sunnyvale, USA) using the Bradford assay.[30] External calibration was carried out at an absorption maximum at 595 nm by using a dilution series of bovine serum albumin (Sigma Aldrich, Taufkirchen, Germany).

2.4. Antibody tagging *via* MeCAT (metal coded tag)

A detailed description of the antibody tagging procedure is given in ref. 17. For our investigation we have chosen MeCAT (Pr) (Proteome Factory, Berlin) for tagging of the anti-lysozyme antibody. Briefly, the tagging method started with a partial reduction of the antibody with a molar excess rate of 600 of TCEP relative to antibody molarity for 30 min at 37 °C. After purification by ultra-filtration at 7500 × *g* of the partially reduced antibody the modification was made using a 20 fold molar excess of MeCAT (Pr) (Proteome Factory AG, Berlin) which was agitated for 60 min at 37 °C. After reaction the MeCAT excess was removed from the antibody solution by ultra-filtration as described above.

2.5. Protein tagging *via* MeCAT

The model proteins (lysozyme, BSA, ovalbumin) were tagged with MeCAT (Er) (Proteome Factory, Berlin) reagent. The tagging was performed similar to the previously utilized antibody tagging protocol (see Section 2.4).

2.6. Sodium dodecyl sulfate polyacrylamide gel electrophoresis

Sodium Dodecyl Sulfate Polyacrylamide Gel Electrophoresis (SDS-PAGE) was carried out for the standard proteins on a miniVE electrophoresis (Amersham Biosciences, Freiburg, Germany). The separation took place according to the protocol of Laemmli[31] by using a 6% (w/v) stacking gel and a 10% (w/v) separation gel (70 mm × 80 mm, layer thickness 0.75 mm). Standard protein samples were denatured with 0.15% (w/v) DTT

and dissolved in a 1 : 1 ratio with Laemmli sample buffer. Subsequently the samples were heated for 5 min to 95 °C prior to loading the gel (10 μL). Electrophoresis conditions were as follows: a constant current of 32 mA with a maximum of 150 V was used for sample separation until the Laemmli sample buffer's bromophenol blue color marker reached the end of the gel.

2.7. Semi-dry blotting

After separation *via* SDS-PAGE the proteins were transferred to a NC blot membrane[32] by semi-dry electro-blotting using the Nova blotting unit from GE Healthcare (München, Germany). Proteins were transferred onto "Protan"-nitrocellulose membranes (NC) (Whatmann GmbH, Dassel, Germany) with a pore-size of 0.45 μm. The blotting was performed using a current of 0.8 mA per cm^2 blot area for 1 h at room temperature.

2.8. Western blot immunoassay

Directly after electro-blotting the NC membranes were washed for 10 min with TBS-T (20 mM Tris–HCl, pH 7.3, 150 mM NaCl, 0.1% Tween 20). Following the washing process, the blots were incubated overnight with blocking solution (TBS-T, 5% (w/v) gelatin) followed by three washing steps with TBS-T for 10 min each. The blot membrane was incubated for 2 h with the tagged antibody diluted in TBS-T at a concentration of 0.5 μg mL^{-1}. Unbound antibodies were removed by washing 5 times for 10 min each with TBS-T. Subsequently, the membrane was dried in air for detection by LA-ICP-MS.

2.9. Printing with spiked custom ink

Spiked inks were produced on request by Proteome Factory AG. Two different inks were produced – Ink I: Laser Ablation-Indium ink (LA-In-ink: 4 mg In per L) contained yellow ink with In as an internal standard and Ink II: multi-lanthanide ink (LA-multi-Ln-ink: 50 mg Ln per L) contained yellow ink with Pr and Er. The spiked inks were filled into empty printer cartridges and 10 DIN A4-pages of a color test print were made to equilibrate the printing system. Printing on an NC membrane was performed with a conventional ink jet printer (Pixma iP4950, Canon, Krefeld, Germany). Settings for regular paper were selected and color management was disabled. The calibration standard series was printed first and overlaid by the internal standard ink after electroblotting of PAGE separated proteins on NC membranes.

2.10. LA-ICP-MS detection

A commercial LA system (New Wave 213, ESI, Portland, USA) with a beam expander and laser spot sizes between 4 μm and 250 μm was attached to an ICP sector field mass spectrometer (Element XR, Thermo Fisher Scientific, Germany). The ICP-MS was synchronized with the LA unit in an external triggering mode. The NC membranes were fixed on a sample holder and inserted into the two volume cell. The aerosol was transported by helium at a flow rate of 1 L min^{-1} and argon was added at a flow rate of 0.8 L min^{-1} in front of the ICP torch. The LA-ICP-MS was tuned daily for maximum ion intensity on a microscopic glass slide as a standard tuning for the ablation by the oxide ratio ((ThO/Th) <5%). Samples were ablated line by line under optimized LA-ICP-MS conditions as summarized in Table S1 (ESI).† The isotopes ^{115}In, ^{166}Er and ^{141}Pr were selected for analysis. The whole area of the membrane was ablated continuously by line scans with a spot size of 200 μm, a scan speed of 200 μm s^{-1} and an overlap of 180 μm between the lanes. The laser spot size and scan speed were adapted to provide optimal ablation.

For the application of the developed printing standardization the sample must have had the same size based on the surface. Standardization is only possible under the same laser ablation conditions. The acquired LA-ICP-MS data were exported with a custom Matlab (MathWorks, USA) based application into Origin 8 (Originlab Corporations, Northhampton, USA) where intensity time profiles or color coded images were produced by transforming the scan time into a micrometer scale. Signal intensities were color coded with low intensities shown in blue and high intensities in red color. Raw data normalization was performed in Excel (Microsoft, Redmond, USA).

2.11. ICP-MS of liquid samples

2.11.1. Degree of metal tagging of proteins. The determination of the tagging degree was done according to Waentig *et al.*[17] In short, the samples were desalted and their protein content was determined by the Bradford assay. The content of metal bound to the protein was determined by liquid ICP-MS.

2.11.2. Printing of the internal standard. For internal standardization LA-indium (Ink I) ink was used. The ink was printed with a printing density of 20% over the entire NC membrane (56 cm^2) which is a good compromise between color intensity of the LA-indium ink and light absorbance of the thin layer in the LA process. For comparing and testing the ink homogeneity four membrane spots of 0.5 cm^2 each at different positions on the membrane were excised after drying of the ink. Subsequently the membrane slices were dissolved with 1 mL 69% HNO_3. The samples were diluted in a 1 : 100 ratio using 50 ng L^{-1} Pr in 3.5% HNO_3 as the internal standard for solution analysis. A sample volume of 1 mL was prepared for relative quantification *via* liquid ICP-MS. For this purpose the Element XR (Thermo Fisher Scientific, Bremen, Germany) was connected to a MicroMist nebulizer with a Twinnabar cyclonic spray chamber (Glass Expansion, Melbourne, Australia) using a nebulizer gas flow rate of 1.0 L min^{-1} Ar.

2.11.3. Printed calibration standards. For internal calibration a dilution series was produced by changing the printing density (10–60%) of the LA-multi-ink (Ink II 50 mg L^{-1}) containing the metals Er and Pr. Three squares 3 by 3 mm each were printed onto the same NC membrane next to the area onto which the proteins are electro-blotted (matrix matching) in a first step. For using these calibration standards the metal content has to be measured separately. Therefore, the same set of squares was printed onto a second membrane. They were excised and dissolved by 1 mL 69% HNO_3 and diluted in a

1 : 100 ratio using 3.5% HNO_3 including additional 50 ng L^{-1} indium as the internal standard. For external calibration a series from 100 pg L^{-1} to 1 µg L^{-1} was prepared using a multi element standard solution (^{166}Er, ^{141}Pr; 500 mg L^{-1}). This procedure can be used for absolute quantification in unit areas if the standards are fully ablated. The detection was carried out as described above (2.11.2).

2.11.4. Western blot immunoassay. After the immunological reaction of the MeCAT tagged antibody with its respective antigen (anti-lysozyme and lysozyme) the protein bands were reversibly stained using Ponceau S.[33] The visualized bands of about 1 cm^2 were excised and solubilized in a way similar to the internal standard series slices and quantified *via* liquid ICP-MS (see 2.11.3) for validation.

3. Results and discussion

In this work standardization and calibration protocols were developed for an application in LA-ICP-MS imaging of biological samples such as Western blot membranes, microarrays or thin tissue sections. The common point of these samples was that the element of interest was distributed in a very thin layer and was completely ablated by laser rastering or line scanning in the first run. Either, only under these conditions quantification of the metal tagged biomolecules was simplified and becomes independent of the ablated laser volume and material density, or the standards used should be matrix matched, present in a thin layer as well and analyzed under the same conditions. These test samples were analyzed by proof-of-principle experiments.

Therefore metal spiked inks (Ink I/II) were applied onto the previously evaluated matrix of NC membranes with a conventional ink-jet printer. To show that application of an internal standard and calibration series was adequate for LA-ICP-MS analysis, all experiments were validated by liquid ICP-MS in parallel. Fig. 1 and 2 show the sample preparation sequence. The evaluation of the novel calibration standard was performed by two approaches: direct *versus* indirect detection.

The direct approach was applied for all types of metals present in proteins on blot membranes, micro-arrays and in tissue sections. To simulate the metal containing biomolecules the direct detection was tested by using a metal tagged protein. For this purpose we have tagged bovine serum albumin, ovalbumin and lysozyme with Er as model proteins. These samples were loaded into the wells of lane A and separated by the gel electrophoresis process (illustrated in Fig. 1-1, lane "A").

For the indirect approach representing all types of immunoassays the model protein lysozyme was detected in an immunoassay using a Pr tagged antibody. For this purpose lysozyme was loaded into well B and separated in the same run with the proteins of lane A (see Fig. 1, lane "B").

Fig. 1 illustrates the biochemical work-flow with the initial step of SDS-PAGE protein separation of the mixture of model proteins for the direct approach and lysozyme for the indirect approach in separate lanes. In the second step (Fig. 1-2) the separated proteins were electro-blotted onto the NC membrane to produce a thin protein layer. Subsequently the immobilized proteins on the NC membrane were incubated with a praseodymium tagged antibody in an immunoassay (see Fig. 1-3). This reaction resulted in the final membrane containing 3 metal tagged proteins and one immobilized protein–antibody conjugate on the same membrane. This test sample was used to investigate both the standardization and the calibration concept.

The preparation of the calibration standards is discussed in Fig. 2. For this purpose the metal spiked ink containing erbium was printed in a protein free section of the membrane with different densities (10–60%) to be used again as a dilution series. The intention of this series was the quantification of the

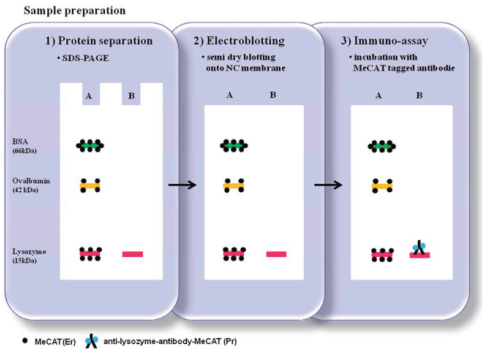

Fig. 1 Schematic workflow of the Western blot immunoassay: on the left (1): the protein separation scheme with its two sample lane tagged proteins (lane A) and an unmodified protein (lane B) suitable as antigens; in the middle (2): electro-blotting; right (3): scheme of the immunoreaction between tagged antibodies and its respective antigens.

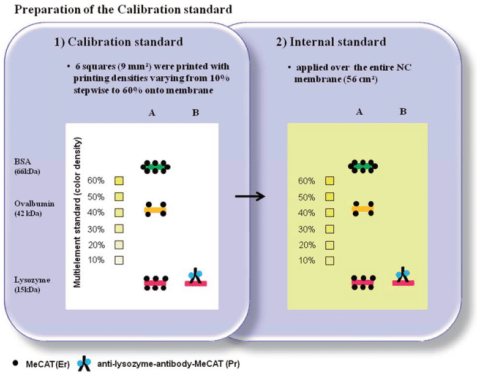

Fig. 2 Scheme of calibration (1) and internal standardization (2). For the proof of principle experiment proteins are electro blotted onto a membrane. After immunoreaction a series of calibration standards (1) are printed with Ink II in squares with varying printing densities. In the second step (2) the internal standard is printed with Ink I at 20% density over the entire membrane (marked as the yellow area).

metal tagged proteins in lane A (Er tagged). Additionally this ink contained a second metal Pr which was used as a calibration standard for quantification of the immunoassay based on the Pr tagged anti-lysozyme antibody. Regarding the internal standard, after drying of the calibration ink (Ink II) series an internal standard was applied by printing indium (Ink I) spiked ink over the entire membrane (yellow color in Fig. 2-2). Thus the final sample (Fig. 2-2) was investigated by LA-ICP-MS containing three metal-tagged proteins simulating metal-containing molecules (lane A), and a single metal immunoassay (lane B). For both types of samples a calibration series coded by the elements Er and Pr (yellow color series left hand side of lane A in Fig. 2-1) was used for quantification. Additionally indium was printed as an internal standard (yellow color in Fig. 2-2) covering the entire membrane.

For application of the printing procedure for standardization and calibration the following prerequisite had to be fulfilled; the calibration standard and the analyte sample must have the same size based on the surface and needed complete ablation in just one run. Standardization and calibration was possible under the same working conditions (laser energy density, laser spot size and scan speed) for laser ablation of standards (calibration standard, internal standard) and analyte (metal-tagged proteins and metal-tagged antibody), which was fulfilled because all samples were located on the single NC membrane and measured simultaneously in one run. A perfect matrix matching and mixing of standard elements with analyte tagging elements in the laser aerosol were achieved due to the fact that the thickness of the printed element standards and the analytes on the membrane was small compared to the ablated volume (and depth) of the membrane material.

3.1. Internal standard

For proof-of-principle experiments, metal spiked inks were printed onto the matrix of NC membranes with a conventional ink-jet printer in accordance to Fig. 2, but without blotted proteins on the surface. In the first set of preliminary studies the printing process and the internal standard concept were evaluated whereas in the second set of investigations the calibration and quantification concepts were analyzed in more detail. Most results achieved were validated by liquid ICP-MS in parallel processed samples.

3.1.1. Influence of the ink matrix on laser absorption. As a prerequisite, it has to be shown that the Ink I which was used to print the internal standard over the entire membrane was as transparent as possible for the UV light of the laser. For evaluation the absorption spectra (not shown) of the ink were determined as follows. The ink was diluted to a similar concentration as detected during LA-ICP-MS. The absorption spectrum was recorded using a Cary Bio 100 absorption spectrometer (Varian, USA) with water as the reference indicating that the ink pigmentation did not significantly affect the absorption of the laser's energy.

3.1.2. Homogeneity and reproducibility of ink printing on membranes. To look at homogeneity, the distribution of the internal standard over a large area must fulfill at least two requirements: sufficient macro-homogeneity over the printed whole area and micro-local homogeneity down to the diameter of the laser ablation spot size.

Concerning macro-homogeneity, the content of the indium layer printed on membranes was determined by analyzing four membrane slices (size: 1 cm^2) each taken from a different area of the NC membrane. The slices were weighed and solubilized in HNO_3. The samples were diluted with 3.5% HNO_3 containing 50 ng L^{-1} Pr as an internal standard for quantification *via* liquid ICP-MS. The results of ICP-MS detection are shown in the ESI (ESI†, Table S2). The normalized In signal relative to the weight of the sampled membrane slice exhibited a relative standard deviation of only 5%, which also included weighing errors which was the main source of deviations in this experiment. In the previous experiment it was not clear as to which portion of the RSD was related to the printing process on the NC membrane and to ICP-MS detection of the dissolved ink membrane slices. Thus homogeneity had to be analyzed by the short term stability of LA signals, which was a measure of the LA stability and of the inks' homogeneity. For this purpose six identical squares of 1 mm^2 size were printed on NC membranes using Indium spiked ink to illustrate the reproducibility of the printing technique even for small areas or acquisition points. The printed squares were entirely ablated and detected *via* LA-ICP-MS. This experiment revealed an excellent RSD of 2% (see also ESI,† Fig. S1 and Table S3), which demonstrated good short term stability of the laser ablation process and sufficient reproducibility of the printing process. The homogenous distribution was further ascertained on a micro-scale, because the size of the individual ink pixels (15 μm) was far below the laser spot diameter (180 μm laser crater diameter – not shown here).

3.1.3. Compensation of drift effects by use of a printed internal standard. It was demonstrated that homogeneity is sufficient at micro- and macro-scales. Another experiment was performed to demonstrate the compensation of intensity drift effects during an extended laser ablation measurement. Laser ablation experiments of large-scale samples can be time-consuming depending on the laser spot size, scan speed and the ablated area. The ablation of an area of 100 mm × 100 mm which is a common size for blot membranes takes 5 hours for 180 μm laser diameters. Therefore, signal stability over an extended time is an important issue. An example is given in Fig. 3 showing the change in LA-ICP-MS detected intensity over time of a NC membrane homogenously printed with indium containing ink (laser spot size 180 μm). The signal intensities measured in a line scan when the instrument has just started operating (morning) looked very noisy which is expressed in an RSD of 15%, it improved with time, a few hours later (afternoon) to an RSD of 13%, demonstrating that the laser needed a few hours to stabilize. In the over-night experiment a drift effect was observed (which might be related to a change of temperature in the lab) and the RSD increased to 18%. These long term deviations of more than 10% of the original intensity emphasize the need for an internal standard to compensate instrumental drifts caused during the measurement.

The application of the printed internal standard is shown in Fig. 4. For this purpose a number of 5 squares each of 9 mm^2

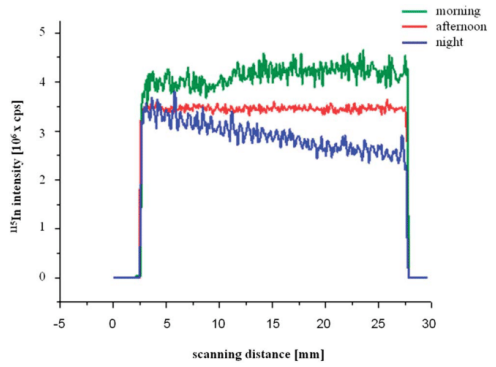

Fig. 3 The diagram shows the indium intensity measured per laser ablation line scan during a day. Green was the intensity after acquisition start; red after 4 h, and blue was the signal 12 h after the start of the instrument. Laser parameters: laser spot size 180 μm, repetition rate 20 Hz, and laser energy 0.20–0.25 mJ.

area (similar to typical protein spot sizes) were printed using a Pr containing ink (Ink II) to simulate an analytical element of interest directly onto NC membranes by changing the printing density stepwise. For internal standardization the squares of selected density were dried and an indium spiked ink (Ink I) was printed all over the entire membrane as an internal standard. The acquired LA-ICP-MS data of the printed membrane were normalized by calculating an average intensity of In for the entire indium covered area. Each indium signal intensity of the matrix was normalized to the In average of the signal intensity (matrix) (In [cps]/$\overline{\text{In}}$ [cps]). The new resulting normalized indium signal intensities (matrix) fluctuates around the value 1. Subsequently the initial praseodymium (Pr) signal intensity (matrix) was divided by the calculated indium matrix which is illustrated in Fig. 4(B) (Pr [cps]/In [cps]/$\overline{\text{In}}$ [cps]).

The image of the initial Pr signals measured for the analyte exhibited a gradient with the highest intensities on the left side of the squares (see Fig. 4(A), on the left), which hints

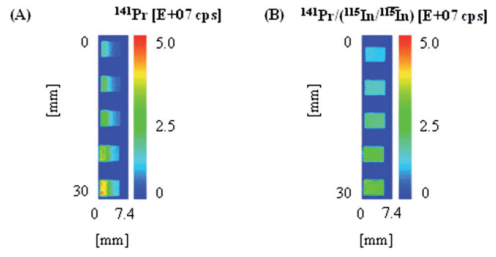

Fig. 4 Images of 5 squares printed onto the NC membrane with an internal standard (Ink I). (A) illustrates the initial signal of Pr and (B) the In normalized praseodymium intensity profile. Laser parameters: laser spot size 180 μm, laser scan speed 200 μm s^{-1}, repetition rate 20 Hz, laser energy 0.20–0.25 mJ, and detection time 2.5 h.

fluctuations in the detection system. After correction by the internal standard a homogenous distribution was calculated (shown in part B of Fig. 4), which clearly demonstrated the successful normalization by the internal standard for all squares measured.

3.2. Development of a calibration method

In the previous experiments it was shown that ink jet printing was reproducible, homogenous and thus looks promising for internal standardization. The following experiments showed how this technology was applied for calibration of metal containing proteins in Western blot assays as well.

3.2.1. Determination of linearity of the printed calibration standard by LA-ICP-MS. To calibrate Western blot assays, the calibration graph was plotted by using a dilution series of the original ink. This was done by changing the printing density of the color over a given dynamic range which depends on the content of the analyte element in the sample. This graph should be linear, have adequate limits of detection and good accuracy for the analyte element of interest. For matrix matching the calibration standard was printed on a different section of the same membrane (see also Fig. 2). However, as a prerequisite to our custom-made calibration standard method the metal content of the printed area must be determined by liquid ICP-MS. The analyte intensity measured in a protein spot can then be converted directly to an absolute amount of metal in the spot area. Due to the fact that we are interested in measuring different metal-tagged proteins or antibodies simultaneously, our calibration procedure can be applied simultaneously in a multiplex or multi-parametric assay as well.

Before starting with a complex sample as it is discussed in Fig. 1 and 2 the linearity of a dilution series was investigated using an ink (Ink II) spiked with a lanthanide mixture containing Er and Pr (50 mg L^{-1}). These elements were selected for detection of tagged proteins and antibodies (see Fig. 2). The multi-lanthanide ink (Ink II: 50 mg Ln per L^{-1}) was introduced into a different container of the printer (placeholder for cyan colored ink).

A number of 6 ($N = 6$) squares each of 9 mm^2 area (similar to typical protein spot sizes) were printed directly onto NC membranes by changing the printing density stepwise from 10% to 60%. This range was determined as the linear dynamic range in initial experiments (data not shown).

For internal standardization the squares of selected density were dried and reapplied into the printer to apply indium spiked ink *via* the yellow channel of the printer over the entire membrane as an internal standard. The complete area of printing was ablated in total and the acquired data were integrated and normalized to the internal standard indium.

The results are compiled in Fig. 5 where the ratios of the element of interest (Er and Pr) normalized to the internal standard In are shown for the ink of 50 mg L^{-1} concentration. Surprisingly high normalized intensities in the range 10^6 to 10^7 cps were measured for both elements. Calibration graphs were calculated from the intensity ratios (see ESI,† Fig. S3). Tight linear correlation between printing density and the peak area

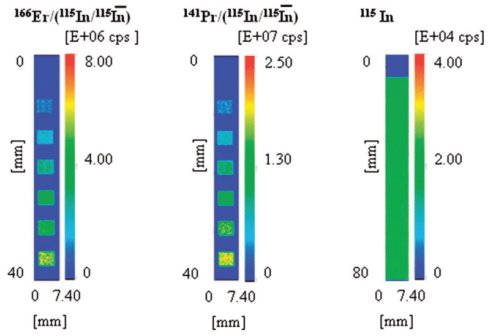

Fig. 5 Normalized intensity profiles of the printed NC membrane with the Ink II concentration (^{166}Er and ^{141}Pr) 50 mg L^{-1} and In Ink I (4 mg L^{-1}) as the internal standard. The data of the three images are generated from the same ablated area. Laser parameters: laser spot size 180 µm, repetition rate 20 Hz, laser energy 0.20–0.25 mJ. $\overline{\text{In}}$: indium average intensity of the indium matrix.

(R^2 for 50 mg L^{-1}: ^{166}Er 0.9987 and ^{141}Pr 0.9980) was achieved for the tested density range from 10 to 60% which is a prerequisite for calibration done by application of an ink (Ink II) dilution series in a simple way.

3.2.2. Analytical figures of merit of the calibration procedure. In the second step the metal concentration in the printed squares had to be determined in order to convert measured laser ablation ion intensities into an absolute amount of metal being present in the given surface area. For this purpose the absolute amount of lanthanides was measured in the printed calibration standard using two squares ($N = 2$) of printing density 10–60% for 50 mg L^{-1} ink each printed in the previous experiment on the same membrane, but without overprinting with the indium containing ink. These squares were cut out and solubilized in 69% HNO_3. The resulting solutions were diluted with 3.5% HNO_3 containing indium and subjected to liquid ICP-MS to be quantified with an external calibration series. The results of the liquid ICP-MS showed a linear relationship similar to LA-ICP-MS data described in Section 3.3.1. As for the LA-ICP-MS analysis the coefficient of correlation was greater than 0.99 for the detected elements (see Table 1).

To summarize, single analysis of the printed calibration standards (^{166}Er, ^{141}Pr; 50 mg L^{-1} each) *via* LA-ICP-MS (3.3.2) and the analysis *via* liquid ICP-MS (3.3.1) were combined in order to develop a calibration method for Western blot immunoassays. This combination resulted in a calibration curve consisting of LA-ICP-MS data [counts] on the abscissa and the respective data determined by liquid ICP-MS [pmol] on the ordinate (see Fig. S4 in ESI†). By changing the printing density we were able to simply cover one order of magnitude of the calibration graph with convincing linearity in a dilution series. The absolute amount of metal in the squares ranged from a low range of 40 to 200 fmol. All analytical results from the calibration graph are summarized in Table 1. The slope of the calibration graph is very high and amounts to 1.5×10^8 and 3.4×10^8 counts per pmol for ^{166}Er and ^{141}Pr, respectively.

Table 1 Linearity and calibration data for the printed calibration standards containing 50 mg L^{-1} erbium and praseodymium

50 mg L^{-1} ink	^{166}Er	^{141}Pr
Slope [counts/pmol]	1.48×10^8	3.35×10^8
y-Interception [counts]	-1.91×10^6	-6.24×10^6
Coeff. of determination	0.99987	0.99959
y-Standard deviation [counts]	7.47×10^4	4.05×10^5
Procedure standard deviation [fmol]	0.50	1.21
Relative process standard deviation [%]	1	1
Detection limit (LOD) [fmol]	1.50	3.6

Beside the coefficients of correlation – which were all greater or equal than 0.999 – the limit of detection (LOD), the relative standard deviation of the procedure and the procedure's standard deviation as a proof for the method's stability were calculated (calculated with respect to ref. 34). The values for the relative standard deviation of the procedure were better or equal to 1% which recommends the method for quantification. Absolute LOD of greater than 4 fmol could be calculated for both elements. For a protein carrying a single metal tag with an assumed molecular weight of 50 kDa the absolute LOD would be 0.2 ng.

The statistical data and the low detection limit of the new printing approach are very promising for application of metal tag quantification due to its simplicity and applicability in conventional bio-chemical and immunological workflows, which will be demonstrated in the next section.

3.3. Application of the printed standard for protein quantification

In this chapter all previously developed strategies were applied in just a single assay (see also Fig. 1 and 2). For this purpose a special test sample was designed to demonstrate the applicability of both, the concept of an internal standard and the calibration procedure discussed in the previous section. The evaluation of the calibration approach was tested for two different applications: direct *versus* indirect protein detection. For the direct approach a set of three metal tagged proteins of different molecular weights were prepared and the tagging degrees were determined.

3.3.1. Determination of the tagging degree. Concerning metal tagging, we used a protocol developed by Waentig *et al.*[17] for MeCAT modification of antibodies under physiological conditions. The reactive maleimide group of the reagent binds to free sulfhydryl residues of cysteines. To generate these, the disulfide bridges of the protein/antibody are partially reduced. For our experiment three proteins (BSA, ovalbumin and lysozyme) were selected for partial MeCAT modification of covering a molecular weight range from 21 kDa to about 100 kDa and a number of cysteines from 6 to 35. After cysteine directed modification of three proteins with MeCAT (Er) each of the proteins was purified and separated from an excess of reagent by ultra-filtration. The degree of protein tagging with MeCAT was quantified by the ratio of lanthanides measured by liquid

ICP-MS against the amount of protein determined by the Bradford assay.

The theoretical tagging degree derived from the quantity of sulfhydryl groups exposed by quantitative reduction in contrast to the degree quantified *via* liquid ICP-MS, each protein showed relative tagging degrees of less than 60% for the three model proteins. The deviation from the theoretical amount of tags illustrates the soft reduction strategy adopted from antibody tagging where partial reduction is preferable.

The tagging procedure resulted in a metal bound covalently to the protein and represented an artificial "metalloprotein". The metal was strongly bound, which means it could not get lost during electrophoretic separation in the gel or during the electro-blotting process. In our proof-of-principle experiment these metalloproteins were electro-blotted onto the membrane, just to generate very thin metalloprotein spots on the membrane surface. Our calibration strategy was used in the next experimental step to quantify the metal content of the protein spot.

3.3.2. Direct approach: LA-ICP-MS quantification of the total amount of a protein electro-blotted onto a membrane. As described in the previous chapter we have calculated the tagging degree of all three proteins under investigation. The results are shown in Table 2. This information was used for calculation of the total amount of protein being present in the protein spot after electro-blotting on the membrane surface. By using calibration the total amount of metal present in the protein spot was calculated. The total amount of protein was derived by dividing the amount of metal by the tagging degree. For the three model proteins the following metal tag amounts were determined (see Table 2): BSA 0.52 pmol, ovalbumin 0.06 pmol, and lysozyme 0.10 pmol. These values were calculated from the LA-ICP-MS analysis of two parallel sample sets which exhibited a difference of only 1–8% (see ESI Table S4 and Fig. S6†). In order to validate the LA-ICP-MS mediated quantification the results were compared to the amounts determined by liquid ICP-MS (see Table 2).

Both methods showed coherent values for all three model proteins. Then these values were used in combination with the known tagging degrees for calculation of the protein amounts on the membrane. The protein amounts derived from the experiments were significantly lower than the amounts applied at the start of the sample preparation (see Fig. 1 and Table 2, *n*(protein) per lane SDS-PAGE). This is not very surprising, because electro-blotting is usually incomplete and its process is a function of the protein molecular weight.[35] To further evaluate weight-related blotting efficiency against other effects additional experiments were carried out with the result that the molecular weight was the main factor in blotting efficiency. The data revealed that the molecular weight increase of up to 30 kDa for BSA lowered the blotting efficiency to a significant extent (data not shown), if the tagging degree is properly determined. Thus we have a simple method to determine gel separation and electro-blotting losses of proteins, from which – once known – the protein amount being present in the sample can be calculated (which has to be demonstrated in a separate study – not shown here). Independent of the limitations of sample preparation, the successful validation of the results *via* liquid ICP-MS demonstrate the applicability of the LA-ICP-MS based quantification concept to determine the metal content of proteins in biological samples.

3.3.3. Indirect approach: quantification of a lysozyme antibody conjugate. The concept presented in the previous chapter can be applied for all types of samples onto which printer inks can be printed homogenously to determine the amount of metal bound to a biomolecule or, if the stoichiometry is known, the total amount of the biomolecule directly. In this chapter it will be shown that the same concept works for immunoassays as well. In order to quantify proteins after a Western blot immunoassay lysozyme and anti-lysozyme antibody were selected (see also Fig. 1 and 2). The antibody conjugated protein bands immobilized on a NC membrane were used for two approaches. One half of the bands was stained by Ponceau S before excision followed by liquid ICP-MS detection. The other half was used in LA-ICP-MS experiments. While the liquid ICP-MS data could be quantified by the use of external metal standard solutions the LA-ICP-MS signal areas were quantified by correlation with an ink-jet printed standard series which was applied on the membrane prior to a secondary application of the internal standard. Validation of the methodology was carried out with a set of samples consisting of six replicates per detection method. The praseodymium quantification for LA-ICP-MS by a dilution series of Pr containing ink *vs.* liquid ICP-MS is summarized in Table 3.

For both approaches similar absolute amounts of Pr were determined. The relative deviations were calculated with 8% for the repetition of the LA-ICP-MS experiments and 5% for the experiments performed with liquid ICP-MS. Knowing the

Table 2 Summary of the comparison of the two quantification approaches LA-ICP-MS *vs.* liquid ICP-MS

	Serum albumin (bovine)	Ovalbumin (chicken)	Lysozyme (chicken)
Detected tagging degree (metal per protein)	18.8	3.3	4.8
Lanthanide of the tagging reagent	Er	Er	Er
n(Protein-Er) per lane SDS-PAGE [pmol]	14.50	14.50	14.50
Calibration curve LA-ICP-MS (50 mg L^{-1} ink; Er)	$y = 1.48 \times 10^8 x - 1.91 \times 10^6$; ($R^2 = 0.9999$)		
n(Er) La-ICP-MS [pmol]	0.52	0.06	0.10
n(Protein) [pmol]	0.028	0.018	0.021
Calibration curve liquid ICP-MS (multi-element standard; Er)	$y = 5.04 \times 10^6 x - 2.02 \times 10^3$; ($R^2 = 0.9999$)		
n(Er) liquid ICP-MS [pmol]	0.42	0.05	0.12
n(Protein) [pmol]	0.022	0.016	0.025

Table 3 Comparison of total amounts of Pr in protein spots detected by the metal tagged lysozyme antibody

	Liquid ICP-MS	LA-ICP-MS
Band 1 [pmol Pr]	0.104	0.102
Band 2 [pmol Pr]	0.111	0.103
Band 3 [pmol Pr]	0.102	0.102
Band 4 [pmol Pr]	0.093	0.100
Band 5 [pmol Pr]	0.111	0.109
Band 6 [pmol Pr]	0.116	0.112
Average [pmol Pr]	0.106	0.105
SD [pmol Pr]	0.008	0.005
RSD [%]	8	5
Calibration curve for LA-ICP-MS (50 mg L^{-1} ink)	$y = 3.35 \times 10^8 x - 6.24 \times 10^6$; ($R^2 = 0.9996$)	
Calibration curve liquid ICP-MS (multi-element standard)	$y = 1.04 \times 10^5 x - 6.80 \times 10^3$; ($R^2 = 0.9999$)	

tagging degree of the antibody (tagging degree of anti-lysozyme antibody: 3.14), the number of antibodies bound to the antigens can be calculated from the metal amount easily, but fragmentation of the antibody during the derivatization has to be taken into account (see ref. 36).

4. Conclusion

This paper describes the successful application of a novel calibration standard and internal standard methodology for bio imaging with LA-ICP-MS using a conventional ink-jet printer and metal spiked inks. In this investigation one ink contained indium as an internal standard whereas the second ink contained multiple lanthanide metals for a calibration series allowing the quantification of metal tagged proteins after electro-blotting and antibodies detected by LA-ICP-MS in Western blot immunoassays. Liquid ICP-MS was used for validation of the proof-of-principle experiments. The printed internal standard achieved adequate RSD values of 5% for homogeneity of the printed areas and 2% for reproducibility. Additionally the calibration approach revealed excellent relative process standard deviations of 1% and detection limits as low as 1–4 fmol. While each of the approaches for standardization and calibration can be used independently their combination is even more powerful. Therefore the evaluation of the newly developed ink-jet mediated standardization and calibration was utilized for protein quantification of Western blot immunoassays of three model proteins. In these experiments the model proteins were either targeted by metal tagged antibodies for indirect quantification or quantified *via* immediate metal tagging of the proteins. The relative standard deviations for the blotted proteins were 1–6% for LA-ICP-MS and 8–20% for liquid ICP-MS, which can be attributed to the fact that in LA-ICP-MS standards and samples are analyzed in the same sequence simultaneously.

The developed calibration approach offers a broad range of applications for membrane bound samples, keeping in mind that absolute quantification of Western blot immunoassays requires an advanced determination of blotting efficiency for compensation. Nevertheless the ink-jet mediated printing of defined layers can further be used for absolute quantification of antigens in dot blot or micro-arrays.[37] Besides membrane bound samples immobilized tissue samples can be homogenously printed with defined amounts of standards, which will be demonstrated in a future application. Furthermore printing technology is not limited to artificial tags like MeCAT, but also allows the quantification of naturally present hetero-elements of proteins (biomolecules) in all kinds of biological samples.

Acknowledgements

We thank Peter Lampen (ISAS Dortmund, Germany) for providing his Matlab based software for data analysis. We are grateful to Benita Schmidt (*Humboldt Universität zu Berlin*) for reading this manuscript. The work was financially supported by the "Bundesministerium für Wirtschaft und Technologie, Projektnummer: MNPQ 10/09."

References

1 J. S. Becker, U. Breuer, H. F. Hsieh, T. Osterholt, U. Kumtabtim, B. Wu, A. Matusch, J. A. Caruso and Z. Y. Qin, *Anal. Chem.*, 2010, **82**, 9528–9533.
2 D. Hare, F. Burger, C. Austin, F. Fryer, R. Grimm, B. Reedy, R. A. Scolyer, J. F. Thompson and P. Doble, *Analyst*, 2009, **134**, 450–453.
3 R. C. Murphy and A. H. Merrill, Jr, *Biochim. Biophys. Acta*, 2011, **1811**, 635–636.
4 L. S. Eberlin, X. H. Liu, C. R. Ferreira, S. Santagata, N. Y. R. Agar and R. G. Cooks, *Anal. Chem.*, 2011, **83**, 8366–8371.
5 E. H. Seeley and R. M. Caprioli, *Proteomics: Clin. Appl.*, 2008, **2**, 1435–1443.
6 D. Hare, C. Austin and P. Doble, *Analyst*, 2012, **137**, 1527–1537.
7 R. W. Hutchinson, A. G. Cox, C. W. McLeod, P. S. Marshall, A. Harper, E. L. Dawson and D. R. Howlett, *Anal. Biochem.*, 2005, **346**, 225–233.
8 S. D. Müller, R. A. Diaz-Bone, J. Felix and W. Goedecke, *J. Anal. At. Spectrom.*, 2005, **20**, 907–911.
9 C. Zhang, F. B. Wu, Y. Y. Zhang, X. Wang and X. R. Zhang, *J. Anal. At. Spectrom.*, 2001, **16**, 1393–1396.
10 L. Waentig, P. H. Roos and N. Jakubowski, *J. Anal. At. Spectrom.*, 2009, **24**, 924–933.
11 L. Waentig, N. Jakubowski, H. Hayen and P. H. Roos, *J. Anal. At. Spectrom.*, 2011, **26**, 1610–1618.
12 L. Waentig, N. Jakubowski and P. H. Roos, *J. Anal. At. Spectrom.*, 2011, **26**, 310–319.
13 T. C. de Bang, P. P. Pedas, J. K. Schjoerring, P. E. Jensen and S. Husted, *Anal. Chem.*, 2013, **85**, 5047–5054.
14 X. D. Lou, G. H. Zhang, I. Herrera, R. Kinach, O. Ornatsky, V. Baranov, M. Nitz and M. A. Winnik, *Angew. Chem., Int. Ed.*, 2007, **46**, 6111–6114.
15 R. Ahrends, S. Pieper, A. Kühn, H. Weisshoff, M. Hamester, T. Lindemann, C. Scheler, K. Lehmann, K. Taubner and M. W. Linscheid, *Mol. Cell. Proteomics*, 2007, **6**, 1907–1916.

16 R. Ahrends, S. Pieper, B. Neumann, C. Scheler and M. W. Linscheid, *Anal. Chem.*, 2009, **81**, 2176–2184.
17 L. Waentig, N. Jakubowski, S. Hardt, C. Scheler, P. H. Roos and M. W. Linscheid, *J. Anal. At. Spectrom.*, 2012, **27**, 1311–1320.
18 I. Konz, B. Fernandez, M. L. Fernandez, R. Pereiro and A. Sanz-Medel, *Anal. Bioanal. Chem.*, 2012, **403**, 2113–2125.
19 T. W. M. Fan, E. Pruszkowski and S. Shuttleworth, *J. Anal. At. Spectrom.*, 2002, **17**, 1621–1623.
20 C. Giesen, L. Waentig, T. Mairinger, D. Drescher, J. Kneipp, P. H. Roos, U. Panne and N. Jakubowski, *J. Anal. At. Spectrom.*, 2011, **26**, 2160–2165.
21 I. Konz, B. Fernandez, L. Fernandez, R. Pereiro, H. González, L. Álvarez, M. Coca-Prados and A. Sanz-Medel, *Anal. Bioanal. Chem.*, 2013, **405**, 3091–3096.
22 J. H. Macedone, D. J. Gammon and P. B. Farnsworth, *Spectrochim. Acta, Part B*, 2001, **56**, 1687–1695.
23 M. Zoriy, A. Matusch, T. Spruss and J. S. Becker, *Int. J. Mass Spectrom.*, 2007, **260**, 102–106.
24 M. V. Zoriy, M. Dehnhardt, G. Reifenberger, K. Zilles and J. S. Becker, *Int. J. Mass Spectrom.*, 2006, **257**, 27–33.
25 E. Hoffmann, C. Luedke, J. Skole, H. Stephanowitz, E. Ullrich and D. Colditz, *Fresenius' J. Anal. Chem.*, 2000, **367**, 579–585.
26 J. S. Becker, M. V. Zoriy, C. Pickhardt and K. Zilles, *J. Anal. At. Spectrom.*, 2005, **20**, 912–917.
27 D. Pozebon, V. L. Dressler, M. F. Mesko, A. Matusch and J. S. Becker, *J. Anal. At. Spectrom.*, 2010, **25**, 1739–1744.
28 I. Feldmann, C. U. Koehler, P. H. Roos and N. Jakubowski, *J. Anal. At. Spectrom.*, 2006, **21**, 1006–1015.
29 D. J. Bellis and R. Santamaria-Fernandez, *J. Anal. At. Spectrom.*, 2010, **25**, 957–963.
30 M. M. Bradford, *Anal. Biochem.*, 1976, 248–254.
31 U. K. Laemmli, *Nature*, 1970, 227.
32 A. Venkatachalam, C. U. Koehler, I. Feldmann, P. Lampen, A. Manz, P. H. Roos and N. Jakubowski, *J. Anal. At. Spectrom.*, 2007, **22**, 1023–1032.
33 W. Steffen and R. W. Linck, *Electrophoresis*, 1989, **10**, 714–718.
34 F. W. Küster, *Rechentafel für die chemische Analytik*, ed. A. Ruland, Walter de Gruyter, Berlin, 2nd edn, 2003, vol. 105, ch. 6, pp. 311–319.
35 W. N. Burnette, *Anal. Biochem.*, 1981, **112**, 195–203.
36 L. Mueller, T. Mairinger, G. Hermann, G. Koellensperger and S. Hann, *Anal. Bioanal. Chem.*, 2014, **406**, 163–169.
37 L. Waentig, S. Techritz, N. Jakubowski and P. H. Roos, *Analyst*, 2013, **138**, 6309–6315.

Electronic Supplementary Material (ESI):

Table 1 Summary of the acquisition parameters.

ICP-MS (Element XR)	
RF plasma source power	1350 W
Plasma gas flow	15 L min^{-1} Ar
Auxiliary gas flow	0.8 L min^{-1} Ar
Transport gas flow	0.8 L min^{-1} Ar
Mass resolution ($m/\Delta m$)	300
Scanning mode	E scan
Sample time	2 ms
LA system (New Wave 213)	
Wavelength	213 nm
Helium gas flow	1 L min^{-1}
Laser energy	0.20 - 0.25 mJ
Laser spot sizes	200 µm
Scan speeds	200 µm s^{-1}
Repetition frequency	20 Hz
Ablation mode	Scanning line per line
Analysis time	1 – 2 h

Table 2 Results of the liquid ICP-MS of solubilized NC-membrane slices (normalized to a size of 1 mm^2) printed with indium spiked ink.

	Square 1	**Square 2**	**Square 3**	**Square 4**
^{115}In [cps]	2.29E+04	2.31E+04	2.30E+04	2.14E+04
^{114}Pr [cps]	4.59E+06	4.69E+06	4.69E+06	4.79E+06
norm. ^{115}In (^{115}In/^{141}Pr) [cps]	4.99E-03	4.92E-03	4.91E-03	4.47E-03
m (membrane slice) [g]	1.30E-03	1.33E-03	1.42E-03	1.17E-03
norm. ^{115}In/m [cps/g]	3.84E+00	3.70E+00	3.46E+00	3.82E+00
average [cps/g]	3.70E+00			
RSD [cps]	1.76E-01			
relative RSD [%]	5			

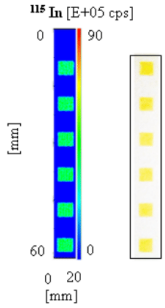

Figure 1 Images of the NC membrane. Left: ^{115}In intensity time profile of a printed NC membrane, right: photographic scan of identical area .

Table 3 Reproducible raw data of the six printed squares measured with LA-ICP-MS (See Figure 1, ESI).

squares	^{115}In Peakarea
1	8.78E+07
2	9.13E+07
3	9.21E+07
4	9.29E+07
5	9.17E+07
6	9.31E+07
average [counts]	9.15E+07
RSD [counts]	1.93E+06
relative RSD [%]	2

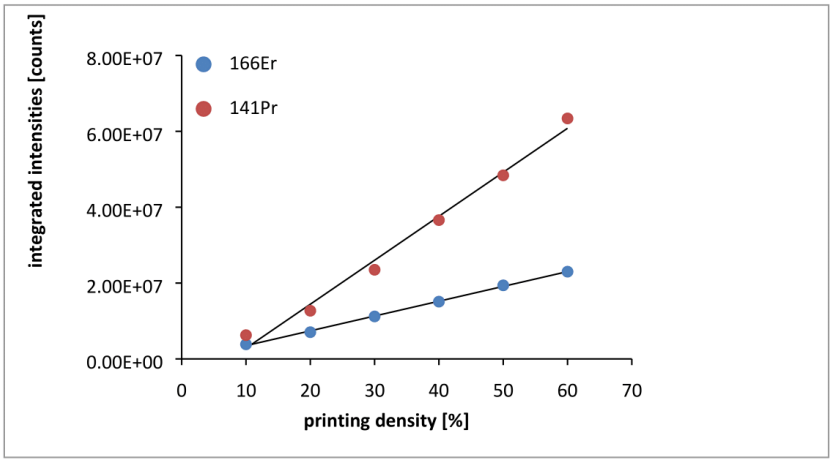

Figure 2 Linearity of the printed calibration standards detected via LA-ICP-MS. Calibration graph for the LA-ICP-MS integrated peak area [counts] vs printing density for 50 mg L^{-1} spiked ink (^{166}Er,^{141}Pr).

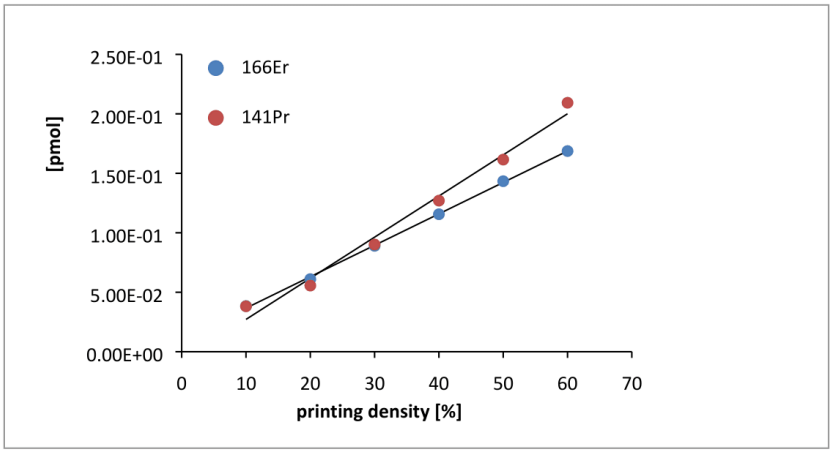

Figure 3 Linearity of the printed calibration standards detected via liquide-ICP-MS. Calibration graph for the liquide-ICP-MS integrated peak area [pmol] vs printing density for 50 mg L^{-1} spiked ink. Calibration graph for the liquide-ICP-MS [pmol] vs printing density for 50 mg L^{-1} spiked ink (^{166}Er,^{141}Pr).

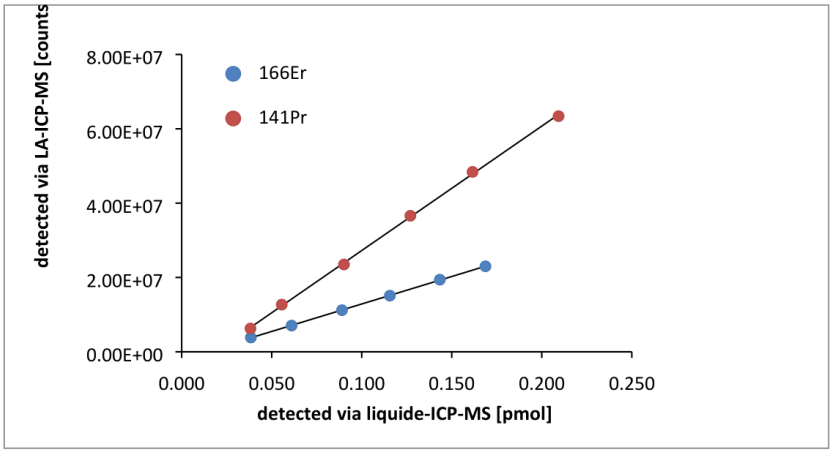

Figure 4 Calibration graph consisting of integrated data of LA-ICP-MS [counts] on the abscissa and the absolute metal amount determined by liquid-ICP-MS [pmol] on the ordinate of the printed calibration squares with the 50 mg L^{-1} spiked ink (^{166}Er,^{141}Pr).

Table 4 Protein quantification via erbium tagged protein molecular weight.

LA-ICP-MS	**serum albumin (bovine)**	**ovalbumin (chicken)**	**lysozym (chicken)**
lanthanide	Er	Er	Er
integrated peak area (1) [counts]	8.06E+07	6.52E+06	1.77E+07
integrated peak area (2) [counts]	7.96E+07	6.01E+06	1.72E+07
difference in percent [%]	1	8	3
average [counts]	8.01E+07	6.27E+06	1.75E+07
calibration curve (50 mg/L ink; ^{166}Er)	y [counts] = 1.48E+08 x [pmol] -1.91E+06; R^2=0.9999		

n (Er) [pmol]	0.52	0.06	0.10

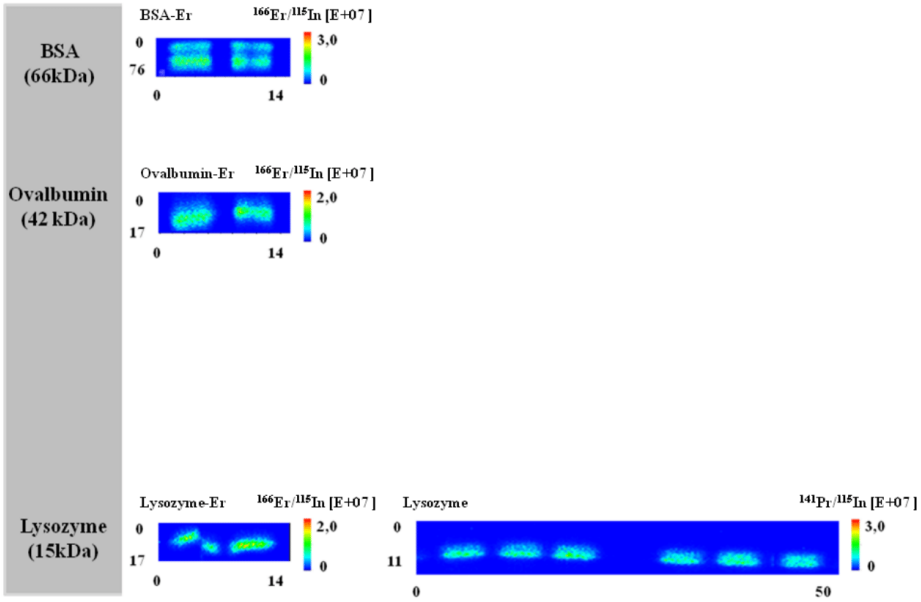

Figure 5 Left: MeCAT tagged standard proteins. Right: Multiplex immunoassay with MeCAT tagged antibodies and its respective antigens detected via LA-ICP-MS.

Publikation 4: Internal standardization of LA-ICP-MS immuno imaging via printing of universal metal spiked inks onto tissue sections

JAAS

TECHNICAL NOTE

View Article Online
View Journal

Cite this: DOI: 10.1039/c5ja00409h

Internal standardization of LA-ICP-MS immuno imaging *via* printing of universal metal spiked inks onto tissue sections†

Simone Hoesl,[ae] Boris Neumann,[bf] Sandra Techritz,[a] Guido Sauter,[c] Ronald Simon,[c] Hartmut Schlüter,[d] Michael W. Linscheid,[e] Franz Theuring,[f] Norbert Jakubowski[a] and Larissa Mueller[a]

Formalin-fixed paraffin-embedded (FFPE) specimen from biopsy materials are a widespread sample format for pathologists and medical researchers. Pathologists are archiving vast numbers of FFPE samples which can be stored for decades. Conventional immunohistochemical staining (IHC) of biomarkers on FFPE tissue sections is one of the most important analytical techniques for cancer diagnosis and pathology in general. However standardization for IHC samples and quality management is tedious and differs significantly from clinic to clinic. Combining established IHC staining strategies with modern mass spectrometry mediated methods would increase it's potential and enable access of large FFPE archives for multiplexed quantitation purposes. In this work element mass spectrometry and a new ink-jet printed internal standardization approach was successfully combined with IHC staining to facilitate quantitative multiplex assays for archived FFPE samples. The printing strategy improves elemental image resolution and reproducibility of paraffin embedded breast cancer tissue sections in laser ablation inductively coupled plasma mass spectrometry (LA-ICP-MS) using conventional IHC staining as a model system to investigate the new capabilities of this technique. For the internal standardization we applied a conventional CD-ink-jet printer to print a metal spiked ink onto the top of thin layer tissue sections with constant density. Printing was carried out in a direct comparison to an iodination of the tissue section as previously described as an alternative standardization method. The use of the printed internal standard allowed correction of the fluctuation during the laser ablation process and compensated instrumental drift effects. Mediated by the ink correction approach we achieved better signal-to-background-ratios (SBR) of 74 and better spatial resolution of 30 μm compared to iodination (SBR = 23). This improved performance was demonstrated on tumorous areas in FFPE breast cancer tissue sections and allowing detection of Her-2 in tumorous areas of this tissue with significantly improved contrast.

Received 8th October 2015
Accepted 15th December 2015

DOI: 10.1039/c5ja00409h

www.rsc.org/jaas

1 Introduction

Various diseases are linked to changes in the abundance of characteristic biomarkers. In the clinical diagnostic field the detection of characteristic biomarkers in tissue sections is essential for the identification and classification of tumor cells and for the choice of the therapy. Currently, immunohistochemistry (IHC)[1] from formalin-fixed paraffin-embedded (FFPE) samples is used as a routine methodology for the visualization of expression levels and intracellular localization of tumor biomarkers in tissue sections. FFPE samples can be stored for decades. The high number achieved samples present a prosperous fundament for IHC mediated analyses. Although IHC staining is used in the diagnostic field frequently, standardization, quantification and inter-facility reproducibility remains a challenging task.[2,3] Tissue Micro Arrays (TMA) were developed for studying up to 1000 different biopsy samples located on a single microscopic glass slide after IHC staining. By this approach all the tissue samples can be investigated in parallel, which allows better comparability of the tissues after the staining procedure and thus is providing a high reproducibility.[4] LA-ICP-MS is a technique for direct analysis of tissues with little sample preparation effort for qualitative imaging

[a]BAM Federal Institute for Materials Research and Testing, Richard-Willstaetter-Str. 11, 12489 Berlin, Germany
[b]Proteome Factory AG, Magnusstr. 11, 12489 Berlin, Germany. E-mail: neumann@proteomefactory.com
[c]Department of Pathology, University Medical Center Hamburg-Eppendorf, Martinistraße 52, D-20246 Hamburg, Germany
[d]Department of Clinical Chemistry, University Medical Center Hamburg-Eppendorf, Martinistraße 52, D-20246 Hamburg, Germany
[e]Department of Chemistry, Humboldt-Universitaet zu Berlin, Brook-Taylor Str. 2, 12489 Berlin, Germany
[f]Charité Institute of Pharmacology, Hessische Straße 3-4, 10115 Berlin, Germany
† Electronic supplementary information (ESI) available. See DOI: 10.1039/c5ja00409h

studies of endogenously incorporated metals, non-metals[5] and artificial modifications in biological samples.[6] Therefore, LA-ICP-MS looks promising in combination with diagnostical workflows such as IHC staining. LA-ICP-MS offers high sensitivity, spatial resolution in the μm range, large dynamic range (9 orders of magnitude)[7–9] and multi-elemental capability, which enables the detection of most elements of the periodic table.[10] Furthermore, the possibility of multiplex assays allows a higher sample throughput due to the time savings of this multiplex analytical method for clinical diagnoses.[11,12]

However, LA-ICP-MS is still limited by the lack of standards for reproducible elemental micro mapping of biological samples. The first application of biochemical imaging *via* LA-ICP-MS was applied 1994 by Wang *et al.*[13] for detection of the strontium distribution in fish scales. During the last years the LA-ICP-MS detection of non-metals[14] such as phosphorus and sulfur[5] and of metals such as copper, zinc, iron and manganese in tissue sections were applied[15] to correlate the distribution of metallo-proteins with disease patterns.

Although metal detection in tissue samples is quite common, immuno-assays combined with ICP-MS are still in a stage of examination, although an increasing number of element tagged antibodies suitable for IHC is under development.[16–18]

In our previous work we reported a LA-ICP-MS based standardization and quantification strategy for western blots, and applied metal-tagged antibodies for immuno-imaging.[19] This procedure should now be adapt for quantitative imaging of complex tissue samples. For all quantitative imaging applications it is a prerequisite to establish a reliable internal standard for correction of laser and ICP-MS fluctuations such as instrumental drifts or variations in the ablated mass.[20] Internal standard approaches for solid sample matrices are well established in particular for geological materials.[21] However, due to the inhomogeneity of biological samples the selection of an internal standard with a homogeneous distribution is critical. Only a few examples exist, in which a matrix element was applied as internal standard. For example, calcium isotopes ($^{43}Ca/^{44}Ca$) have been used for normalization in tooth samples, in order to investigate the composition of the calcium tooth hydroxyapatite.[22,23]

In medical applications tissue sections have been investigated with LA-ICP-MS absolute measurements already without internal standard or with home-made matrix-matched standards.[24,25] The isotope ^{13}C is sometimes used for signal normalization,[26] but it was shown to be not suited as internal standard by Frick and Guenther due to its easy conversion to CO_2 in some compounds leading to transport in the gas phase rather than in the particulate fraction of the aerosol generated by laser ablation.[27]

Alternatively tissue samples can be modified with artificial element labels. Giesen *et al.* optimized the iodination of tissue sections for correction of tissue thickness.[20] Recently a new application of an iridium DNA intercalator as potential internal standard for tissue sections was presented by Frick *et al.*[28]

An additional internal standardization based on the deposition of a thin homogeneous gold film layer on the tissue surface and the use of the $^{197}Au^+$ signal was investigated by Konz *et al.*[17] and Bonta *et al.*[29] Feldmann *et al.*[30] used an ink-jet pattern to optimize a laser ablation cell for detection of hetero-elements in proteins blotted onto membrane by LA-ICP-MS while Bellis *et al.*[31] used such as a reference for biological samples in LA-ICP-SFMS.

The aim of this study was the application of indium containing ink for internal standardization in LA-ICP-MS for immuno imaging of thin tissue sections. Due to the inherent inhomogeneity of tissue some statistical measures can't be derived for the tissue sections. However the proof of concept was already shown on nitrocellulose membranes (western blots) in a previous work (see ref. 19). The similarity to biological samples (*e.g.* high carbon content) as well as the homogenous and smooth characteristics of nitrocellulose membranes allowed adequate optimization and validation. Metal spiked inks were printed onto the top of western blot membranes for simultaneous internal standardization and calibration of LA-ICP-MS. In the case of internal standardization a standard deviation (RSD) value of 2% was achieved. In a second approach the metal content of lanthanide tagged proteins and antibodies was quantified by LA-ICP-MS on nitrocellulose membranes. In this case the inks spiked with varying metals were printed on the membranes in well-defined squares and different densities to produce matrix matched calibration standards. For the printed calibration standard limits of detection (LOD) of <4 fmol for different metals and relative process standard deviations of only 1–2% were determined *via* LA-ICP-MS. Validation of the procedure was performed *via* liquid ICP-MS analysis.[19]

For the current work the printing hardware and the ink have been optimized for direct printing of an arbitrary standard element over inhomogeneous biological tissue sections by use of a conventional ink-jet printer.

The application of the ink-jet printing procedure as a standardization method for LA-ICP-MS imaging of tissue samples will be shown on two different types of tissue sections incubated with MeCAT modified antibodies. First a mouse brain tissue section was incubated with a MeCAT (Er) modified antibody against glyceraldehyde-3-phosphate dehydrogenase (GAPDH) followed by printing the internal standard indium (In) for investigation of drift effects during the LA-ICP-MS measurement. GAPDH is known as a "house-keeping protein" and is considered to be ubiquitously and constitutively expressed in every tissue.[32,33]

But the main intention of this paper is the comparison of results achieved by application of element tagged inks in comparison to iodination of tissue samples, developing high throughput multiplex assays for immuno-imaging. For this purpose, non-tumorous and tumor areas of deparaffinized FFPE breast tissue sections were used for detection of the tumor marker Her-2. For detection a MeCAT (Ho) modified anti-Her-2 antibody was incubated with a breast tissue section,[34] followed by iodination to correct for variations of the tissue thickness.[20] Subsequently, the internal standard In was printed onto the tissue prior to detection by LA-ICP-MS to correct the laser ablation fluctuation. For comparison, a conventional IHC detection was conducted using the modified anti-Her-2 antibody.

2 Experimental

2.1. Chemicals

All solutions were prepared using ultrapure water (Milli-Q water purification system, Millipore, Bedford, MA). The following chemicals were used: LA-In Ink (Proteome Factory AG, Germany); MeCAT kits loaded with holmium and erbium (Proteome Factory); Bradford reagent (Proteome Factory, Berlin, Germany), tris(2-carboxylethyl)phosphine·HCl (TCEP) (PIERCE, Thermo Fisher Scientific, Schwerte, Germany), the following reagents and antibody were purchased from Dako (Hamburg, Germany): xylene, anti-Her-2 antibody (A0485), target retrieval solution pH 6 (S1700), TBS/Tween buffer (S3306), secondary antibody (Real™ EnVision™ HRP Rabbit K4002/Mouse K4001), EnVision™ Kit including Real™ peroxidase-blocking solution and (DAB) substrate-chromogen solution (Real™ EnVision™ HRP Rabbit/Mouse K3467). A second antibody against GAPDH (mAbcam 9484) was purchased for mouse brain tissue section. For the pre-treatment of the mouse brain tissue Neo-Clear (Merck, Darmstadt, Germany), 10 mM citrate puffer (pH 6–6.8) (Sigma-Aldrich, Taufkirchen, Germany), 0.3% peroxidase-blocking solution and PBS buffer (12 mM phosphate, 137 mM NaCl, 2.7 mM KCl, pH 7.4) were used.

2.2. Immunohistochemistry and antibody labeling

Antibodies were labeled according to Waentig *et al.*[35] Further information are given in the ESI.† A detailed treatment description of mouse brain tissue section and breast cancer tissue section is explained in the ESI (1.3/1.4).†

2.3. Printing

Spiked inks were produced by the Proteome Factory AG on request. Laser ablation-indium ink (LA-In-ink: 4 mg In per L), Ink I, consisted of a yellow ink matrix with In as an internal standard. The In spiked ink was filled into an empty printer cartridge. The printing system was equilibrated afterwards by printing 10 DIN A4-pages. Printing on tissue sections was performed with a conventional ink jet printer (Pixma iP4950, Canon, Krefeld, Germany). Settings for regular paper were selected and color management was disabled. To mount glass slides with the tissue sections for printing, two square cut-outs (25 mm × 75 mm) were milled into a conventional compact disk (CD) using a CNC machine (Kosy A5, EMC, Thalheim, Germany). The CD with the glass slides was inserted *via* the dedicated printing drawer supplied with the printer similar to Baluya *et al.*[36] The tissue sections were printed choosing the spiked color channel with a 20% printing saturation.[19]

2.4. LA-ICP-MS

A commercial LA system (New Wave 213, Portland, USA) provided with a beam expander and laser spot sizes between 4 μm and 250 μm, was attached to an ICP sector field mass spectrometer (Element XR, Thermo Fisher Scientific, Germany). The ICP-MS was synchronized using the LA unit in an external trigger mode. The slides with the fixed thin FFPE tissue sections were placed on the sample holder and inserted into the two volume cell (New Wave 213). The aerosol was transported by helium at a flow rate of 1 L min^{-1}. Argon was added at a flow rate of 0.8 L min^{-1} in front of the ICP torch. The LA-ICP-MS was tuned daily for maximum ion intensity and low oxide ratio ((ThO/Th) < 3%) on a microscopic glass slide. Samples were completely ablated line by line under optimized LA-ICP-MS conditions as summarized in Table 1 (ESI).† The following isotopes have been selected: ^{115}In, ^{127}I, ^{166}Er and ^{165}Ho. ^{115}In and ^{127}I were used for data normalization. Holmium was chosen as the tagging reagent for the antibody. For analysis of the tissue sections spot with a size of 50–200 μm and scan speeds of 50–200 μm s^{-1} were selected. The selected tissue sections have a thickness of 5 μm which allows full ablation of the material with a single laser shot. Overlapping laser spots and high repetition rates result in a differential scanning mode, so that a lateral resolution which is better than the selected laser spot diameter was achieved.

The LA-ICP-MS data files were imported to Origin 8 (Origin lab Corporations, Northampton, USA) to create intensity time profiles or color coded images by transforming the scan time into a micrometer scale. The data normalization was performed in Excel (Microsoft, Redmond, USA).

3 Results and discussion

An effective internal standard should exhibit similar behavior as the analyte during the laser ablation process and the transport in the ICP-MS. Furthermore, a defined amount of internal standard should be available at each time point of the sample detection. An internal standard must be homogeneously distributed in the sample or must reach the detector in a constant flow, in order to utilize it as a reference for normalization of inaccuracy during the analysis. Giesen *et al.*[20] employed the detection of iodine in tissue sections as an internal standard signal after chemical modification of proteins. This method was shown to be reliable in a certain optimized parameter range for the purpose of internal standardization. Using spot diameters of 200 μm the iodine signal corrects for changes in the thickness of the tissue sections. To achieve better spatial resolution over a wide range of laser spot diameters and scan speeds we developed an internal standardization process an indium-containing ink.[19] To achieve a homogeneous distribution and constant concentration on the sample matrix the indium ink was printed onto the surface of an entire thin tissue section using a conventional CD-ink-jet printer. Indium's first ionization energy (In: 5.786 eV; Ho: 6.02 eV *vs.* I: 10.451 eV)[37] and atomic mass is comparable with the lanthanide elements and may behave similar during the ionization process. Additionally indium and lanthanides offer a low natural background in biological samples. The selection of an element in the ink with similar mass and ionization potential, as the elements of interest may have advantage over Au as an internal standard with a high mass and a high first ionization potential.

In this work, ink-jet printed indium solution was used as an internal standard to correct for drift effects and for matrix

effects.[19] Matrix effects can be caused by changes in the positive charge density of the ion-beam in the interface region of the LA-ICP-MS instrument which alters the ionization transport efficiency, thus reflecting changes in the sensitivity for the standard element. Indium for internal standardization purposes was already examined in a western blot assay and will be evaluated for thin tissue sections during this study.[19]

3.1. Compensation of drift effects by use of the printed standard on tissue sections

Laser ablation experiments of tissue sections might be time-consuming depending on laser spot size, scan speed and ablated area. Therefore, signal stability over extended periods of time is an important issue. An example is presented in Fig. 1 showing the change of ^{166}Er intensity over time of a FFPE mouse brain tissue section incubated with a MeCAT modified antibody against a selected house-keeping protein (GAPDH) and homogenously printed with indium ink (laser spot size 35 μm). The image of the initial ^{166}Er signals measured for the analyte exhibits a gradient with highest intensities in the left hand section (see Fig. 1A). During the beginning of the ablation process which starts always at the left hand side of the tissue section, higher sensitivities are achieved. After correction by the internal standard a homogenous distribution is calculated (shown in Fig. 1B), which clearly demonstrates the successful normalization by the internal standard for all tissue sample measured.

3.2. Distribution of iodine and indium in the examined tissue sections

The application of printing internal standards onto tissue sections to improve the reproducibility and signal-to-background-ratio (SBR) will be demonstrated for Her-2 positive breast cancer tissue sections. In order to obtain a direct comparison between IHC staining and the laser ablation approach, the tumor marker Her-2 protein was detected with a holmium MeCAT modified anti-Her-2 antibody as the primary antibody. Afterwards the MeCAT (^{165}Ho) antibody–antigen conjugate was visualized with a secondary antibody against mouse IgG *via* IHC staining with a brown color. Experiments with an unmodified Her-2 antibody exhibited identical IHC staining intensities (data not shown). It is mandatory to show binding of the secondary antibody after bioconjugation in advance. If successful a direct comparison of the conventional IHC staining and the LA-ICP-MS immunoassay is possible. For a direct comparison between the new developed internal standard indium and the common iodination, the tissue sections were iodinated prior to printing and detection (see also Fig. 2). This was performed on high tumorous ("positive") and non-tumorous ("negative") breast tissue sections as previously determined by conventional IHC staining.

For validation, all measurements were carried out in direct comparison to the internal standard iodine and to IHC staining. In accordance to ref. 19, the acquired LA-ICP-MS data of the printed tissue section was normalized by calculating the average intensity of each standard (^{115}In and ^{127}I) for the entire measured area.

Each detected indium signal of the matrix was normalized to the ^{115}In average of the matrix ($\mathrm{In[cps]}/\overline{\mathrm{In}}\mathrm{[cps]}$). This normalization is preferred for the internal standards to get a factor which fluctuates around a value of 1. The normalization

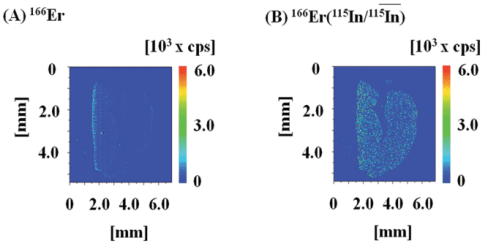

Fig. 1 (A) shows the raw data of a LA-ICP-MS ^{166}Er intensity profile of GAPDH in a FFPE mouse brain tissue section. (B) Illustrates the successful indium normalization of the erbium intensity profile. Laser parameters: laser spot size 50 μm, scan speed 50 μm s^{-1}, spot overlap 20 μm, repetition rate 20 Hz (pixel 30 μm × 2.5 μm), laser energy 0.20–0.25 mJ (35%). Signal intensities were color coded in a way that low intensities are shown in blue and high intensities in red color.

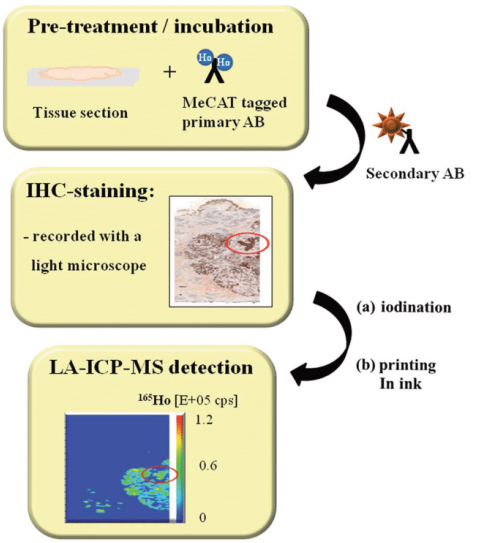

Fig. 2 Workflow for the detection of tumor areas in FFPE breast tissue sections. Deparaffinized tissue sections were incubated with the holmium tagged anti-Her-2 primary antibody, followed by the application of a secondary antibody (IHC-staining) and by iodination. The tissue sections were first characterized by histology after application of a secondary antibody suitable for IHC. Afterwards the tissue sections were covered with the internal standard indium. After drying of the applied ink the tissue sections were subjected to LA-ICP-MS for holmium, iodine and indium detection.

of iodine was performed accordingly. Subsequently the initial analyte (^{165}Ho) matrix was divided by the calculated indium matrix and iodine matrix respectively which is illustrated in Fig. 5 (Ho[cps](In[cps]/$\overline{\text{In}}$[cps])).

Fig. 3 shows the acquired indium signal (C) in comparison to IHC staining (A). Beside the expected variation of the iodine signal (B) due to changes in the tissue thickness, the structural information of the tissue in case of high laser resolution, has an impact on the signal intensity. This effect can be explained with the chemical mechanism of iodination. Iodine primarily modifies aromatic groups of amino acids in proteins such as tyrosine or histidine. As a result, signal strength correlates with the tissue's protein density. Highly tumorous areas can therefore show an elevated iodine signal due to altered protein abundance levels. Geiger *et al.* reported a >50-fold increase of Her-2 in breast cancer cells.[38] The signal variance of normalized ^{127}I (I[cps]/$\overline{\text{I}}$[cps]) *vs.* ^{115}In (In[cps]/$\overline{\text{In}}$[cps]) derived from a vertical line scan is shown in Fig. 3D. The graph illustrates the high oscillation of the iodine signal in the center regions in contrast to the more stable indium signal. This observation can be confirmed by comparison of the RSDs of the detected element intensities over the entire measured sample area of positive and negative breast cancer tissue sections for Her-2 antibody (see Fig. 5 and ESI Fig. 1†). As expected the RSDs of the ^{165}Ho intensities representing the MeCAT tagged Her-2 antibody differs strongly between the positive (average ^{165}Ho: 8.8×10^3 cps, RSD: 80%) and negative control (average ^{165}Ho: 1.06×10^3 cps, RSD: 60%), because the positive control possess some areas with a high increase of ^{165}Ho intensities (see also Fig. 5). Compared to this, the signal intensities of the printed indium standard have a RSD of approx. 30% in both samples (negative control RSD: 29%, average ^{115}In: 4.10×10^4 cps; positive control RSD: 34%, average ^{115}In: 5.79×10^4 cps) indicating the low influence of sample characteristics like protein density or tissue thickness. The indium internal standard reveals a very good sensitivity while allowing indium amount to be regulated over the entire surface *via* printing density. This allows a flexible conversion of the ^{115}In intensities at the range of the analyte.[19] The variations can be accounted to the printer's operation regime for CD printing and matrix effects.[10,39]

The RSD as a factor for signal oscillation of iodine (positive control RSD: 66%, average ^{127}I: 5.98×10^7 cps; negative control: 56%, average ^{127}I: 1.30×10^8 cps) is 2-fold elevated compared to the printed indium standard, which again demonstrates that iodine is not the best choice. In case of, LA-ICP-MS imaging with low spot diameters (<50 μm) and high spatial resolution iodine delivers information of protein accumulations (see also Fig. 3).

3.3. Compensation of non-uniform sampling by use of the printed standard on tissue sections

The term non-uniform sampling includes different effects during the laser ablation process such as matrix effects or irregularities in the size of ablated sample material which influence the analyte signal. The printed standard does not normalize differences in tissue thickness or protein density within the sample.

To demonstrate the influence of the printed internal standard on the measured analyte signals in detail (^{165}Ho) selected line scans of the 2D intensity profile of a breast cancer tissue section positive for Her-2 antibody are given in Fig. 4. Marked

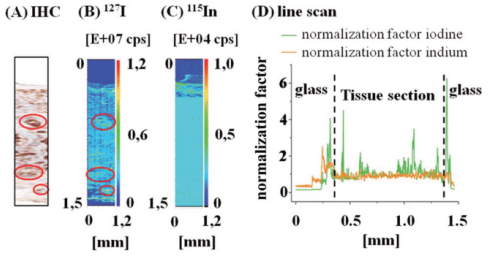

Fig. 3 Immunohistochemical staining (A) of a 5 μm breast cancer tissue section positive for anti-Her-2 antibody and corresponding LA-ICP-MS images of iodine (B) and indium (C) was shown. The positive tumor areas are highlighted with a red circle. The calculated line scan (D) shows the normalization factors (In[cps]/$\overline{\text{In}}$[cps]) of both internal standards in a direct comparison. Laser parameters: laser spot size 50 μm, scan speed 50 μm s^{-1}, spot overlap 20 μm, repetition rate 20 Hz (pixel 30 μm × 2.5 μm), laser energy 0.20–0.25 mJ (35%).

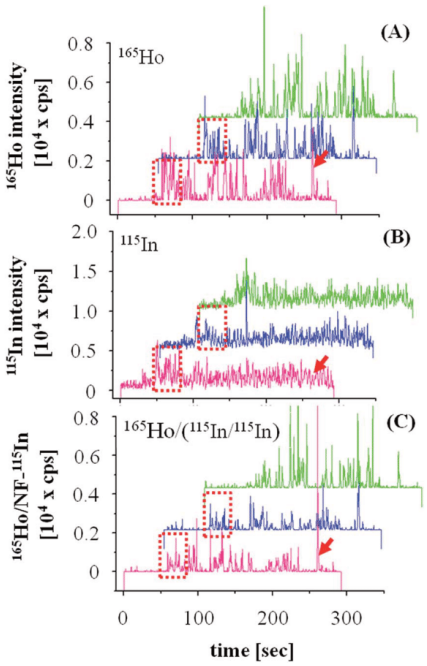

Fig. 4 Shows selected line scans (no. 17–19) of the 2D intensity profiles of Fig. 5. Section (A) shows the courses of the holmium signal, while section (B) gives the courses for indium, the internal standard. In section (C) the result of standardization is given.

areas (red rectangle) showing the influence of the standardization procedure. ^{165}Ho intensity starts at background level outside the tissue. The signals increase up to around 0.2×10^4 cps. In the same area, detected ^{115}In intensities of the printed standard are elevated up to around 0.5×10^4 cps as well. The resulting line scan of the normalized analyte signals shows a similar peak pattern compared to the detected ^{165}Ho line scan in diagram A, but with lower intensities (approx. 0.1×10^4 cps).

Another example showing the influence of the standardization procedure is marked by red arrows in Fig. 4. In this case the detected signal of ^{115}In (B) decreases for a short period whereas a peak is observed in the ^{165}Ho line scan (A). The resulting line scan of the normalized data in diagram C has still a high analyte peak at this position. Therefore internal standardization by our ink approach allows the correction of artifacts caused by non-uniform laser ablation sampling.

3.4. Internal standardization of tissue section signals

Assessment of both standardization techniques (I, In) for imaging and detection of Her-2 positive areas was carried out using each of the standard signals for normalization of the holmium signal individually; the IHC image (A) and the raw holmium intensity image (B) are shown in Fig. 5 as reference.

Fig. 5C shows the holmium intensity image normalized using indium (Ln[cps](In[cps]/$\overline{\text{In}}$[cps])) to correct for fluctuations or drift effects during the LA-ICP-MS detection. Fig. 5D shows the holmium intensity normalized using iodine for the theoretical correction of tissue thickness. A direct comparison of the two intensity images with the commercial IHC staining provided the same positive areas in the tissue section but with different spatial resolutions (see Fig. 5 and 6, marked with a red circle). The iodine normalization exhibited higher background signals and lower signal-to-background ratios (SBR). However, due to the normalization with indium, a clear differentiation of positive regions was achieved enabling observation of a significant accentuation (contrast) of tumorous areas in the tissue section (see Fig. 5 and 6, marked with a black circle). The printed standard compensates for variations in the size of the ablated area per laser shot resulting in higher SBR (^{165}Ho/^{115}In: 39 *vs.* ^{165}Ho/^{127}I: 11) and better spatial image contrast.

The lower image contrast of the holmium intensity image normalized by iodine can be explained with the elevated distribution of proteins in the cancer tissue areas. These proteins are detected by the antibody and as well by the iodine which binds to tyrosine and histidine residues. Normalization using iodine is consequently resulting in a lower spatial image contrast. However, iodine is an excellent measure for protein density and may provide extremely useful information for medical and biochemical studies.

In consideration of the evaluated standard deviations the SBRs for the positive tissue with a resolution of 30 μm were determined (see ESI Table 2†). While the raw signal for holmium exhibits a SBR of 18 for the positive tissue, normalization by indium increases this value significantly to 39. The iodine normalization, which is influenced by the discussed factors, exhibits a comparatively low SBR of 11. Using ^{165}Ho/^{127}I normalization (Fig. 5D) a much higher background noise in contrast to the other images is observed. In Fig. 6 zoomed images of Her-2 positive areas (circled area) are given allowing closer visual inspection of the tissue sections. On the left of each set the IHC reference picture of the area is given. Row I shows a highly tumorous spot in the center of the slide (see Fig. 6). Conventional IHC staining results in brownish areas of visual homogenous coloring level. The holmium (I B: ^{165}Ho) and the ^{165}Ho/^{127}I intensity profiles (I D) show images with low contrast (I B) and low SBR (I D), whereas the printing mediated ^{165}Ho/^{115}In image displays graduated intensities for details within the positive areas.

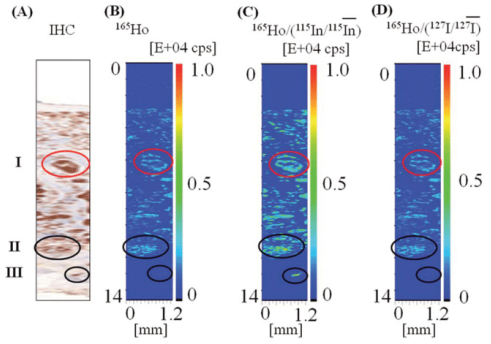

Fig. 5 Different 2D intensity profiles of one 5 μm breast cancer tissue section, positive for anti-Her-2 antibody are shown. (A) Conventional IHC staining, (B) uncorrected holmium intensity distribution, (C) indium normalized holmium intensity profile (Ho[cps](In[cps]/$\overline{\text{In}}$[cps])),[19] (D) iodine corrected holmium intensity profile. The positive tumor areas are highlighted with a red circle and the differences are highlighted with a black circle. The Fig. 6 shows a magnified image of the marked areas in the intensity profile. Laser parameters: laser spot size 50 μm, scan speed 50 μm s^{-1}, spot overlap 20 μm, repetition rate 20 Hz (pixel 30 μm × 2.5 μm), laser energy 0.20–0.25 mJ (35%).

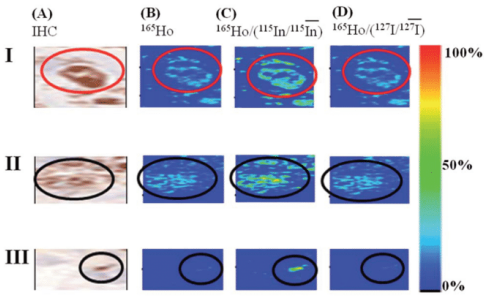

Fig. 6 Zoomed details of selected areas of Fig. 4. (A) Conventional IHC staining, (B) uncorrected holmium intensity distribution, (C) indium normalized holmium intensity profile (Ho[cps](In[cps]/$\overline{\text{In}}$[cps])), (D) iodine corrected holmium intensity profile. The positive tumor areas are highlighted with a red circle, differences with a black circle.

In row II of Fig. 6 graduation and accentuation of the $^{165}Ho/^{115}In$ image is better compared to the ^{165}Ho and the $^{165}Ho/^{127}I$ image and reveals hot spots of Her-2 positive areas.

Looking at row III of Fig. 6 a small spot in the positive area is clearly visible supporting the increased contrasting effect of the Ho/In normalization for Her-2 positive areas. On the other hand the Ho/I image results in a weak contrast.

In summary, all conventional IHC stained positive areas were also detected by LA-ICP-MS measurements, confirming that metal-tagging is not affecting the binding capability of the antibody. Although IHC staining is conventionally applied in clinical applications, the technique is hard to normalize and exhibits only a linear dynamic range of less than one decade. To achieve comparable results standard protocols have to be followed consequently. LA-ICP-MS based immuno assays on the other hand can be developed and modified under compromise conditions to detect many metal-tagged antibodies simultaneously so that multiplex approaches can be easily established.[11] In particular the standardization by the printing process allows day to day normalization and can be used as a standard protocol for inter-laboratory comparisons. IHC provides a color which allows individual interpretation whereas LA-ICP-MS once calibrated provides absolute numbers which are free from every personal bias and can be used to develop quantitative imaging methods, which will be discussed in more details in a future publication.

4 Conclusions

We demonstrate the successful application of ink-jet printed internal standards on thin tissue sections mounted on glass slides for LA-ICP-MS imaging at low μm resolution (<50 μm). The applicability was shown on different types of tissue sections incubated with MeCAT modified antibodies and was compared to an established standardization procedure the chemical modification of tissue samples with iodine. The developed printing technique produces almost homogenous signals of the internal standard indium and is not affected by the protein density like iodine. Application of the indium spiked ink using a conventional ink jet printer is advantageous to improve the image quality with respect of resolution. The developed metal ink printing strategy is a promising technology, ensures a homogeneous distribution of an internal standard onto biological tissue section, corrects for drift effects and improves the reproducibility of measurements.

Furthermore the printing standardization is not limited to a single element but enables a universal application of a broad number of elements and isotopes.[19] Recently the technique was applied for comparison of the different nephrotoxic behavior of platinum drugs by LA-ICP-MS imaging.[40] Overall the technique is an important tool for standardization of soft biological samples in laser ablation ICP-MS experiments.

Although we found that iodine is not a perfect standard for normalization in case of high resolution images measured by LA-ICP-MS, the iodine modification allows to measure the protein density in tissue, and thus might become a new diagnostic tool for various applications in future.

Acknowledgements

We thank Inge Brandt and Christina Koop from the Universitätsklinikum Hamburg-Eppendorf for assistance in breast cancer tissue sectioning and IHC staining and the coordination during sample preparation. Likewise, we thank Mandy Magbagbeolu and Dr Karima Schwab from Charité Institute of Pharmacology in Berlin for preparation and IHC staining of mouse brain tissue sections. This work was financially supported by the "Bundesministerium für Wirtschaft und Technologie Projektnummer: MNPQ 09/10".

Notes and references

1 J. S. Becker, U. Breuer, H. F. Hsieh, T. Osterholt, U. Kumtabtim, B. Wu, A. Matusch, J. A. Caruso and Z. Y. Qin, *Anal. Chem.*, 2010, **82**, 9528–9533.
2 D. Grube, *Arch. Histol. Cytol.*, 2004, **62**(2), 115–134.
3 G. Sauter, R. Simon and K. Hillan, *Nat. Rev. Drug Discovery*, 2003, **2**, 962–972.
4 L. Bubendorf, A. Nocito, H. Moch and G. Sauter, *J. Pathol.*, 2001, **195**, 72–79.
5 D. Hare, F. Burger, C. Austin, F. Fryer, R. Grimm, B. Reedy, R. A. Scolyer, J. F. Thompson and P. Doble, Elemental bioimaging of melanoma in lymph node biopsies, *Analyst*, 2009, **134**, 450–453.
6 L. Waentig, P. H. Roos and N. Jakubowski, Labelling of antibodies and detection by laser ablation inductively coupled plasma mass spectrometry, *J. Anal. At. Spectrom.*, 2009, **24**, 924–933.
7 R. C. Murphy and A. H. J. Merrill, *Biochim. Biophys. Acta*, 2011, **1811**, 635–636.
8 E. H. Seeley and R. M. Caprioli, *Proteomics: Clin. Appl.*, 2008, **2**, 10–11.
9 L. S. Eberlin, X. H. Liu, C. R. Ferreira, S. Santagata, N. Y. R. Agar and R. G. Cooks, *Anal. Chem.*, 2011, **83**, 8366–8371.
10 D. Hare, C. Austin and P. Doble, *Analyst*, 2012, **137**, 1527–1537.
11 C. Giesen, H. A. O. Wang, D. Schapiro, N. Zivanovic, A. Jacobs, B. Hattendorf, P. J. Schüffler, D. Grolimand, J. M. Buhmann, S. Brandt, Z. Varga, P. J. Wild, D. Günther and B. Bodenmiller, *Nat. Methods*, 2014, 417–422.
12 J. S. Becker and D. Salber, *TrAC, Trends Anal. Chem.*, 2010, **29**, 966–979.
13 S. Wang, R. Browm and D. J. Gray, *Appl. Spectrosc.*, 1994, **48**, 1321–1325.
14 A. Sanz-Medel, *Anal. Bioanal. Chem.*, 2008, **391**, 885–894.
15 A. Matusch, C. Depboylu, C. Palm, B. Wu, G. U. Hoglinger, M. K. H. Schafer and J. S. Becker, *J. Am. Soc. Mass Spectrom.*, 2010, **21**, 161–171.
16 C. Giesen, L. Waentig, U. Panne and N. Jakubowski, *Spectrochim. Acta, Part B*, 2012, **76**, 27–39.
17 I. Konz, B. Fernandez, M. L. Fernandez, R. Pereiro and A. Sanz-Medel, *Anal. Bioanal. Chem.*, 2012, **403**, 2113–2125.

18 R. Liu, P. Wu, L. Yang, X. Hou and Y. Lv, Inductively coupled plasma mass spectrometry-based immunoassay: a review, *Mass Spectrom. Rev.*, 2014, **33**, 373–393.
19 S. Hoesl, B. Neumann, S. Techritz, M. Linscheid, F. Theuring, C. Scheler, N. Jakubowski and L. Mueller, *J. Anal. At. Spectrom.*, 2014, **29**, 1282–1291.
20 C. Giesen, L. Waentig, T. Mairinger, D. Drescher, J. Kneipp, P. H. Roos, U. Panne and N. Jakubowski, *J. Anal. At.Spectrom.*, 2011, **26**, 2160–2165.
21 H. P. Longerich, S. E. Jackson and D. Gunther, *J. Anal. At. Spectrom.*, 1996, **11**, 899–904.
22 D. Kang, D. Amarasiriwardena and A. H. Goodman, *Anal. Bioanal. Chem.*, 2004, **378**, 1608–1615.
23 E. Hoffmann, H. Stephanowitz, E. Ullrich, J. Skole, C. Ludke and B. Hoffmann, *J. Anal. At. Spectrom.*, 2000, **15**, 663–667.
24 D. J. Hare, P. Lei, S. Ayton, B. R. Roberts, R. Grimm, J. L. George, D. P. Bishop, A. D. Beavis, S. J. Donovan, G. McColl, I. Volitakis, C. L. Masters, P. A. Adlard, R. A. Cherny, A. I. Bush, D. I. Finkelstein and P. A. Doble, *Chem. Sci.*, 2014, **5**, 2160–2169.
25 M. Angelo, S. C. Bendall, R. Finck, M. B. Hale, C. Hitzman, A. D. Borowsky, R. M. Levenson, J. M. Lowe, S. D. Liu, S. Y. Zhao and G. P. Nolan, *Nat. Med.*, 2014, 1–7.
26 C. Austin, F. Fryer, J. Lear, D. Bishop, D. Hare, T. Rawling, L. Kirkup, A. McDonagh and P. Doble, *J. Anal. At. Spectrom.*, 2011, **26**, 1494–1501.
27 D. A. Frick and D. Gunther, *J. Anal. At. Spectrom.*, 2012, **27**, 1294–1303.
28 D. A. Frick, C. Giesen, T. Hemmerle, B. Bodenmiller and D. Günther, *J. Anal. At. Spectrom.*, 2015, **30**, 254–259.
29 M. Bonta, H. Lohninger, M. Marchetti-Deschmann and A. Limbeck, *Analyst*, 2014, **139**, 1521–1531.
30 I. Feldmann, C. U. Koehler, P. Roos and N. Jakubowski, *J. Anal. At. Spectrom.*, 2006, **21**, 1006–1015.
31 D. Bellis and R. Santamaria-Fernandez, *J. Anal. At. Spectrom.*, 2010, **25**, 957–963.
32 R. E. Ferguson, H. E. Carroll, A. Harris, E. R. Maher, P. Selby and R. Banks, *Proteomics*, 2007, **5**, 566–571.
33 R. Mori, Q. Wang, K. Danenberg, J. Pinski and P. Danenberg, *Prostate*, 2008, **68**, 1555–1560.
34 C. Giesen, T. Mairinger, L. Khoury, L. Waentig, N. Jakubowski and U. Panne, *Anal. Chem.*, 2011, **83**, 8177–8183.
35 L. Waentig, N. Jakubowski, S. Hardt, C. Scheler, P. Roos and M. W. Linscheid, *J. Anal. At. Spectrom.*, 2012, **27**, 1311–1320.
36 D. L. Baluya, T. J. Garrett and R. A. Yost, *Anal. Chem.*, 2007, **79**, 6862–6867.
37 D. R. Lide, *CRC Handbook of Chemistry and Physics*, CRC Press, Boca Raton, Florida, 2003, p. 84.
38 T. Geiger, J. Cox and M. Mann, *Global Proteomic Analysis of Genomic Alterations*, 2010, **6**, 1–11.
39 I. Rodushkin, M. D. Axelsson, D. Malinovsky and D. C. Baxter, *J. Anal. At. Spectrom.*, 2002, **17**, 1231–1239.
40 I. Moraleja, D. Esteban-Fernández, A. Lázaro, B. Humanes, B. Neumann, A. Teje, M. Mena, N. Jakubowski and M. Gómez-Gómez, *Anal. Bioanal. Chem.*, 2015, submitted.

Electronic Supplementary Material (ESI):

1.1 Protein determination

The concentrations of tagged proteins were determined by a micro plate spectrophotometer Spectramax Plus 384 (Molecular Devices, Sunnyvale, USA) using the Bradford assay. External calibration was carried out at an absorption maximum at 595 nm by using a dilution series of bovine serum albumin (Sigma Aldrich, Taufkirchen, Germany).

1.2 Antibody tagging via MeCAT (metal coded tag)

A detailed description of the of antibody tagging procedure is given in reference [1]. For our investigation we have chosen MeCAT (Ho) (Proteome Factory AG, Berlin) for tagging of anti-Her 2 antibody. Summary, the tagging method started with a partial reduction of the antibody with a molar excess rate of 600 of TCEP relative to antibody molarity for 30 min at 37°C. After purification by ultra-filtration at 7500 x g of the partial reduced antibody the modification was made using a 20 fold molar excess of MeCAT (Ho) (Proteome Factory AG, Berlin) which was agitated for 60 min at 37°C. After reaction the MeCAT excess was removed from the antibody solution by ultra-filtration as described above.

1.3 Immunohistochemistry (IHC) staining of FFPE breast cancer tissue sections for LA-ICP-MS detection

The human epidermal growth factor receptor 2 (Her-2) is an important tumour marker, which is detected in the clinical routine diagnostic in breast cancer tissue section with IHC staining. FFPE breast cancer tissue and normal breast tissue were sectioned using a commercial sliding microtome (HM355S, Microm International GmbH, Walldorf, Germany) with a thickness of 5 µm for an IHC staining and subsequent LA-ICP-MS measurement. All sections were immobilized onto Superfrost Plus slides (Thermo Fisher Scientific, Braunschweig, Germany) and deparaffinised in xylene, followed by a series of graded alcohols. All tissue sections were pretreated with a target retrieval solution pH 6 (S1700, Dako) for 20 min at 90°C. After cooling to room temperature, the tissue was washed with a TBS / Tween buffer (S3306, Dako) for 5 min. To block endogenous peroxidase, the tissues were incubated with the Dako Real TM peroxidase-blocking solution (Dako EnVisionTM Kit) for 10 minutes by room temperature. This was followed by repeating washing steps for 2 x 5 minutes with TBS/Tween buffer.

In this work, anti- Her-2 antibody was tagged via MeCAT (Ho) as described in ESI section 1.2. The holmium tagged antibody was diluted with Dako Real TM Antibody Diluent (S2022, DAKO). The tissue section was incubated with a tagged antibody for 1 h by 37°C in an incubator with a concentration25 of 1 µg mL^{-1}. In order to prevent the drying of the tissue section, the incubation was performed in a hybridization chamber. This was followed by two washing steps with TBS/Tween-washing buffer for 5 minutes each. Subsequently treatment with the secondary antibody (Dako REAL TM EnVision TM HRP Rabbit/Mouse) was carried out for 30 min at room temperature. After incubation the unbound antibody was removed by washing steps with buffer as described above. Visualization was performed by incubation with a 3,3`diaminobenzidine (DAB) substrate-chromogen solution (Dako REALTM EnVisionTM HRP Rabbit/Mouse) for 10 min according to the manufacturer of the kit resulting in brownish coloring. For laser ablation, the tissue was dehydrated through a graded alcohol series consisting of 70%, 90% and 100% ethanol according to conventional IHC protocols.

1.4 Pre-treatment of mouse tissue sections for LA-ICP-MS detection

In a pretest formalin-fixed mouse brain tissue section was incubated with an MeCAT loaded erbium tagged antibody against an “house-keeping protein” called GAPDH. The tissue section was deparaffinized in Neo-Clear (alternative xylene) for 3 x 5 min and rehydrated through a series of alcohols (100%, 96%, 70%) for 2 x per 30 sec. After rehydration the tissue section was transferred into distilled water. For the unmasking of antigens the tissue section a 10 mM citrate buffer (PH 6-6.8) was used. The buffer was heated for 2 min at 650 watt in a microwave. Subsequently, the tissue was boiled in the warm buffer for 2 x 5 min in the microwave (650 watt). With the aid of ice the tissue section with the citrate buffer was cooled. Thereafter, the tissue section was incubated with a 0.3 % peroxidase blocking solution for 5 min. This was followed by three brief wash steps with PBS buffer (12 mM phosphate, 137 mM NaCl, 2.7 mM KCl, pH 7.4). The MeCAT (Er) modified antibody was 1:50 or 1:300 (depending on the antibody) with BSA PBS buffer diluted. The tissue section was incubated with 250 µL of the modified antibody for 1 h at room temperature in a hybridization chamber. In the following step the tissue section was rinsed with 12 mM PBS buffer (137 mM NaCl, 2.7 mM KCl, pH 7.4) to remove unbound antibodies, and dehydrated through graded alcohols (70%, 96%, 100%) prior to laser ablation.

1.5 Iodination

Iodination of tissues sections was performed with a saturated KI3 solution in accordance with reference.2 After termination of the reaction with sodium dithionite (Merck, Darmstadt, Germany) and rinsing with PBS-T (phosphate buffered saline pH 7.3: 137 mM NaCl, 2.7 mM KCl,4.3 mM Na2HPO4, KH2PO4 (all from Merck, Darmstadt, Germany) the tissue sections were dried in the air.

Table 1 Summary of the acquisition parameters for LA-ICP-MS.

ICP-MS (Element XR)	
RF plasmasource power	1350 W
Plasma gas flow	15 L min^{-1} Ar
Auxiliary gas flow	0.8 L min^{-1} Ar
Transport gas flow	0.8 L min^{-1} Ar
Mass resolution (*m*/Δ*m*)	300
Scanning mode	E scan
Sample time	2 ms
LA system (New Wave 213)	
Wavelength	213 nm
Helium gas flow	1 L min^{-1}
Laser energy	0.20 - 0.25 mJ (35%)
Laser spot size	200; 100;50 µm
Scan speed	200; 100; 50 µm s^{-1}
Overlap of the laser spot size	180; 80; 30 µm
Repetition frequency	20 Hz
Ablation mode	Scanning line per line
Analysis time per slice	1 – 2 h

Table 2 Summary of the calculated values (3.0-7.6 mm). Laser parameters: laser spot size 50 µm, scan speed 50 µm s^{-1}, resolution of 30 µm.

	^{165}**Ho**	^{165}**Ho/**^{127}**I**	^{165}**Ho/**^{115}**In**
signal-to-background ratio (SBR)	18	11	39

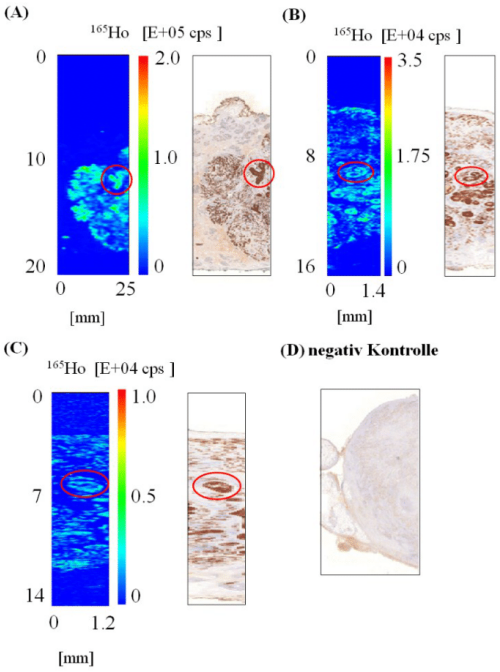

Fig. 1 LA-ICP-MS images and corresponding immunohistochemical (IHC) staining of a 5 µm breast cancer tissue section. Positive areas for anti-Her-2 antibody are shown in (A-C), while (D) shows a negative control for Her-2 in comparison. Images resulting from LA-ICP-MS acquisition using different laser parameters are pointed out in part (A), (B) and (C) with their IHC counterparts. The individual positive tumour areas are marked with red circles. Laser parameters: (A) laser spot size 200 µm, scan speed 200 µm s^{-1}, overlap of the laser spot size of 180 µm, (B) laser spot size 100 µm, scan speed 100 µm s^{-1}, overlap of the laser spot size of 80 µm, (C) laser spot size 50 µm, scan speed 50 µm s^{-1}, overlap of the laser spot size of 30 µm, repetitions rate 20 Hz, laser energy 0.20 - 0.25 mJ (35%).

Publikation 5: Multiplex LA-ICP-MS bio-imaging of brain tissue of a parkinsonian mouse model stained with metal-coded affinity-tagged antibodies and coated with indium-spiked commercial inks as internal standards

Journal of Neuroscience Methods 334 (2020) 108591

Contents lists available at ScienceDirect

Journal of Neuroscience Methods

journal homepage: www.elsevier.com/locate/jneumeth

Multiplex LA-ICP-MS bio-imaging of brain tissue of a parkinsonian mouse model stained with metal-coded affinity-tagged antibodies and coated with indium-spiked commercial inks as internal standards

Boris Neumann[a,b], Simone Hösl[b], Karima Schwab[a,*], Franz Theuring[a], Norbert Jakubowski[c]

[a] Charité – Universitätsmedizin Berlin, Corporate Member of Freie Universität Berlin, Humboldt-Universität Zu Berlin, and Berlin Institute of Health, Center for Cardiovascular Research, Institute of Pharmacology, Hessische Strasse 3-4, 10115 Berlin, Germany
[b] Proteome Factory AG, Magnusstrasse 11, 12489 Berlin, Germany
[c] Spetec GmbH, Berghamer Str. 2, 85435 Erding, Germany

ARTICLE INFO

Keywords:
LA-ICP-MS
Imaging
Internal standardization
Inkjet-Printing
DOTA-labelling immunohistochemistry
Parkinson's disease

ABSTRACT

Background: Immunohistochemistry techniques represent a powerful tool to detect and quantify disease related proteins. Improvements were accomplished by tagged antibodies using laser ablation and inductively coupled plasma mass spectrometry (LA-ICP-MS). However, these approaches are effected by day-to-variations due to instrumental drift.
New Method: Brain tissue from line 62, a Parkinson's disease model, and control mice were incubated with four antibodies relevant to the disease and standardized to three house-keeping proteins. In addition, a new standardization approach was developed and the results compared. This new approach consisted of coating specimens with gelatin and printing an indium-doped ink with a commercial ink jet printer. Furthermore, the method was evaluated for different ablation spot sizes with respect to resolution and signal-to-noise ratio.
Results: Normalization using house-keeping proteins led to high background signals even at high resolution. Normalization using indium-doped ink improved the signal-to-noise ratio even when small laser spot sizes were used and further improved by overlaying tissue specimen with gelatin.
Comparison with Existing Methods: Line 62 mice had more α-Synuclein and gliosis but decreased numbers of neurons, as found by conventional immunohistochemistry. These data are in line with the results obtained by LA-ICP-MS with indium standardization. However, differences between L62 and controls for tyrosine hydroxylase were only detected by LA-ICP-MS.
Conclusions: Internal standardisation using indium-doped inks is an effective method to overcome day-to-day variations and instrumental drifts. The new approach results in an increased signal-to-noise ratio and only under these conditions small but significant changes were detected, as seen for tyrosine hydroxylase.

1. Introduction

The first clinical immunoassay for detection of disease-related proteins using antigen-antibody-interactions was developed by Yalow and Berson in 1960s to quantify insulin in human blood (Yalow and Berson, 1996). For this technique, enzymes such as peroxidases were used to tag antibodies and, by addition of hydrogen peroxide as a substrate and tetramethylbenzidine as a chromogen, the reaction was photometrically detected. In the following years, such conjugates have been used during immunohistochemistry (IHC) investigations to target antigens directly in tissue samples, allowing the assessment of protein abundance at the cellular level (Grossman et al., 1998)

Later, IHC was combined with laser ablation inductively coupled plasma mass spectrometry (LA-ICP-MS) for element microscopy (Seuma et al., 2008). They used commercially available metal-tagged antibodies and a laser for ablating the whole tissue sample line by line. The

Abbreviations: DOTA, 1,4,7,10-tetraazacyclododecane-1,4,7,10-tetraacetic acid; DTPA, diethylenetriaminepentaacetic acid; GAPDH, glyceraldehyde 3-phosphate dehydrogenase; GFAP, glial fibrillary acidic protein; IHC, immunohistochemistry; LA-ICP-MS, laser ablation inductively coupled plasma mass spectrometry; MeCAT, metalcoded affinity tag; NeuN, neuronal nuclear antigen; Oxct1, Succinyl-CoA:3-ketoacid coenzyme A transferase 1; RSD, relative standard deviation; RT, room temperature; TH, tyrosine hydroxylase; α-Syn, α-synuclein

* Corresponding author.
E-mail address: karima.schwab@charite.de (K. Schwab).

https://doi.org/10.1016/j.jneumeth.2020.108591
Received 3 September 2019; Received in revised form 18 December 2019; Accepted 7 January 2020
Available online 08 January 2020

detected "mass fingerprints" of the multiple line scans were converted into two dimensional intensity profiles presenting the local distribution of the metal isotope and thus of the target protein. Imaging by LA-ICP-MS convinces with easy sample preparation, multi-elemental detection capabilities with high sensitivity and a spatial resolution in the micrometre range.

This first IHC approach from Seuma et al. (Seuma et al., 2008) was improved by Giesen et al. to a threefold multiplex using antibodies directed against three different biomarkers for breast cancer (Giesen et al., 2011). In 2014 and for the first time, Giesen et al. reached subcellular resolution (1 µm) for tissue samples in a multiplex immunoimaging approach using polymer tagged antibodies and LA-ICP-MS based on a time of flight instrument (Giesen et al., 2014). Thirty-two proteins and their modifications were simultaneously analysed in formalin-fixed paraffin-embedded human breast cancer sections and human mammary epithelial cells by use of metal-tagged antibodies (Giesen et al., 2014). Though feasibility of the LA-ICP-MS technology per se was well demonstrated, the study was limited however to samples derived from cancer tissue with well validated and highly abundant biomarkers, all of which with very high signal to noise ratio.

Various tagging methods for LA-ICP-MS were reported in literature (Giesen et al., 2012; Schwarz et al., 2014). For tagging chelates, macrocyclic compounds based on 1,4,7,10-tetraazacyclododecane-1,4,7,10-tetraacetic acid (DOTA) or linear chelates such as diethylenetriaminepentaacetic acid (DTPA) are used to strongly bind a metal, the latter is often a lanthanide element or one of its isotopes. Historically, chelating tagging compounds were first combined with radioactive tracers. McDevitt et al. presented a method for binding ^{225}Ac to a isothiocyanatobenzyl (SCN)-DOTA, and attached the complex to an IgG antibody (McDevitt et al., 2002). Soon after and for reasons related to safety, radioactive central ions were replaced by fluorescent lanthanides (e.g. Eu, Sm, Tb or Dy). The first immunoassay with ICP-MS and detection of metal labelled antibodies was introduced by the research group of Scott Tanner (Baranov et al., 2002). Later the technique was further improved by using polymer based lanthanide tags to increase sensitivity. Recently, Cruz-Alonso et al. used antibodies bio-conjugated with gold-nanoclusters which provide a high amplification factor in contrast to DOTA based labels (Cruz-Alonso et al., 2018).

Metal coding was first discussed by Whetstone et al. (Whetstone et al., 2004) while two years before Krause et al. (Krause et al., 2002) applied for a patent for a DOTA-based reagent with a cysteine reactive maleimide group with a biotin modification for purification and enrichment of tagged peptides via biotin-avidin affinity chromatography, named and patented as metal-coded affinity tag (MeCAT). Initially, tags containing only one detectable element atom per tag were used, but the sensitivity of ICP-MS was significantly increased through polymer tags (Lou et al., 2007).

To improve sensitivity, we have compared commercially available tagging reagents, such as polymer tags, SCN-DOTA and MeCAT. We found no high variations in sensitivity but a superior signal to noise (S/N) ratio for MeCAT (Waentig et al., 2012). Therefore, MeCAT was used in this investigation. A crucial point of LA-ICP-MS at a micrometre scale lies in the reduced laser spot size, which leads to a reduced ablated sample material and consequently to a severely decreased number of detectable atoms in the ablated area. Thus, a compromise between the number of tags per antibody and the size of the laser spot for ablation has to be found for every individual application. However, other factors such as total analysis time and analysis costs play an important role as well.

Noteworthy is also, that a valid normalisation is essential to overcome effects related to instrumental drift where high number of samples is ablated over a longer time period (Konz et al., 2012). Additionally, quantitative information can be gained if matrix matched calibration standards are applied (Wang et al., 2013). For internal standardisation and calibration in LA-ICP-MS, we have recently investigated a new approach using inks from commercial ink jet printer and, which are spiked with different elements (In, Th, Er and Pr). We have used this approach successfully on electroblot membranes (Hoesl et al., 2014) and tissue sections (Hoesl et al., 2016).

Therefore, it is the aim of this study to apply LA-ICP-MS in a multiplex mode using MeCAT tagged antibodies for simultaneous detection of proteins relevant to a disease. This approach is combined here with the concept of standardisation using metal-doped inks printed on top of the tissues, which will compensate for drift effects of the LA-ICP-MS instrument and guarantee day-to-day reproducibility. A conventional normalisation using housekeeping proteins such as ß-actin, GAPDH and OxcT1 (relatively quantified with MeCAT labelled antibodies) was used as a reference method.

As a model for Parkinson's disease, we used brain tissue from h-α-SynL62 mice and their wild-type controls. These mice overexpress α-synuclein, which accumulates in different neuronal populations. Indeed, accumulation of α-synuclein in substantia nigra neurons and the consequent dopamine deficit is a hallmark of Parkinson's disease, as these neurons seem highly susceptible to α-synuclein toxicity (Nieto et al., 2006). These neurons express the enzyme tyrosine hydroxylase (TH) to produce dopamine. Besides α-synuclein and TH, neuronal degeneration as well as inflammation have been associated with Parkinson's disease (Gelders et al., 2018).

We applied a multiplex LA-ICP-MS imaging approach to measure some proteins relevant to our mouse model. We report the successful use of indium-doped inks as internal standard to substitute housekeeping proteins. This approach allows a more accurate comparison between larger sample cohorts and to detect minimal differences otherwise not detected using conventional IHC. Moreover, we have demonstrated the feasibility of multiplexing MeCAT-tagged antibodies, an important aspect in research areas with limited access to valuable samples, as it is the case for various neurodegenerative disorders.

2. Material and methods

2.1. Animals

Homozygous male and female α-synuclein transgenic mice (h-α-Syn L62, hereinafter termed L62) and C57BL6/J wild-type litters (WT), aged 7 months, were used in this study and were all naïve. Detailed characterisation of these mice can be found in Frahm et al. (Frahm et al., 2018). Transgenic mice overexpress full-length human α-synuclein, fused to a membrane-targeting N-terminal signal sequence, under control of the mouse *Thy1*-promoter. A total of twenty mice were group-caged and maintained in acclimatised holding rooms with a 12 h light/dark cycle (lights on at 6 a.m.) and with food and water *ad libitum*. Mice were euthanised in the morning by cervical dislocation; the top of the skull was exposed, and the overlying bone plates removed to allow harvest of the brain in an intact state. The right brain hemisphere was fixed overnight in neutral buffered formalin, embedded in paraffin and used for histological analysis. All animal experiments were performed in accordance with the European Communities Council Directive (2010/63/EU) and approved by the German Animal Research Ethics Committee of LAGESO (A0213/13). Ten mice per genotype with equal male/female numbers were used. The choice to include both genotypes is based on previous findings, where no gender differences were identified in terms of histopathology (Frahm et al., 2018).

2.2. Antibodies

Neuronal α-synuclein accumulation was relatively quantified with an antibody against α-Syn (Syn 204, Santa Cruz Biotechnology). Mature neurons were stained with an antibody against the neuronal nuclear antigen (NeuN, Clone A60, Merck Millipore), while an antibody against tyrosine hydroxylase (TH, H-196 Santa Cruz Biotechnology), the rate-limiting enzyme of dopamine synthesis, was used to relatively quantify dopaminergic neurons. As marker for inflammation, glial cells were

Table 1
Description of antibodies used for MeCAT labelling. AB: antibody, mAB: monoclonal antibody, pAB: polyclonal antibody.

Antigen	Antibody	Immunogen/ Epitope	Provider	Concentration AB [µg µL^{-1}]	Contaminants	Clean up	MeCAT-metal	Concentration AB-MeCAT [µg µL^{-1}]
α-Syn	Syn 204 (mAB)	human AA 95-109	SC Biotechnology (sc-32280)	1.0	0.1% gelatin	+	Eu	0.295
GFAP	Anti-GFAP (pAB)	cow spinal cord; not specified	Dako (# Z0334)	1.0	–	–	Ho	0.422
NeuN	Anti-NeuN (mAB)	mouse; not specified	Merck Millipore (Clone A60)	1.0	–	–	Pr	0.592
TH	Anti-TH (pAB)	human AA 1-196	SC Biotechnology (sc-14007)	1.0	0.1% gelatin	+	Tb	0.456
Oxct1	Anti-Oxct1 (pAB)	human AA 171-434	Abcam (ab105320)	1.0	–	–	Lu	0.825
ß-Actin	Anti-ß-Actin (mAB)	mouse; N-terminal	Sigma (A1978)	1.0	–	–	Nd	0.502
GAPDH	Anti-GAPDH (mAB)	Human full length	Abcam (ab9484)	1.0	–	–	Er	0.079

stained with an antibody against glial fibrillary acidic protein (GFAP, Dako). Antibodies against the housekeeping proteins ß-actin, glyceraldehyde 3-phosphate dehydrogenase (GAPDH) and Succinyl-CoA:3-ketoacid coenzyme A transferase 1 (OxcT1) were used as reference proteins for conventional normalisation.

Seven antibodies were tagged with MeCAT reagents (see Table 1) and used for antigen labelling of formalin-fixed paraffin-embedded brain sections as described below.

Conventional IHC experiments were conducted with unlabelled antibodies against α-Syn (Supplementary Table 2), TH (Supplementary Table 3), NeuN (Supplementary Table 4) or GFAP (Supplementary Table 5).

LA-ICP-MS imaging was performed with MeCAT-tagged antibodies. Experiments were run either in a single-plex manner (either α-Syn, TH, NeuN and GFAP, see Supplementary Tables 6–9 respectively), or in a multiplex manner, where each section was incubated with all seven antibodies at the same time (Syn 204, GFAP, NeuN, TH, ß-actin, GAPDH and Oxct1 altogether, see Supplementary Tables 10-13.

2.3. Clean up of antibodies formulated with gelatin

To remove excessive protein contamination of antibodies formulated with gelatin (see Table 1), a dedicated clean-up kit was used following the manufacturer's protocol (Pierce Antibody Clean-Up Kit, Cat# 44600, Thermo Scientific).

2.4. Lanthanide labelling of antibodies with MeCAT reagent

For MeCAT labelling, the method described earlier was used (Waentig et al., 2012). MeCAT loaded with the lanthanide of choice was prepared by Proteome Factory (Berlin, Germany). Reaction steps were performed in a centrifugal ultra-filtration device (30 kDa cut-off; Nanosep, VWR, Darmstadt, Germany). All reagents were dissolved in Tris buffer (20 mM Tris, 150 mM NaCl, 2.5 mM EDTA, pH 7). A molar excess rate of 600 of TCEP relative to antibody molarity was used for 30 min at 37 °C. For purification two washing steps using Tris buffer (see above) were conducted using ultra-filtration at 7,500 x *g* until hold-up volume was reached. After washing, the antibodies were tagged with the respective MeCAT-reagent with a 20-fold molar excess of MeCAT. The mixture was incubated for 60 min at 37 °C, followed by two washing steps using Tris buffer (see above) to purify the labelled antibody on the ultra-filtration membrane.

2.5. IHC and LA-ICP-MS imaging

Formalin-fixed, paraffin-embedded brain tissue was cut into 5 µm thin coronal sections (HM 325 Rotary Microtome, Thermo Scientific) at levels containing the substantia nigra, an area responsible for dopamine production and at Bregma 3.80 ± 0.25 mm, (Paxinos and Franklin, 2008). Duplicate consecutive sections for each animal and antibody were collected on SuperFrost® plus microscope glass slides (R. Langenbrinck GmbH, Germany), deparaffinised and used for IHC and LA-ICP-MS imaging. For IHC and single-plex- LA-ICP-MS ten mice per genotype and antibody were used (if not otherwise stated), while for multiplex experiments, six mice per genotype were used (see Table 2).

For IHC a method described earlier was used (Frahm et al., 2018). Briefly, sections were boiled in 10 mM citric buffer for antigen retrieval, incubated in 0.3% (v/v) hydrogen peroxidase solution and blocked for 20 min in blocking buffer (0.1% (w/v) BSA in PBS). Sections were then incubated either with antibodies Syn 204 (diluted 1:100), GFAP (diluted 1:500), NeuN (diluted 1:500) or TH (diluted 1:100) for 1 h at RT, followed by incubation with corresponding biotinylated secondary antibody (Dako, Denmark). Sections were developed with diaminobenzidine solution (Dako, Denmark), counterstained with Ehrlich haematoxylin solution (Carl Roth, Germany), embedded in Neo-Mount® (Merck Millipore, Germany) and images taken using a light microscope (Carl Zeiss, Jena, Germany). Those sections underwent conventional IHC evaluation. For this, immune-reactive signals for α-synuclein, NeuN or GFAP were quantified in relative manner for the whole right brain hemisphere without region specificity, while TH-positive dopaminergic neurons were counted in substantia nigra. Alpha-synuclein and TH positive neurons were counted manually, while NeuN and GFAP immunoreactivity was quantified as integrated density in 8-bit images using the ImageJ software (version 1.48v, NIH Image, National Institutes of Health, USA).

For single-plex (Syn 204, GFAP, NeuN or TH) and multiplex (Syn 204, GFAP, NeuN, TH, ß-actin, GAPDH and Oxct1) experiments, the antibodies (for details see Table 1) were applied for 1 h at RT, after antigen retrieval and blocking as described above. Syn 204 and TH were diluted 1:100, GFAP and NeuN were diluted 1:500, anti-ß-actin, anti-Oxct1 and anti-GAPDH were diluted to 0.5 µg/ml. Thereafter, the tissue was washed three times in 12 mM PBS buffer and air-dried overnight. After complete dryness, sections were coated with gelatin as described below.

2.6. Gelatin coating of microscope glass slides bearing brain tissue sections

To improve the efficacy of ablation and reduced in-between-sample variations, brain sections for LA-ICP-MS were treated with gelatin prior spiking of the internal standard. Treatment of glass slides with gelatin at different concentrations versus non-treated glass slides was evaluated during these pilot-experiments. Briefly, gelatin (Carl Roth, Karlsruhe) was dissolved in water, boiled and kept at 80 °C. SuperFrost® plus microscope glass slides with tissue sections were immersed into the hot

gelatin solution (either 2% or 5%) for about two seconds. After wiping the glass slide's bottom side and outer edges to remove excess gelatin solution, the slides were heated at 95 °C in horizontal position to allow the gelatin solution to completely dry. The gelatin coating procedure was conducted three times to guarantee an appropriate surface for printing of the standard solution. At this point the evenness of the gelatin layer itself was negligible since the ablation plane is identical to the plane of the internal standard application. Nevertheless, the thickness of the gelatin layers was measured as described below. Furthermore, the UV laser intensity was adjusted to completely ablate all of the UV-recipient organic material while leaving the glass slides blank.

To measure the thickness of the gelatin layer under final coating conditions, three glass slides without tissue sections were used. Three positions were marked on the glass slide and the thickness of each uncoated glass slide was determined using a 25 mm micrometer gauge (Carl Zeiss, Jena, Germany) for each of these three positions. Subsequently, the slides were coated five times with 5% gelatin solution as described above. After drying, the thickness at each of the three positions on each slide was measured. The coating procedure was repeated for additional 5 times (10 coating layers in total) and the thickness determined. The resulting 27 data points (3 positions on 3 glass slides and with 0, 5 and 10 coating layers) were plotted and to generate a standard curve for estimating the thickness of the gelatin.

2.7. Inkjet printer mediated spiking of indium as an internal standard

Indium-containing ink was used as internal standard and was printed on top of microscope glass slides (containing brain tissue sections) as previously described with some modifications (Hoesl et al., 2014). The standard was intentionally not spiked into the gelatin solution to circumvent variations of the standard concentration, which might emerge from unequal drying of the gelatin as observed for the edges of the glass slides.

In brief, the gelatin-coated glass slides were heated to 95 °C using a heat plate (Heidolph MR3100, Germany), transfered to the compact disc printing drawer (polystyrol, $t_m \approx 100$ °C) of a commercially available inkjet printer. The glass slides were printed three times with yellow ink spiked with 100 µg mL^{-1} indium (100 ppm). A relative printing density of 20% was selected in the printer settings dialog. Printing was performed in high-resolution mode (4800 dpi x 2400 dpi) with printing colour management disabled. In between printing cycles, the glass slides were incubated at 95 °C on the heat plate for rapid drying.

2.8. LA-ICP-MS imaging

A commercial LA system (NWR213, New Wave Portland, USA) with a beam expander and laser spot size between 4 µm and 250 µm, was attached to an ICP sector field mass spectrometer (Element XR, Thermo Fisher Scientific, Germany). The ICP-MS was synchronised with the LA unit in an external trigger mode. The slides with the brain tissue sections, coated with gelatin and spiked with indium-containing ink, were placed in the sample holder and inserted into a two-volume cell (NWR213). Ablation was conducted in a differential line scan mode with an approximate overlap of 10% in laser ablation areas to its preceding line as described by Giesen et al. (Giesen et al., 2014).

The aerosol was transported by helium at a flow rate of 1 L min^{-1} and argon was added at a typical flow rate of 0.8 L min^{-1} in front of the ICP torch. The LA-ICP-MS was tuned daily for maximum ion intensity and low oxide ratio (ThO/Th ratio < 3%) and a relative standard deviation (RSD) for thorium ≤ 5%. The tuning was conducted on a microscopic glass slide. Samples were completely ablated line by line under optimised LA-ICP-MS conditions (0.20-0.25 mJ) as summarised in supplementary Table 1. The following isotopes were selected: ^{113}In, ^{141}Pr, ^{146}Nd, ^{153}Eu, ^{159}Tb, ^{165}Ho, ^{166}Er, ^{175}Lu.

For analysis of the tissue sections, spot sizes of 35 and 130 µm and scan speeds of 50 and 150 µm s^{-1} were used, respectively.

The LA-ICP-MS data were imported to Origin 8 (Origin lab Corporations, Northampton, USA) where intensity time profiles or color-coded images were produced by transforming the scan time into a micrometre scale. Signal intensities were colour coded in a way that low intensities are shown in blue and high intensities in red colour. The data normalisation was performed in Excel (Microsoft, Redmond, USA) by multiplication of each lanthanide data point with an individual normalisation factor derived from the indium signal:

$$I_{norm.}^{Lanthanide} = I^{Lanthanide} * \frac{I_{mean}^{Indium}}{I^{Indium}}$$

For quality assessment, the ICP-MS instrumentation was optimised weekly using a micro mist nebuliser and a liquid standard in a cyclone spray chamber (Glass Expansion, Melbourne, Australia) at a transport gas rate of 1 L min^{-1}. The settings for the ion lenses and the high frequency power were optimised with a tune standard solution containing sodium, indium and uranium at a concentration of one ng mL^{-1}. All optimisation steps were carried out at a low-resolution setting of R = 300 at a sample uptake rate of 1 mL min^{-1}. Minimal signal parameters for the optimisation were chosen as follow: 1.2×10^6 cps for indium and 1.8×10^6 for the uranium signal at a RSD < 2%. Additionally, for the LA-ICP-MS analysis, an optimisation of the gas flows, the plasma torch position and the ion lenses settings were conducted daily. Conventional nickel cones were used for the interface regions of LA-ICP-MS instrument (Element XR, Thermo Fisher Scientific, Bremen, Germany). For comparison with the results from IHC, all measured samples were normalised, and background corrected intensities were integrated for the whole brain section.

2.9. Data analyses

Data for IHC and LA-ICP-MS were expressed as group mean and standard error (S.E). Statistical analyses were conducted with GraphPad Prism (version 6.00; GraphPad Software Inc., La Jolla, CA, USA), using unpaired t-test. The null hypothesis was accepted for $\alpha < 0.05$ and only significant terms are given in the text.

3. Results and discussion

3.1. Study design

Within this study, the abundance of four Parkinson's disease-related proteins was analysed in brain tissue of L62 α-synuclein transgenic mice using LA-ICP-MS imaging and IHC. These mice overexpress human α-synuclein under control of the *Thy-1*-promoter and are characterised by accumulation of α-synuclein in different neuronal populations, neuronal degeneration and progressive motor deficits (Frahm et al., 2018). Further, these mice exhibit dopamine depletion without frank loss of TH-positive, dopamine-producing neurons of the substantia nigra, the main source of dopamine (Frahm et al., 2018). It has been shown before that L62 released less dopamine under pharmacological stimulation. Nevertheless, no changes in the number of dopamine-producing, TH-positive cells was found using IHC, nor in the abundance of TH as found by electroblotting (Frahm et al., 2018). In addition, L62 mice exerted some gliosis, evident as elevated number of GFAP-positive neurons in multiple brain areas, such as the cortex, the hippocampus and the substantia nigra (data not shown). In focus of this work were therefore the four proteins α-Syn, TH, NeuN and GFAP. Brain sections from L62 (n = 10) and their WT controls (n = 10) were used to access the relative protein abundance. Each group had identical distribution of gender (5 female (f) and 5 male (m)). Furthermore, for each animal two adjacent sections were prepared (two technical replicates).

To evaluate the robustness of LA-ICP-MS imaging, a parallel approach with conventional IHC was performed using replicate brain sections. In deviation to conventional IHC staining, primary antibodies

used here were tagged with MeCAT.

An obvious reason for superiority of LA-ICP-MS over IHC is that LA-ICP-MS imaging can be operated in a multiplex mode. Theoretically, for lanthanide elements a 32-plex mode is possible, using enriched isotopes. However, some isotopes can have interferences with other lanthanide elements and should be selected accordingly. In general, IHC is mostly operated in a single-plex manner, except for immunofluorescence, where three antibodies can be applied simultaneously. Further, IHC is based on peroxidase-tagged antibodies with 3,3′-Diaminobenzidine as a substrate and is not an endpoint reaction. Consequently, and because any standardisation is lacking, day-to-day or lab-to-lab variations cannot be excluded. Consequently, study cohorts need to undergo the IHC procedure at the exact same time, which is not convenient for large cohorts. On the contrary, such variations can be well managed during LA-ICP-MS simply by introducing internal standards. One approach to address this standardisation issue for LA-ICP-MS imaging examinations is either using different housekeeping proteins or spiked internal standards, and both will be discussed below.

3.2. Internal standardisation using housekeeping proteins

To correct for instrument drift, minimise background noise and to compensate for small variations of tissue section thickness, internal standardisation using different housekeeping proteins was applied. For this, the respective signals for the four Parkinson's disease-related antibodies directed against the proteins α-Syn (^{153}Eu), TH (^{159}Tb), NeuN (^{141}Pr) and GFAP (^{165}Ho) were extracted from the acquired data and normalised to the signals of the three antibodies directed against the housekeeping proteins GAPDH(^{166}Er), Oxct1 (^{175}Lu) and β-Actin (^{146}Nd). Those normalised values were used to generate 2D-intensity profiles and representative images are shown in Fig. 1.

As shown in the Fig. 1 normalisation using each of three housekeeping proteins resulted in obviously different images. While the Oxct1-normalised signal shows low background for the four proteins of interest, it also lowers the contrast for positive areas (e.g. TH^{159}Tb/^{175}Lu). On the other hand, β-Actin normalisation provides satisfactory results for α-Syn (^{153}Eu), as it results in a homogenous distribution, but fails for GFAP (^{165}Ho/^{146}Nd) where it enhances the area of false positive staining. Moreover, normalisation via housekeeping proteins leads to high background signals, when data were acquired at higher resolution using 35 µm (data not shown). Mixed effects were observed for all three housekeeping protein mediated normalisation approaches. For some antigens, they enhanced the contrast or minimised the background but there was no obvious improvement of the data. Overall, the distribution of the selected housekeeping proteins is too heterologous to be recommended to act as a reference for internal standardisation. However, it appears that housekeeping protein related normalisation could be useful in selected limited cases only.

3.3. Internal Standardisation using inkjet printer spiked indium as internal standard

As an alternative for internal standardisation during LA-ICP-MS examination, ink jet printing of metal containing inks were already applied to overcome instrumental drift effects of the laser ablation and ICP-MS system. We have recently published an approach using ink spiked with different elements, such as In, Th, Er and Pr. The ink was applied to samples with a commercial ink jet printer and this was successfully used on electro blot membranes (Hoesl et al., 2014) and tissue sections (Hoesl et al., 2016; Moraleja et al., 2018, 2016). This approach will be used here to overcome also day-to-day variations, which is a prerequisite for a long-term study.

Microscope glass slides have an individual surface character, which may cause inhomogeneity during application of hydrophilic ink formulations for standardisation. For example, we observed that in some areas the ink might roll off the surface and accumulate in certain droplet clusters. To overcome this obstacle, empty glass slides (with no brain tissue sections) were coated with a layer of gelatin (Moraleja et al., 2016). Gelatin was applied at two different concentrations of either 2% or 5%. The homogeneity of the printed indium-spiked ink application was evaluated using two different laser spot sizes for the ablation (130 µm vs. 35 µm). Random areas within the printed areas of the glass slides were ablated and with LA-ICP-MS. The resulting signal heights, as well as absolute and relative standard deviations (SD and RSD) were extracted or calculated respectively and plotted. The false-colour heat-maps for the acquired data of around 3 mm x 5 mm area are given in Fig. 2.

Application of internal standard onto uncoated sample slides resulted in inhomogeneity, which is reflected by the insufficient RSD value (44%, see Fig. 2). The RSD was improved to 27% through coating with 2% gelatin and using a spot size of 130 µm. The improvement was ameliorated when the gelatin concentration was increased to 5% (8 % RSD). The enhancement of the homogeneity mediated by the treatment with 5% gelatin solution was also observed using a laser spot size of 35 µm (RSD 14%).

In summary, these experiments revealed that gelatin coating greatly enhances the homogeneity of the internal standard distribution (^{115}In) applied by inkjet printing. Therefore, all following LA-ICP-MS imaging experiments were done using 5% gelatin for brain tissue coating followed by indium printing and all intensity measurements were normalised to this isotope. The gelatine layer had a thickness of 6.47 ± 0.62 µm (data not shown).

3.4. Effect of laser spot size on image resolution and quality

Obvious from the heat map figure from the gelatin experiments described above (Fig. 2), the resolution of the measurement is significantly dependent on the laser spot size. During LA-ICP-MS imaging, a huge amount of data is being acquired, with to date no software available for automatic data evaluation and construction of the surface plots. Thus, a compromise between resolution and time consumption must be found.

Using the sections designed for LA-ICP-MS imaging and after antibody application (α-Syn (^{153}Eu), TH (^{159}Tb), NeuN (^{141}Pr) and GFAP (^{165}Ho)), gelatin coating (5%) and indium-spiking (^{115}In), sections were ablated with laser spot sizes of either 130 µm or 35 µm. Velocity of the laser was changed to match the spot size, as given in the figure legends (Fig. 3 and Fig. 4). For the 130 µm, spot size we used a laser scanning velocity of 150 µm s^{-1} and for the 35 µm spot size a velocity of 50 µm s^{-1} was used.

A characteristic distribution for the four proteins of interest was detected with either spot size. This is obvious from comparison with the IHC results obtained in this work (see micrograph in Fig. 5) and, which are in line with previously published data (Frahm et al., 2018). Though reducing the spot size from 130 µm to 35 µm decreased the amount of ablated sample and consequently of the measured signal, nevertheless the signal intensity obtained with 35 µm had enough signal to noise ratio. As expected, the resolution and the contrast of the pictures obtained was enhanced with the lower size of the laser spot (compare Fig. 3 for 130 µm and Fig. 4 for 35 µm), as the pictures obtained with 35 µm spot size seem less blurry. Apparent is also that the difference in local protein distribution is quite large, and this was much less appreciated from staining derived from IHC. From this data, it is obvious that the dynamic range is one of the main differences between LA-ICP-MS imaging and IHC and this have been well reviewed (Bodenmiller, 2016).

As stated above, a higher local resolution is achieved using a smaller spot size but the total analysis time for each sample is increased to 8 h, whereas for the spot size of 130 µm only 3 h are needed. For this reason, six samples were selected for measurements with the higher local resolution, to demonstrate the high quality of the multiplex measurements, but for data analysis and for comparison with the IHC all

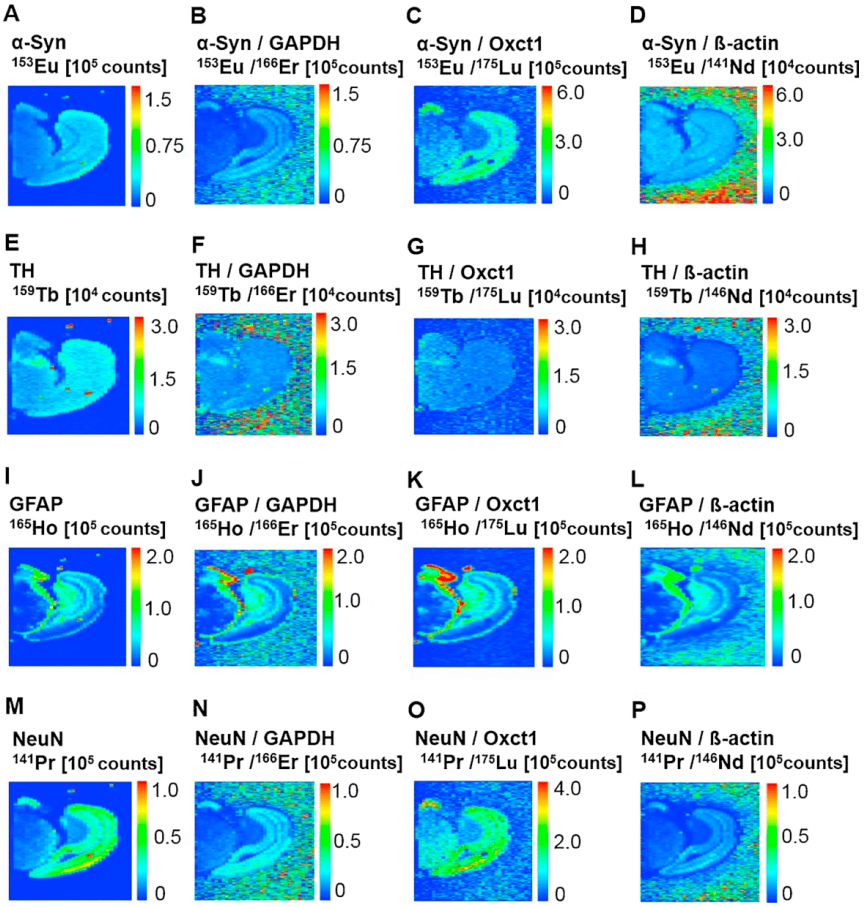

Fig. 1. The effect of normalisation based on housekeeping proteins. Representative intensity images for the four proteins α-Syn (A–D), TH (E–H), GFAP (I–L) and NeuN (M–P) with and without housekeeping protein-based normalisation. The ablation was conducted using a laser spot size of 130 µm. The intensity profiles without normalisation are shown for α-Syn (A), TH (E), GFAP (I) and NeuN (M). Three different housekeeping proteins were used for normalisation: GAPDH (B for α-Syn, F for TH, J for GFAP and N for NeuN), Oxct1 (C for α-Syn, G for TH, K for GFAP and O for NeuN) and ß-actin (D for α-Syn, H for TH, L for GFAP and P for NeuN). All antibodies used were labelled with MeCAT-lanthanides: anti-α-Syn-MeCAT(^{153}Eu), anti-TH-MeCAT(^{159}Tb), anti-GFAP-MeCAT(^{165}Ho), anti-NeuN-MeCAT(^{141}Pr), anti-GAPDH-MeCAT (^{166}Er), anti-Oxct1-MeCAT(^{175}Lu) and anti-β-actin-MeCAT(^{146}Nd).

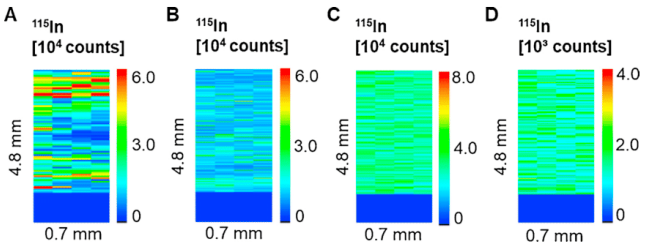

Fig. 2. The effect of gelatin-coating on ablation of the internal standard ^{115}In. Representative intensity images zoomed for illustration of ^{115}In-spiked glass slides non-coated (A) and coated with 2% gelatin (B) or 5 % gelatin (C) and ablated with a laser spot size of 130 µm (A–C) or 35 µm (D). The internal standard ^{115}In was applied using a commercial inkjet printer.

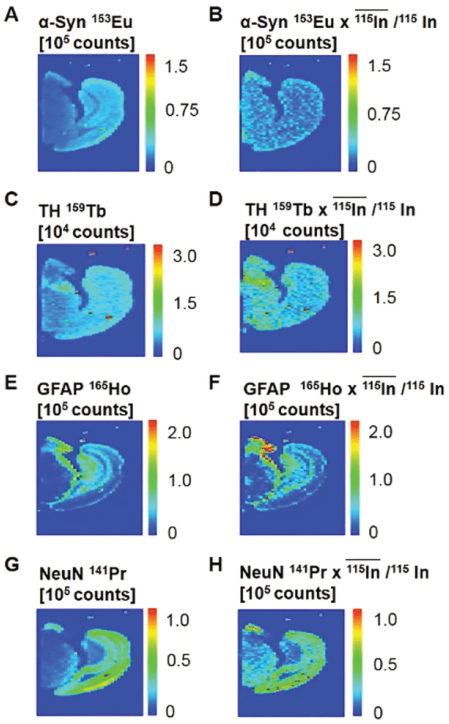

Fig. 3. Normalisation of α-Syn, TH, GFAP and NeuN using ^{115}In as a standard and a large laser size for ablation. Representative midbrain image plots from sections tagged with antibodies against α-Syn (A and B), TH (C and D), GFAP (E and F) and NeuN (G and H) using no normalisation (A, C, E and G) or normalisation with the internal standard ^{115}In (B, D, F and H). The internal standard ^{115}In was applied on top of the brain sections using an inkjet printer. Samples were ablated with a laser spot size of 130 µm and analysed by ICP-MS. All antibodies used were labelled with MeCAT-lanthanides: anti-α-Syn-MeCAT(^{153}Eu), anti-TH-MeCAT(^{159}Tb), anti-GFAP-MeCAT(^{165}Ho), anti-NeuN-MeCAT(^{141}Pr). All data were acquired with simplex LA-ICP-MS.

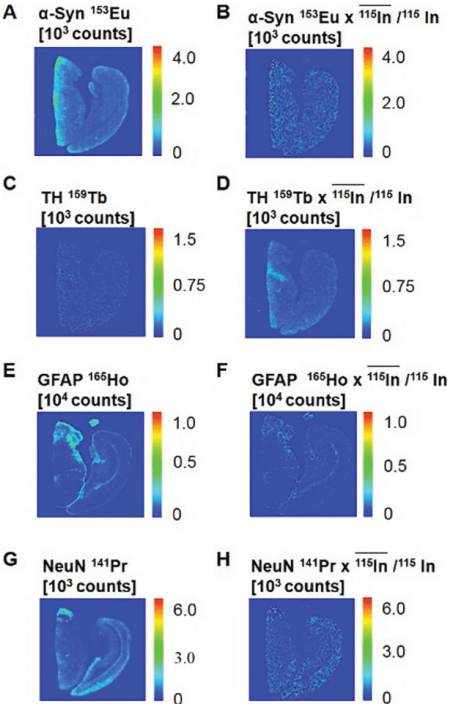

Fig. 4. Normalisation of α-Syn, TH, GFAP and NeuN using ^{115}In as a standard and a small laser size for ablation. Representative midbrain image plots with antibodies against α-Syn (A and B), TH (C and D), GFAP (E and F) and NeuN (G and H) using no normalisation (A, C, E and G) or normalisation with the internal standard ^{115}In (B, D, F and H). The internal standard ^{115}In was applied on top of the brain section using an inkjet printer. Samples were ablated with a laser spot size of 35 µm and analysed by ICP-MS. All antibodies used were labelled with MeCAT-lanthanides: anti-α-Syn-MeCAT(^{153}Eu), anti-TH-MeCAT(^{159}Tb), anti-GFAP-MeCAT(^{165}Ho), anti-NeuN-MeCAT(^{141}Pr). All data were acquired with simplex LA-ICP-MS.

information were gained with the lower resolution of 130 µm only. The integrated raw data were normalised to the respective ^{115}In signals acquired at identical location.

3.5. Critical review of IHC and LA-ICP-MS imaging

As stated above, L62 mice were presented with accumulation of α-Syn (increased number of α-Syn-positive neurons), neuronal degeneration (decreased number of NeuN-positive neurons), gliosis (increased number of GFAP-positive neurons), as well as a hypodopaminergic state. Though we were not able to measure any changes related to TH, neither with IHC (current work and (Frahm et al., 2018)), not electro blotting (Frahm et al., 2018), the dopaminergic phenotype was evident from pharmacological studies and was highly significant (Frahm et al., 2018). During the current work, we aimed to relatively quantify the four above-mentioned proteins using single-plex and multiplex-LA-ICP-MS. Those results were further compared and validated with conventional IHC.

Representative IHC micrographs for WT and L62 mice are shown in Fig. 5(A–D for WT and E–H for L62). During IHC examinations, α-Syn-positive and TH-positive neurons were counted manually, while GFAP and NeuN relative immunoreactivity signals were quantified as integrated density using the ImageJ tool. As shown in Fig. 5, L62 mice exhibited a significantly higher number of α-Syn-positive neurons ($p < 0.0001$, Fig. 5I), while no differences in TH-positive neurons were seen (Fig. 5J), when compared to WT. Relative to WT, GFAP-immunoreactivity significantly increased ($p = 0.0043$, Fig. 5K) and NeuN-immunoreactivity was significantly decrease ($p < 0.0001$, Fig. 5L) in L62 mice. All those observations are in line with data reported before (Frahm et al., 2018).

Relative quantification for single-plex LA-ICP-MS derived plots revealed very similar results for α-Syn ($p < 0.0001$, Fig. 6A), GFAP ($p < 0.0001$, Fig. 6C) and NeuN ($p < 0.0001$, Fig. 6D), but the statistical power for the GFAP results obtained by LA-ICP-MS imaging was superior to that obtained by IHC. As for TH, examination with LA-ICP-MS revealed a subtle but a statistically highly significant relative decrease of TH-signal in L62 compared to WT ($p = 0.009$, Fig. 6B). This agrees with the pharmacologically measured hypodopaminergic state and reveals clearly that this extra information could be obtained by LA-ICP-MS imaging only. The discrepancy for TH results derived from LA-ICP-MS and IHC might be related to higher dynamic range offered by LA-ICP-MS and, which is enhanced by internal standardisation. In summary, we found for LA-ICP-MS imaging a higher dynamic range and

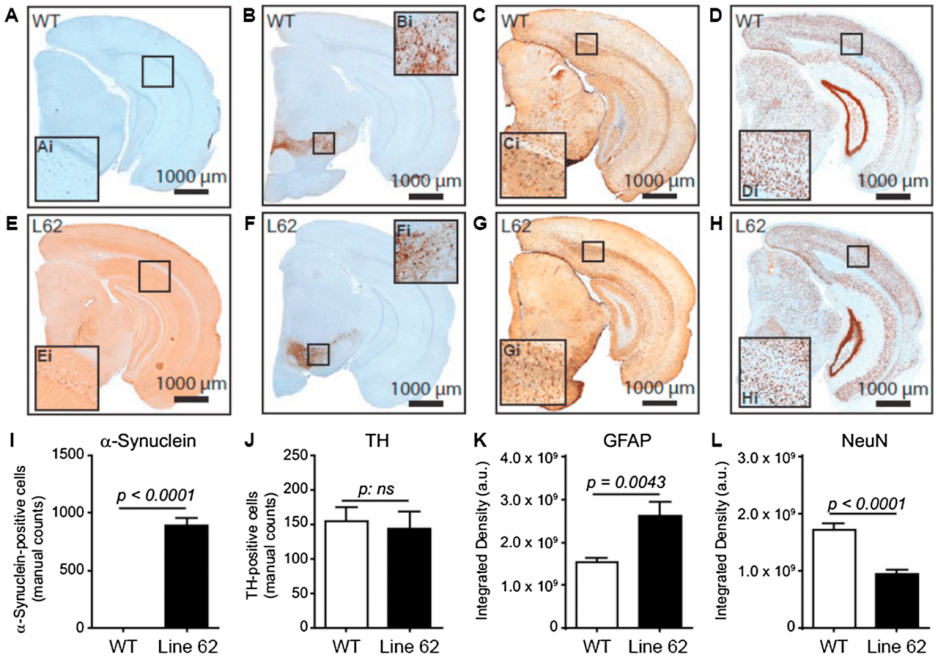

Fig. 5. Quantification of α-Syn, TH, GFAP and NeuN using IHC. Representative micrographs from midbrain of WT (A–D) and L62 (E–H) brain sections stained with antibodies against α-Syn (A and E), TH (B and F), GFAP (C and G) and NeuN (D and H) using conventional IHC. Immuno-reactive signals for α-Syn, NeuN and GFAP were relatively quantified in the whole right brain hemisphere without region specificity, while TH-positive dopaminergic neurons were counted in substantia nigra, the only immune-reactive region in the brain area analysed. Alpha-Syn and TH positive neurons were counted manually, while NeuN and GFAP immune-reactivity was quantified relatively as integrated density using the ImageJ software. Two sections per mouse and antibody were analysed and the mean value over sections for each mouse was calculated and used for analyses. Quantitative values are shown as group mean + S.E. for α-Syn (I), TH (J), GFAP (K) and NeuN (L). Statistical analysis was conducted with unpaired t-test. N = 6–10 for WT and 9–10 for L62 per antibody. For more details on cohorts, see Supplementary Tables.2–5.

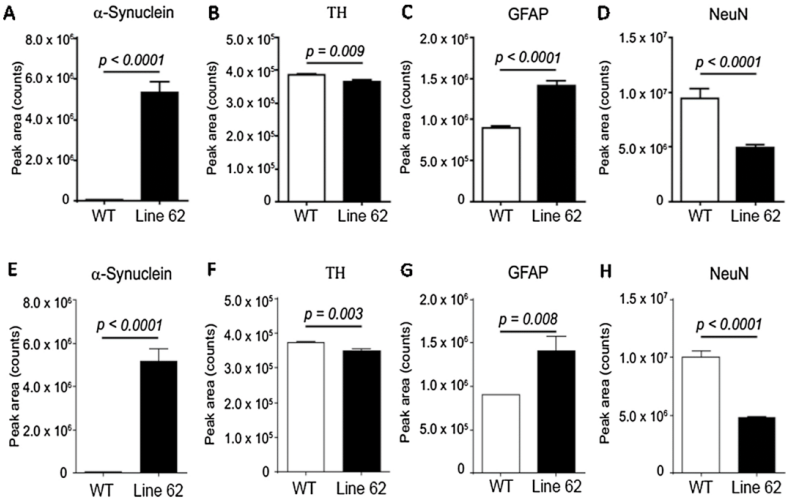

Fig. 6. Relative quantification of α-Syn, TH, GFAP and NeuN using single-plex LA-ICP-MS (A–D) and multiplex- LA-ICP-MS (E–H). Proteins from brain sections of WT and L62 were detected using MeCAT-tagged antibodies against α-Syn (A and E), TH (B and F), GFAP (C and G) and NeuN (D and H) and spiked with the internal standard ^{115}In using an inkjet printer. Samples were ablated with a laser spot size of 130 µm and analysed by ICP-MS. All antibodies used were tagged with MeCAT-lanthanides: anti-α-Syn-MeCAT(^{153}Eu), anti-TH-MeCAT(^{159}Tb), anti-GFAP-MeCAT(^{165}Ho), anti-NeuN-MeCAT(^{141}Pr). For each antibody, the acquired values were normalised to the internal standard ^{115}In. Two sections per mouse and antibody were analysed and the mean value over sections for each mouse was calculated and used for analyses. Semi-quantitative values are shown as group mean + S.E. for α-Syn (A and E), TH (B and F), GFAP (C and G) and NeuN (D and H). Statistical analysis was conducted with unpaired t-test. N = 5–9 for WT and 4–10 for L62 per antibody. For more details on cohorts and their respective size, see Supplementary Tables 6–9 for single-plex and 10–14 for multiplex LA-ICP-MS.

higher sensitivity compared to IHC, which allowed unravelling small changes, otherwise not detectable. Furthermore, the specificity of the four antibodies used here was not compromised by the lanthanide-MeCAT labelling procedure and was preserved during multiplex experiments, where we applied seven antibodies simultaneously (Fig. 6E–H). As obvious from bar graphs, multiplex-LA-ICP-MS revealed similar results as the single-plex experiments: α-Syn-positive neurons were increased in L62 compared to WT mice ($p < 0.0001$, Fig. 6E), TH-positive neurons were decreased in L62 mice ($p = 0.003$ Fig. 6F), GFAP-immunoreactivity was significantly increased ($p = 0.008$, Fig. 6G) and NeuN-immunoreactivity significantly decreased ($p < 0.0001$, Fig. 6H) in L62 mice relative to WT. Thus, for the tagging conditions used here our results are not limited by molecular hindering or loss of specificity.

4. Conclusion

Collectively, we have shown that the internal standardisation using indium-doped inks printed onto samples by a commercial printer is an effective method to overcome day-to-day variations and instrumental drifts. The distribution of the standard was further improved by coating the samples by gelatin. This relatively simple approach was a pre-requisite for a long-term large cohort study. It could be used to overcome in-between lab variations if applied together with known reference material. Further, we have shown the feasibility of multiplexing MeCAT-tagged antibodies without compromising antibody specificity in an imaging approach using LA-ICP-MS. This study was limited to seven isotopes but only by the relatively slower scanning ability of our ICP-MS instrument. Theoretically, this number can reach 40 isotopes (Wang et al., 2013) if fast scanning CyTOF-MS is coupled to a novel laser ablation system with much shorter wash out times. Thus, the higher laser repetition rates and faster laser scanning conditions could be used in future studies to reduce analysis time or alternatively to use a higher lateral resolution.

Author contributions

BN, SH and KS designed and performed experiments and analysed the data; KS performed statistical analyses; BN, KS and NJ conceived the project and wrote the paper and all authors read and reviewed the final manuscript.

Funding

SH received financial support by the “Bundesministerium fuer Wirtschaft und Energie, Projektnummer MNPQ 09/10″.

Declaration of Competing Interest

BN and SH were employed by Proteome Factory AG. NJ was employed by Spetec GmbH. The other authors declare that the research was conducted in the absence of any commercial or financial relationships that could be construed as a potential conflict of interest.

Acknowledgments

The authors acknowledge Mandy Magbagbeolu for the technical support with brain tissue sectioning and immunohistological staining. We also thank Prof. Christian Scheler for his support of this study. The MS-data was acquired at Bundesanstalt für Materialforschung und -prüfung (BAM), Richard-Willstaetter-Strasse 11, 12,489 Berlin, Germany in the former research group of Nobert Jakubowski (retired). We thank TauRx Therapeutics Ltd. (Singapore) for their permission to use the L62 mice.

Appendix A. Supplementary data

Supplementary material related to this article can be found, in the online version, at doi:https://doi.org/10.1016/j.jneumeth.2020.108591.

References

Baranov, V.I., Quinn, Z., Bandura, D.R., Tanner, S.D., 2002. A sensitive and quantitative element-tagged immunoassay with ICPMS detection. Anal. Chem. 74, 1629–1636. https://doi.org/10.1021/ac0110350.

Bodenmiller, B., 2016. Multiplexed epitope-based tissue imaging for discovery and healthcare applications. Cell Syst. 2, 225–238. https://doi.org/10.1016/J.CELS.2016.03.008.

Cruz-Alonso, M., Fernandez, B., García, M., González-Iglesias, H., Pereiro, R., 2018. Quantitative imaging of specific proteins in the human retina by laser ablation ICPMS using bioconjugated metal nanoclusters as labels. Anal. Chem. 90, 12145–12151. https://doi.org/10.1021/acs.analchem.8b03124.

Frahm, S., Melis, V., Horsley, D., Rickard, J.E., Riedel, G., Fadda, P., Scherma, M., Harrington, C.R., Wischik, C.M., Theuring, F., Schwab, K., 2018. Alpha-Synuclein transgenic mice, h-α-SynL62, display α-Syn aggregation and a dopaminergic phenotype reminiscent of Parkinson’s disease. Behav. Brain Res. 339, 153–168. https://doi.org/10.1016/j.bbr.2017.11.025.

Gelders, G., Baekelandt, V., Van der Perren, A., 2018. Linking neuroinflammation and neurodegeneration in parkinson’s disease. J. Immunol. Res. 2018, 1–12. https://doi.org/10.1155/2018/4784268.

Giesen, C., Mairinger, T., Khoury, L., Waentig, L., Jakubowski, N., Panne, U., 2011. Multiplexed immunohistochemical detection of tumor markers in breast cancer tissue using laser ablation inductively coupled plasma mass spectrometry. Anal. Chem. 83, 8177–8183. https://doi.org/10.1021/ac2016823.

Giesen, C., Waentig, L., Panne, U., Jakubowski, N., 2012. History of inductively coupled plasma mass spectrometry-based immunoassays. Spectrochim. Acta - Part B At. Spectrosc. 76, 27–39. https://doi.org/10.1016/j.sab.2012.06.009.

Giesen, C., Wang, H.A.O., Schapiro, D., Zivanovic, N., Jacobs, A., Hattendorf, B., Schüffler, P.J., Grolimund, D., Buhmann, J.M., Brandt, S., Varga, Z., Wild, P.J., Günther, D., Bodenmiller, B., 2014. Highly multiplexed imaging of tumor tissues with subcellular resolution by mass cytometry. Nat. Methods 11, 417–422. https://doi.org/10.1038/nmeth.2869.

Grossman, H.B., Liebert, M., Antelo, M., Dinney, C.P., Hu, S.X., Palmer, J.L., Benedict, W.F., 1998. p53 and RB expression predict progression in T1 bladder cancer. Clin. Cancer Res. 4, 829–834.

Hoesl, S., Neumann, B., Techritz, S., Linscheid, M., Theuring, F., Scheler, C., Jakubowski, N., Mueller, L., 2014. Development of a calibration and standardization procedure for LA-ICP-MS using a conventional ink-jet printer for quantification of proteins in electro- and Western-blot assays. J. Anal. At. Spectrom. 29, 1282–1291. https://doi.org/10.1039/c4ja00060a.

Hoesl, S., Neumann, B., Techritz, S., Sauter, G., Simon, R., Schlüter, H.W., Linscheid, M., Theuring, F., Jakubowski, N., Mueller, L., 2016. Internal standardization of LA-ICP-MS immuno imaging via printing of universal metal spiked inks onto tissue sections. J. Anal. At. Spectrom. 31, 801–808. https://doi.org/10.1039/c5ja00409h.

Konz, I., Fernández, B., Fernández, M.L., Pereiro, R., Sanz-Medel, A., 2012. Laser ablation ICP-MS for quantitative biomedical applications. Anal. Bioanal. Chem. 403, 2113–2125. https://doi.org/10.1007/s00216-012-6023-6.

Krause, M., Scheler, C., Bottger, U., Weisshoff, H., Linscheid, M.W., 2002. Method and Reagent for Specifically Identifying and Quantifying One or More Proteins in a Sample.

Lou, X., Zhang, G., Herrera, I., Kinach, R., Ornatsky, O., Baranov, V., Nitz, M., Winnik, M.A., 2007. Polymer-based elemental tags for sensitive bioassays. Angew. Chemie - Int. Ed. 46, 6111–6114. https://doi.org/10.1002/anie.200700796.

McDevitt, M.R., Ma, D., Simon, J., Frank, R.K., Scheinberg, D.A., 2002. Design and synthesis of225Ac radioimmunopharmaceuticals. Appl. Radiat. Isot. 57, 841–847. https://doi.org/10.1016/S0969-8043(02)00167-7.

Moraleja, I., Esteban-Fernández, D., Lázaro, A., Humanes, B., Neumann, B., Tejedor, A., Mena, M.L., Jakubowski, N., Gómez-Gómez, M.M., 2016. Printing metal-spiked inks for LA-ICP-MS bioimaging internal standardization: comparison of the different nephrotoxic behavior of cisplatin, carboplatin, and oxaliplatin. Anal. Bioanal. Chem. 408, 2309–2318. https://doi.org/10.1007/s00216-016-9327-0.

Moraleja, I., Mena, M.L., Lázaro, A., Neumann, B., Tejedor, A., Jakubowski, N., Gómez-Gómez, M.M., Esteban-Fernández, D., 2018. An approach for quantification of platinum distribution in tissues by LA-ICP-MS imaging using isotope dilution analysis. Talanta 178, 166–171. https://doi.org/10.1016/j.talanta.2017.09.031.

Nieto, M., Gil-Bea, F.J., Dalfó, E., Cuadrado, M., Cabodevilla, F., Sánchez, B., Catena, S., Sesma, T., Ribé, E., Ferrer, I., Ramírez, M.J., Gómez-Isla, T., 2006. Increased sensitivity to MPTP in human α-synuclein A30P transgenic mice. Neurobiol. Aging 27, 848–856. https://doi.org/10.1016/j.neurobiolaging.2005.04.010.

Paxinos, G., Franklin, K.B.J., 2008. The Mouse Brain in Stereotaxic Coordinates, 3rd edn. Elsevier Academic Press, New York.

Schwarz, G., Mueller, L., Beck, S., Linscheid, M.W., 2014. DOTA based metal labels for protein quantification: a review. J. Anal. At. Spectrom. 29, 221–233. https://doi.org/10.1039/c3ja50277e.

Seuma, J., Bunch, J., Cox, A., McLeod, C., Bell, J., Murray, C., 2008. Combination of immunohistochemistry and laser ablation ICP mass spectrometry for imaging of cancer biomarkers. Proteomics 8, 3775–3784. https://doi.org/10.1002/pmic.

200800167.
Waentig, L., Jakubowski, N., Hardt, S., Scheler, C., Roos, P.H., Linscheid, M.W., 2012. Comparison of different chelates for lanthanide labeling of antibodies and application in a Western blot immunoassay combined with detection by laser ablation (LA-)ICP-MS. J. Anal. At. Spectrom. 27, 1311. https://doi.org/10.1039/c2ja30068k.
Wang, H.A.O., Grolimund, D., Giesen, C., Borca, C.N., Shaw-Stewart, J.R.H., Bodenmiller, B., Günther, D., 2013. Fast chemical imaging at high spatial resolution by laser ablation inductively coupled plasma mass spectrometry. Anal. Chem. 85, 10107–10116. https://doi.org/10.1021/ac400996x.
Whetstone, P.A., Butlin, N.G., Corneillie, T.M., Meares, C.F., 2004. Element-coded affinity tags for peptides and proteins. Bioconjug. Chem. 15, 3–6. https://doi.org/10.1021/bc034150l.
Yalow, R.S., Berson, S.A., 1996. Immunoassay of endogenous plasma insulin in man. Obes. Res. 4, 583–600. https://doi.org/10.1002/j.1550-8528.1996.tb00274.x.

Supplementary Material

SUPPLEMENTARY TABLE 1 Summary of the acquisition parameters for ICP-MS and LA systems. ICP-MS: inductively coupled plasma mass spectrometry, LA: Laser ablation.

ICP-MS (Element XR)	
RF plasma source power	1350 W
Plasma gas flow rate	15 L min^{-1} Ar
Auxiliary gas flow rate	0.8 L min^{-1} Ar
Transport gas flow rate	0.8 L min^{-1} Ar
Nebulizer	Micro Mist with cyclonic spray chamber
Mass resolution	400 ($m/\Delta m$)
Selected Isotopes	^{115}In, ^{141}Pr, ^{153}Eu, ^{159}Tb, ^{165}Ho, ^{166}Er, ^{169}Tm, ^{175}Lu, ^{146}Nd
Scanning mode	E-scan
Sample time, ms	2
LA system (New Wave 213)	
Wavelength	213 nm
Helium gas flow rate	1 L min^{-1}
Laser energy	0.20 - 0.25 mJ (35% of full energy)
Laser spot size	35 or 130 µm
Scan speed	50 or 150 µm s^{-1}
Repetition frequency	20 Hz
Ablation mode	Scanning line per line with 10 % overlap
Analysis time	8h (50 µm s^{-1}) – 3h (150 µm $^{-1}$)

SUPPLEMENTARY TABLE 2 Alpha-synuclein positive cell counts in the whole right brain hemisphere without region specificity in sections stained with conventional IHC.

Sample ID	α-Syn positive cells (IHC)							
	Number of cells	Mean over replicates	SD replicate	RSD % replicate	Mean over genotype	SD genotype	RSD % genotype	Genotype
L62_842_replicate 1	924	991.5	95.5	9.6	893.8	191.1	21.4	L62
L62_842_replicate 2	1059							
L62_844_replicate 1	1053	1025.0	39.6	3.9				
L62_844_replicate 2	997							
L62_846_replicate 1	1124	1085.5	54.4	5.0				
L62_846_replicate 2	1047							
L62_847_replicate 1	462	545.0	117.4	21.5				
L62_847_replicate 2	628							
L62_848_replicate 1	1069	1067.0	2.8	0.3				
L62_848_replicate 2	1065							
L62_850_replicate 1	759	743.5	21.9	2.9				
L62_850_replicate 2	728							
L62_851_replicate 1	640	645.5	7.8	1.2				
L62_851_replicate 2	651							
L62_856_replicate 1	985	928.0	80.6	8.7				
L62_856_replicate 2	871							
L62_897_replicate 1	946	851.0	134.4	15.8				
L62_897_replicate 2	756							
L62_900_replicate 1	---	1056.0						
L62_900_replicate 2	1056							
WT_262_replicate 1	0	0	0	n.a	0	n.a	n.a	WT
WT_262_replicate 2	0							
WT_263_replicate 1	0	0	0	n.a				
WT_263_replicate 2	0							
WT_264_replicate 1	---	n.a	n.a	n.a				
WT_264_replicate 2	---							
WT_267_replicate 1	---	n.a	n.a	n.a				
WT_267_replicate 2	---							
WT_269_replicate 1	---	n.a	n.a	n.a				
WT_269_replicate 2	---							
WT_270_replicate 1	0	0	0	n.a				
WT_270_replicate 2	0							
WT_272_replicate 1	---	n.a	n.a	n.a				
WT_272_replicate 2	---							
WT_276_replicate 1	0	0	0	n.a				
WT_276_replicate 2	0							
WT_279_replicate 1	0	0	0	n.a				
WT_279_replicate 2	0	n.a	n.a	n.a				
WT_280_replicate 1	0	0	0	n.a				
WT_280_replicate 2	0							

SUPPLEMENTARY TABLE 3 TH positive cell counts in the whole right brain hemisphere without region specificity in sections stained with conventional IHC. TH: tyrosine hydroxylase.

Sample ID	TH positive cells (IHC)							
	Number of cells	Mean over replicates	SD replicate	RSD % replicate	Mean over genotype	SD genotype	RSD % genotype	Genotype
L62_842_replicate 1	167	150.5	23.3	15.5	143.5	74.8	52.1	L62
L62_842_replicate 2	134							
L62_844_replicate 1	195	205.5	14.8	7.2				
L62_844_replicate 2	216							
L62_846_replicate 1	95	88.5	9.2	10.4				
L62_846_replicate 2	82							
L62_847_replicate 1	109	93.5	21.9	23.4				
L62_847_replicate 2	78							
L62_848_replicate 1	74	62.5	16.3	26.0				
L62_848_replicate 2	51							
L62_850_replicate 1	108	104.5	4.9	4.7				
L62_850_replicate 2	101							
L62_851_replicate 1	104	86.5	24.7	28.6				
L62_851_replicate 2	69							
L62_856_replicate 1	208	224.5	23.3	10.4				
L62_856_replicate 2	241							
L62_897_replicate 1	---	n.a	n.a	n.a				
L62_897_replicate 2	---							
L62_900_replicate 1	314	275.5	54.4	19.8				
L62_900_replicate 2	237							
WT_262_replicate 1	94	92.5	2.1	2.3	155.0	62.1	40.0	WT
WT_262_replicate 2	91							
WT_263_replicate 1	171	136	49.5	36.4				
WT_263_replicate 2	101							
WT_264_replicate 1	99	83.5	21.9	26.3				
WT_264_replicate 2	68							
WT_267_replicate 1	166	120.5	64.3	53.4				
WT_267_replicate 2	75							
WT_269_replicate 1	246	198	67.9	34.3				
WT_269_replicate 2	150							
WT_270_replicate 1	256	192.5	89.8	46.7				
WT_270_replicate 2	129							
WT_272_replicate 1	248	221	38.2	17.3				
WT_272_replicate 2	194							
WT_276_replicate 1	81	78.5	3.5	4.5				
WT_276_replicate 2	76							
WT_279_replicate 1	194	170.5	33.2	19.5				
WT_279_replicate 2	147							
WT_280_replicate 1	---	257	n.a	n.a				
WT_280_replicate 2	257							

SUPPLEMENTARY TABLE 4 Integrated density of NeuN positive neurones in the whole right brain hemisphere without region specificity in sections stained with conventional IHC. NeuN: neuronal nuclear antigen.

Sample ID	NeuN integrated density (IHC)							
	Integrated density	Mean over replicates	SD replicate	RSD % replicate	Mean over genotype	SD genotype	RSD % genotype	Genotype
L62_842_replicate 1	---	9.54E+08	n.a	n.a	9.37E+08	2.36E+08	25.17	L62
L62_842_replicate 2	9.54E+08							
L62_844_replicate 1	8.09E+08	8.10E+08	1.41E+06	0.17				
L62_844_replicate 2	8.11E+08							
L62_846_replicate 1	8.15E+08	1.08E+09	3.71E+08	34.45				
L62_846_replicate 2	1.34E+09							
L62_847_replicate 1	1.05E+09	1.33E+09	3.96E+08	29.77				
L62_847_replicate 2	1.61E+09							
L62_848_replicate 1	1.33E+09	1.24E+09	1.34E+08	10.88				
L62_848_replicate 2	1.14E+09							
L62_850_replicate 1	---	7.82E+08	n.a	n.a				
L62_850_replicate 2	7.82E+08							
L62_851_replicate 1	1.04E+09	1.04E+09	0.00E+00	0.00				
L62_851_replicate 2	1.04E+09							
L62_856_replicate 1	9.13E+08	8.45E+08	9.62E+07	11.38				
L62_856_replicate 2	7.77E+08							
L62_897_replicate 1	6.13E+08	5.72E+08	5.87E+07	10.27				
L62_897_replicate 2	5.30E+08							
L62_900_replicate 1	8.00E+08	7.26E+08	1.05E+08	14.52				
L62_900_replicate 2	6.51E+08							
WT_262_replicate 1	1.35E+09	1.55E+09	2.83E+08	18.25	1.71E+09	3.60E+08	21.06	WT
WT_262_replicate 2	1.75E+09							
WT_263_replicate 1	1.31E+09	1.31E+09	n.a	n.a				
WT_263_replicate 2	---							
WT_264_replicate 1	1.79E+09	2.43E+09	9.05E+08	37.25				
WT_264_replicate 2	3.07E+09							
WT_267_replicate 1	1.49E+09	1.81E+09	4.45E+08	24.68				
WT_267_replicate 2	2.12E+09							
WT_269_replicate 1	1.45E+09	1.69E+09	3.32E+08	19.72				
WT_269_replicate 2	1.92E+09							
WT_270_replicate 1	1.03E+09	1.41E+09	5.30E+08	37.75				
WT_270_replicate 2	1.78E+09							
WT_272_replicate 1	---	2.08E+09	n.a	n.a				
WT_272_replicate 2	2.08E+09							
WT_276_replicate 1	1.22E+09	1.41E+09	2.69E+08	19.06				
WT_276_replicate 2	1.60E+09							
WT_279_replicate 1	---	1.46E+09	n.a	n.a				
WT_279_replicate 2	1.46E+09							
WT_280_replicate 1	1.98E+09	1.98E+09	0.00E+00	0.00				
WT_280_replicate 2	1.98E+09							

SUPPLEMENTARY TABLE 5 Integrated density of GFAP positive neurones in the whole right brain hemisphere without region specificity in sections stained with conventional IHC. GFAP: glial fibrillary acidic protein.

Sample ID	GFAP integrated density (IHC)							
	Integrated density	Mean over replicates	SD replicate	RSD % replicate	Mean over genotype	SD genotype	RSD % genotype	Genotype
L62_842_replicate 1	1.48E+09	1.53E+09	7.07E+07	4.62	2.63E+09	9.19E+08	35.03	L62
L62_842_replicate 2	1.58E+09							
L62_844_replicate 1	1.42E+09	1.49E+09	9.90E+07	6.64				
L62_844_replicate 2	1.56E+09							
L62_846_replicate 1	2.39E+09	2.20E+09	2.69E+08	12.21				
L62_846_replicate 2	2.01E+09							
L62_847_replicate 1	2.38E+09	2.38E+09	n.a	n.a				
L62_847_replicate 2	---							
L62_848_replicate 1	2.98E+09	2.89E+09	1.34E+08	4.66				
L62_848_replicate 2	2.79E+09							
L62_850_replicate 1	1.81E+09	1.81E+09	n.a	n.a				
L62_850_replicate 2	---							
L62_851_replicate 1	6.30E+08	2.71E+09	2.94E+09	108.54				
L62_851_replicate 2	4.79E+09							
L62_856_replicate 1	3.06E+09	3.27E+09	2.97E+08	9.08				
L62_856_replicate 2	3.48E+09							
L62_897_replicate 1	5.94E+09	4.07E+09	2.65E+09	65.23				
L62_897_replicate 2	2.19E+09							
L62_900_replicate 1	5.29E+09	3.91E+09	1.95E+09	49.91				
L62_900_replicate 2	2.53E+09							
WT_262_replicate 1	2.24E+09	2.03E+09	2.97E+08	14.63	1.54E+09	3.32E+08	21.58	WT
WT_262_replicate 2	1.82E+09							
WT_263_replicate 1	2.58E+09	2.02E+09	7.99E+08	39.65				
WT_263_replicate 2	1.45E+09							
WT_264_replicate 1	1.38E+09	1.31E+09	1.06E+08	8.13				
WT_264_replicate 2	1.23E+09							
WT_267_replicate 1	1.38E+09	1.30E+09	1.13E+08	8.70				
WT_267_replicate 2	1.22E+09							
WT_269_replicate 1	8.27E+08	1.95E+09	1.59E+09	81.40				
WT_269_replicate 2	3.07E+09							
WT_270_replicate 1	1.28E+09	1.11E+09	2.42E+08	21.81				
WT_270_replicate 2	9.38E+08							
WT_272_replicate 1	1.33E+09	1.41E+09	1.06E+08	7.55				
WT_272_replicate 2	1.48E+09							
WT_276_replicate 1	1.66E+09	1.42E+09	3.39E+08	23.90				
WT_276_replicate 2	1.18E+09							
WT_279_replicate 1	9.07E+08	1.48E+09	8.08E+08	54.67				
WT_279_replicate 2	2.05E+09							
WT_280_replicate 1	1.20E+09	1.38E+09	2.55E+08	18.45				
WT_280_replicate 2	1.56E+09							

SUPPLEMENTARY TABLE 6 Alpha-synuclein counts in the whole right brain hemisphere without region specificity in sections stained with singleplex IMC.

Sample ID	α-Syn-MeCAT(Eu) singleplex-IMC							
	α-Syn counts (Eu/In)	Mean over replicates	SD replicate	RSD % replicate	Mean over genotype	SD genotype	RSD % genotype	Genotype
L62_842_replicate 1	6.98E+06	6.85E+06	1.91E+05	2.79	5.36E+06	1.52E+06	28.4	L62
L62_842_replicate 2	6.71E+06							
L62_844_replicate 1	7.43E+06	7.54E+06	1.48E+05	1.97				
L62_844_replicate 2	7.64E+06							
L62_846_replicate 1	7.47E+06	7.56E+06	1.20E+05	1.59				
L62_846_replicate 2	7.64E+06							
L62_847_replicate 1	---	n.a	n.a	n.a				
L62_847_replicate 2	---							
L62_848_replicate 1	4.18E+06	4.17E+06	1.41E+04	0.34				
L62_848_replicate 2	4.16E+06							
L62_850_replicate 1	5.12E+06	4.90E+06	3.11E+05	6.35				
L62_850_replicate 2	4.68E+06							
L62_851_replicate 1	4.21E+06	3.88E+06	4.67E+05	12.03				
L62_851_replicate 2	3.55E+06							
L62_856_replicate 1	3.64E+06	4.99E+06	1.91E+06	38.26				
L62_856_replicate 2	6.34E+06							
L62_897_replicate 1	4.03E+06	4.11E+06	1.13E+05	2.75				
L62_897_replicate 2	4.19E+06							
L62_900_replicate 1	5.79E+06	4.24E+06	2.20E+06	51.93				
L62_900_replicate 2	2.68E+06							
WT_262_replicate 1	---	n.a	n.a	n.a	5.76E+04	9.84E+03	17.1	WT
WT_262_replicate 2	---							
WT_263_replicate 1	6.32E+04	6.21E+04	1.56E+03	2.51				
WT_263_replicate 2	6.10E+04							
WT_264_replicate 1	---	n.a	n.a	n.a				
WT_264_replicate 2	---							
WT_267_replicate 1	---	n.a	n.a	n.a				
WT_267_replicate 2	---							
WT_269_replicate 1	---	n.a	n.a	n.a				
WT_269_replicate 2	---							
WT_270_replicate 1	6.58E+04	6.55E+04	4.24E+02	0.65				
WT_270_replicate 2	6.52E+04							
WT_272_replicate 1	---	n.a	n.a	n.a				
WT_272_replicate 2	---							
WT_276_replicate 1	6.33E+04	6.33E+04	7.07E+01	0.11				
WT_276_replicate 2	6.32E+04							
WT_279_replicate 1	6.34E+04	5.58E+04	1.08E+04	19.41				
WT_279_replicate 2	4.81E+04							
WT_280_replicate 1	4.13E+04	4.12E+04	1.41E+02	0.34				
WT_280_replicate 2	4.11E+04							

SUPPLEMENTARY TABLE 7 TH counts in the whole right brain hemisphere without region specificity in sections stained with singleplex IMC. TH: tyrosine hydroxylase.

Sample ID	TH-MeCAT(Tb) singleplex-IMC							
	TH counts (Tb/In)	Mean over replicates	SD replicate	RSD % replicate	Mean over genotype	SD genotype	RSD % genotype	Genotype
L62_842_replicate 1	3.58E+05	3.73E+05	2.12E+04	5.69	3.64E+05	1.95E+04	5.4	L62
L62_842_replicate 2	3.88E+05							
L62_844_replicate 1	3.83E+05	3.89E+05	8.49E+03	2.18				
L62_844_replicate 2	3.95E+05							
L62_846_replicate 1	3.73E+05	3.71E+05	3.54E+03	0.95				
L62_846_replicate 2	3.68E+05							
L62_847_replicate 1	3.24E+05	3.25E+05	1.41E+03	0.44				
L62_847_replicate 2	3.26E+05							
L62_848_replicate 1	3.66E+05	3.62E+05	6.36E+03	1.76				
L62_848_replicate 2	3.57E+05							
L62_850_replicate 1	3.75E+05	3.75E+05	0.00E+00	0.00				
L62_850_replicate 2	3.75E+05							
L62_851_replicate 1	3.74E+05	3.78E+05	4.95E+03	1.31				
L62_851_replicate 2	3.81E+05							
L62_856_replicate 1	---	n.a	n.a	n.a				
L62_856_replicate 2	---							
L62_897_replicate 1	3.31E+05	3.43E+05	1.70E+04	4.95				
L62_897_replicate 2	3.55E+05							
L62_900_replicate 1	3.42E+05	3.60E+05	2.55E+04	7.07				
L62_900_replicate 2	3.78E+05							
WT_262_replicate 1	3.84E+05	3.97E+05	1.77E+04	4.46	3.88E+05	8.29E+03	2.1	WT
WT_262_replicate 2	4.09E+05							
WT_263_replicate 1	3.65E+05	3.84E+05	2.69E+04	7.00				
WT_263_replicate 2	4.03E+05							
WT_264_replicate 1	---	n.a	n.a	n.a				
WT_264_replicate 2	---							
WT_267_replicate 1	---	n.a	n.a	n.a				
WT_267_replicate 2	---							
WT_269_replicate 1	4.08E+05	3.95E+05	1.91E+04	4.84				
WT_269_replicate 2	3.81E+05							
WT_270_replicate 1	3.56E+05	3.86E+05	4.17E+04	10.82				
WT_270_replicate 2	4.15E+05							
WT_272_replicate 1	3.90E+05	3.74E+05	2.26E+04	6.05				
WT_272_replicate 2	3.58E+05							
WT_276_replicate 1	3.89E+05	3.84E+05	7.07E+03	1.84				
WT_276_replicate 2	3.79E+05							
WT_279_replicate 1	3.90E+05	3.96E+05	8.49E+03	2.14				
WT_279_replicate 2	4.02E+05							
WT_280_replicate 1	---	n.a	n.a	n.a				
WT_280_replicate 2	---							

SUPPLEMENTARY TABLE 8 NeuN counts in the whole right brain hemisphere without region specificity in sections stained with singleplex IMC. NeuN: neuronal nuclear antigen.

Sample ID	NeuN-MeCAT(Pr) singleplex-IMC							
	NeuN counts (Pr/In)	Mean over replicates	SD replicate	RSD % replicate	Mean over genotype	SD genotype	RSD % genotype	Genotype
L62_842_replicate 1	6.38E+06	5.98E+06	5.66E+05	9.46	4.95E+06	7.47E+05	15.1	L62
L62_842_replicate 2	5.58E+06							
L62_844_replicate 1	6.78E+06	5.96E+06	1.17E+06	19.59				
L62_844_replicate 2	5.13E+06							
L62_846_replicate 1	6.36E+06	5.84E+06	7.42E+05	12.72				
L62_846_replicate 2	5.31E+06							
L62_847_replicate 1	4.34E+06	4.20E+06	2.05E+05	4.89				
L62_847_replicate 2	4.05E+06							
L62_848_replicate 1	4.86E+06	4.74E+06	1.77E+05	3.73				
L62_848_replicate 2	4.61E+06							
L62_850_replicate 1	5.53E+06	5.28E+06	3.61E+05	6.84				
L62_850_replicate 2	5.02E+06							
L62_851_replicate 1	4.07E+06	4.07E+06	n.a	n.a				
L62_851_replicate 2								
L62_856_replicate 1	4.39E+06	4.44E+06	7.07E+04	1.59				
L62_856_replicate 2	4.49E+06							
L62_897_replicate 1	4.97E+06	4.60E+06	5.30E+05	11.54				
L62_897_replicate 2	4.22E+06							
L62_900_replicate 1	5.29E+06	4.41E+06	1.24E+06	28.22				
L62_900_replicate 2	3.53E+06							
WT_262_replicate 1	---	n.a	n.a	n.a	9.43E+06	2.38E+06	25.3	WT
WT_262_replicate 2	---							
WT_263_replicate 1	9.94E+06	9.86E+06	1.20E+05	1.22				
WT_263_replicate 2	9.77E+06							
WT_264_replicate 1	6.50E+06	6.34E+06	2.26E+05	3.57				
WT_264_replicate 2	6.18E+06							
WT_267_replicate 1	9.84E+06	1.09E+07	1.46E+06	13.40				
WT_267_replicate 2	1.19E+07							
WT_269_replicate 1	8.95E+06	9.03E+06	1.13E+05	1.25				
WT_269_replicate 2	9.11E+06							
WT_270_replicate 1	1.24E+07	1.20E+07	6.36E+05	5.33				
WT_270_replicate 2	1.15E+07							
WT_272_replicate 1	1.31E+07	1.26E+07	7.78E+05	6.20				
WT_272_replicate 2	1.20E+07							
WT_276_replicate 1	8.75E+06	8.75E+06	7.07E+03	0.08				
WT_276_replicate 2	8.74E+06							
WT_279_replicate 1	6.23E+06	6.09E+06	2.05E+05	3.37				
WT_279_replicate 2	5.94E+06							
WT_280_replicate 1	---	n.a	n.a	n.a				
WT_280_replicate 2	---							

SUPPLEMENTARY TABLE 9 Alpha-synuclein counts in the whole right brain hemisphere without region specificity in sections stained with singleplex IMC. GFAP: glial fibrillary acidic protein.

Sample ID	GFAP-MeCAT(Ho) singleplex-IMC							
	GFAP counts (Ho/In)	Mean over replicates	SD replicate	RSD % replicate	Mean over genotype	SD genotype	RSD % genotype	Genotype
L62_842_replicate 1	---	n.a	n.a	n.a	1.42E+06	1.65E+05	11.6	L62
L62_842_replicate 2	---							
L62_844_replicate 1	1.78E+06	1.74E+06	5.66E+04	3.25				
L62_844_replicate 2	1.70E+06							
L62_846_replicate 1	1.50E+06	1.46E+06	5.66E+04	3.87				
L62_846_replicate 2	1.42E+06							
L62_847_replicate 1	1.16E+06	1.26E+06	1.41E+05	11.22				
L62_847_replicate 2	1.36E+06							
L62_848_replicate 1	1.29E+06	1.26E+06	4.24E+04	3.37				
L62_848_replicate 2	1.23E+06							
L62_850_replicate 1	1.30E+06	1.45E+06	2.05E+05	14.19				
L62_850_replicate 2	1.59E+06							
L62_851_replicate 1	1.42E+06	1.39E+06	4.95E+04	3.57				
L62_851_replicate 2	1.35E+06							
L62_856_replicate 1	1.26E+06	1.35E+06	1.20E+05	8.94				
L62_856_replicate 2	1.43E+06							
L62_897_replicate 1	1.58E+06	1.59E+06	7.07E+03	0.45				
L62_897_replicate 2	1.59E+06							
L62_900_replicate 1	1.24E+06	1.26E+06	2.12E+04	1.69				
L62_900_replicate 2	1.27E+06							
WT_262_replicate 1	9.00E+05	9.08E+05	1.13E+04	1.25	9.02E+05	5.65E+03	0.6	WT
WT_262_replicate 2	9.16E+05							
WT_263_replicate 1	9.20E+05	9.05E+05	2.12E+04	2.34				
WT_263_replicate 2	8.90E+05							
WT_264_replicate 1	8.76E+05	8.99E+05	3.18E+04	3.54				
WT_264_replicate 2	9.21E+05							
WT_267_replicate 1	9.25E+05	9.06E+05	2.76E+04	3.05				
WT_267_replicate 2	8.86E+05							
WT_269_replicate 1	---	n.a	n.a	n.a				
WT_269_replicate 2	---							
WT_270_replicate 1	8.81E+05	9.02E+05	2.90E+04	3.22				
WT_270_replicate 2	9.22E+05							
WT_272_replicate 1	9.03E+05	8.93E+05	1.48E+04	1.66				
WT_272_replicate 2	8.82E+05							
WT_276_replicate 1	8.92E+05	9.08E+05	2.19E+04	2.42				
WT_276_replicate 2	9.23E+05							
WT_279_replicate 1	8.89E+05	8.95E+05	8.49E+03	0.95				
WT_279_replicate 2	9.01E+05							
WT_280_replicate 1	9.13E+05	9.06E+05	9.90E+03	1.09				
WT_280_replicate 2	8.99E+05							

SUPPLEMENTARY TABLE 10 Alpha-synuclein counts in the whole right brain hemisphere without region specificity in sections stained with multiplex IMC.

Sample ID	α-Syn-MeCAT(Eu) multiplex-IMC							
	α-Syn counts (Eu/In)	Mean over replicates	SD replicate	RSD % replicate	Mean over genotype	SD genotype	RSD % genotype	Genotype
L62_842_replicate 1	---	n.a	n.a	n.a	5.18E+06	1.12E+06	21.6	L62
L62_842_replicate 2	---							
L62_844_replicate 1	---	n.a	n.a	n.a				
L62_844_replicate 2	---							
L62_846_replicate 1	---	n.a	n.a	n.a				
L62_846_replicate 2	---							
L62_847_replicate 1	6.87E+06	6.72E+06	2.12E+05	3.16				
L62_847_replicate 2	6.57E+06							
L62_848_replicate 1	4.09E+06	4.06E+06	4.95E+04	1.22				
L62_848_replicate 2	4.02E+06							
L62_850_replicate 1	5.12E+06	5.10E+06	2.83E+04	0.55				
L62_850_replicate 2	5.08E+06							
L62_851_replicate 1	---	n.a	n.a	n.a				
L62_851_replicate 2	---							
L62_856_replicate 1	---	n.a	n.a	n.a				
L62_856_replicate 2	---							
L62_897_replicate 1	4.89E+06	4.86E+06	4.24E+04	0.87				
L62_897_replicate 2	4.83E+06							
L62_900_replicate 1	---	n.a	n.a	n.a				
L62_900_replicate 2	---							
WT_262_replicate 1	---	n.a	n.a	n.a	5.79E+04	9.75E+03	16.9	WT
WT_262_replicate 2	---							
WT_263_replicate 1	---	n.a	n.a	n.a				
WT_263_replicate 2	---							
WT_264_replicate 1	---	n.a	n.a	n.a				
WT_264_replicate 2	---							
WT_267_replicate 1	5.94E+04	6.77E+04	1.17E+04	17.25				
WT_267_replicate 2	7.59E+04							
WT_269_replicate 1	---	n.a	n.a	n.a				
WT_269_replicate 2	---							
WT_270_replicate 1	6.50E+04	6.45E+04	7.07E+02	1.10				
WT_270_replicate 2	6.40E+04							
WT_272_replicate 1	5.04E+04	5.04E+04	7.07E+01	0.14				
WT_272_replicate 2	5.03E+04							
WT_276_replicate 1	6.19E+04	6.19E+04	0.00E+00	0.00				
WT_276_replicate 2	6.19E+04							
WT_279_replicate 1	---	n.a	n.a	n.a				
WT_279_replicate 2	---							
WT_280_replicate 1	4.06E+04	4.49E+04	6.08E+03	13.54				
WT_280_replicate 2	4.92E+04							

SUPPLEMENTARY TABLE 11 TH counts in the whole right brain hemisphere without region specificity in sections stained with multiplex IMC. TH: tyrosine hydroxylase.

Sample ID	TH-MeCAT(Tb) multiplex-IMC							
	TH counts (Tb/In)	Mean over replicates	SD replicate	RSD % replicate	Mean over genotype	SD genotype	RSD % genotype	Genotype
L62_842_replicate 1	---	n.a	n.a	n.a	3.49E+05	1.10E+04	3.2	L62
L62_842_replicate 2	---							
L62_844_replicate 1	---	n.a	n.a	n.a				
L62_844_replicate 2	---							
L62_846_replicate 1	---	n.a	n.a	n.a				
L62_846_replicate 2	---							
L62_847_replicate 1	3.38E+05	3.51E+05	1.84E+04	5.24				
L62_847_replicate 2	3.64E+05							
L62_848_replicate 1	3.57E+05	3.63E+05	8.49E+03	2.34				
L62_848_replicate 2	3.69E+05							
L62_850_replicate 1	3.16E+05	3.37E+05	2.90E+04	8.62				
L62_850_replicate 2	3.57E+05							
L62_851_replicate 1	---	n.a	n.a	n.a				
L62_851_replicate 2	---							
L62_856_replicate 1	---	n.a	n.a	n.a				
L62_856_replicate 2	---							
L62_897_replicate 1	3.46E+05	3.46E+05	0.00E+00	0.00				
L62_897_replicate 2	3.46E+05							
L62_900_replicate 1	---	n.a	n.a	n.a				
L62_900_replicate 2	---							
WT_262_replicate 1	---	n.a	n.a	n.a	3.73E+05	5.09E+03	1.4	WT
WT_262_replicate 2	---							
WT_263_replicate 1	---	n.a	n.a	n.a				
WT_263_replicate 2	---							
WT_264_replicate 1	---	n.a	n.a	n.a				
WT_264_replicate 2	---							
WT_267_replicate 1	3.71E+05	3.82E+05	1.48E+04	3.89				
WT_267_replicate 2	3.92E+05							
WT_269_replicate 1	---	n.a	n.a	n.a				
WT_269_replicate 2	---							
WT_270_replicate 1	3.81E+05	3.71E+05	1.41E+04	3.81				
WT_270_replicate 2	3.61E+05							
WT_272_replicate 1	3.92E+05	3.71E+05	2.97E+04	8.00				
WT_272_replicate 2	3.50E+05							
WT_276_replicate 1	3.81E+05	3.69E+05	1.77E+04	4.80				
WT_276_replicate 2	3.56E+05							
WT_279_replicate 1	---	n.a	n.a	n.a				
WT_279_replicate 2	---							
WT_280_replicate 1	3.99E+05	3.75E+05	3.39E+04	9.05				
WT_280_replicate 2	3.51E+05							

SUPPLEMENTARY TABLE 12 NeuN counts in the whole right brain hemisphere without region specificity in sections stained with multiplex IMC. NeuN: neuronal nuclear antigen.

Sample ID	NeuN-MeCAT(Pr) multiplex-IMC							
	NeuN counts (Pr/In)	Mean over replicates	SD replicate	RSD % replicate	Mean over genotype	SD genotype	RSD % genotype	Genotype
L62_842_replicate 1	---	n.a	n.a	n.a	4.76E+06	3.36E+05	7.1	L62
L62_842_replicate 2	---							
L62_844_replicate 1	---	n.a	n.a	n.a				
L62_844_replicate 2	---							
L62_846_replicate 1	---	n.a	n.a	n.a				
L62_846_replicate 2	---							
L62_847_replicate 1	4.76E+06	4.76E+06	7.07E+03	0.15				
L62_847_replicate 2	4.75E+06							
L62_848_replicate 1	4.43E+06	4.49E+06	8.49E+04	1.89				
L62_848_replicate 2	4.55E+06							
L62_850_replicate 1	5.21E+06	5.23E+06	2.83E+04	0.54				
L62_850_replicate 2	5.25E+06							
L62_851_replicate 1	---	n.a	n.a	n.a				
L62_851_replicate 2	---							
L62_856_replicate 1	---	n.a	n.a	n.a				
L62_856_replicate 2	---							
L62_897_replicate 1	4.59E+06	4.55E+06	5.66E+04	1.24				
L62_897_replicate 2	4.51E+06							
L62_900_replicate 1	---	n.a	n.a	n.a				
L62_900_replicate 2	---							
WT_262_replicate 1	---	n.a	n.a	n.a	1.00E+07	1.27E+06	12.7	WT
WT_262_replicate 2	---							
WT_263_replicate 1	---	n.a	n.a	n.a				
WT_263_replicate 2	---							
WT_264_replicate 1	---	n.a	n.a	n.a				
WT_264_replicate 2	---							
WT_267_replicate 1	9.91E+06	1.04E+07	7.00E+05	6.73				
WT_267_replicate 2	1.09E+07							
WT_269_replicate 1	---	n.a	n.a	n.a				
WT_269_replicate 2	---							
WT_270_replicate 1	1.24E+07	1.13E+07	1.56E+06	13.77				
WT_270_replicate 2	1.02E+07							
WT_272_replicate 1	1.09E+07	1.10E+07	1.41E+05	1.29				
WT_272_replicate 2	1.11E+07							
WT_276_replicate 1	8.63E+06	8.78E+06	2.05E+05	2.34				
WT_276_replicate 2	8.92E+06							
WT_279_replicate 1	---	n.a	n.a	n.a				
WT_279_replicate 2	---							
WT_280_replicate 1	8.34E+06	8.55E+06	2.90E+05	3.39				
WT_280_replicate 2	8.75E+06							

SUPPLEMENTARY TABLE 13 GFAP counts in the whole right brain hemisphere without region specificity in sections stained with multiplex IMC. GFAP: glial fibrillary acidic protein.

Sample ID	GFAP-MeCAT(Ho) multiplex-IMC							
	GFAP counts (Ho/In)	Mean over replicates	SD replicate	RSD % replicate	Mean over genotype	SD genotype	RSD % genotype	Genotype
L62_842_replicate 1	---	n.a	n.a	n.a	1.41E+06	3.17E+05	22.4	L62
L62_842_replicate 2	---							
L62_844_replicate 1	---	n.a	n.a	n.a				
L62_844_replicate 2	---							
L62_846_replicate 1	---	n.a	n.a	n.a				
L62_846_replicate 2	---							
L62_847_replicate 1	1.12E+06	1.16E+06	5.66E+04	4.88				
L62_847_replicate 2	1.20E+06							
L62_848_replicate 1	1.20E+06	1.22E+06	2.83E+04	2.32				
L62_848_replicate 2	1.24E+06							
L62_850_replicate 1	1.30E+06	1.41E+06	1.48E+05	10.57				
L62_850_replicate 2	1.51E+06							
L62_851_replicate 1	---	n.a	n.a	n.a				
L62_851_replicate 2	---							
L62_856_replicate 1	---	n.a	n.a	n.a				
L62_856_replicate 2	---							
L62_897_replicate 1	1.87E+06	1.86E+06	1.41E+04	0.76				
L62_897_replicate 2	1.85E+06							
L62_900_replicate 1	---	n.a	n.a	n.a				
L62_900_replicate 2	---							
WT_262_replicate 1	---	n.a	n.a	n.a	9.03E+05	6.96E+03	0.8	WT
WT_262_replicate 2	---							
WT_263_replicate 1	---	n.a	n.a	n.a				
WT_263_replicate 2	---							
WT_264_replicate 1	---	n.a	n.a	n.a				
WT_264_replicate 2	---							
WT_267_replicate 1	9.12E+05	9.01E+05	1.63E+04	1.81				
WT_267_replicate 2	8.89E+05							
WT_269_replicate 1	---	n.a	n.a	n.a				
WT_269_replicate 2	---							
WT_270_replicate 1	9.15E+05	9.03E+05	1.77E+04	1.96				
WT_270_replicate 2	8.90E+05							
WT_272_replicate 1	9.18E+05	8.92E+05	3.68E+04	4.12				
WT_272_replicate 2	8.66E+05							
WT_276_replicate 1	9.07E+05	9.08E+05	1.41E+03	0.16				
WT_276_replicate 2	9.09E+05							
WT_279_replicate 1	---	n.a	n.a	n.a				
WT_279_replicate 2	---							
WT_280_replicate 1	9.44E+05	9.10E+05	4.88E+04	5.36				
WT_280_replicate 2	8.75E+05							

9 Lebenslauf

Mein Lebenslauf wird aus datenschutzrechtlichen Gründen in der elektronischen Version meiner Arbeit nicht veröffentlicht.

10 Publikationsliste

Begutachtete Veröffentlichungen

Bader J., Neumann B., Schwab K., Popović M.K., Scheler C., Bajpai R. (2006) *α-Amylase Production in Fed Batch Cultivation of Bacillus caldolyticus: An Interpretation of Fermentation Course Using 2-D Gel Electrophoresis. Chemical and Biochemical Engineering Quarterly 20 (4): 413–420*

Bader J., Schwab K., Popović M.K., Bajpai R., Neumann B. (2007) *Application of pH and pO2 probes during Bacillus caldolyticus fermentation: An additional approach for improving a feeding strategy. Chemical and Biochemical Engineering Quarterly 12 (4): 315-320*

Ahrends R., Pieper S., Neumann B., Scheler C., Linscheid M.W. (2009) *Metal-Coded Affinity Tag Labeling: A Demonstration of Analytical Robustness and Suitability for Biological Applications; Anal. Chem. 2009, 81, 6, 2176–2184*

Schwab K., Neumann B., Scheler C., Jungblut P.R., Theuring F. (2011) *Adaptation of proteomic techniques for the identification and characterization of protein species from murine heart; Amino Acids Volume 41 (2); 2011*

Schwab K., Neumann B., Vignon-Zellweger N., Fischer A., Stein R., Jungblut P.R. Scheler C., Theuring F. (2011) *Dietary Phytoestrogen Supplementation induces Sex Differences in the Myocardial Protein Pattern of Mice: A Comparative Proteomics Study; Proteomics Volume 11; 2011*

Chen X., Muthoosamy K., Pfisterer A., Neumann B., Weil T. (2012) *Site-Selective Lysine Modification of Native Proteins and Peptides via Kinetically Controlled Labeling; Bioconjugate Chem. 2012, 23, 3, 500–508*

Bergmann U., Ahrends R., Neumann B., Scheler C., Linscheid M.W. (2012) *Application of Metal-Coded Affinity Tags (MeCAT): Absolute Protein Quantification with Top-Down and Bottom-Up Workflows by Metal-Coded Tagging; Anal. Chem. 2012, 84, 12, 5268–5275*

von Neuhoff N., Oumeraci T., Wolf T., Kollewe K., Bewerunge P., Neumann B., Brors B., Bufler J., Wurster U., Schlegelberger B., Dengler R., Zapatka M., Petri S. (2012) *Monitoring CSF Proteome Alterations in Amyotrophic Lateral Sclerosis: Obstacles and Perspectives in Translating a Novel Marker Panel to the Clinic. PLoS ONE 7(9)*

Chen X., Henschke L., Wu Q., Muthoosamy K., Neumann B., Weil T. (2013) *Site-selective azide incorporation into endogenous RNase A via a “chemistry” approach; Org Biomol Chem. 2013 Jan 14;11(2):353-61)*

Hoesl S., Neumann B., Techritz S., Linscheid M.W., Theuring F., Scheler C., Jakubowski N., Mueller L. (2014) *Development of a calibration and standardization procedure for LA-ICP-MS using a conventional ink-jet printer for quantification of proteins in electro- and Western-blot assays; Journal of Analytical Atomic Spectrometry 29(7):1282*

He Y., Esteban-Fernández D., Neumann B., Bergmann U., Bierkandt F., Linscheid M.W. (2016) *Application of MeCAT-Click labeling for protein abundance characterization of E. coli after heat shock experiments; Journal of Proteomics, Volume 136, 16 March 2016, Pages 68-76*

Hoesl S., Neumann B., Techritz S., Sauter G., Simon R., Schlüter H., Linscheid M.W., Theuring F., Jakubowski N., Mueller L. (2015) Internal standardization of LA-ICP-MS immuno imaging via printing of universal metal spiked inks onto tissue sections; Journal of Analytical Atomic Spectrometry 31(3)

Moraleja I., Esteban-Fernández D., Lázaro A., Humanes B., Neumann B., Tejedor A., Luz Mena M., Jakubowski N, Milagros Gómez-Gómez M. (2016) *Printing metal-spiked inks for LA-ICP-MS bioimaging internal standardization: comparison of the different nephrotoxic behavior of cisplatin, carboplatin, and oxaliplatin. Anal Bioanal Chem 408, 2309–2318*

Lehmann G.U.C., Lehmann K., Neumann B., Lehmann A.W., Scheler C., Jungblut P.R. (2017) *Protein analysis of the spermatophore reveals diverse compositions in both the ampulla and the spermatophylax in a bushcricket; Physiological Entomology 43(1), 1-9*

Moraleja I., Mena M.L., Lázaro A., Neumann B., Tejedor A., Jakubowski N., Gómez-Gómez M.M., Esteban-Fernández D. (2017) *An approach for quantification of platinum distribution in tissues by LA-ICP-MS imaging using isotope dilution analysis; Talanta Volume 178, 1 February 2018, Pages 166-17*

Aboulmagd S., Esteban-Fernández D., Moreno-Gordaliza E., Neumann B., El-Khatib A.H., Lázaro A., Tejedor A., Gómez-Gómez M.M., Linscheid M.W. (2017) *Dual Internal Standards with Metals and Molecules for MALDI Imaging of Kidney Lipids; Anal. Chem. 2017, 89, 23, 12727–12734*

Theuring F., Neumann B., Scheler C., Jungblut P.R., Schwab K. (2017) Sex differences in murine myocardium are not exclusively regulated by gonadal hormones; Journal of Proteomics, Volume 178, 30 April 2018, Pages 43-56

Nickel C., Horneff R., Heermann R., Neumann B., Jung K., Soll J., Schwenkert S. (2018) *Phosphorylation of the outer membrane mitochondrial protein OM64 influences protein import into mitochondria; Mitochondrion Volume 44, Pages 93-10*

El-Khatib A.H., Radbruch H., Trog S., Neumann B., Paul F., Koch A., Linscheid M.W., Jakubowski N., Schellenberger E. (2018) *Gadolinium in human brain sections and colocalization with other elements; Neurology Neuroimmunology & Neuroinflammation 6(1):e515*

Neumann B., Hösl S., Schwab K., Theuring F., Jakubowski N. (2020) *Multiplex LA-ICP-MS bio-imaging of brain tissue of a parkinsonian mouse model stained with metal-coded affinity-tagged antibodies and coated with indium-spiked commercial inks as internal standards; Journal of Neuroscience Methods Volume 334, 15 March 2020, 108591*

Lemke N., Melis V., Lauer D., Magbagbeolu M., Neumann B., Harrington C., Riedel G., Wischik C., Theuring F., Schwab K. (2020). *Differential compartmental processing and phosphorylation of pathogenic human tau and native mouse tau in the Line 66 model of frontotemporal dementia. Journal of Biological Chemistry. 295(52):18508-18523.*

Sonstige Veröffentlichungen, Poster und Tagungsbeiträge

Neumann B., Scheler C., Popovic M. (2003) Produktion von Aprotinin auf fermentationstechnischem Wege. TFH Forschungsbericht 2003/2004, 67-68

Popovic M., Neumann B., Scheler C. (2004) Einsatz von 2D-Gelelektrophorese zum besseren Verständnis der Vorgänge während einer rekombinanten Hochzelldichte-Kultivierung. Poster Chemie Ingenieur Technik, Vol. 76(9), 1252

Neumann B., Scheler C., Popovic M. (2004) *2D-Gel electrophoresis as useful tool for analysis of a glucose limited fermentation of E. coli*, Poster DECHEMA Jahrestagung

Bader J., Neumann B., Schwab K., Popović M.K., Scheler C., Bajpai R. (2005) α-*amylase production in fed-batch cultivation of Bacillus caldolyticus*. Poster Chemie Ingenieur Technik 77 (8): 1199-1200

Bader J., Schwab K., Neumann B., Popovic M.K., Scheler C., Pajpai R.; *Preliminary investigation: interpretation of a two component feeding strategy with the help of 2D-gel electrophoresis; 12. European Congress of Biotechnology, Copenhagen, Denmark, 21-24 August 2005*

Bader J., Neumann B., Schwab K., Popović M.K., Scheler C., Bajpai R. (2005) Preliminary investigation: *Development of a two component feeding strategy with the help of proteome analysis.* Poster *Journal of Biotechnology 118S1: 27*

Schwab K., Vignon-Zellweger N., Neumann B., Scheler C., Theuring F. (2005); *Proteome analysis of mouse heart: effects of gender, age, genetic polymorphism and hormonal manipulation in mice; International Symposium of CCR,* Berlin, Deutschland, 21.-22. Oktober 2005

Schwab K., Neumann B., Brokamp C., Popovic M.K. (2006) *Dual feeding strategy for the production of α-amylase by Bacillus caldolyticus; European Symposium on Biochemical Engineering Science, Salzburg, Austria,* 27.-30. August 2006

Schwab K., Neumann B., Vignon-Zellweger N., Theuring F. (2006) Proteome analysis of mouse hearts: effects of sex, age, diet and genetic background; Day of Science, CCR, Berlin, Deutschland, 23. November 2006

Vignon-Zellweger N., Relle K., Kienlen E., Heiden S., Voss F., Kalk P., Schwab K., Neumann B., Scheler C. *(2008) Additional lack of eNOS promotes cardiac fibrosis in ET-1 transgenic mice; 23rd Annual Scientific Meeting of the American Society of Hypertension, New Orleans, USA*, 14 – 17 Mai 2008

Schwab K., Neumann B., Vignon-Zellweger N., Scheler C., Theuring F. (2008); *Sex specific proteome and phosphoproteome analysis and the effects of phytoestrogens in heart and kidney of mice; J. Hypertension Volume 26 (Supplement 1); 2008*

Schwab K., Neumann B., Vignon-Zellweger N., Scheler C., Theuring F (2009) *Investigations of sex, age and dietary phytoestrogen related differential proteome patterns of murine heart and kidney; IUBMB Life Volume 61 (Issue 3); 2009*

Hardt S., Scheler C., Jakubowski N., Waentig L., Linscheid M.W. (2012) D*evelopment and application of metal-tagged antibodies for efficient diagnostic methods", 11th European Workshop on Laser ablation (11. EWLA),* 2012, Gijón, Spanien

Hardt S., Scheler C., Waentig L., Neumann B., Linscheid M.W., Jakubowski N. (2013) *Development and Application to metal-tagged Antibodies for immunoimaging by use of LA-ICP-MS, European Winter Conference on Plasma Spectrochemistry,* Krakau

Hardt S., Neumann, Waentig L., Scheler C., Schlüter H., Sauter G., Linscheid M.W., Theuring F., Jakubowski N. (2013) Entwicklung und Anwendung einer neuartigen internen Standardisierung zur Verbesserten Bildauflösung von Gewebeschnitten in der LA-ICP-MS46. Konferenz der Deutschen Gesellschaft für Massenspektrometrie (DGMS), 2013, Berlin Adlershof

Hoesl S., Neumann B., Linscheid M.W., Theuring F., Scheler C., Jakubowski N., Mueller L. (2014) 8-fach Multiplex Immunoassay unter Verwendung einer neuen internen Standardisierung zur Verbesserung der qualitativen Bildqualität, ICP-MS Anwendertreffen- HZG, Geesthacht bei Hamburg

11 Danksagung

An erster Stelle möchte ich mich bei Herrn Prof. Dr. Franz Theuring, Institut für Pharmakologie und Toxikologie der Charité, für die Überlassung des interessanten Themas, die umfängliche Unterstützung, seine inspirierende interdisziplinäre Offenheit gegenüber neuen Analysetechniken und das Analysematerial in Form von Gewebeproben und -schnitten bedanken. Aus seinem Arbeitskreis danke ich Frau Dr. Karima Schwab und Frau Nora Lemke für die wissenschaftliche Zusammenarbeit und ihre Mitwirkung für das Zustandekommen dieser Arbeit, Frau Magbagbeolu danke ich für die Anfertigung der IHC-Schnitte und ihre Hilfe bei der Präparation von Gewebeproben.

Mein Dank gilt außerdem Herrn Prof. Dr. Scheler, meinem Betreuer in der Proteome Factory AG, für die Vermittlung des Promotionsplatzes und die Unterstützung meines Promotionsvorhabens. Letzteres gilt im Besonderen auch für seine Nachfolgerin als Vorstand der Proteome Factory AG, Frau Dr. Karola Lehmann. Meinen Kollegen Julia Schendel, Ulf Bergmann und Konstantin Katsarov danke ich für ihre Unterstützung. Meiner Schwester Nadine danke ich für ihre initiale praktische Mithilfe am Entstehen dieser Arbeit.

Ich danke Herrn Dr. Norbert Jakubowski, ehemaliger Fachbereichsleiter an der Bundesanstalt für Materialforschung und -prüfung (BAM), Abteilung 1.1 Anorganische Spurenanalytik für seine Anregungen und sein fachübergreifendes Wissen, die zu dieser Arbeit beigetragen haben. Frau Dr. Simone Hösl, ehemals BAM, möchte ich meinen Dank für die Zusammenarbeit an diesem Projekt aussprechen.

Darüber hinaus möchte ich mich bei Herrn Prof. Dr. M. Linscheid, Institut für Chemie an der Humboldt Universität zu Berlin für die Zusammenarbeit und Unterstützung vieler Projekte und die Nutzung der Messgeräte bedanken. Herrn Prof. M. Popovic danke ich für seine vielfältige und langjährige Förderung wissenschaftlicher Projekte und Biografien.

Abschließend möchte ich meinen Eltern, aber vor allem meiner Frau Yasmin, für die moralische Unterstützung und anhaltendes Verständnis von ganzem Herzen Dank aussprechen.